# ENERGY DISSIPATION FROM ELASTIC INSTABILITIES OF COSINE-CURVED DOMES FOR SEISMIC PROTECTION IN REINFORCED CONCRETE STRUCTURES

By

Mansour Turki M Alturki

#### A DISSERTATION

Submitted to
Michigan State University
in partial fulfillment of the requirements
for the degree of

Civil Engineering - Doctor of Philosophy

2019

#### **ABSTRACT**

# ENERGY DISSIPATION FROM ELASTIC INSTABILITIES OF COSINE-CURVED DOMES FOR SEISMIC PROTECTION IN REINFORCED CONCRETE STRUCTURES

By

#### Mansour Turki M Alturki

Conventional seismic design is based on designing structures to resist the imposed seismic loads within their inelastic range of response. This requires the structures to undergo large permanent deformations. Although this design strategy usually satisfies safety requirements, the economic aspects are not usually met due to extensive irreparable damage to the structures in case of strong ground motion. Therefore, research trends are now focused on satisfying safety requirements as well as making structures operational immediately after an earthquake. This has led to the development of new and innovative systems of seismic structural protection that aim to minimize seismic energy input and to localize demands in replaceable or elastic elements. Several supplemental passive energy dissipation devices have been developed to achieve this goal. However, they possess some performance shortcomings such as the requirement of repair or replacement and the significant increase in the initial stiffness of the host structural system.

In this research, a new self-centering energy dissipation system that relies on elastic instabilities is proposed as a damping mechanism in structures resisting seismic actions. The system is composed of serially connected multistable cosine-curved domes (CCD) featuring snapthrough instability. The system exhibits a hysteretic response via the generation of multiple consecutive snap-through buckling events. Numerical studies and experimental tests were conducted on the geometric and material properties of individual CCD units and on a system of units proposed to examine the force-displacement and energy dissipation characteristics. Finite element analyses (FEA) were performed to: (1) study the controlling geometric and material

properties of the CCD to characterize the snap-through response, and (2) simulate the hysteretic response of the system to develop a multilinear analytical model, which was used to study the energy dissipation characteristics of the system. Experimental tests were conducted on 3D printed CCD units and system specimens to: (1) validate the FEA model of the units, and (2) to analyze the system and validate the analytical model. Good agreement was observed using the developed relations for the CCD response and the analytical model with the results from FEA and experimental tests. Results show that the energy dissipation of the system mainly depends on the number and the apex height-to-thickness ratio of the CCD units.

The damping characteristics of the proposed system were investigated to facilitate the direct displacement-based seismic design of structures incorporating such systems as the main damping mechanism to dissipate seismic energy. Time-history analyses of linear and nonlinear single degree of freedom systems were performed to compare spectral displacements and the equivalent viscous damping (EVD) ratios of the hysteretic response of the system to their substitute linear systems in terms of maximum displacements. A set of 62 ground motion records were considered for the analysis. A statistical study was conducted on the resulting displacements and the EVD ratios to develop expressions for EVD ratios of the hysteretic response. Results show that using proposed EVD ratios for the substitute linear systems yield good approximation for the peak spectral displacements compared to the original nonlinear systems. Finally, the seismic performance of typical reinforced concrete structures incorporating the proposed system in various configurations was evaluated. Direct displacement-based design and nonlinear time-history analyses of example structures subjected to two historic ground motion records were conducted. The modified structures using the proposed system showed an enhanced seismic response compared to the original structures by increasing damping and eliminating damage.

#### **ACKNOWLEDGMENTS**

First, I thank Allah (God), the most gracious, the most merciful, for endowing me with health, patience, and knowledge to complete this work.

I would like to express my deepest gratitude to my advisor and mentor Prof. Rigoberto Burgueño for his guidance, support, and encouragement during my research work. I thank him for guiding me with his knowledge and experience during many lengthy discussions on various topics related to my work. Also, for the discipline he instilled in me regarding hard work and professionalism.

I would also like to extend my appreciation to Professors Patrick Kwon, Mahmoodul Haq and Weiyi Lu for serving on my guidance committee and helping me undertake the work in this dissertation.

Appreciations are also due to my colleagues in the Department of Civil and Environmental Engineering who shared their knowledge and experience with me during my research; including, Ata Babazadeh, Nan Hu, Saleh Alogla, Ali Imani Azad, and Abdullah Alfehaid. Special thanks are also due to Department of Civil and Environmental Engineering, particularly Laura Post and Laura Taylor for their constant administrative support.

Acknowledgement is due to Qassim University, Kingdom Saudi Arabia, for granting me a scholarship to pursue my Ph.D. program at Michigan State University. Special thanks are due the Saudi Arabian Cultural Mission to the United States for administrating the scholarship.

Finally, I would like to express my gratitude to my mother, my wife Abeer, and my family for their unconditional support and prayers at all times.

# TABLE OF CONTENTS

LIST OF	TABLES	ix
LIST OF	F FIGURES	x
CHAPT	ER ONE	1
1 Intr	oduction	1
1.1 N	Motivation and Vision	1
1.2 E	Background	5
1.2.1	e	
1.2.2		
1.3 F	Research Hypothesis and Significance	
1.3.1	• •	
1.3.2	• ±	
	Research Objectives	
	Outline	
CHAPT	ER TWO	13
	erature Review	
	Overview	
	Elements and Systems with Elastic Instabilities	
2.2.1	·	
2.2.2	• · · · · · · · · · · · · · · · · · · ·	
2.2.3	Elements with surface of revolution	
2.2.4	Elements with buckling instabilities	
2.3 S	Structural Systems with Passive Energy Dissipation Devices	
2.3.1		
2.3.2	Sliding friction energy dissipation devices	
CHAPT	ER THREE	22
3 Cha	aracterization of Cosine-Curved Domes	22
3.1	Overview	22
3.2 E	Background	22
	Methods	
3.3.1	Research aim and scope	
3.3.2	Modeling and analysis	26
3.3.3	Experimental validation	
	Parametric Study	
3.4.1	Effect of length (l)	
3.4.2	Effect of thickness (t)	
3.4.3		
3.4.4		
	Effect of modulus of elasticity (E)	

3.4.6	Effect of Poisson's ratio (v)	40
3.5 I	Design Expressions for CCDs	41
3.5.1	Critical limit-point (snap-through) load (F <sub>c</sub> )	43
3.5.2	Minimum Load (F <sub>n</sub> )	
3.5.3	Critical limit-point displacement ( $\delta_c$ )	
3.5.4	Displacement at $F_n(\delta_n)$	
3.5.5	Post snap-through stiffness (k <sub>III</sub> )	
3.5.6	Limiting h/t for pseudo-bistable state	
3.5.7	Example: Approximate analysis of single and multiple CCDs	
	Conclusions	
CHAPT	ER FOUR	55
	ltiple Cosine-Curved Dome System	
	Overview	
	Background	
	Multiple Cosine-Curved Dome (MCCD) System	
	Response of a single CCD unit	
4.3.2		62
4.3.3		
	Analytical Model for MCCD System	
	Loading stages	
4.4.2		
4.4.	<u>.</u>	
	2.2 Unloading path	
4.4.	0 1	
	Experimental Validation	
4.5.1	1	
4.5.2	Model validation.	
4.5.3	Model modification for strength variation	
	Loading rate	
	Energy Dissipation Characteristics	
	Conclusions	
1.7	0010101010	
CHAPT	ER FIVE	88
	iivalent Viscous Damping	
_	Overview	
	Background	
5.2.1		
5.2.2		
	Methods	
5.3.1	Idealized hysteretic response of the MCCD system	
5.3.1	· · · · · · · · · · · · · · · · · · ·	
5.3. 5.3.		
5.3.2	Considered cases for the study	
5.3.3	Ground motion records	
	Analysis procedure	
+	/ VIIII VOID 1/11/XAAIIII V	

5.4	Results and Discussion	107
5.4.1	1 Ratio of nonlinear to linear spectral displacements	107
5.4.2	2 Equivalent viscous damping ratios	108
5.4.3		
5.5	Conclusions	
CHAP'	TER SIX	115
6 Se	eismic Performance Evaluation	115
6.1	Introduction	115
6.2	Seismic Hazards	115
6.3	Bridge Pier-Wall	116
6.3.1	1 Modified system	117
6.3.2	2 Material properties	118
6.3.3	3 Conventional design of the pier-wall	119
6.	3.3.1 Idealized system	119
6.	3.3.2 Design	119
6.3.4	4 Design of the modified pier-wall	122
6.	3.4.1 Idealized system	122
6.	3.4.2 Design of the inner column	125
6.	3.4.3 Design of the MCCD system	126
6.3.5	5 Time-history analysis	128
6.4	Building Frame	131
6.4.1	1 Modified system	133
6.4.2	2 Conventional design of the frame	133
6.	4.2.1 Idealized system	133
6.	4.2.2 Design	134
6.4.3	B Design of the modified frame	136
6.	4.3.1 Idealized system	136
6.	4.3.2 Design of the MCCD system	137
6.4.4	4 Time-history analysis	139
6.5	Coupled Rocking Walls	141
6.5.1	1 Modified system	143
6.5.2	2 Conventional design of the coupled walls	143
6.	5.2.1 Idealized system	143
6.	5.2.2 Design	
6.5.3	B Design of the modified coupled walls	147
6.	5.3.1 Idealized system	147
6.	5.3.2 Design of the MCCD system	
6.5.4	4 Time-history analysis	150
6.6	Design Recommendations	152
6.7	Conclusions	154
CHAP'	TER SEVEN	155
7 C	onclusions	155
7.1	Research Contributions	
7.2	Conclusions	156

7.3	Future Research	158
APPE	NDIX	160
REFE	RENCES	176

# LIST OF TABLES

Table 3.1 Design and 'as-printed' dimensions of experimentally tested CCDs	27
Table 5.1 Recorded earthquake used in this study	105
Table 6.1 Ground motion records used in this study	115
Table 6.2 Properties of concrete and reinforcing steel used for the pier-wall	118
Table 6.3 Properties of the MCCD system for the modified pier-wall	126
Table 6.4 Properties of the MCCD system for the modified frame	137
Table 6.5 Properties of the unboned post-tensioning tendon used for the coupled walls	145
Table 6.6 Properties of the MCCD system for the modified coupled walls	147
Table 6.7 Scale factors used for the NLTHA for the coupled walls example	150

# LIST OF FIGURES

Figure 1.1 Example applications of the MCCD system incorporated in typical structural systems:  (a) frame with chevron braces, (b) pier-wall, (c) single-column, and (d) double-column MCCD systems
Figure 1.2 The MCCD system: (a) cross-section of a single CCD unit, (b) schematic force-displacement response of a single CCD, (c) MCCD composed of multiple CCDs, and (d) schematic hysteretic response of an MCCD system. Note that $\delta$ is the local CCD displacement while $\Delta$ is the global system displacement.
Figure 1.3 Typical strain energy-displacement and force-displacement of an element with snap-through behavior
Figure 1.4 Effect of increasing the number of serially connected elements on the dissipated energy
Figure 2.1 Examples for multistable inclined elements and unit cells: (a) identical tilted beams [20], (b) shallow geodesic lattice domes [25], and (c) shallow reticulated truss [26]
Figure 2.2 Examples for energy dissipation systems with inclined elements: (a) shape-reconfigurable materials [21], (b) multiple tetra-beam-plate lattice [23], and (c) periodic arrays of inclined beams [27]
Figure 2.3 Examples for multistable curved elements and unit cells: (a) curved double beams under tension [36], (b) T-shaped double curved beams [37], and (c) bistable arches [39]15
Figure 2.4 Examples for energy dissipation systems with curved elements: (a) Negative stiffness honeycombs [29], (b) 3D hexagonal micro-lattices [34], and (c) multistable modular structures [37]
Figure 2.5 Geometry of a clamped spherical dome
Figure 2.6 Examples for metallic energy dissipation devices: (a) bar-fuse damper [52], (b) seesaw slit damper [53], and (c) accordion metallic damper [59]
Figure 2.7 Examples for friction energy dissipation devices: (a) friction discs damper [61], (b) ring spring damper [65], and (c) self-centering friction braces [66]
Figure 3.1 Geometric parameters of a typical CCD: (a) a cross-section at the apex, and (b) the idealized system
Figure 3.2 Test setup for CCD under axial compression
Figure 3.3 Loading stages for: (a) monostable CCD, and (b) bistable CCD28

Figure 3.4 (a) $F$ - $\delta$ curves for specimen 5M from experiment compared to FEA, and (b) experimental $F$ - $\delta$ curves for specimens 11P, 12B, and 6M30
Figure 3.5 Actual and normalized $F$ - $\delta$ curves of CCDs with constant $t$ and $h$ , and varying $l$ 32
Figure 3.6 Actual and normalized $F$ - $\delta$ curves of CCDs with constant $h$ and $l$ , and varying $t$ 34
Figure 3.7 Actual and normalized $F$ - $\delta$ curves of CCDs with constant $t$ and $l$ , and varying $h$ 36
Figure 3.8 (a) $F$ - $\delta$ curves of CCDs with constant $h$ and $l$ , and varying $h/t$ and $d/l$ ; (b) original profile shape of the CCD; and (c) modified shape of CCD with added loading area38
Figure 3.9 Actual and normalized $F$ - $\delta$ curves of CCDs with constant $t$ , $h$ and $l$ , and varying $E$ 39
Figure 3.10 $F$ - $\delta$ curves of CCD with constant $t$ , $h$ , and $l$ , and varying $v$
Figure 3.11 Twelve monostable CCD units connected in series (a) hysteretic response from FEA, and (b) stacking configuration and idealized system
Figure 3.12 Actual and multilinear $F$ - $\delta$ responses of a CCD
Figure 3.13 $C_c$ curves with $h/t$ for different values of $v$
Figure 3.14 (a) $C_n$ curves with $h/t$ for different values of $v$ , and (b) zoom-in at $C_n = 0$ 46
Figure 3.15 Data and fit curves for $\delta_c/h$ and $\delta_n/h$ with $h/t$
Figure 3.16 (a) Critical height-to-thickness ratio $(h/t)_{cr}$ vs. $v$ ; (b) stability state for 3D printed specimens with $v = 0.33$ and $(h/t)_{cr} = 3.05$
Figure 3.17 Experimental, FEA, and approximate multilinear $F$ - $\delta$ responses of (a) a single CCD, and (b) system of 4 CCDs connected in series
Figure 3.18 Test setup for the four CCDs connected in series
Figure 4.1 Boundary conditions for: (a) curved-beams system, and (b) MCCD system57
Figure 4.2 Geometric parameters of a typical CCD: (a) cross-section at the apex, and (b) idealized system
Figure 4.3 (a) Normalized $F$ - $\delta$ response for monostable and bistable CCDs; (b) multilinear approximation of the $F$ - $\delta$ response of a CCD61
Figure 4.4 Possible configurations of CCD units in the vertical direction: (a) parallel stacking ( $n_p$ = 2), and (b) series stacking ( $n_s$ = 2)63
Figure 4.5 <i>F</i> -∆ curves for CCDs in (a) parallel configuration, and (b) series configuration64
Figure 4.6 The idealized MCCD system

Figure 4.7 Force-deformation curves from FEA for MCCD systems: (a) monostable, and (b) bistable
Figure 4.8 Number of CCDs in regions I, II, and III during loading stages for a system of $n_s = 4$
Figure 4.9 (a) Schematic $F$ - $\Delta$ response of the MCCD system with quantities used to develop the multilinear model; (b) Actual and multilinear $F$ - $\delta$ responses of a CCD unit71
Figure 4.10 $F$ - $\Delta$ curves from FEA and analytical model using (a) linear equations, and (b) nonlinear equations to calculate $k_{el}$ , $k_{elll}$ , $F_{bdi}$ and $F_{ndi}$
Figure 4.11 Test set up for an MCCD system with ten CCDs ( $n_s = 10$ )
Figure 4.12 <i>F-∆</i> curves for the MCCD system from experimental tests and (a) the analytical model and (b) modified model
Figure 4.13 Experimental $F-\Delta$ curves for an MCCD system at varying loading rates: 1, 3, 9, and 15 mm/s
Figure 4.14 (a) Normalized $F$ - $\delta$ curve for a CCD with $h/t = 2.75$ under force and displacement control conditions, and (b) loss factor with $h/t$ for different $n_s$ values
Figure 4.15 (a) $F$ - $\Delta$ curves for MCCDs with $h/t = 2.5$ and $n_s = 8$ and 14, and (b) loss factor with $n_s$ for different $h/t$ ratios
Figure 5.1 Concept of equivalent viscous damping in DDBD method: (a) hysteretic response, (b) relation between $\xi$ and $\mu_{\Delta}$ , and (c) displacement response spectra for different values of $\xi$ 91
Figure 5.2 Full cycle hysteretic response of the MCCD system with parameters for the modified Jacobsen' approach
Figure 5.3 (a) $F$ - $\Delta$ response of the MCCD system, and (b) $F$ - $\delta$ responses of a CCD unit with key response quantities
Figure 5.4 The actual and the idealized $F$ - $\Delta$ curves for an MCCD system with $n_s = \infty$ 97
Figure 5.5 (a) EVD ratios based on modified Jacobsen's approach $(\xi_J)$ and the ideal stiffness ratio $(k_z/k_b)$ with $h/t$ , and (b) displacement ductility $(\mu_d)$ and force difference ratio $(\beta_F)$ with $h/t$ 98
Figure 5.6 The actual and the idealized $F-\Delta$ curves for an MCCD system with $n_s \ll \infty$ 100
Figure 5.7 The relation between displacement ductility ( $\mu_{\Delta}$ ) with $n_s$ for a range of $h/t$ values101
Figure 5.8 (a) The relation between $\xi_J$ with $n_s$ for different $h/t$ ratios, and (b) $\beta_F$ with $h/t$ for different $n_s$ values
Figure 5.9 Hysteresis models considered: (a) Case 1-response of an MCCD system, and (b) Case 2-response of an MCCD system coupled with a non-yielding linear system

Figure 5.10 Scaled displacement response spectra of the motion records at 5 % damping and their average response
Figure 5.11 Average ratios of linear to nonlinear spectral displacements and coefficient of variation for Case 1 [(a) and (b)], and for Case 2 [(c) and (d)]
Figure 5.12 Average equivalent viscous damping ratio ( $\xi$ ) with $T_{eff}$ and $h/t$ for Case 1 [(a) and (c)], and Case 2 [(b) and (d)]
Figure 5.13 Developed expression for EVD compared with other expressions111
Figure 5.14 Averaged ratio of linear to nonlinear spectral displacements using the developed expression for Case 1 (a) and (b) Case 2,
Figure 6.1 Ground acceleration time histories for the earthquake used in the study: (a) 1940 El Centro N00E, and (b) 1985 Chile 1985 N10E
Figure 6.2 Example structure 1: (a) original pier-wall, and (b) modified pier-wall117
Figure 6.3 System idealization for analysis: (a) original pier-wall, and (b) modified pier-wall.119
Figure 6.4 Displacement response spectrum of the 1940 El Centro ground motion record used for the design
Figure 6.5 Cross-sectional details: (a) original pier-wall, and (b) modified pier-wall121
Figure 6.6 Force-displacement responses: (a) original pier-wall, and (b) modified pier-wall122
Figure 6.7 Relation between the lateral ( $\Delta_V$ ) and axial ( $\Delta$ ) displacements with lengths $h_b$ and $l_t$
Figure 6.8 (a) Loading mechanism for one chain of the CCD units, and (b) force-displacement response of the MCCD system
Figure 6.9 Lateral displacement time-history of the bridge pier-walls: (a) 1940 El Centro, and (b) 1985 Chile earthquakes
Figure 6.10 Hysteretic shear force-lateral displacement responses for the original pier-wall (a, c), and the modified pier-wall (b, d)
Figure 6.11 Example structure 2: (a) original frame, and (b) modified frame with chevron brace
Figure 6.12 System idealization for analysis: (a) original frame, and (b) modified frame134
Figure 6.13 Force-displacement responses: (a) original frame, and (b) modified frame136
Figure 6.14 Force-displacement response of the MCCD system

Figure 6.15 Lateral displacement time-history of the RC frame: (a) 1940 El Centro, and (b) 1985 Chile earthquakes
Figure 6.16 Hysteretic shear force-lateral displacement responses for the original frame (a, c), and the modified frame (b, d)
Figure 6.17 Example 3: (a) original coupled walls, and (b) modified coupled walls142
Figure 6.18 System idealization for analysis: (a) original coupled walls, and (b) modified coupled walls
Figure 6.19 Force-displacement responses: (a) original coupled wall, and (b) modified coupled walls
Figure 6.20 (a) Loading mechanism of the MCCD system, and (b) force-displacement response of the MCCD system
Figure 6.21 Lateral displacement response time-histories: (a-d) 1940 El Centro, and (e-f) 1985 Chile earthquakes
Figure 6.22 Hysteretic shear force-lateral displacement responses for the original coupled walls (a), and the modified coupled walls (b-d)
Figure A.1 Pier-wall cross-section and reinforcements details
Figure A.2 Shear force-lateral displacement response of the designed pier-wall based on plastic analysis
Figure A.3 Stiffness matrix formulation for the building frame
Figure A.4 Bending moment diagram (BMD) and shear force diagram (SFD) for the building frame
Figure A.5 (a) An unbounded post-tensioned precast concrete wall, and (b) shear force-displacement curve with response limit states
Figure A.6 Free body diagram for each limit state of the precast wall: (a) decompression, (b) softening, and (c) tendons yielding (TY) and concrete crushing (CC)172

# **CHAPTER ONE**

# 1 Introduction

#### 1.1 Motivation and Vision

Earthquakes can impose serious and devastating damage to structures that imply several safety and economic issues. Even though the seismic design of building, bridges, and other structures has been highly improved in the past decades, there are still concerning problems not only affecting economic aspects but also life safety and life sustaining serviceability [1–3]. In the last few decades, engineers and researchers were able to develop design methods and improve the seismic performance of structures by allowing the design and the construction of structures to resist induced seismic loads by localizing damage in designed-specified locations, called plastic hinges, that allow a structure to inelastically dissipate the energy induced by earthquakes and prevent structural collapse [4,5]. To practically achieve this, plastic hinges should be carefully detailed to accept large inelastic deformations without significant strength degradation, while ensuring other parts of the structure remain elastic – or undamaged.

Conventional seismic design is based on designing structures to a load level that is typically 2 to 8 times lower than that required to resist the imposed seismic loads within their elastic response regime [6]. This requires that the structure to undergo large inelastic deformations [4,5]. Although this design strategy usually satisfies safety requirements, the economic aspects are not usually met. The reason is that relying on the inherited ductility of a structure to dissipate seismic induced energy means accepting extensive irreparable damage to the structure in case of strong earthquake motion. Therefore, research trends are now focused on satisfying safety requirements as well as making structures operational immediately after an earthquake [7]. This is achieved by

avoiding damage or limiting and localizing inelastic deformations in replaceable supplementary elements. This design philosophy is called Damage Avoidance Design [8].

Relying on inelastic deformations to resist seismic demands has led to the development of new and innovative systems of seismic structural protection that aim to achieve one or more of the following objectives: (1) minimize seismic energy input, (2) localize demands in replaceable or elastic elements, and (3) increase damping to minimize or avoid damage. Several passive energy dissipation devices have been developed to achieve these objectives, which can be classified into two categories: (a) viscous damping devices [7], and (b) hysteresis devices [9].

Most of the hysteresis energy dissipation devices currently used or proposed in the literature rely on metallic yielding or sliding friction as mechanisms for energy dissipation. A common problem with metallic devices is the requirement of repair or replacement of the device after a strong seismic action due to damage. A problem with friction-based devices is that they significantly increase the initial stiffness and strength of the host structure, which in turn increases force demands on other members of the structure that should remain elastic. In addition, neither type of the noted hysteresis devices offers self-centering capability. On the other hand, viscus damping devices are rate-dependent and require high excitation frequency to be effective.

Increased attention has been recently given to systems that utilize elastic instabilities for energy dissipation and shock absorption. The reason is that the mechanical deformations of such systems are fully reversible since the total response is within the elastic regime of the constituent base material [10–12]. Usually, these systems consist of parallel chains of multistable elements or unit cells that are connected in series and respond to a common load in a progressive manner. When these elements are loaded under displacement control they show a negative stiffness region due to geometric nonlinearity [13]. The consecutive snap-through events of the repeating units

enable attaining a hysteretic force-deformation response. These systems can thus be used to elastically absorb and dissipate energy.

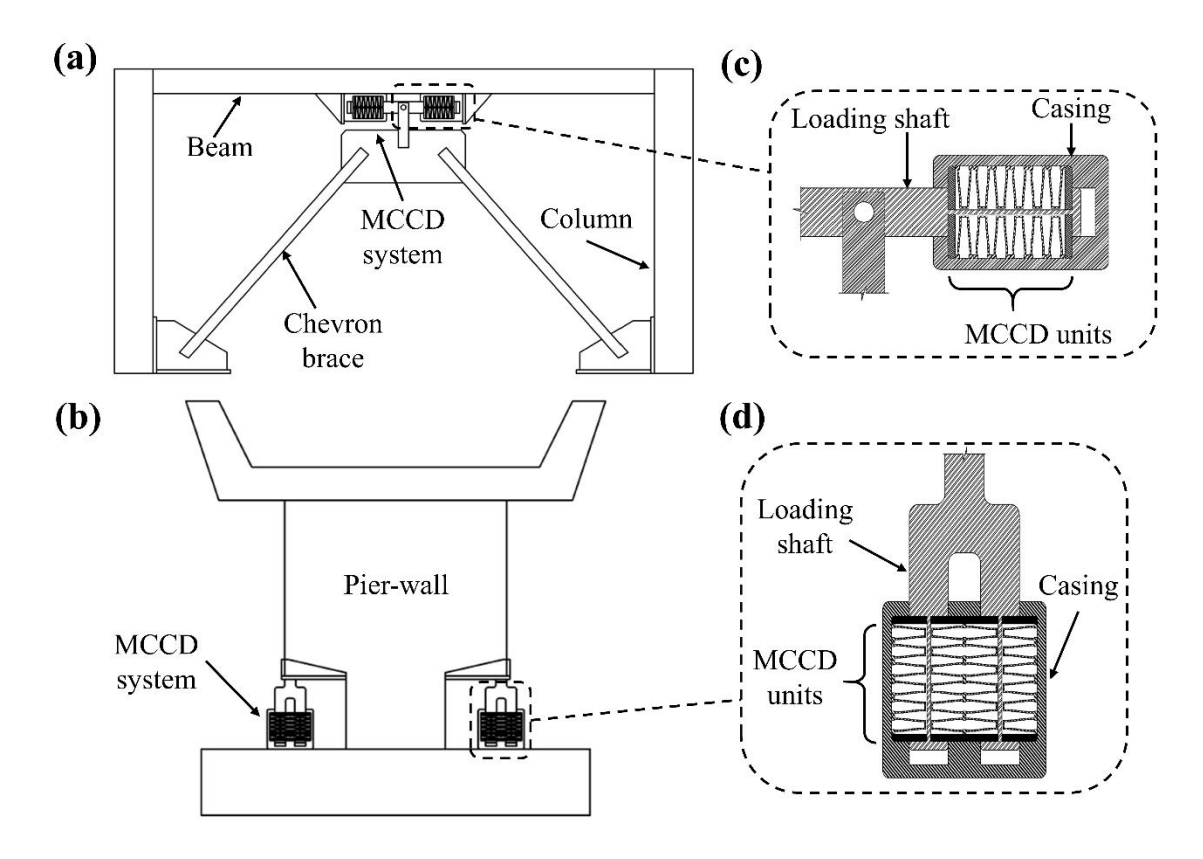


Figure 1.1 Example applications of the MCCD system incorporated in typical structural systems: (a) frame with chevron braces, (b) pier-wall, (c) single-column, and (d) double-column MCCD systems

Recent developments in innovative discrete systems with energy dissipation from elastic instabilities has facilitated the potential of using such systems for energy dissipation and shock absorption applications [11,12]. One potential application of discrete systems is the damping mechanism in structures resisting seismic actions as shown in Figure 1.1. The figure shows example structural systems equipped with supplementary energy dissipation devices comprised of chains of multistable elements. The possibility of using such elements for seismic protection enables avoiding the previously noted shortcomings of commonly used passive hysteresis energy dissipation devices and also offers self-centering capability.

However, a reliable multistable element that is able to withstand seismic induced loads and maintains its design behavior under loading is not yet available. Therefore, proving this idea requires developing and characterizing a reliable elastic multistable element and an elastic energy dissipation system, and then incorporating the developed mechanism into typical structural systems under seismic loading. In this research, a new shallow dome-shaped multistable element with cosine-curved profile [Figure 1.2(a)], called cosine-curved dome (CCD), and a new energy dissipation system comprised of multiple cosine-curved domes (MCCD) connected in series [Figure 1.2(c)] are developed and characterized. The damping characteristics of the proposed system were also investigated in support of the displacement-based seismic design philosophy. Finally, the seismic performance of structures incorporating the proposed system was evaluated.

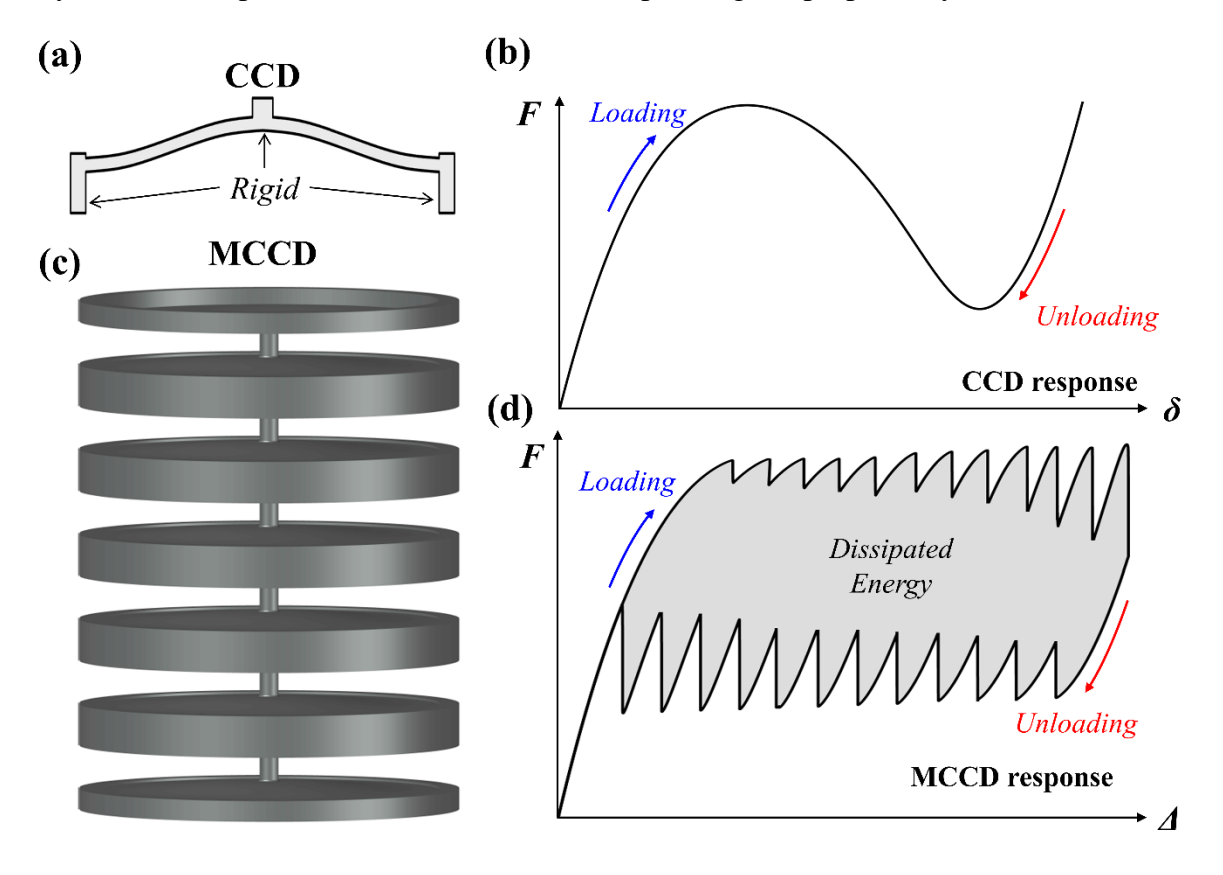


Figure 1.2 The MCCD system: (a) cross-section of a single CCD unit, (b) schematic force-displacement response of a single CCD, (c) MCCD composed of multiple CCDs, and (d) schematic hysteretic response of an MCCD system. Note that  $\delta$  is the local CCD displacement while  $\Delta$  is the global system displacement.

### 1.2 Background

#### 1.2.1 Stability states of snap-through response

In civil structures, elastic instabilities have been usually regarded as a failure mode to be avoided. However, recent research directions have shown that elastic instabilities of various types of structural elements can be considered as a useful phenomenon for diverse applications because they offer reversible deformations and their response can be tailored, which allows controlling the magnitude and the recoverability state of the deformations.

Snap-through response is a form of elastic instability that occurs when a transversely loaded element of a geometric shape that primarily develops membrane stresses reaches a limit point in its response that causes the element to change its shape before experiencing buckling by developing local bending stresses [13].

The potential energy,  $U_p$ , of a conservative system (ideally constrained elastic body under external work), such as the CCDs considered in this work, consists of the applied work, W, on the system and the elastic strain energy, U, as follows [14]:

$$U_p = U + W \tag{1.1}$$

The stability state along the equilibrium path of the system is governed by the second variation of the potential energy with respect to the displacement,  $\delta$ , (the Lagrange variational equation) as follows:

- 1. The equilibrium is stable if  $\partial^2 U_p / \partial \delta^2 > 0$ .
- 2. The equilibrium is unstable if  $\partial^2 U_p / \partial \delta^2 \le 0$ .

The first condition represents the equilibrium path between the origin point and the point on the force-displacement  $(F-\delta)$  curve at  $\delta_c$ , and from point  $\delta_n$  and on as shown in Figure 1.3(d-f). The unstable path between the points on the curve  $\delta_c$  and  $\delta_n$  in Figure 1.3(d-f) satisfies the second

condition. This can be inferred by knowing that mathematical sign of the slope of a tangent line (current stiffness) along the F- $\delta$  curve, or

$$\partial^2 U_p / \partial \delta^2 = \partial F / \partial \delta \tag{1.2}$$

The post-snap-through response of a multistable element can be classified into three categories as shown in Figure 1.3 [15]. Each type of response depends mainly on the shape of the strain energy-displacement  $(U-\delta)$  curve, which is related to the force-displacement curve  $(F-\delta)$ . Knowing the geometric and material limits allow controlling the type of response (stability state) of the element.

Figure 1.3(a) and (d) show a bistable response, where the U- $\delta$  curve has a local maximum strain energy point,  $U_{max}$ , and a local minimum strain energy point,  $U_{min}$ , at non-zero displacements before the energy (U) continues to increase with increasing displacement ( $\delta$ ). In this type of response, the element snaps into a new configuration and cannot restore its original configuration upon unloading without the application of an external restoring force (i.e., not self-recoverable). In this case, some of the induced energy is trapped in the system and hence the F- $\delta$  curve has a negative force part (in opposite direction to the deformation being generated).

A monostable response [Figure 1.3(b) and (e)] is defined when the E- $\delta$  curve is monotonic and the F- $\delta$  curve has no negative force part. In this type of response, the element snaps back to its original configuration upon unloading, without application of an external restoring force, as long as material damage does not occur.

In a pseudo-bistable response [Figure 1.3 (c) and (f)] the E- $\delta$  curve has a flat segment (i.e.,  $U_{max} = U_{min}$ ) before the energy continues to increase with increasing  $\delta$ , and the F- $\delta$  curve has a zero force value at a non-zero displacement. This response represents a transition state between bistable and monostable responses where the element snaps and restores its original configuration

after unloading, and without the application of an external restoring force, but with a time delay depending on the viscoelastic properties of the material [16].

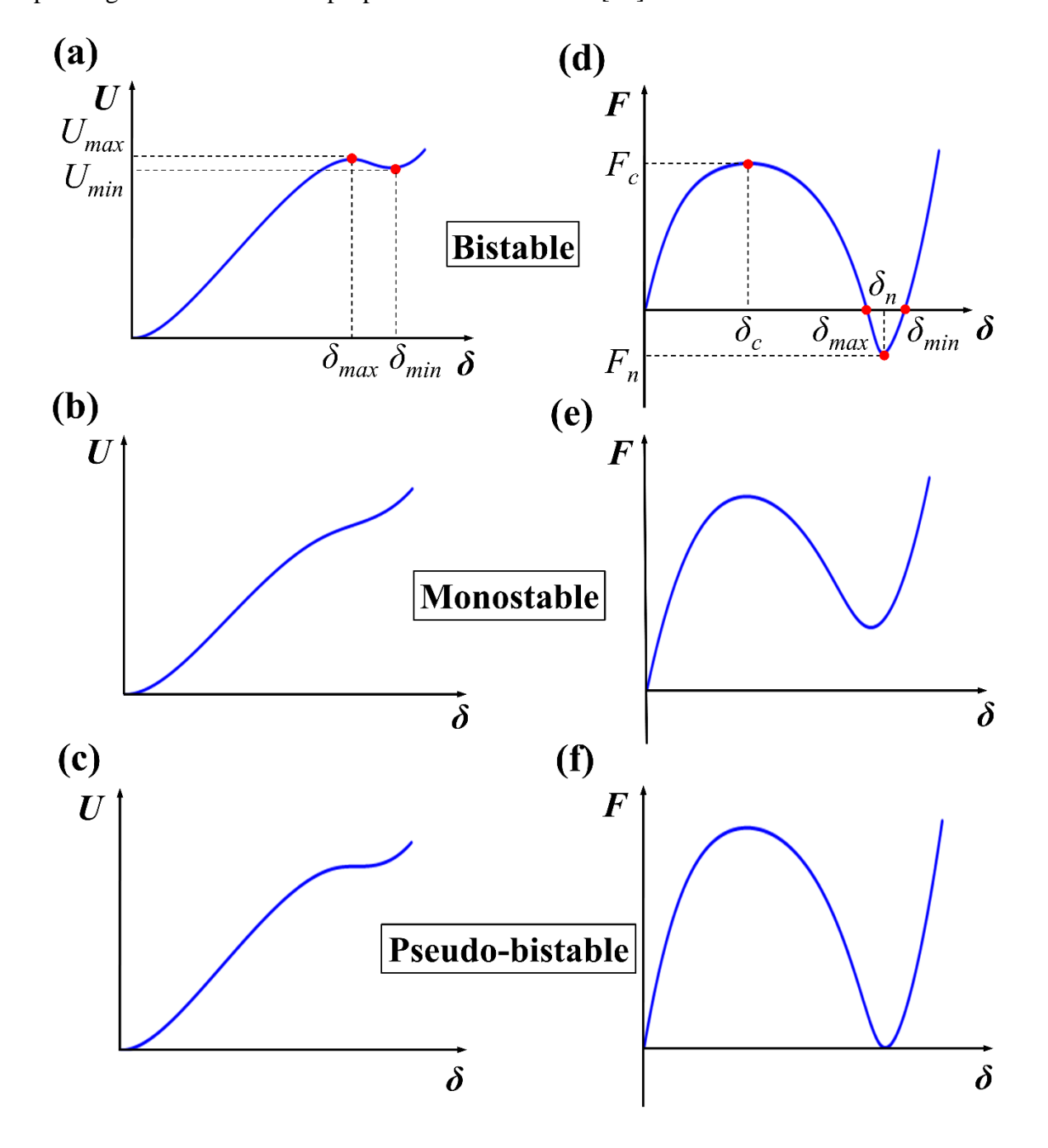


Figure 1.3 Typical strain energy-displacement and force-displacement of an element with snap-through behavior

#### 1.2.2 Energy dissipation from elastic instabilities

When a system of several multistable elements connected in series is mechanically loaded the units consecutively snap-through to a new stability state within their elastic range. Upon unloading the system, the units consecutively snap-back to their original configuration, either by a restoring external force for bistable elements or by self-recoverability (preferred) for monostable elements. If a sufficient number of connected units in series is used the system follows distinct loading and unloading paths resulting in a hysteretic response, as shown in the system response in Figure 1.2(d). The area enclosed by the loading and unloading curves represents the elastically dissipated energy.

Several systems comprised of straight and curved elements developed and proposed in the literature [11,12] have been shown to display the noted hysteretic response. The amount of dissipated energy from these systems depends on: (1) the number of linked elements in series, and (2) the difference between local energy maxima and minima (Figure 1.3) of the individual element's response. The higher the values of these two factors the larger the area enclosed by the hysteretic response will be.

The energy dissipation in such elastic systems is due to the transformation of some of the induced mechanical energy of the applied work into elastic vibrations that are damped by the base material of the repeating units and converted to irreversible thermal energy (heat) with each snap-through event [10]. These elastic vibrations occur when the deforming system has at least 3 or more elements connected in series to allow the relative movement of the units at a given system displacement of a snapping event. Increasing the number of linked elements in series has two effects on the response of the system as can be inferred from Figure 1.4: (a) it increases the number of vibrating elements in the system, and (b) it increases the number of events of system disturbance

that causes vibrations. Thus, it can be concluded that the relation between dissipated energy and number of units is nonlinear. This is discussed in detail in Chapter 4.

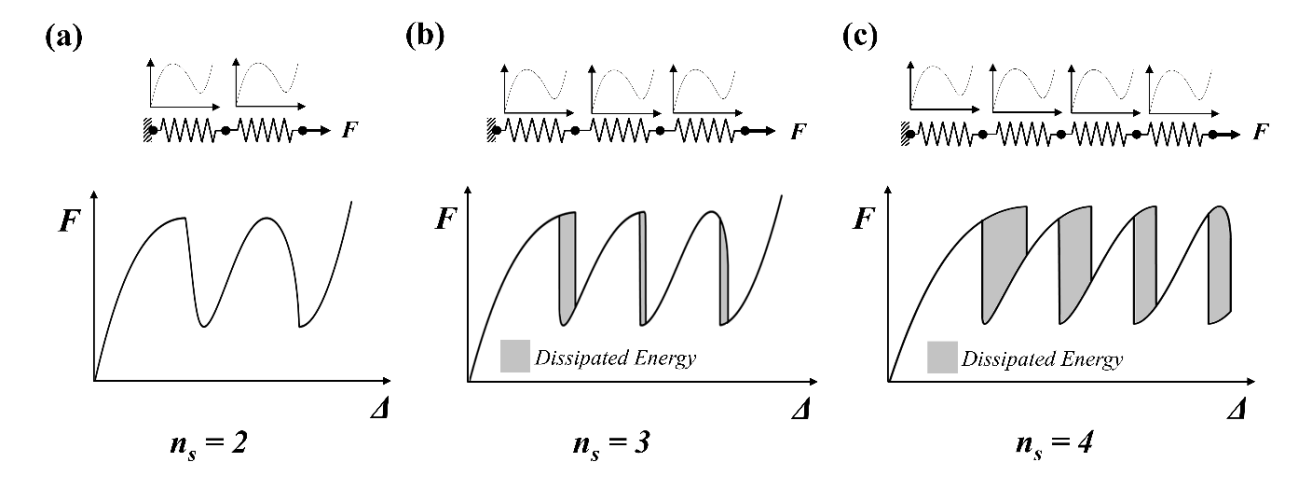


Figure 1.4 Effect of increasing the number of serially connected elements on the dissipated energy

Studies [17,18] on the dynamic behavior of discrete chains with multistable elements indicate that loading rate (in addition to other factors) has dynamic effects on the response of such systems. In fact, even at quasi-static loading conditions, discrete systems exhibit high frequency vibrations from the snap-through events [18]. These damped vibrations are the main contributor to the dissipated energy from the discrete system even at very low loading rates. Thus, the hysteretic response of these multi-element systems can be seen as independent from loading rate. Furthermore, it could be said that increasing the loading rates has a positive effect on the amount of dissipated energy since it was shown in [19] that increasing the loading rate results in a wider hysteresis response envelope.

# 1.3 Research Hypothesis and Significance

#### 1.3.1 Hypothesis

Elastic energy dissipation through hysteretic response of the consecutive snap-through instabilities of multiple multistable cosine-curved domes can be effectively used as the main damping and energy dissipation source to resist seismic induced loads in reinforced concrete (RC) structures.

#### 1.3.2 Significance

Utilizing the hysteretic response and energy dissipation resulting from the consecutive snap-through instabilities of multiple multistable elements in structural systems to resist seismic demands is an underexplored topic. This work introduces a new concept for energy dissipation from elastic instabilities as a damping mechanism to reduce seismic induced structural demands, eliminate or limit permanent deformation, and offer self-centering capabilities.

#### 1.4 Research Objectives

The objective of this work is to develop and characterize the response of a reliable multistable element and an elastic energy dissipation system to withstand seismic induced loads as the main damping mechanism in RC building and bridge structures, and to evaluate the seismic performance of these structures under ground motion records. The objective was achieved through the following tasks:

Task 1 Development of a multistable element:

<u>Task 1.1 Development of cosine-curved domes (CCD).</u> To develop a self-confined multistable elastic element capable of achieving snap-through instability with controllable response over a wide range of geometric parameters.

<u>Task 1.2 Response characterization.</u> To investigate the response and the stability characteristics of the proposed CCDs by studying the controlling geometric and material properties numerically and experimentally.

<u>Task 1.3 Design expressions.</u> To develop design expressions for the limit that governs the transitional stability state and to construct a simplified multilinear response of the element.

#### Task 2 Elastic energy dissipation system:

<u>Task 2.1 Response characterization</u>. To investigate numerically and experimentally the response and the energy dissipation characteristics of the MCCD system by studying the number of units and the controlling geometric properties.

<u>Task 2.2 Hysteresis Model</u> To develop an analytical model that describes the hysteretic response of the MCCD system including the intermediate unloading and reloading paths based on numerical results and validated by experimental tests.

#### Task 3: Equivalent viscous damping:

<u>Task 3.1 Response idealization.</u> To idealize the hysteretic response of the MCCD system for the nonlinear time-history analysis of structures incorporating the MCCD system by maintaining the energy balance between the actual and the idealized responses.

<u>Task 3.2 Equivalent damping.</u> To investigate the equivalent viscous damping for the hysteretic response of the MCCD system by performing a parametric study for a set of ground motion records.

#### Task 4: Evaluation of the seismic performance:

<u>Task 4.1 Incorporation of the MCCD system in structures.</u> To conduct the seismic design RC structures incorporating the MCCD system using the direct displacement-based design method.

<u>Task 4.1 Performance evaluation.</u> To evaluate the seismic performance of the designed RC structures incorporating the MCCD system under real ground motion records through nonlinear time-history analyses.

#### 1.5 Outline

This dissertation is divided into seven chapters. A brief description of the contents of each of the subsequent chapters is presented as follows. Chapter 2 reviews elements and systems with elastic instabilities in terms of their geometric design and response characteristics. The chapter also presents a review on passive hysteresis energy dissipation devices for seismic protection. Chapter 3 presents the development and the response characterization of CCDs, including numerical modeling, experimental testing, and a parametric study to develop design expressions for the CCDs. Chapter 4 presents the development of the MCCD system and studies its response and energy dissipation characteristics through the development of an analytical model and experimental testing. Chapter 5 introduces the hysteretic response of the MCCD system to seismic design by investigating the equivalent viscous damping and considering the unique characteristics of the systems' response. Chapter 6 evaluates the seismic performance of the MCCD system incorporated in different configurations in typical reinforced concrete structures as the main damping mechanism for seismic protection. Chapter 7 summaries the conducted work and provides the conclusions and recommendations for future research work.

# **CHAPTER TWO**

# 2 Literature Review

#### 2.1 Overview

This chapter is divided into two parts. The first part presents a review on elements and systems with elastic instabilities for energy dissipation applications. The review highlights the basic types of elastic instability associated with the presented elements and the response characteristics of systems composed of them. The second part reviews published literature on passive hysteresis energy dissipation devices for seismic protection of structures. The review presents the hysteretic and mechanical behavior of the devices and their advantages and disadvantages.

## 2.2 Elements and Systems with Elastic Instabilities

Several elements with elastic instabilities have been investigated in the literature. These elements can be categorized based on their geometric shape and loading direction into four categories: (1) transversally loaded inclined elements, (2) transversally loaded curved elements, (3) transversally loaded surfaces of revolution, and (4) axially loaded elements. Discussion and examples for each type are presented in the following.

#### 2.2.1 Transversally loaded inclined elements

Transversally loaded inclined elements are direct applications of the classical case of a von Mises truss [13]. Under a transverse load, the members of such a system snap-through from their original configuration to an inverted configuration. The truss exhibits a nonlinear limit-point F- $\delta$  response as shown in Figure 1.3. This response is ensured as long as axial forces (due to the

transverse load) in the inclined members does not cause buckling before snapping. This mainly depends on the inclination angle and the axial stiffness of the members. The members here can be straight beams, rods, or plates. Example applications of this case are those developed in [20–27] as shown in Figure 2.1.

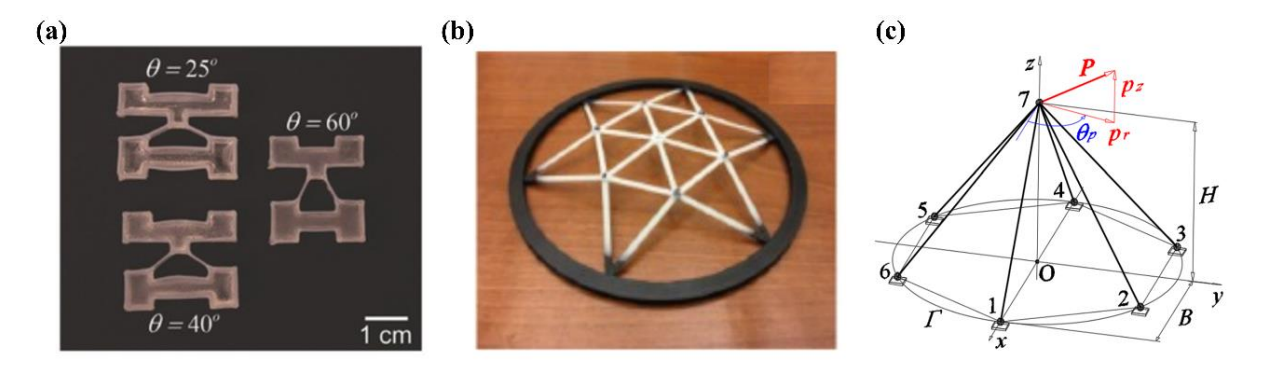


Figure 2.1 Examples for multistable inclined elements and unit cells: (a) identical tilted beams [20], (b) shallow geodesic lattice domes [25], and (c) shallow reticulated truss [26]

Many researchers have used inclined elements as the building units in many structures utilized to elastically absorb and dissipate energy. Haghpanah *et al.* [21] proposed 2D and 3D shape-reconfigurable lattice materials that allow independent multi-axial deformation and exhibit hysteretic response. The unit cells are connected in series and each unit cell comprises several inclined beams as shown in Figure 2.2(a). Ha *et al.* [23] also proposed an energy absorption lattice of serially connected unit cells comprised of four inclined beams confined by rectangular plates as shown in Figure 2.2(b). Liu *et al.* [27] proposed an innovative controllable energy dissipation system consists of arrays of inclined beams that are serially connected as shown in Figure 2.2(c). The inclination of the beams is alternated from on array to the other to allow shear loading in two opposite directions [see Figure 2.2(c)].

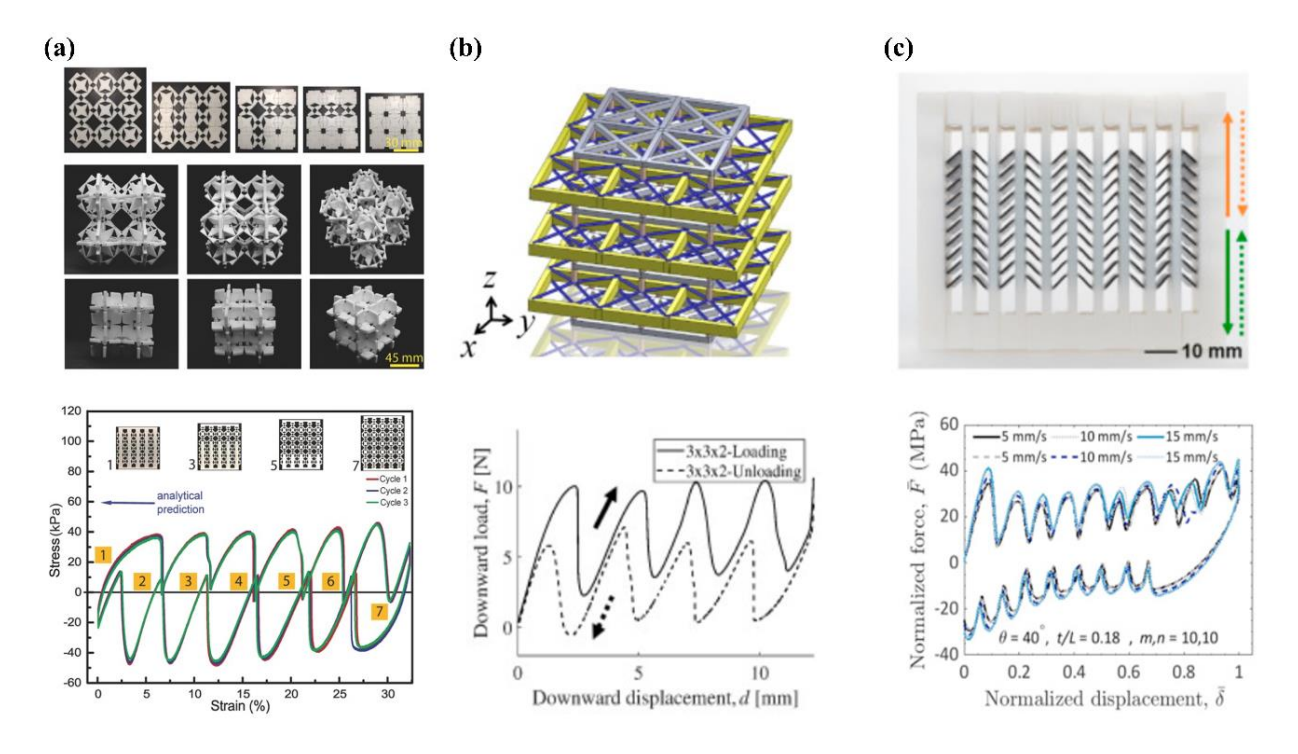


Figure 2.2 Examples for energy dissipation systems with inclined elements: (a) shape-reconfigurable materials [21], (b) multiple tetra-beam-plate lattice [23], and (c) periodic arrays of inclined beams [27]

#### 2.2.2 Transversally loaded curved elements

Transversally loaded curved elements also capable of showing snap-through behavior. Similar to that of inclined elements, and curved elements are also affected by the same factors in addition to the curvature profile of the element. Example applications of this case are those developed in [28–40] as shown in Figure 2.3.

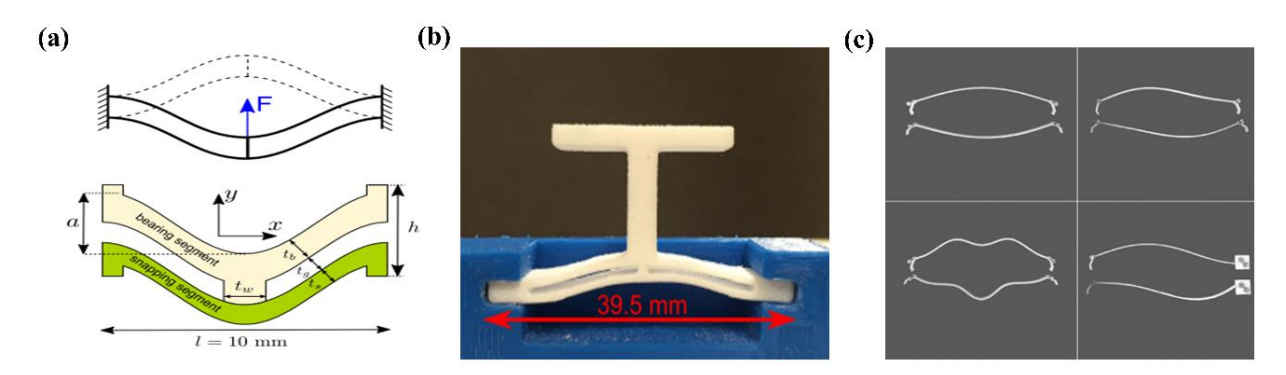


Figure 2.3 Examples for multistable curved elements and unit cells: (a) curved double beams under tension [36], (b) T-shaped double curved beams [37], and (c) bistable arches [39]

Double curved beams and rods are widely investigated and used as building units in energy dissipation systems. The reason is that they can be easily arranged in various configurations in a periodic structure. Correa *et al.* [29] developed an energy dissipation system with a honeycomb configuration. The system comprised of multiple curved double beams. The lateral expansion of the unit cells is restricted by central tie-beams as shown in Figure 2.4(a). Findeisen *et al.* [34] proposed a 3D periodic structure that consists of multiple unit cells. The cells are comprised of 3 rods of a sinusoidal shape confined by hexagonal base structure as shown in Figure 2.4(b). Kidambi *et al.* [37] investigated the characteristics of modular mechanical structure experimentally and numerically. The structure consists of serially connected bistable double-curved beams as shown in Figure 2.4(c).

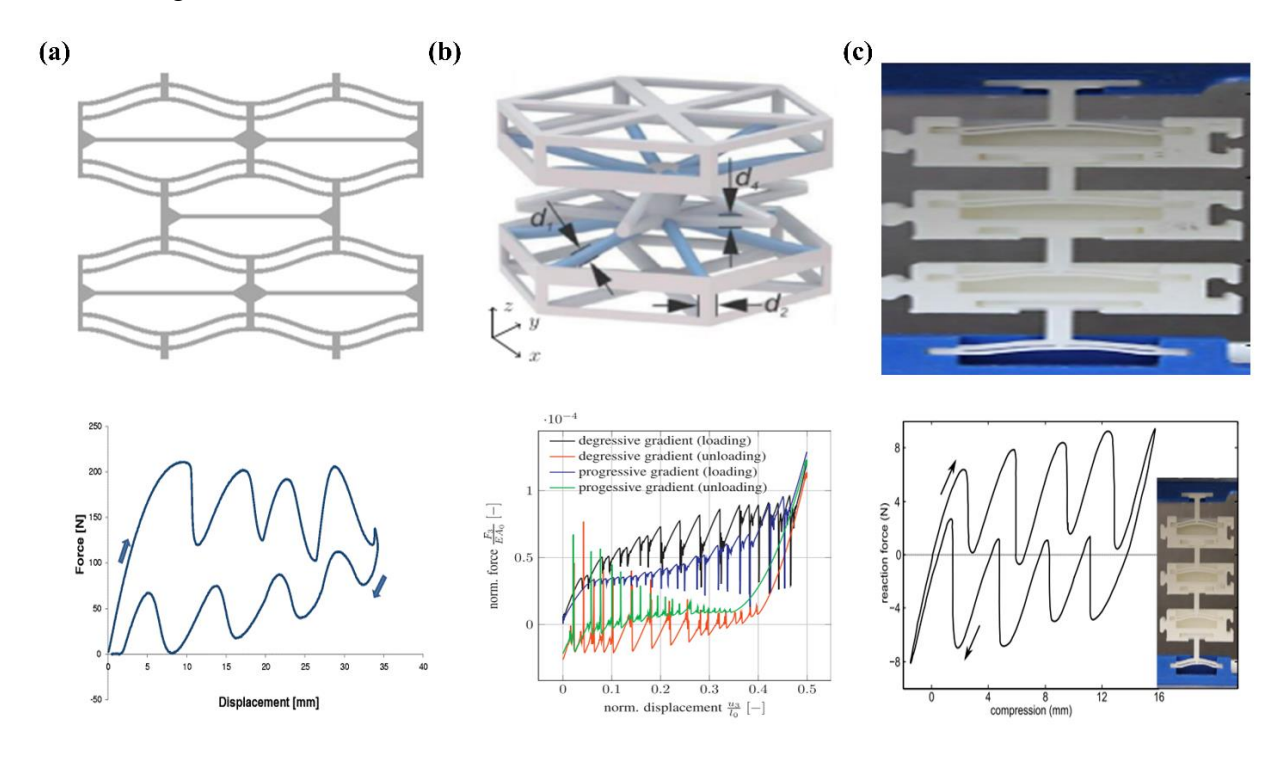


Figure 2.4 Examples for energy dissipation systems with curved elements: (a) Negative stiffness honeycombs [29], (b) 3D hexagonal micro-lattices [34], and (c) multistable modular structures [37]

#### 2.2.3 Elements with surface of revolution

The stability, buckling capacity, post-buckling behavior, and deformation symmetry of spherical domes and shells under a concentrated load at the apex have been the subject of several studies. Mescall [41] performed a numerical study by solving the nonlinear equations governing the axisymmetric deformations of spherical shells, for unrestrained and clamped edges, to examine the effects of geometric parameters and boundary conditions on their response. Penning [42] conducted an experimental investigation to study buckling deformations of clamped spherical shells under a concentrated load. Fitch [43], and Brodland and Cohen [44] conducted an analytical study to investigate the deflection, snap-through buckling, and the occurrence of asymmetric bifurcation points before axisymmetric snap-buckling, by examining a single material-geometry parameter ( $\lambda$ ) that governs this phenomenon for clamped and unrestrained shallow spherical domes. This parameter depends on the geometric and material properties of the domes and is given by Equation (2.1), where a and b are the spherical and base radii, respectively, t is the uniform thickness (see Figure 2.5), and v is the Poisson ratio. It was concluded that asymmetric bifurcation occurs when a spherical dome becomes deeper and thinner (i.e., higher values of  $\lambda$ ).

$$\lambda = [12(1 - v^2)]^{1/4} b / (a t)^{1/2}$$
(2.1)

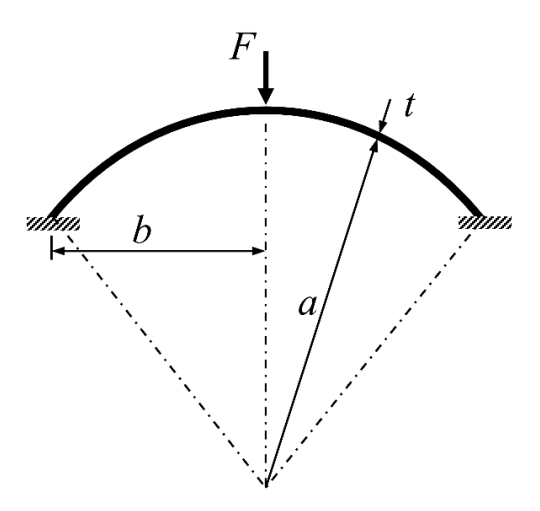


Figure 2.5 Geometry of a clamped spherical dome

Brinkmeyer *et al.* [16] and Madhukar *et al.* [15] also performed combined experimental and numerical studies using finite element analyses (FEA) to examine the effects of geometric and material properties on the stability state of unrestrained spherical domes. Brinkmeyer *et al.* [16] found that pseudo-bistability occurs for domes when  $5.31 \le \lambda \le 5.35$ . Madhukar *et al.* [15] proposed an expression for pseudo-bistability that depends on the geometric parameters of a dome.

The study conducted by Mescall [41] showed that spherical domes with unrestrained and clamped edges could display snap-through instability. Unrestrained domes required  $\lambda > 3.75$  to display snap-through, while clamped domes required  $\lambda \geq 9$ . However, the study by Fitch [43] showed that spherical domes with clamped edges and  $\lambda \geq 9.2$  would have a bifurcation point and asymmetric deformations at a load below the critical load for axisymmetric snapping instability. These two findings impose a very narrow range of  $\lambda$  (i.e., 9 to 9.2) for spherical domes with clamped edges to display axisymmetric snap-through response. Therefore, it seems that clamped spherical domes cannot practically have reversible axisymmetric snap-through instability even when the previous two limits are met. Therefore, it can be noticed that spherical domes are not used in periodic structures for energy dissipation.

#### 2.2.4 Elements with buckling instabilities

Many other structures have been investigated to obtain multiple elastic instabilities for a multistable response. The simplest is an elastic compressed column with continuous bilateral constraints [45,46]. In such a system, compressive axial load is applied to the column causing it to buckle multiple times in an elastic post-buckling regime before reaching material damage. Another example are tailored cylindrical shells under axial compressive loading [47,48], where geometric imperfections are seeded into specific regions to control the elastic post-buckling response. The common phenomenon among these structures is that they undergo elastic post-buckling response

after reaching a critical point. However, they differ in their post-buckling behavior and their relative deformability.

### 2.3 Structural Systems with Passive Energy Dissipation Devices

As mentioned earlier, the trends of seismic protection in building and bridge structures are moving towards directing seismic demands to specific parts of the structural system where supplementary energy dissipation devices accept these demands. This methodology allows concentrating damage in replaceable or elastic parts which in turn make structures operational after short periods of time or even immediately after strong ground motion. Several investigations in the literature applied this concept using various types of energy dissipation devices on various structural configurations [9] and showed excellent performance under loading.

Seismic protection devices and systems can be classified into three categories [7]: (1) seismic isolation systems, (2) passive energy dissipation systems, and (3) active control systems. An overview of metallic yielding and sliding friction based passive hysteretic energy dissipation devices is presented here.

#### 2.3.1 Metallic energy dissipation devices

Metallic dampers are one of the oldest and widely used devices for seismic protection [49]. They rely on inelastic deformations through axial, flexural, or shear actions to dissipate induced seismic energy. This reliance is the main drawback of such devices since these deformations are not recoverable, and hence they require replacement or extensive repairs after strong earthquakes [9]. Nonetheless they offer reliable, stable, and well-defined hysteresis response. These devises show wide hysteresis loops and therefore dissipate a large amount of energy. Classical examples of these devices are the added damping and stiffness [50] and the buckling-restrained brace [51]

dampers. In recent years, many researchers have proposed several new and improved metallic devices aiming to: (a) increase the amount of dissipated energy per unit of deformation, (b) using different loading mechanisms, and (c) facilitate repairs of a device's elements after damage. Examples of these devices include a bar-fuse damper [52], seesaw slit dampers [53], a combined shear-and-flexure yielding damper [54], a piston metallic damper [55,56], a yielding shear panel device [57], a saw type energy dissipater [58], and an accordion metallic damper [59]. Figure 2.6 shows example metallic dampers with their force-deformation responses.

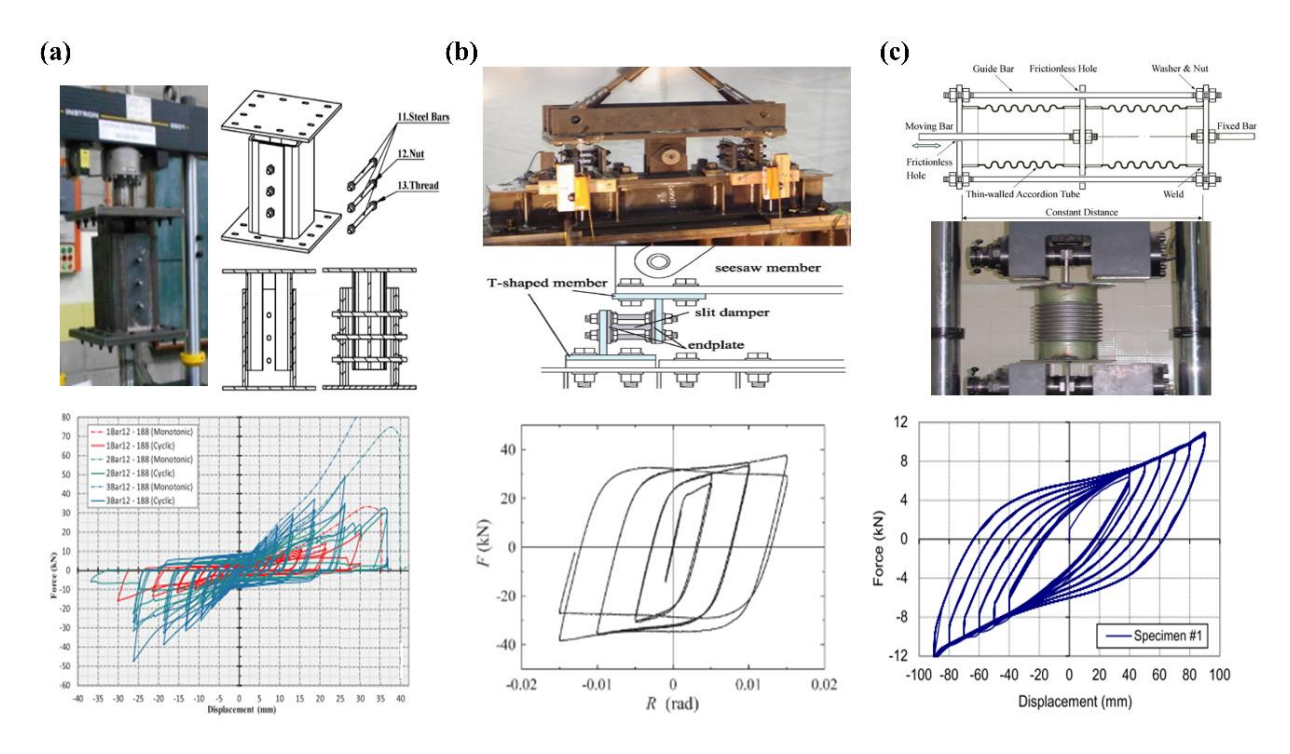


Figure 2.6 Examples for metallic energy dissipation devices: (a) bar-fuse damper [52], (b) seesaw slit damper [53], and (c) accordion metallic damper [59]

#### 2.3.2 Sliding friction energy dissipation devices

Sliding friction devices are also capable of dissipating a large amount of energy comparable to that of metallic devices. They utilize surface friction between two solid bodies moving relative to each other that turn the mechanical motion into heat. A disadvantage of this mechanism is that friction surfaces are susceptible to damage over time and they require a self-centering mechanism

to recover deformations. Their response is characterized by high initial stiffness and large hysteresis; however, their relative energy dissipation capacity is reduced when they are combined with a self-centering mechanism. An early example of using friction as energy dissipation mechanism is the friction joints in precast concrete structures developed by Pall *et al.* [60]. Recently, several sliding friction devices combined with self-centering mechanisms were developed, such as friction disc dampers [61], high-capacity self-centering energy-dissipative dampers [62], spring-based piston bracing [63], ring spring dampers [64,65], and self-centering friction damping braces [66,67]. Figure 2.7 shows example friction dampers with their force-deformation responses.

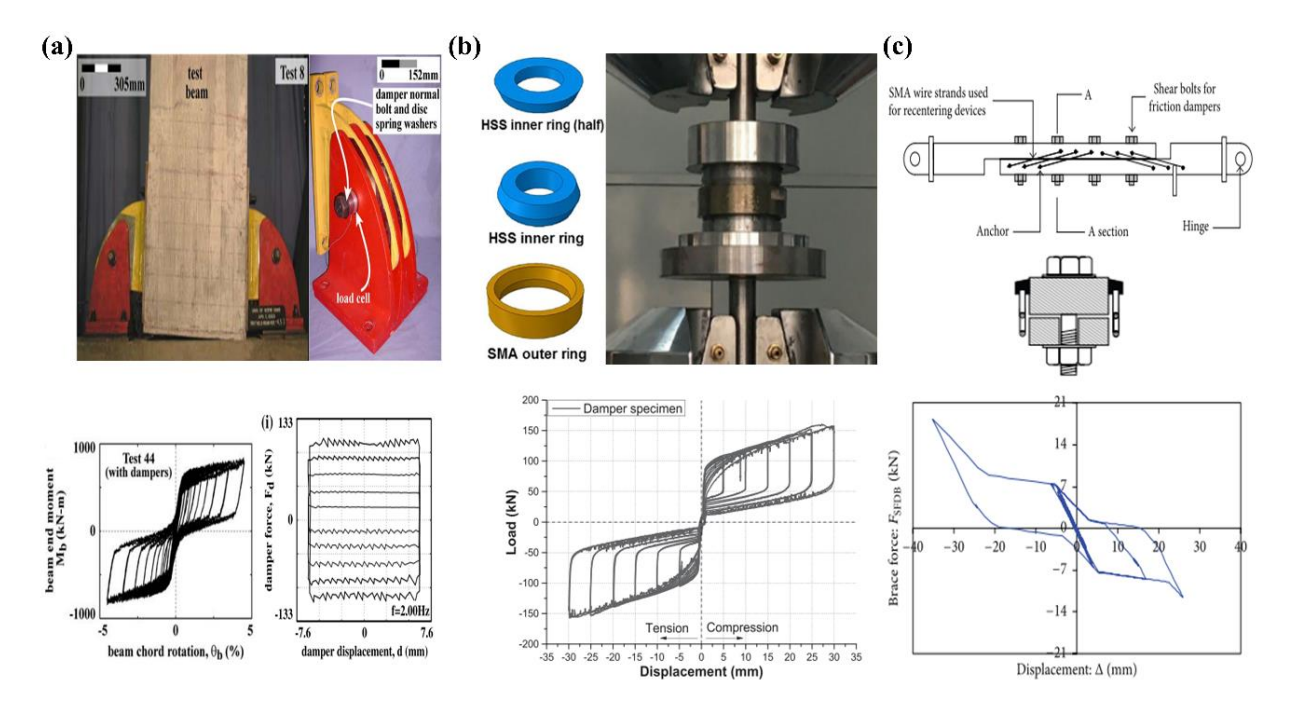


Figure 2.7 Examples for friction energy dissipation devices: (a) friction discs damper [61], (b) ring spring damper [65], and (c) self-centering friction braces [66]

# **CHAPTER THREE**

# 3 Characterization of Cosine-Curved Domes

#### 3.1 Overview

In this chapter, numerical and experimental studies were carried out to study the effects of the geometric and material properties on the behavior of the multistable cosine-curved domes (CCD) under a concentrated transverse load, and to characterize the resulting force-deformation response. This is accomplished by conducting a parametric study using experimentally validated finite element analyses (FEA) on the properties governing the response of the CCD. The limit that governs the transitional state between bistable and monostable states is identified, and a simple expression is proposed to facilitate the design of CCDs with a desired stability state. Empirical design expressions were developed for the controlling parameters to construct a simplified multilinear response that could be used to calculate the response for a system of multiple CCDs, which can attain controllable energy dissipation characteristics. The study presented in this chapter was published in the journal Thin-walled Structures [68].

### 3.2 Background

A new shallow dome-shaped structural element that exhibits multistable elastic behavior is presented in this chapter. The element offers reliable and reversible large elastic deformation that could be used as a building unit for devices subjected to relatively high forces [69] for energy dissipation and repeated use. Such devices usually have a hysteretic response that is based on consecutive snap-through instabilities of a sufficient number of units that are connected in series [70].

The interest in studying shallow domes originates from the fact that they can be fabricated in curved revolved profiles (i.e., aside from spherical shapes) that allow them to have a tunable multistable response. These domes can snap-through to a new configuration within their elastic range of response and snap-back with or without a restoring external force without damage. This deformability enables these domes to absorb and/or trap strain energy and release all or a part of it to restore their original configuration [13].

Several multistable elements with the ability to exhibit snap-through instability with large elastic (reversible) deformations have been investigated and reported as discussed in Chapter 2. Such elements can be used as the building units in many structures utilized to elastically absorb and dissipate energy. Although these structures show the ability to absorb shocks and dissipate energy, they possess some design disadvantages when considering large-scale applications where high force levels are expected, such as applications for seismic protection in buildings and bridges. These disadvantages include high stress concentrations at the elements' constraining edges, low relative threshold forces, and the requirement of constraining other buckling modes to attain a symmetric deformation response.

A possible multistable element to overcome these disadvantages are spherical domes under a concentrated load at the apex, which have been the subject of several studies [41–44]. However, the study by Fitch [43] showed that spherical domes with clamped edges require high apex height-to-thickness ratio to display snap-through instability. However, this high ratio also makes spherical domes with clamped edges highly vulnerable to bifurcation and asymmetric deformations at a load below the critical load for axisymmetric snapping instability. These two findings impose a very narrow range for spherical domes with clamped edges to display axisymmetric snap-through response. Therefore, it seems that clamped spherical domes cannot practically have reversible

axisymmetric snap-through instability even when the previous two limits are met nor have controllable response. In contrast, this investigation shows that the shallow cosine-curved domes (CCD) proposed here have a wide range of geometric ratios for which symmetric snap-through is achievable.

The interest in domes with clamped edges originates from that fact that they can be used in many structural applications as an integrated part of systems, compared to domes with unrestrained edges. For example, the shock absorbers proposed in [19,20,29,36] consist of multistable elements as unit cells where each unit is attached to the adjacent units via rigid segments that provide system integrity to resist a common load, as well as the required constraints for individual units to respond in the desired way.

#### 3.3 Methods

#### 3.3.1 Research aim and scope

The cross-sectional profile shape of the proposed CCD is based on the cosine function given in Equation (3.1) [71], where w(x) is the vertical distance from the horizontal chord line to the dome's profile shape at a distance x from the circumference as shown in Figure 3.1. The dome's base along its circumference is connected to a rigid ring that constrains rotations and edge sliding of the dome under loading.

$$w(x) = h/2[1 - \cos(2\pi x/l)]$$
(3.1)

This equation represents the shape of the first buckling mode of a fixed-fixed straight beam under axial compressive loading. The benefit of using the cosine-curved shape over a spherical one is that it enables the dome to have a symmetric snap-through to a monostable or a bistable state. This profile was inspired by the shape of curved double beams loaded laterally [72].

However, unlike the curved double beams, a CCD doesn't require restricting other buckling modes to have a symmetric reversible snap-through response. They also have lower stress concentrations at the supporting edge compared to systems composed of curved double beams or inclined beams.

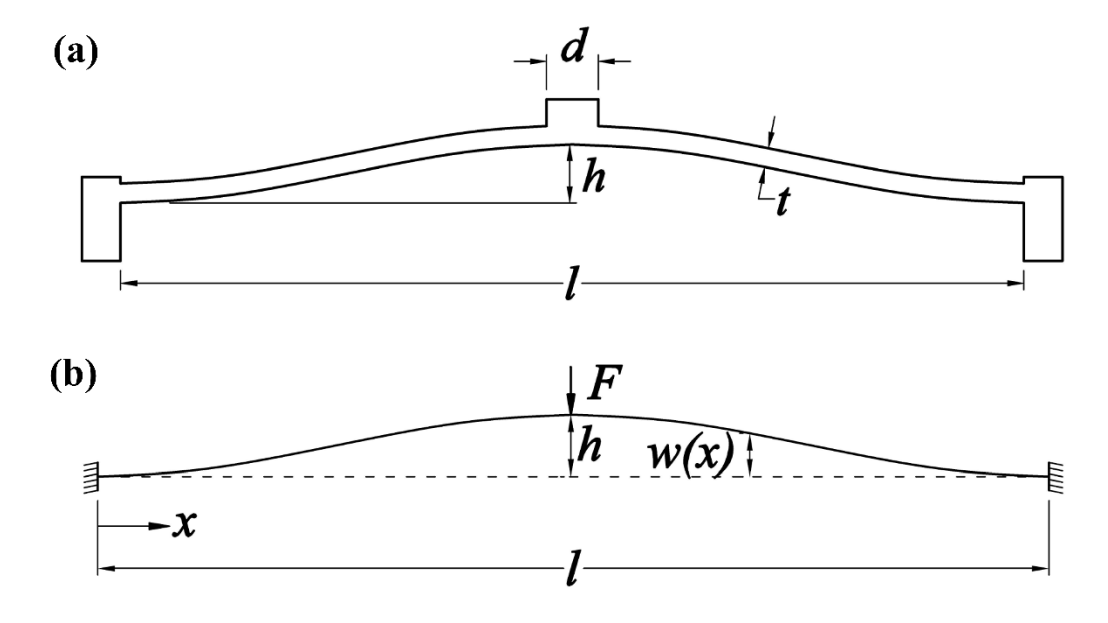


Figure 3.1 Geometric parameters of a typical CCD: (a) a cross-section at the apex, and (b) the idealized system

The scope of this study is thus on the response of shallow CCDs that, upon being transversely loaded at their apex, display an elastic response and limit-point critical instability with a snap-through geometrical transition. When a shallow CCD is loaded beyond its limit-point it snaps-through to a new configuration. The force-deformation response is nonlinear before and after the limit-point snap-through instability (initial loading path and unstable path), with a fairly linear response upon continued loading in the new configuration (Figure 1.3). While the unstable response path (negative tangent stiffness) cannot be obtained under force-controlled loading, it can be attained in a stable manner under displacement-controlled loading. Snap-through instability, also called limit-point instability or snap instability, does not involve any bifurcation of the equilibrium path [13].

#### 3.3.2 Modeling and analysis

The CCD element studied was idealized as shown in Figure 3.1(b). The dome's horizontal orientation is along the shown x-axis and the vertical direction is perpendicular to it. The dome is modeled with clamped boundary conditions along its base circumference. Loading is assumed to be applied by a vertical concentrated load (F) at the dome's apex, and directed downwards. The applied load causes a vertical (transverse) displacement  $\delta$ . The key geometric parameters on the CCD's response are the uniform thickness, t, the base diameter or span length, t, the apex height, t, and the diameter of the loading area, t, as shown in Figure 3.1 (a). The CCDs examined here are considered shallow and thin shells with a height-to-span ratio of less than 1/5 and a thickness-to-radius of curvature ratio of less than 1/20 [69].

Nonlinear geometric finite element analyses (FEA) were used to examine the force-deformation responses of CCDs using the program ABAQUS [73]. The CCD was modeled as a 3D deformable revolved shell object with linear elastic isotropic material properties and four-node shell elements (S4) for the mesh. The mesh size was selected based on a mesh refinement study. Displacement control was used to apply a static incremental displacement at the dome's apex, and large deformations were accounted for by considering geometric non-linearity in the analyses. Eigenvalue analyses were conducted to verify predicted snap-through instability by confirming that the bifurcation loads were higher than the limit-point load. For cases where the analyzed CCD was deep and thin (i.e., high h/t), the automatic stabilization option in ABAQUS's solver was used to facilitate a converged solution.

#### 3.3.3 Experimental validation

Experimental tests were conducted on 3D printed CCDs to examine the three stability states presented in Figure 1.3, and to compare the experimentally obtained F- $\delta$  response to those

generated from the FEA. The CCDs were fabricated using a 3D polymer-based printer (MakerBot Replicator 2) with polylactic acid (PLA) filament. Due to imperfections from the manufacturing process the "as printed" dimensions varied slightly (about 10%) from the nominal design values. The design and the "as-printed" dimensions for the test specimens are given in Table 3.1. This is important since small changes in t or h significantly change the dome's response and the desired stability state. Thus, the FEA simulations were based on the 'as-printed' dimensions. The PLA material has a reported Poisson's ratio, v, of 0.33 and an average modulus of elasticity, E, of 1,582 MPa [29].

Table 3.1 Design and 'as-printed' dimensions of experimentally tested CCDs

Specimen	Design dimensions			'As-printed' dimensions		
	t (mm)	<i>h</i> (mm)	l (mm)	t (mm)	<i>h</i> (mm)	l (mm)
1M	1.5	5.00	120.0	1.82	4.58	119.3
2M	1.5	5.00	120.0	1.74	4.46	119.2
3B	1.00	6.00	100.0	1.26	5.66	98.4
4B	1.00	6.00	100.0	1.17	5.67	98.7
5M	0.84	3.20	102.0	1.13	2.78	100.4
6M	1.00	3.20	102.0	1.18	2.91	101.7
8P	1.20	5.00	100.0	1.39	4.41	101.5
8P	1.20	5.00	128.8	1.45	4.29	126.9
9B	0.60	3.50	60.0	0.70	3.40	59.9
10B	0.60	3.50	60.0	0.87	2.91	59.8
11P	0.60	2.00	50.0	0.72	1.97	49.9
12B	0.60	2.60	60.0	0.74	2.62	59.9
13M	0.65	2.50	65.0	0.86	2.50	64.9
14M	0.60	1.80	50.0	0.73	1.76	50.9
Note: M: monostable, B: bistable, P: pseudo-bistable						

Tests were performed using a universal testing machine with custom fixtures (indenter) to apply a concentrated vertical load at the CCD apex, as shown in Figure 3.2. Loading was done under displacement control, applying an incremental displacement at a constant rate of 0.1 mm/s. For CCD specimens with bistable response ( $F_n < 0$ ), the loading indenter was mechanically attached to the apex of the CCD and the specimen was also clamped to the platen. Figure 3.3 shows

the loading stages for a monostable and a bistable CCDs. The figure illustrates the shape recoverability of the monostable compared to the bistable CCDs.

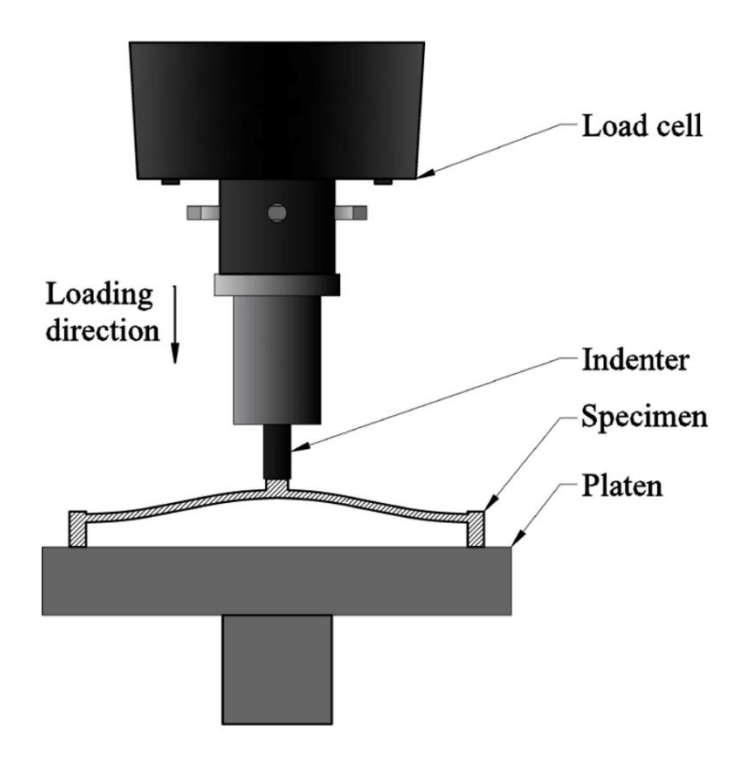


Figure 3.2 Test setup for CCD under axial compression

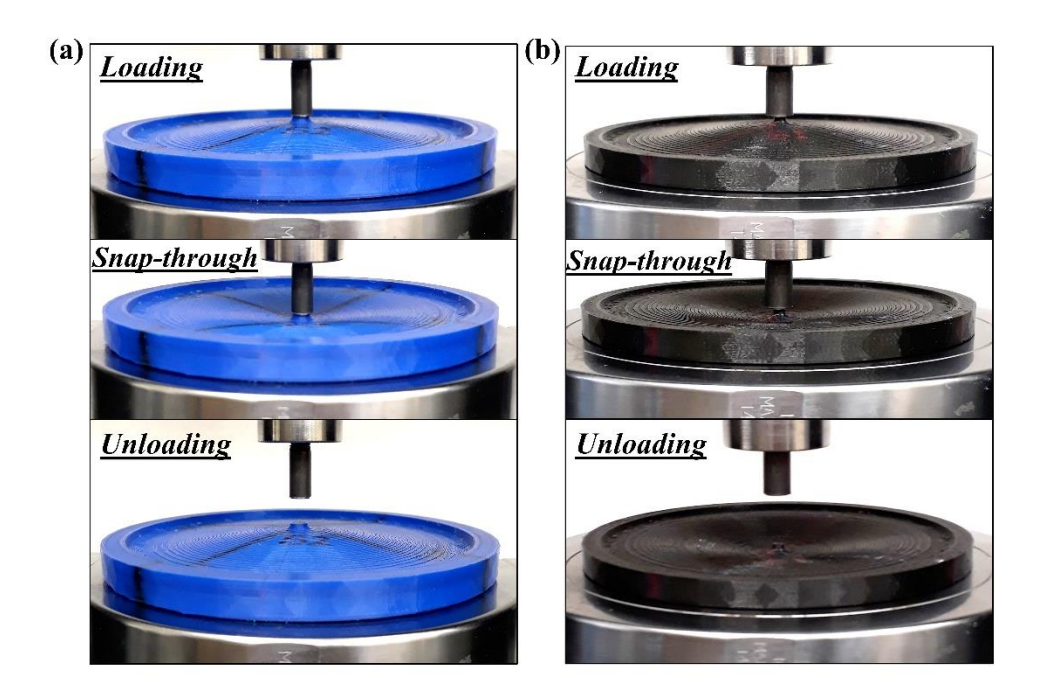


Figure 3.3 Loading stages for: (a) monostable CCD, and (b) bistable CCD

Figure 3.4 shows experimental F- $\delta$  responses for CCD specimens with 'as-printed' dimensions as given in Table 3.1. The actual modulus of elasticity of a 3D printed part is highly sensitive to the orientation of the printed layers and to the direction of loading [74,75]. For example, the investigation conducted by Perkowski [76] on the mechanical properties of 3D printed PLA parts showed that the modulus of elasticity ranged from about 550 to 3,100 MPa in tension and from 570 to 1,650 MPa in compression. Therefore, the FEA F- $\delta$  response in Figure 3.4(a) was scaled for E so that  $F_b$  was equal to that of the experimentally measured data. The scaling factor was determined by conducting a FEA for a CCD with 'as-printed' dimensions and an elastic modulus value of unity and then dividing the value of  $F_c$  (or any other value) on the experimental F- $\delta$  curve by its counterpart of the same displacement on the FEA curve. The scaling factor was 851 MPa, which represents the most representative value of E for the specimen. This procedure is valid as long as most parts of the two curves coincide; however, an exact agreement cannot be obtained because of the presence of imperfections and the non-uniformity of the 'asprinted' dimensions. Moreover, this procedure is only valid for elastic responses as discussed in Section 3.4.5.

Figure 3.4(a) shows a comparison between the experimental and numerical (FEA) F- $\delta$  responses for CCD specimen 5M with 'as-printed' dimensions (given in Table 3.1). Figure 3.4(a) shows two F- $\delta$  responses from FEA based on (1) the scaling factor and (2) an average value for E of 817 MPa. This value of E was determined from a series of tests on 3D printed ASTM D695 specimens, for which the print layers were oriented perpendicularly to the longitudinal axis to closely represent the loading conditions of the tested CCDs.

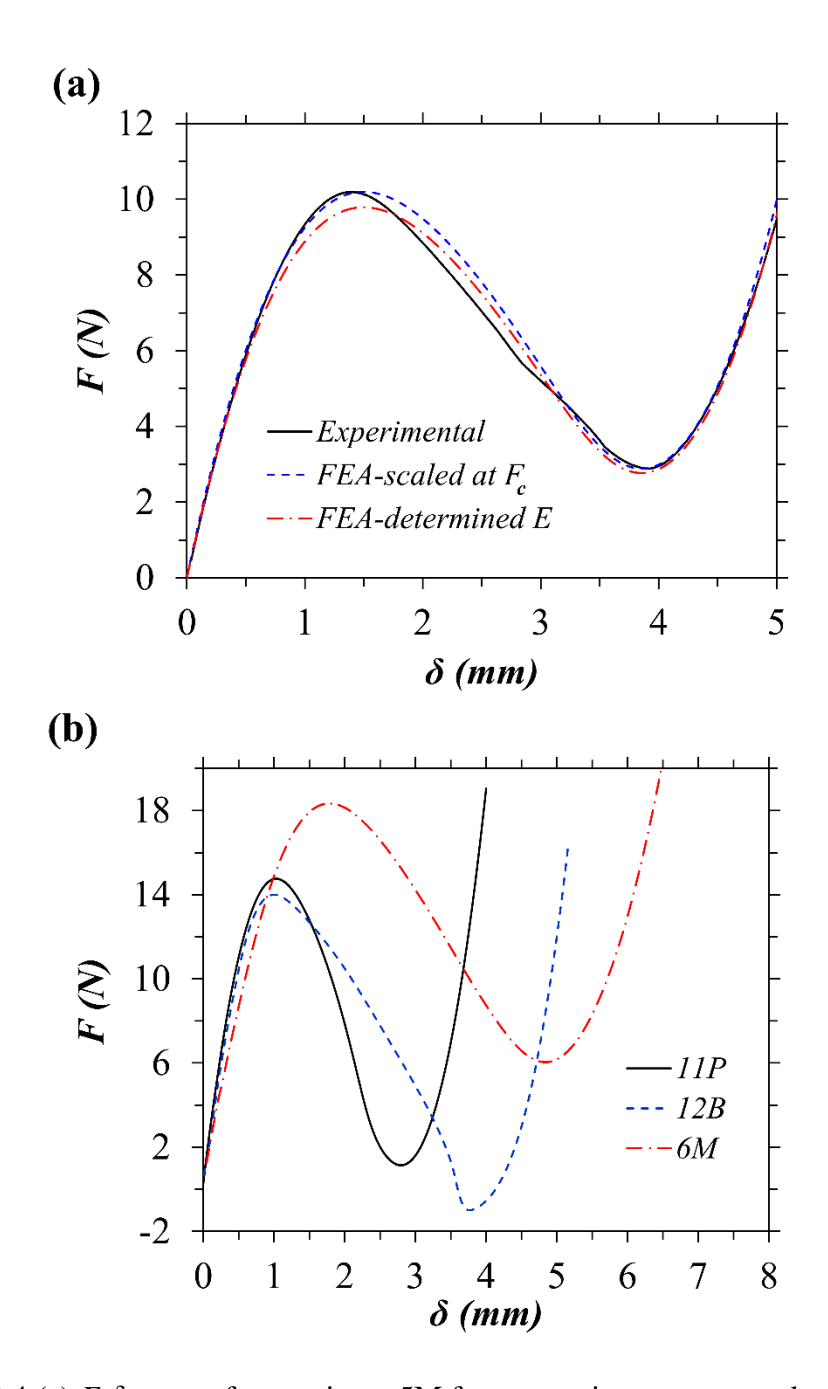


Figure 3.4 (a) F- $\delta$  curves for specimen 5M from experiment compared to FEA, and (b) experimental F- $\delta$  curves for specimens 11P, 12B, and 6M

## 3.4 Parametric Study

A parametric study was carried out on the geometric parameters t, l, h, and d, (see Figure 3.1) and the material properties E and v, to study their effects on the response of CCDs. The study was conducted using FEA by systemically varying one of the parameters, while keeping the others

unchanged. The investigated response quantities [see Figure 1.3(d)] were the critical limit load,  $F_c$ , the critical displacement,  $\delta_b$ , the negative or minimum force,  $F_n$ , and the non-zero displacement at the minimum force,  $\delta_n$ . The study also evaluated the resulting shape of the F- $\delta$  curve since it characterizes the post-buckling behavior. Moreover, normalizing ratios such as  $\delta/h$  and h/t were used to study the curve shapes. The study was conducted for CCDs with  $1.5 \le h/t \le 7.5$  and  $h/l \le 1/16$  [69]. The FEA were performed by varying l and fixing t and t and then repeating the same process for different values of t and t. The material constants were kept unchanged at t = 1500 MPa and t = 0.33.

As discussed in Chapter 1, the F- $\delta$  curve is related to the U- $\delta$  curve (Figure 1.3). The difference between the maximum and minimum strain energies,  $\Delta U$ , (i.e.,  $\Delta U = U_{max} - U_{min}$ ) is directly related to the value and the mathematical sign of  $F_n$ , and hence the stability state of a CCD. When  $\Delta U$  is greater than zero  $F_n$  is negative and the response is bistable. When  $\Delta U$  equals to zero  $F_n$  also equals zero and the response is pseudo-bistable. Local maxima and minima do not exist when the U- $\delta$  curve is monotonic, hence  $F_n$  is greater than zero and the response is monostable. Therefore, this study focuses on the F- $\delta$  curve rather than the U- $\delta$  curve to examine the stability states since dealing with a single quantity ( $F_n$ ) is easier than dealing with two quantities ( $U_{max}$  and  $U_{min}$ ).

#### 3.4.1 Effect of length (l)

The effect of varying l on the F- $\delta$  response curve is shown in Figure 3.5(a). The values of  $F_c$  and  $|F_n|$  decrease with an increase in l, while  $\delta_c$  and  $\delta_n$ , are not affected by the change in l. To further examine the effect of varying l on the shape of the F- $\delta$  curves it is necessary to normalize them to a factor in terms of l. A least square regression analysis [77] was used to determine the value of a power " $\alpha$ " for a factor  $l^{\alpha}$  to be multiplied by F for constant values of t and t. Since the

curves may have different post-buckling responses, regression analyses were performed on the values of  $F_c$ , which resulted in  $\alpha = 2$ . It was found that normalizing the F- $\delta$  curves by the factor  $l^2$  results in exact agreement among them over the entire response range (pre- and post-buckling) as shown in Figure 3.5(b).

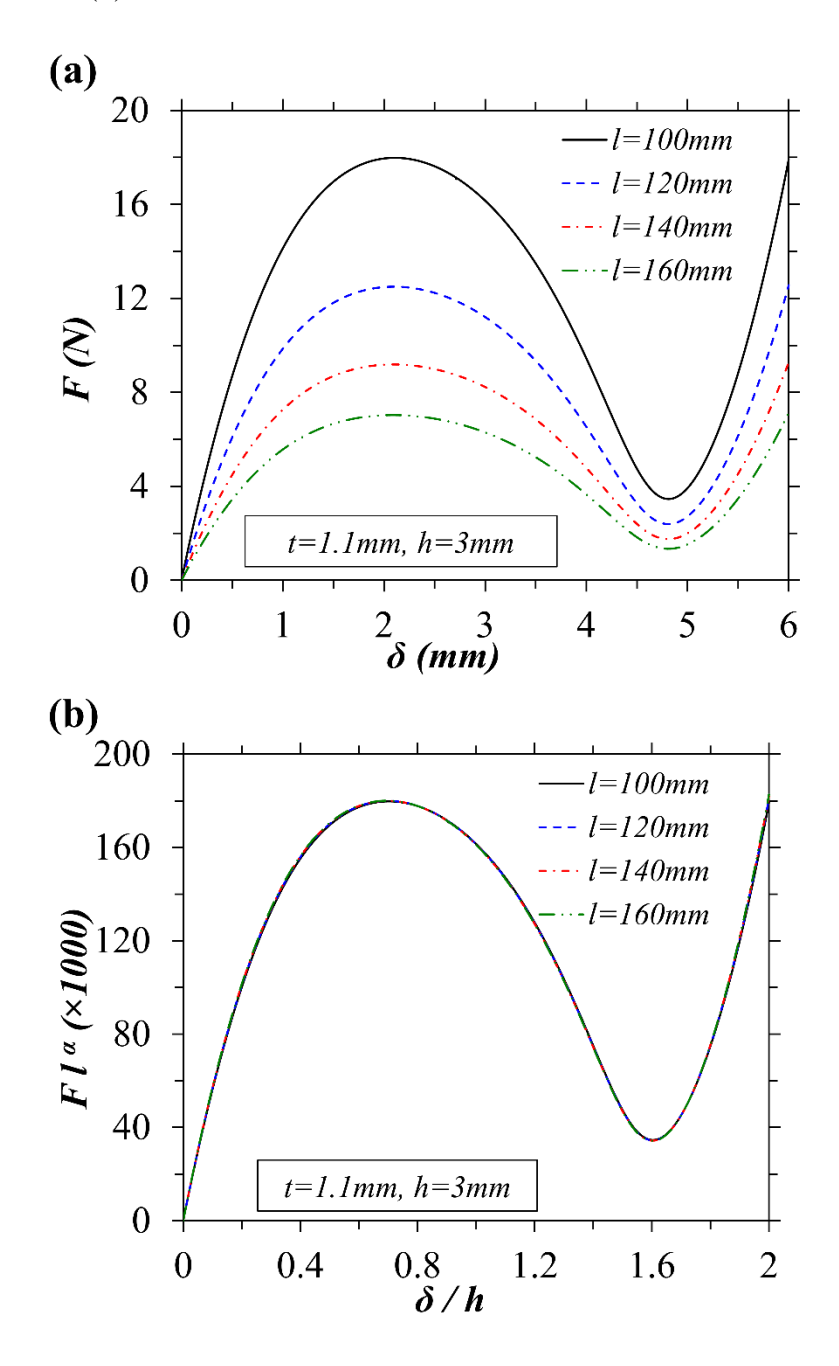


Figure 3.5 Actual and normalized F- $\delta$  curves of CCDs with constant t and h, and varying l

This shows that l has no effect on the type of response of the CCD. Thus, for example, if the F- $\delta$  response has a bistable shape, then this response type will not change to a monostable or pseudo-bistable by changing l. The reason is that since the examined CCDs are shallow where the span-length l is much larger than the thickness t and the apex height h, the variation in length has an insignificant effect on the ratios h/l and t/l.

#### 3.4.2 Effect of thickness (t)

A similar procedure was followed by analyzing CCDs with varying t while fixing other parameters. Analysis results show that t has a dominant effect on the shape of the F- $\delta$  response curve, as shown in Figure 3.6(a), where the values of  $F_c$  and  $F_n$  can be seen to increase with an increase in t. In addition, by increasing t the response changed from bistable to monostable. This means that  $F_n$  increases relative to  $F_c$  and that the ratio h/t is decreasing.

The force values in the curves of Figure 3.6(a) need to be normalized in terms of t to compare them and assess the effect of t. A least squares regression analysis [77] was used to determine the value of " $\beta$ " for the factor  $1/t^{\beta}$  for constant values of h. For this case the value of l has no effect on  $\beta$ , and hence it was not included in the analysis. Since the curves have different post-buckling responses, the regression analysis was performed only on the values of  $F_b$  to find  $\beta$ . A constant value of  $\beta = 2.412$  was found. The same value of  $\beta$  would be determined if the regression analysis was performed on the F- $\delta$  curve data up to  $F_c$ .

The normalized curves are shown in Figure 3.6(b). Comparing Figure 3.6(a) and Figure 3.6 (b) shows that  $\delta_c$  and  $\delta_c/h$  are roughly the same for all cases and thus they are only slightly affected by the change in t or h/t. On the other hand,  $\delta_n$  and  $\delta_n/h$  decrease with increasing t or decreasing h/t. From Figure 3.6(b), the normalized values of  $F_c$  are approximately the same for

varying t, while they are different for the case of  $F_n$  because of the change in post-buckling behavior.

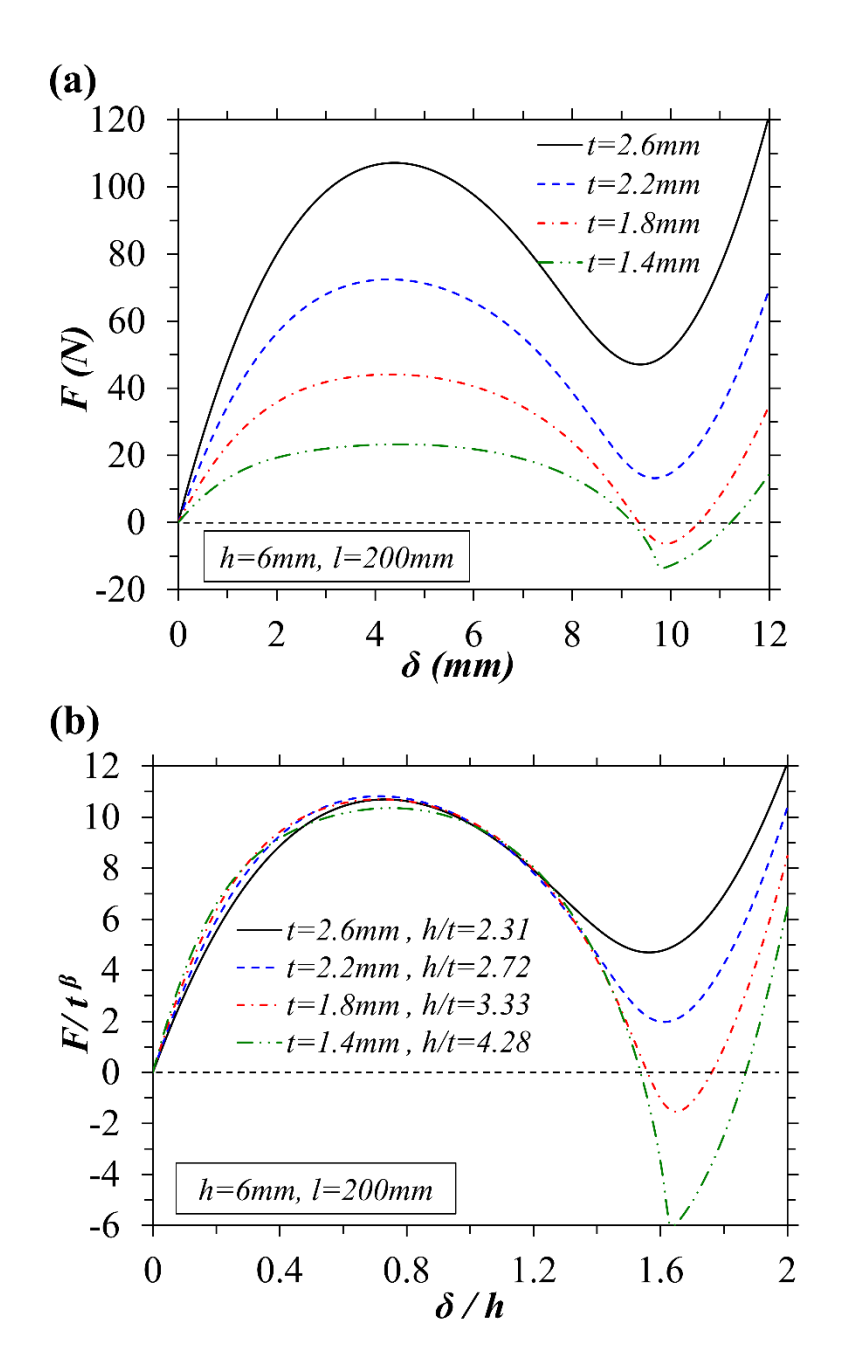


Figure 3.6 Actual and normalized F- $\delta$  curves of CCDs with constant h and l, and varying t

#### 3.4.3 Effect of height (h)

Analysis results showed that CCD height (h) has a complex effect on the shape of the F- $\delta$  curves, as shown in Figure 3.7(a). This effect can be grouped into three features: (1)  $F_c$  increases with h, similar to the effect of t; (2)  $F_n$  decreases with h, opposite to the effect of t; and (3) h increase shifts the F- $\delta$  curve with increased values for the critical displacements  $\delta_c$  and  $\delta_n$ . It can be construed that the ratio h/t mainly controls the shape of the F- $\delta$  curve and hence the stability state. Figure 3.7(a) also shows that  $\delta_c$  and  $\delta_n$ , increase with an increase in h or h/t.

The force values in Figure 3.7(a) were normalized with the factor  $1/h^{\gamma}$  in order to examine the shape of the F- $\delta$  curves. The normalized curves are shown in Figure 3.7(b). The value of " $\gamma$ " was determined to be equal to 1.582 through a least squares regression analysis on the values of  $F_c$ . The normalized curves in Figure 3.7(b) show that  $\delta_c/h$  is approximately the same for all cases and thus they are only slightly affected by the change in h. On the other hand,  $\delta_n$  and  $\delta_n/h$  increase with increasing h. The normalized values of  $F_c$  are roughly the same with varying h while they are different for the case of  $F_n$  because of the change in post-buckling behavior.

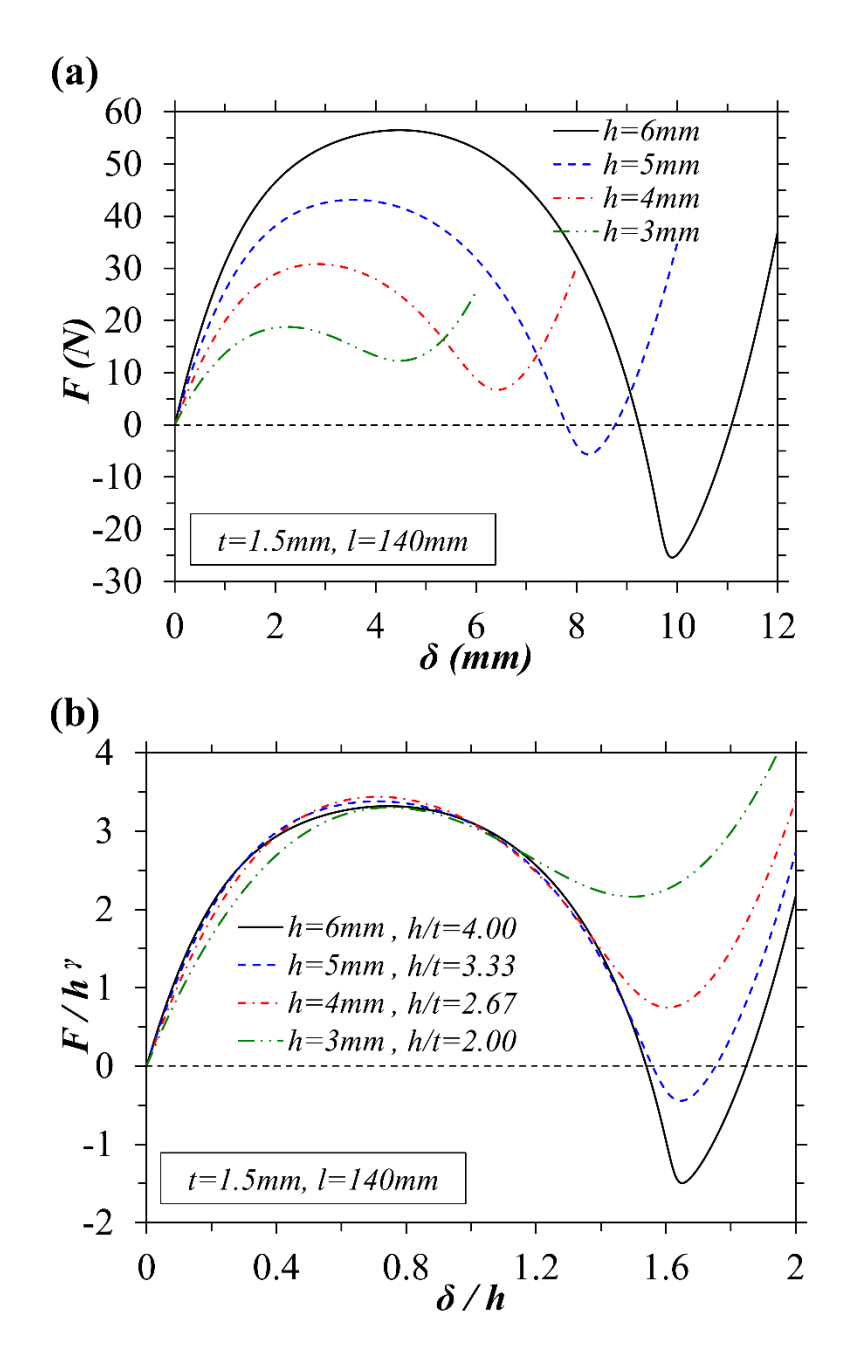


Figure 3.7 Actual and normalized F- $\delta$  curves of CCDs with constant t and l, and varying h

## 3.4.4 Effect of loading area

Another important parameter that affects the shape and the values of the F- $\delta$  curves is the loading area, that is, the circular region around the apex point where the dome is loaded, see Figure 3.8. Since in most applications a theoretical point load cannot be practically applied, there is a

finite area over which the load is distributed. In this study the area is assumed to be circular and perpendicular to the axis of rotation of a CCD. It was found that the size of this area has a significant effect on the shape of the F- $\delta$  curve, but a minimal effect on the stability state a CCD. Figure 3.8(a) shows the effect of increasing the diameter of the loading area (d) on the F- $\delta$  curves for monostable and bistable CCDs. It is shown that the values of  $F_c$  increase with an increase in d; while the values of  $F_n$  slightly increase for monostable responses and slightly decrease for bistable responses with an increase in d. In addition, the effect of d on the F- $\delta$  curve is more pronounced for deeper CCDs (i.e., CCDs with higher h/t). Increasing d also shifts the F- $\delta$  curve by decreasing the values of  $\delta_c$  and  $\delta_n$ .

If the loading area around the axis of rotation increases the original CCD area, as shown in Figure 3.8(c), the loading area has a negligible effect on the response and hence the CCD should be treated as if d = 0 with original length l. In other words, the loading area has no effect on the response as long as the loading region doesn't occupy an area of the original CCD's shape. The total span length (base diameter) is, however, increased by d (i.e., total span length is l + d). Nonetheless, this increase in length should not be considered in the analysis of the dome.

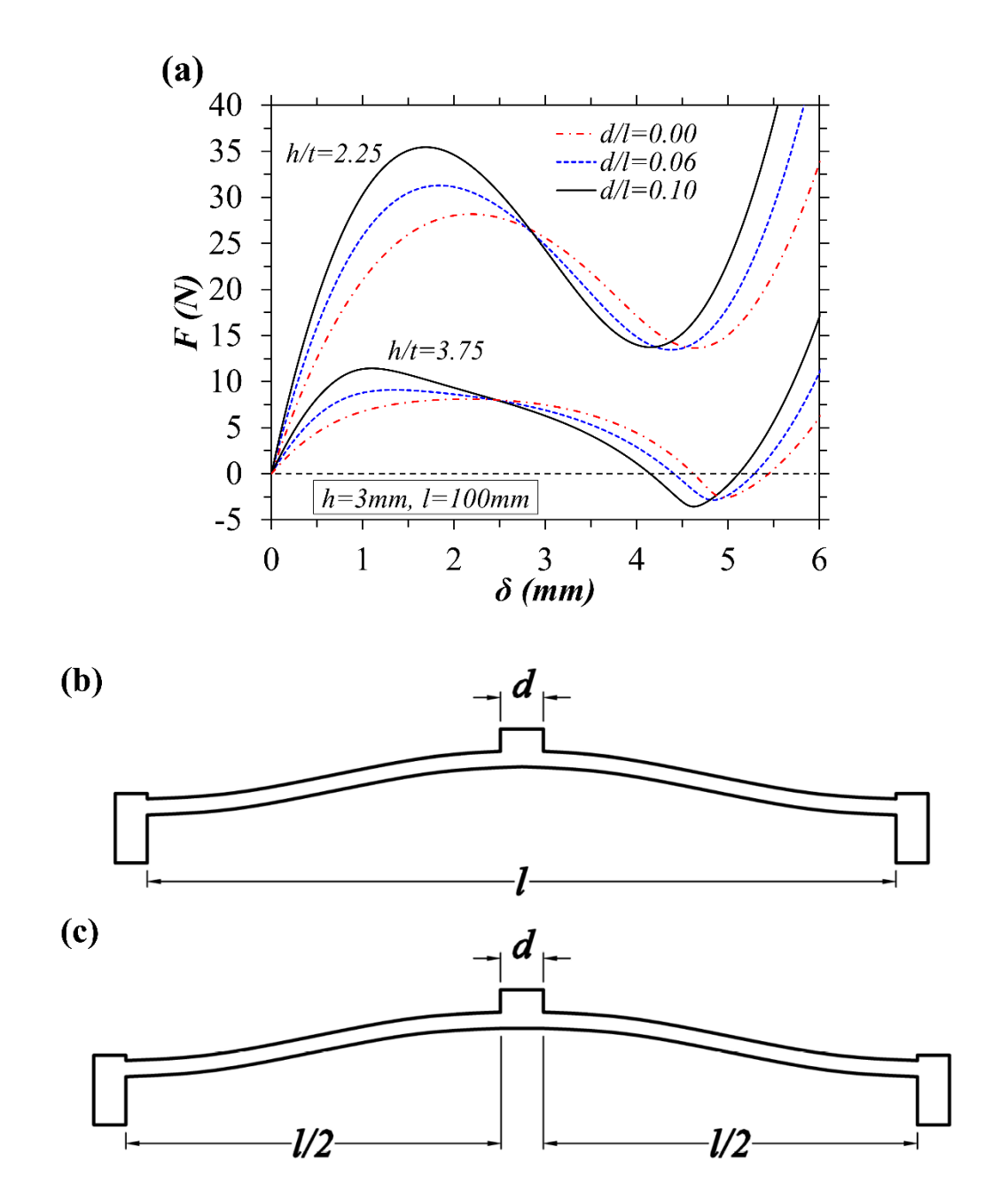


Figure 3.8 (a) F- $\delta$  curves of CCDs with constant h and l, and varying h/t and d/l; (b) original profile shape of the CCD; and (c) modified shape of CCD with added loading area

## 3.4.5 Effect of modulus of elasticity (E)

Since the concern here is the response of the CCD within the elastic range and for linear elastic material, the F- $\delta$  curve has a linear relationship with E and hence can be normalized by 1/E. To show that, several CCDs were analyzed for varying E, with all other parameters fixed and the

resulting F- $\delta$  responses are shown in Figure 3.9(a). It can be seen that  $F_c$  and  $|F_n|$  increase with an increase in E. Figure 3.9(a) also shows that  $\delta_c$  and  $\delta_n$  are the same for all cases, and thus unaffected by E.

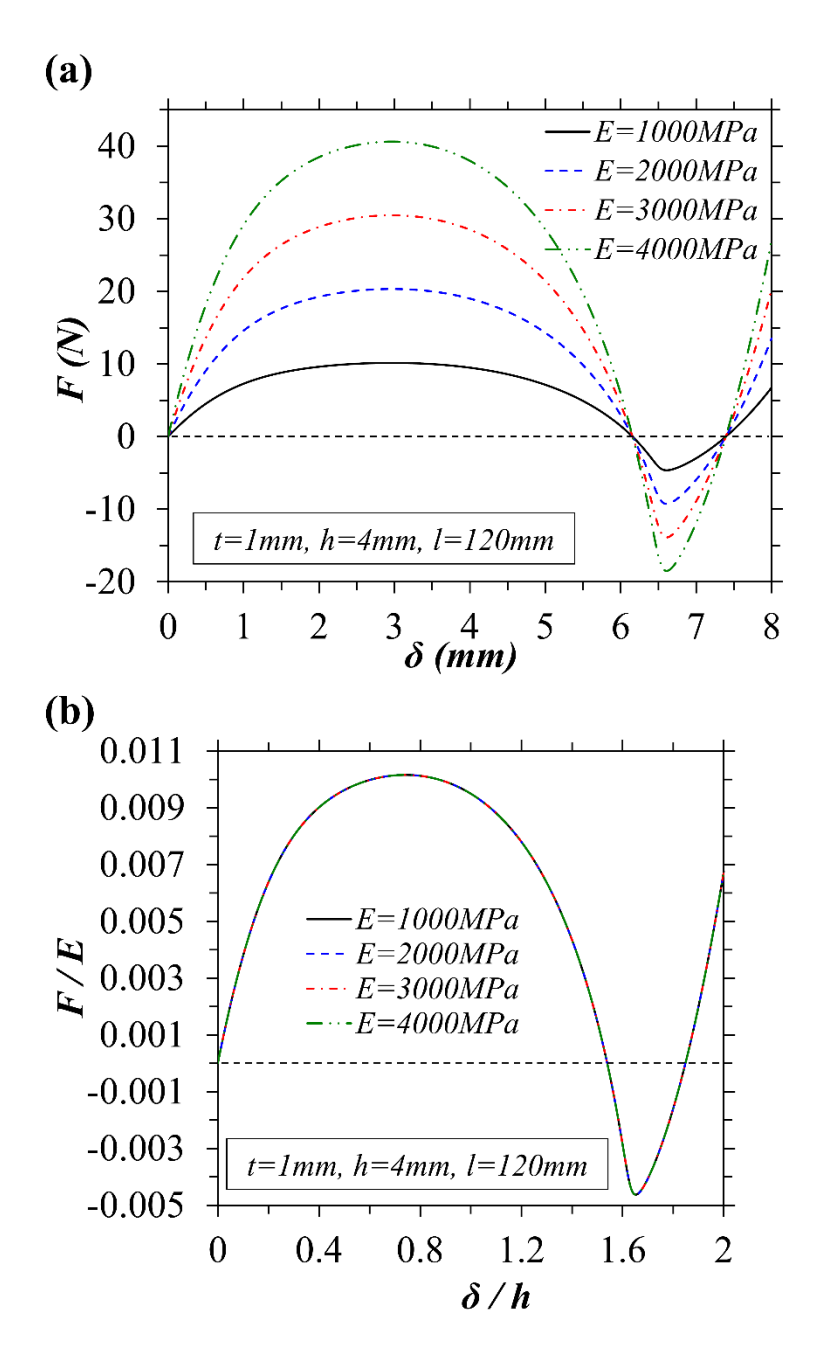


Figure 3.9 Actual and normalized F- $\delta$  curves of CCDs with constant t, h and l, and varying E

As expected, the F- $\delta$  curves for varying E collapse into each other when normalized by 1/E, see Figure 3.9(b). Therefore, E has no effect on the shape of the F- $\delta$  curves and the stability state of CCD if the material is linear elastic. The F- $\delta$  curves can thus be scaled for different E values.

#### 3.4.6 Effect of Poisson's ratio (v)

Figure 3.10 shows that  $F_c$  increases and  $F_n$  decreases with an increase in v. It can also be observed that  $\delta_c$  and  $\delta_n$  do not change for all cases, and thus they are not affected by v. The shape of the F- $\delta$  curves is slightly affected by v. As v increases the response changes from monostable to bistable (and vice versa). Further, can be noted that  $F_n$  can become negative with increasing v as shown in Figure 3.10.

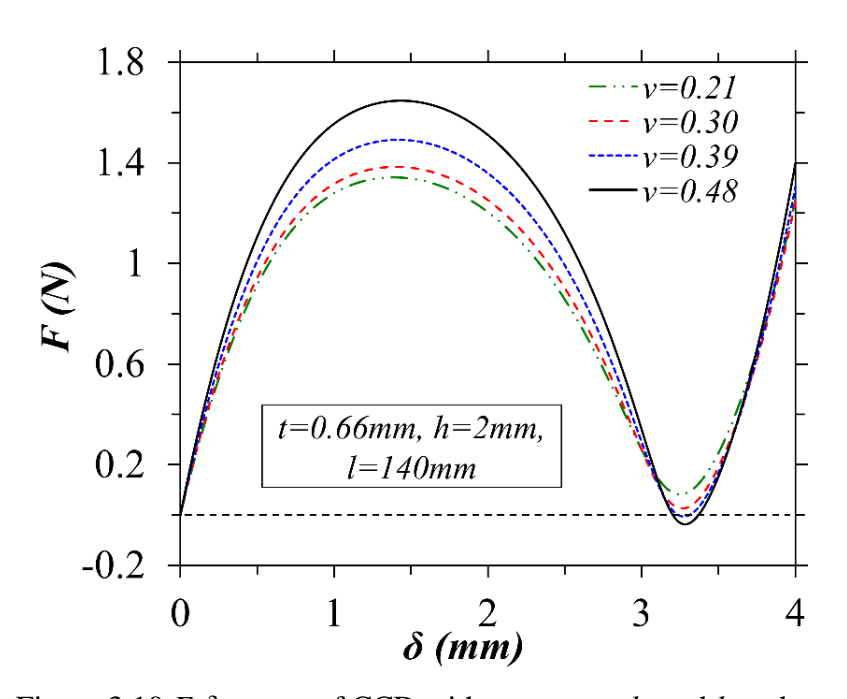


Figure 3.10 F- $\delta$  curves of CCD with constant t, h, and l, and varying v

### 3.5 Design Expressions for CCDs

The F- $\delta$  response in Figure 3.11(a) is the result of a dynamic FEA for 12 monostable CCDs connected in series. Loading on the system was applied by displacement-controlled incremental deformation with geometric non-linearity considered in the analysis. The CCDs in the system were linked in series by connecting them at their confining rings and at the apex tips as shown in Figure 3.11(b). The enclosed area between the loading and unloading curves represents the dissipated energy by the system. Studies by Benichou and Givli [78], and Restrepo *et al.* [33] showed that the response of a system of multistable units [e.g., Figure 3.11(a)] can be accurately calculated based on the simplified multilinear response of a single unit, as that shown in Figure 3.12. The approach greatly simplifies the analysis procedure and it is particularly convenient for design purposes. It is thus of interest to develop a simplified multilinear F- $\delta$  response curve for the CCD units.

Previous sections presented the studies of the effects of geometric and material properties on the F- $\delta$  response of CCDs, and a normalizing factor was determined for each parameter. These factors are now used to develop expressions for the key features of a CCD's F- $\delta$  response to facilitate the construction of a multilinear response as shown in Figure 3.12. It is recommended to use these expressions for CCDs with  $1.5 \le h/t \le 4.5$  and  $h/l \le 1/20$  for more accurate results. The objective is to use this simplified response to obtain the response for a system of multiple CCDs as shown in Figure 3.11(a).

The multilinear response of a CCD (Figure 3.12) is divided into three regions [33]: the initial stable equilibrium path in region I before the snap-through limit-point with an effective stiffness  $k_I$ , the unstable equilibrium, or snap-through, path in region II with negative stiffness  $k_{II}$ , and the post snap-through (or post-critical) stable path in region III with stiffness  $k_{III}$ . Defining the

linear segments requires estimating the buckling load and displacement ( $F_b$  and  $\delta_b$ ), the minimum force and displacement ( $F_n$  and  $\delta_n$ ), and the post snap-through buckling stiffness ( $k_{III}$ ).

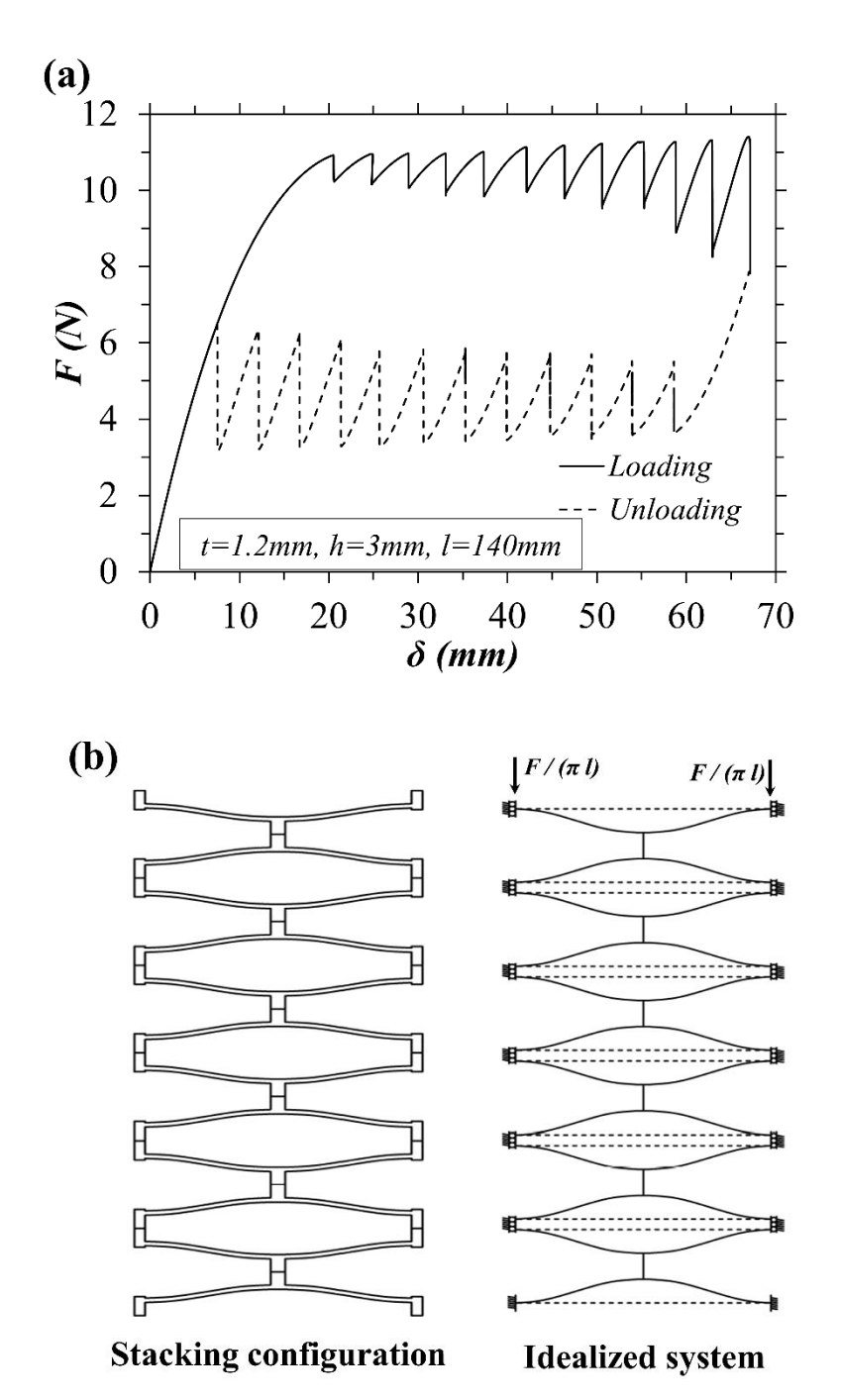


Figure 3.11 Twelve monostable CCD units connected in series (a) hysteretic response from FEA, and (b) stacking configuration and idealized system

In addition, it is of interest to know what type of stability would occur, that is, whether the CCD remains buckled (bistable) or restores to its original configuration (monostable) upon load removal. This can be achieved by knowing the conditions at which the pseudo-bistable response occurs. Thus, a study was also conducted to determine the governing factors of this stability state.

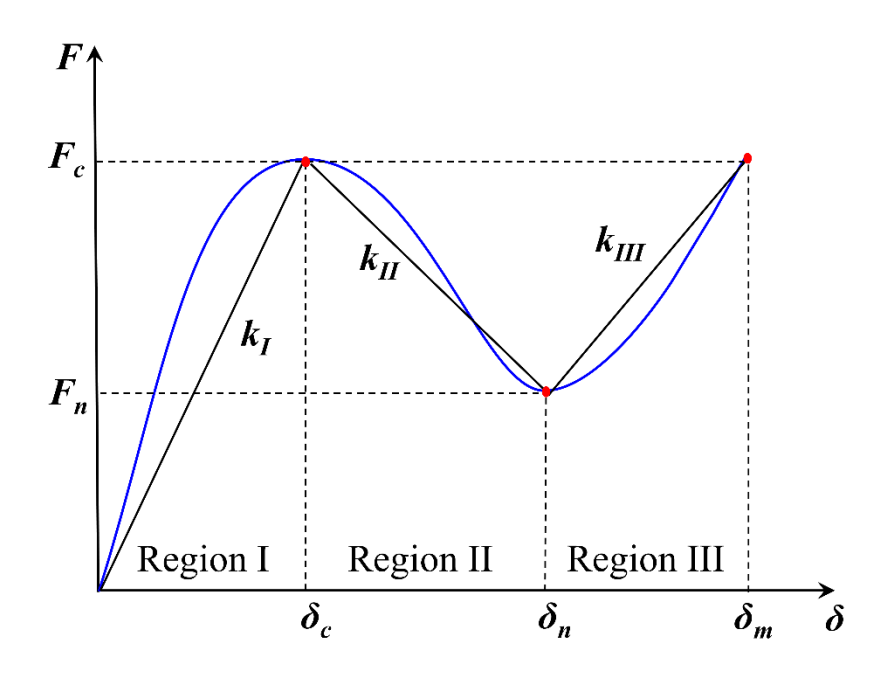


Figure 3.12 Actual and multilinear F- $\delta$  responses of a CCD

#### 3.5.1 Critical limit-point (snap-through) load (F<sub>c</sub>)

The value of  $F_c$  can be estimated by multiplying the inverses of the normalizing factors determined earlier by each other, in addition to a calibration factor,  $C_c$ , as given by Equation (3.2).

$$F_c = C_c t^{\beta} h^{\gamma} E / l^{\alpha} \tag{3.2}$$

The factor  $C_c$  is in terms of h/t and v and can be calculated from the FEA results by normalizing  $F_c$  by  $l^a/t^\beta h^\gamma E$ . Figure 3.13 shows the calculated  $C_c$  values for h/t and v. Each solid-line curve in Figure 3.13 was approximated by a second-degree polynomial in terms of h/t and v, as given in Equation (3.3) with an absolute maximum error of about 2 %.

$$C_c = (-0.466 \text{ v} - 0.251)(h/t)^2 + (3.304 \text{ v}^{0.27})(h/t) + (19.56 \text{ v}^{0.35})$$
(3.3)

The value of  $C_c$  ranges from about 15 to 19 and can be simplified to a constant value of 17 with an 11.7 % maximum absolute error.

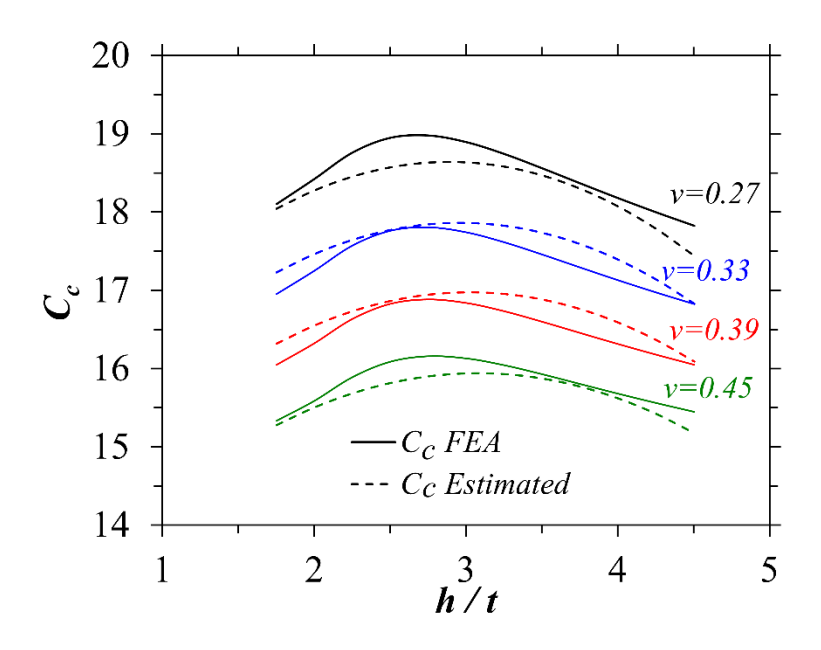


Figure 3.13  $C_c$  curves with h/t for different values of v

As can be seen in Figure 3.8(a), d has a significant effect on the F- $\delta$  response of CCDs, which in turn depends on h/t. To account for this effect,  $F_c$  and  $F_n$  values from FEA for CCDs with d > 0 were normalized by the values of  $F_c$  and  $F_n$  with d = 0. A relation was then established to determine a force modification factor, D, that is related to d/l and h/t as given in Equation (3.4). Therefore, for CCDs with d > 0 [as shown in Figure 3.8(b) only], the buckling force  $F_c$  using Equation (3.2) should be multiplied by D given in Equation (3.4). This factor ranges from 1 to 1.43 and the expression is valid for  $d/l \le 0.1$ .

$$D = 10.6 (h/t)(d/l)^2 - 0.225 (d/l) + 1 \ge 1$$
(3.4)

#### 3.5.2 Minimum Load $(F_n)$

An expression similar to Equation (3.2) was used to estimate  $F_n$  with  $C_c$  replaced by  $C_n$  as given in Equation (3.5). The factor  $C_n$  was also calculated by normalizing  $F_n$  from the FEA results by  $l^{\alpha}/t^{\beta}h^{\gamma}E$ . Figure 3.14 shows the calculated  $C_n$  values with h/t and v. As can be seen,  $C_n$  changes sign from positive to negative with increasing h/t. Thus, this quantity controls the stability state at which the response of a CCD would be monostable or bistable. Figure 3.14 also shows how the FEA results (solid-line curves) can be approximated by a second-degree polynomial in terms of h/t and v, as given in Equation (3.6). The value of  $F_n$  should also be modified by the force correction factor D given in Equation (3.4) for CCDs with d > 0.

$$F_n = C_n t^{\beta} h^{\gamma} E / l^{\alpha} \tag{3.5}$$

$$C_n = (0.336 \text{ v} + 0.889)(h/t)^2 - (13.06 \text{ v} + 10.82)(h/t) + (51.38 \text{ v}^{0.295}) \ge -12$$
 (3.6)

#### 3.5.3 Critical limit-point displacement ( $\delta_c$ )

The value of  $\delta_c$  is related to h and is affected by h/t. Thus, it is best expressed as a ratio of h and in terms of h/t. Figure 3.15 shows the calculated  $\delta_c/h$  against h/t from FEA results for several CCDs. The data points show that the relation between  $\delta_c/h$  and h/t is nonlinear and it was approximated by a second-degree polynomial. The following expression was developed for  $\delta_c/h$ :

$$\delta_c/h = 0.061 (h/t)^2 - 0.4 (h/t) + 1.35$$
 (3.7)

For h/t > 4.5, Equation (3.7) should be evaluated based on h/t = 4.5. Results from FEA compared to estimated values of  $\delta_c/h$  using Equation (3.7) have average absolute error of less than 3 %.

For CCDs with d > 0 [as shown in Figure 3.8(b) only], the calculated displacement  $\delta_c$  using Equation (3.7) should be multiplied by a displacement correction factor,  $G_c$ , that depends on d/l and h/t as given by Equation (3.8). This factor should range from 0.42 to 1.

$$G_c = [-1.67 (h/t) + 1.1](d/l) + 1 \le 1$$
(3.8)

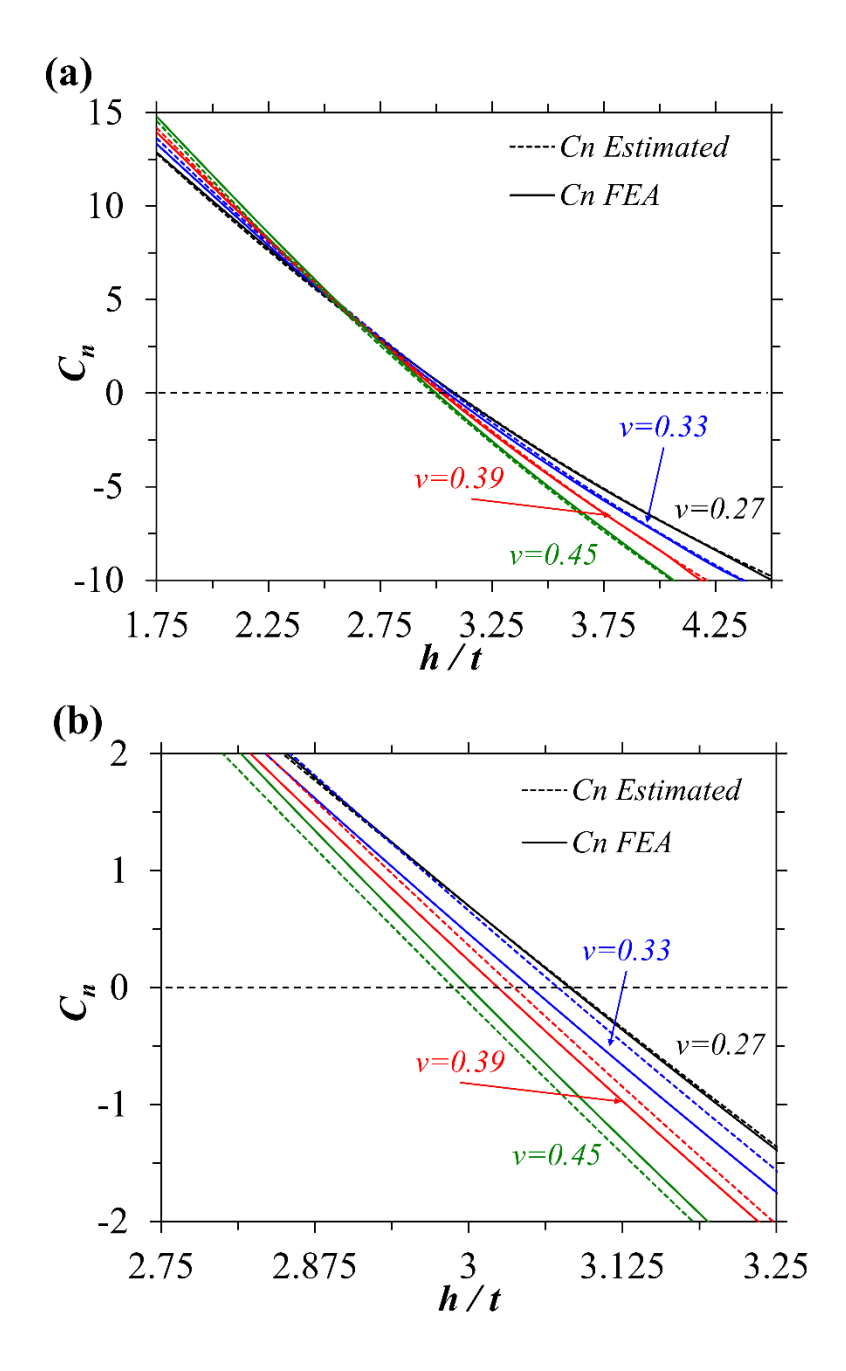


Figure 3.14 (a)  $C_n$  curves with h/t for different values of v, and (b) zoom-in at  $C_n = 0$ 

## 3.5.4 Displacement at $F_n(\delta_n)$

As for  $\delta_c$ ,  $\delta_n$  was normalized by h and expressed in terms of h/t, and the data can be approximated by Equation (3.10), see also Figure 3.15. However, the relation of  $\delta_n$  with respect to h/t seems simpler than that of  $\delta_c/h$ , as shown in Figure 3.15. For h/t > 4.5,  $\delta_n/h$  should be calculated

based on h/t = 4.5. The values of  $\delta_n/h$  using Equation (3.9) have an average absolute error of less than 2% with FEA results.

$$\delta_n/h = -0.081 (h/t)^2 + 0.575 (h/t) + 0.641 \tag{3.9}$$

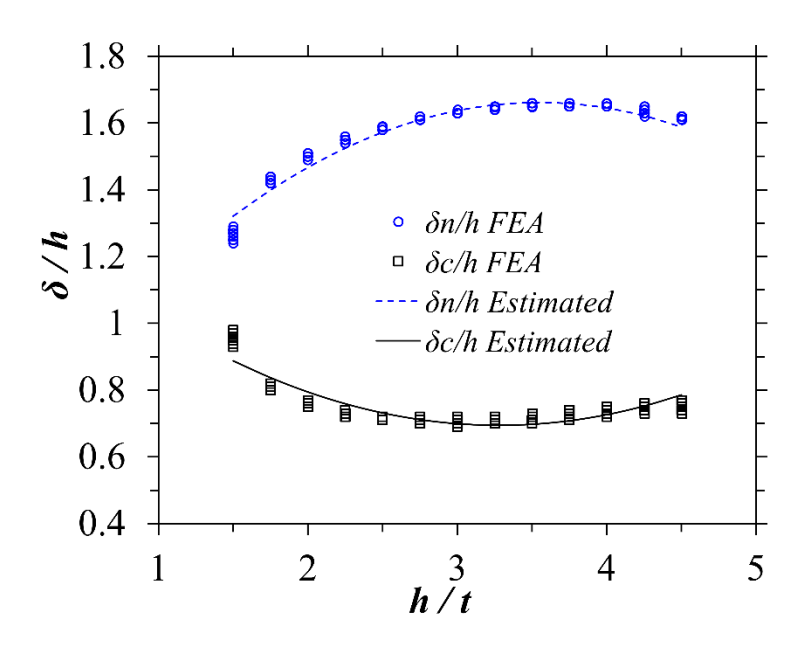


Figure 3.15 Data and fit curves for  $\delta_c/h$  and  $\delta_n/h$  with h/t

For CCDs with d > 0, the displacement  $\delta_n$  using Equation (3.9) should be multiplied by a correction factor,  $G_n$ , that depends on d/l and h/t as given by Equation (3.10). This factor should range from 0.89 to 1.

$$G_n = [0.24 (h/t) - 1.43](d/l) + 1 \le 1$$
(3.10)

#### 3.5.5 Post snap-through stiffness $(k_{III})$

At least two F- $\delta$  points are required to determine the stiffness  $k_{III}$ . The first point is the minimum force  $F_n$  at displacement  $\delta_n$ . The second point is the limit-point force  $F_c$  at displacement  $\delta_m$ , as shown in Figure 3.12. The displacement  $\delta_m$  at  $F_c$  level was determined from FEA for various geometric and material properties. It was found that  $k_{III}$  can be expressed as a ratio of  $k_I$ . This ratio

 $(k_{III} / k_I)$  is mainly affected by h/t and it ranges from 0 at about h/t = 1.45 to 2.78 for  $h/t \ge 4.5$ . As a result, Equation (3.11) can be used to estimate  $k_{III} / k_I$ :

$$k_{III}/k_I = 0.9137 (h/t) - 1.108 \le 2.78$$
 (3.11)

#### 3.5.6 Limiting h/t for pseudo-bistable state

In Section 3.4 it was shown that only t, h, and v affect the stability state of a CCD, and hence the shape of the F- $\delta$  curve; while l and E only affect the amplitude of the F- $\delta$  curve without changing its shape, and hence the post-buckling response. Therefore, the type of response (i.e., shape of the F- $\delta$  curve) is governed by a relation involving t, h, and v based on the values of  $F_n$ . Thus, the aim here is to determine a critical height-to-thickness ratio,  $(h/t)_{cr}$ , at which the value of  $C_n$  equals zero. This was achieved by examining the effect of v on  $C_n$  (or  $F_n$ ), see Figure 3.14.

From Figure 3.14(b) it can be seen that  $(h/t)_{cr}$  decreases with an increase in v. By determining the values of h/t at which  $C_n = 0$  for several values of v, a relation between  $(h/t)_{cr}$  and v was obtained as shown in Figure 3.16(a). An expression to estimate  $(h/t)_{cr}$  was developed in terms of v and is given in Equation (3.12).

$$(h/t)_{cr} = 2.879 / v^{0.052}$$
(3.12)

The value of  $(h/t)_{cr}$  can be used to design a CCD with a specific stability state. A CCD would have a monostable response if h/t is less than  $(h/t)_{cr}$  and a bistable response if h/t is greater than  $(h/t)_{cr}$ . Figure 3.16(b) shows the stability state for the experimentally tested 3D printed specimens with v = 0.33 and  $(h/r)_{cr} = 3.05$  as calculated by Equation (3.12). The specimens showed a consistent behavior with the determined limit of  $(h/r)_{cr}$ . The CCDs below the critical line in Figure 3.16(b) had monostable behavior while CCD above the line had bistable behavior. Pseudo-bistable CCDs had h/t close to  $(h/r)_{cr}$  and recovered their original configuration after a delay, which

indicates viscoelastic material behavior. It should be noted that CCDs with h/t less than 1.5 will exhibit a monotonic F- $\delta$  response and will not have snap-through buckling behavior.

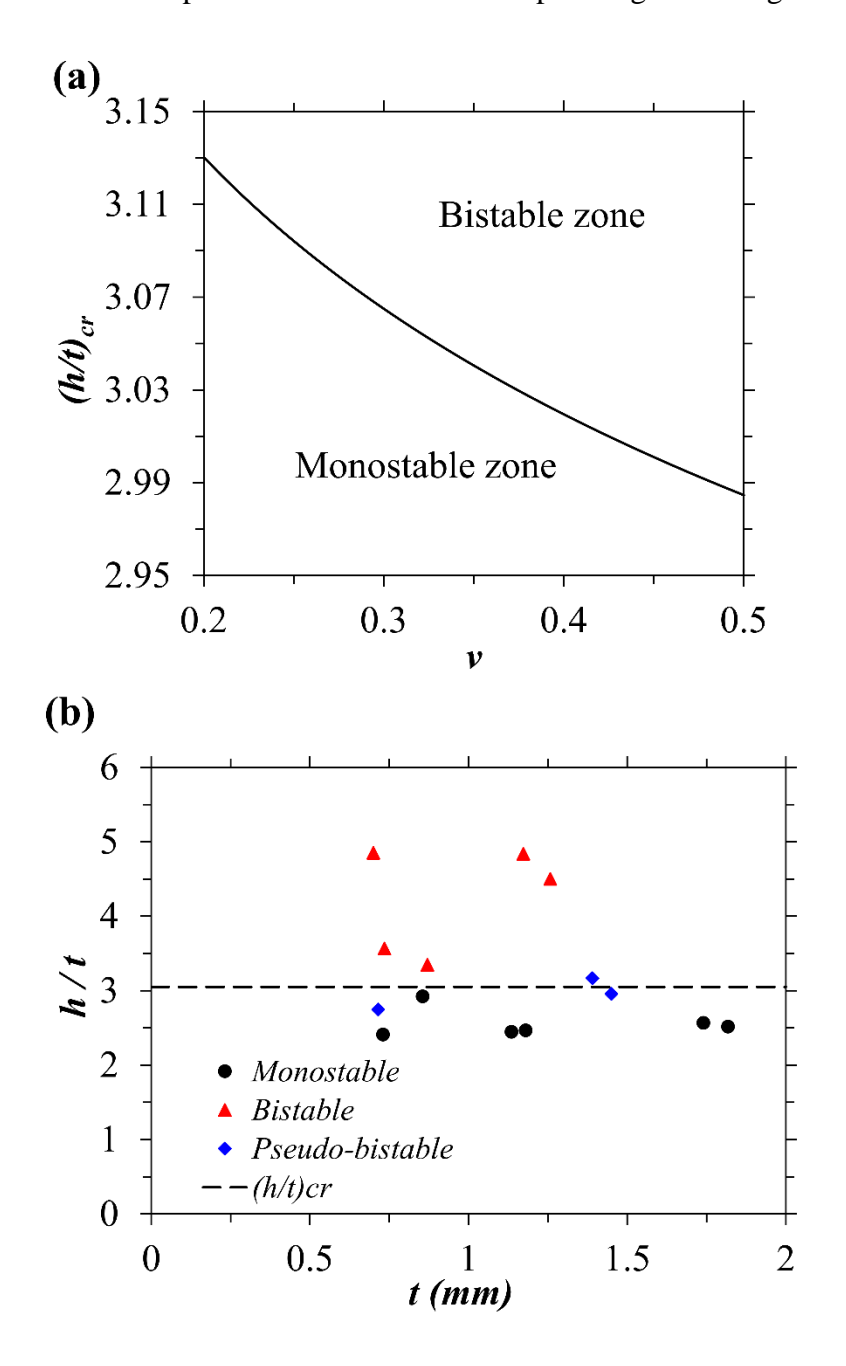


Figure 3.16 (a) Critical height-to-thickness ratio  $(h/t)_{cr}$  vs. v; (b) stability state for 3D printed specimens with v = 0.33 and  $(h/t)_{cr} = 3.05$ 

#### 3.5.7 Example: Approximate analysis of single and multiple CCDs

As discussed at the start of Section 3.5, the multilinear response of a single CCD is useful to obtain the response of a system of multiple CCDs connected in series. The following is an example that illustrates this procedure and compares it to experimental results. It should be noted that a detailed presentation and discussion on the response of multiple CCD is beyond the scope of this work and it is the subject of on-going studies. However, the brief overview provided herein illustrates both the use of CCDs as well as the value of the developed design expressions.

Four CCDs were designed and 3D printed with equal nominal dimensions of t = 0.6 mm, h = 1.8 mm, and l = 50 mm. Due to manufacturing imperfections, the 'as printed' dimensions are  $t = 0.75 \pm 0.03$  mm,  $h = 1.76 \pm 0.02$  mm, and  $l = 50 \pm 1$  mm. The material properties are taken as E = 817 MPa and v = 0.33. Figure 3.17(a) shows the experimental and the FEA F- $\delta$  response of a single CCD. The simplified multilinear response of the CCD specimens, also shown in Figure 3.17(a), was constructed using the developed expressions in Equations (3.2) through (3.11) based on the average dimensions of the printed units. The constructed response slightly underestimates  $\delta_n$  and  $F_n$ ; however, it is in general agreement with the test result. The fabricated specimens recovered their original configuration immediately upon unloading and hence showed a monostable behavior with h/t = 2.35, which is smaller than  $(h/t)_{cr}$  determined as follows:

$$(h/r)_{cr} = 2.879 / v^{0.052} = 3.05$$

Four CCDs units with equal nominal dimensions as the single CCD described above were connected in series and the system was tested under displacement control loading as shown in Figure 3.18. The resulting F- $\delta$  response is shown in Figure 3.17(b). The multilinear F- $\delta$  response shown in Figure 3.17(a) for a single CCD was used to calculate the F- $\delta$  response for the four-unit system, as shown in Figure 3.17(b). The system response was determined using the model by

Benichou and Givli [78]. While the experimental and analytical responses are in relative agreement, the displacement,  $\Delta_{c1}$ , at the first snap-through event of the experimental response is smaller than that of the multilinear response. This is primarily attributed to dimension variations among the printed CCD units, which leads to early snap instability of the CCD with the lowest  $F_c$  in the system before the calculated average snap-through displacement  $\Delta_{c1} = 4\delta_c$ . In other words, the effective stiffness of the tested system is higher than that based on the calculated average response  $(F_c / 4\delta_c)$ . Therefore, during loading, the CCD in the system with lowest  $F_c$  reaches its limit-point instability  $(\delta_c, F_c)$  while other CCDs in the system are below their limit.

Although the snap-through limit variation among CCD units complicates calculating an accurate response for the system, it is an essential feature to obtain a response with progressive snapping instabilities, and hence elastic energy dissipation. The area enclosed between the experimental loading and unloading curves represent the elastic strain energy dissipated by the system. This area depends on the number of connected units and h/t.

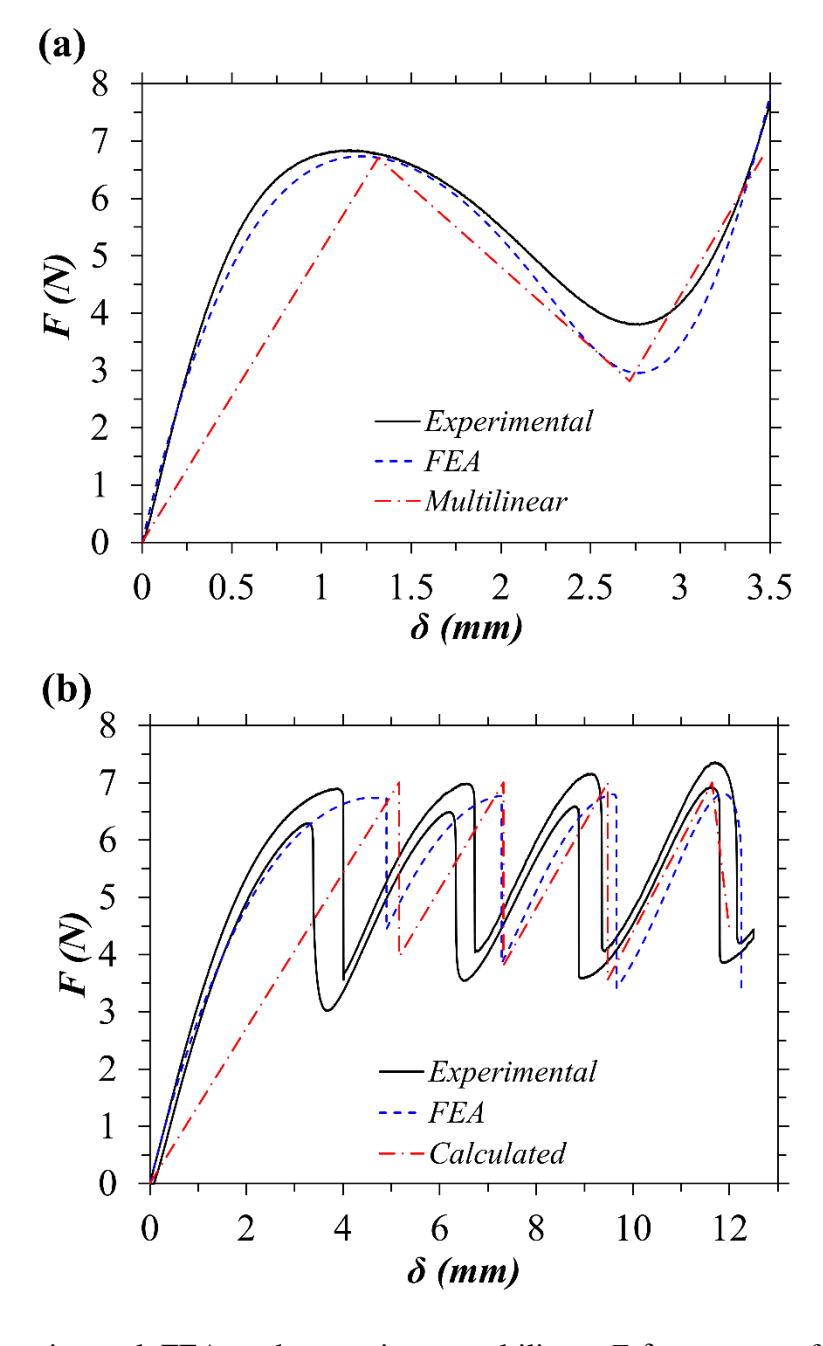


Figure 3.17 Experimental, FEA, and approximate multilinear F- $\delta$  responses of (a) a single CCD, and (b) system of 4 CCDs connected in series

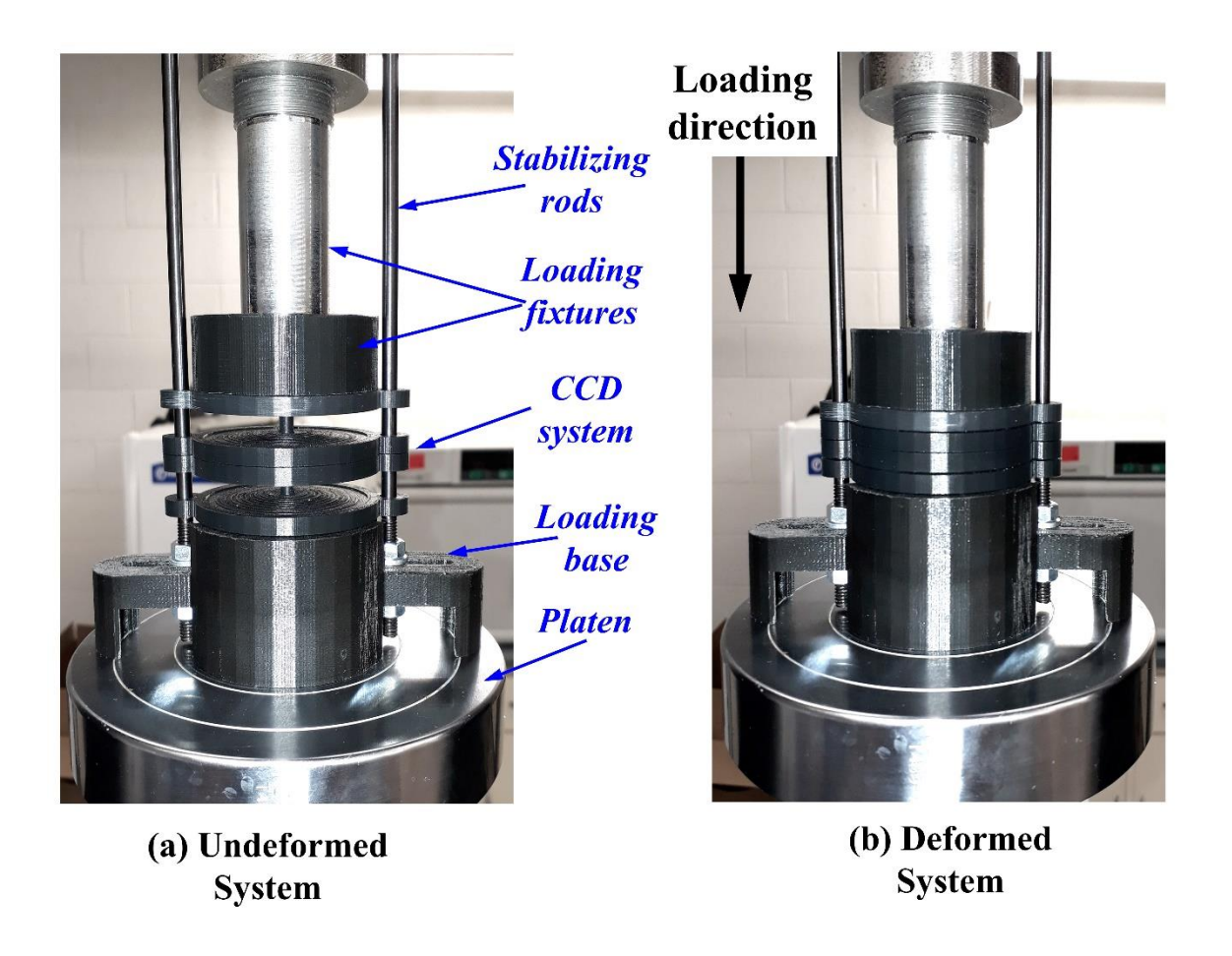


Figure 3.18 Test setup for the four CCDs connected in series

#### 3.6 Conclusions

The presented study showed that cosine-curved domes (CCDs) with constrained edges loaded under a concentrated apex transverse load can attain snap-through instability with symmetric deformations, even with some imperfections. This was validated through finite element simulations and testing of 3D printed specimens for CCDs within the geometrical range of  $1.5 \le h/t \le 7.5$  and  $h/l \le 1/16$ . However, CCDs with higher h/t and h/l ratios are more susceptible to bifurcation and asymmetric deformations. In addition, CCDs within the noted geometry range do not require the restriction of other buckling modes to have a symmetric reversible snapping, offering a multistable element that could be used as a building unit for devices subjected to relatively high forces for energy dissipation and repeated use.

Three types of snap-through instability responses were recognized for the studied CCDs: monostable, pseudo-bistable, and bistable responses. The main factor affecting the response is the height-to-thickness ratio (h/t). Increase of h/t changes the response from monostable to bistable. Increasing value of the material's Poisson's ratio (v) decreases the value of the minimum force ( $F_n$ ), which could change the instability type from monostable to bistable. The study also showed that the base diameter (l) affects the values of the force-deformation curve but it has no effect on its shape. It was found that CCDs have a critical height-to-thickness ratio (h/t)<sub>cr</sub> at which the response is pseudo-bistable ( $F_n = 0$ ). This allows designing CCDs with a targeted snap-through instability type. The ratio is independent of the geometric and material properties except for v. However, the effect of v on (h/t)<sub>cr</sub> is small for common materials. (h/t)<sub>cr</sub> may be taken as a constant value of 3.045. Expressions to estimate key parameters in the force-deformation response were developed to construct a multilinear force-deformation response, and shown to facilitate the response analysis for a system of multiple CCDs.

The multistable elastic behavior possessed by CCDs originates from the cosine curved profile that allows them to have a tunable multistable response. The proposed CCDs offer controllable elastic snap-through behavior that could be used as a building block for elastic energy dissipation mechanisms subjected to relatively high forces. Future studies on the response of CCDs should include the influence of manufacturing imperfections and loading direction.

## **CHAPTER FOUR**

# 4 Multiple Cosine-Curved Dome System

#### 4.1 Overview

In this chapter the behavior of the MCCD systems was studied numerically and experimentally. Finite element analyses (FEA) were performed for MCCD systems to study the effects of geometric properties and the number of the dome units (CCDs) on system behavior under displacement-controlled loading. A multilinear analytical model that describes the system's force-displacement (F- $\Delta$ ) response is proposed. The energy dissipation characteristics of the MCCD system are also studied. Finally, experimental tests on 3D printed specimens were conducted to analyze the system and validate the analytical model. The study presented in this chapter was published in the journal of Applied Mechanics [79].

### 4.2 Background

A new energy dissipation system comprised of multiple cosine-curved domes (MCCD) connected in series is presented herein. The building units of the MCCD system are dome-shaped shell elements called cosine-curved domes (CCD) studied in Chapter 3 [68]. The noted former study introduced the multistable element (CCD), showed how it can attain a controllable snapthrough instability, and presented its response characteristics; with the motivation of using it in a system for elastic energy dissipation.

When an MCCD system [see Figure 1.2(c)] is mechanically loaded, the CCD units in the system consecutively snap-through to a new stability state within their elastic range. When the system is unloaded, the units consecutively snap-back to their original configuration, either by a

restoring external force for bistable CCDs or by self-recoverability (preferred) for monostable CCD units. If a sufficient number of connected units in series is used, the MCCD system follows distinct loading and unloading paths resulting in a hysteretic response, as shown in Figure 1.2(d). The area enclosed by the loading and unloading curves represents the elastically dissipated energy. This energy dissipation is due to the transformation of some of the induced mechanical energy of the applied work to elastic vibrations that are damped by the base material of the repeating units and converted to irreversible thermal energy (heat) with each snap-through buckling event [12,27,34,35].

The proposed MCCD system avoids a few design disadvantages that limit the practicality of other systems presented in the literature. For example, when multiple units in the MCCD are stacked in parallel (see Section 4.3.2), no design modification is required on the system general configuration nor to the size of the constraining edges (rings) compared to systems comprised of curved beams [29,33,36]. The reason is that in a loaded MCCD system with CCD units stacked in parallel, each ring is resisting the same horizontal forces while the units in the system are collectively resisting a much larger vertical force than that can be developed by a single unit. Conversely, systems comprised of curved-beams [29,33,36] require increasing the size of the constraining edges and hence the horizontal tie to resist the additional forces (see Figure 4.1) due to (1) the increased height of the constraining edge, and (2) the additional horizontal forces due to each parallelly stacked beam.

Evaluation of curved beams with multiple beams in parallel showed that when the number of beams is increased, the stability state of the whole unit may change from bistable to monostable (for example) due to increased outward lateral deflection of the supporting edges. In addition, the value of the cumulative vertical force is reduced compared to the expected force by the parallel

units due to the lateral expansion. Thus, a modification to the size of the reaction edges must be made to preserve the required response. A similar evaluation on the MCCD system showed that the units are independent, in terms of the required constraining for the individual unit, from the overall cumulative vertical force resisted by the system. Thus, there is no need for design adjustments.

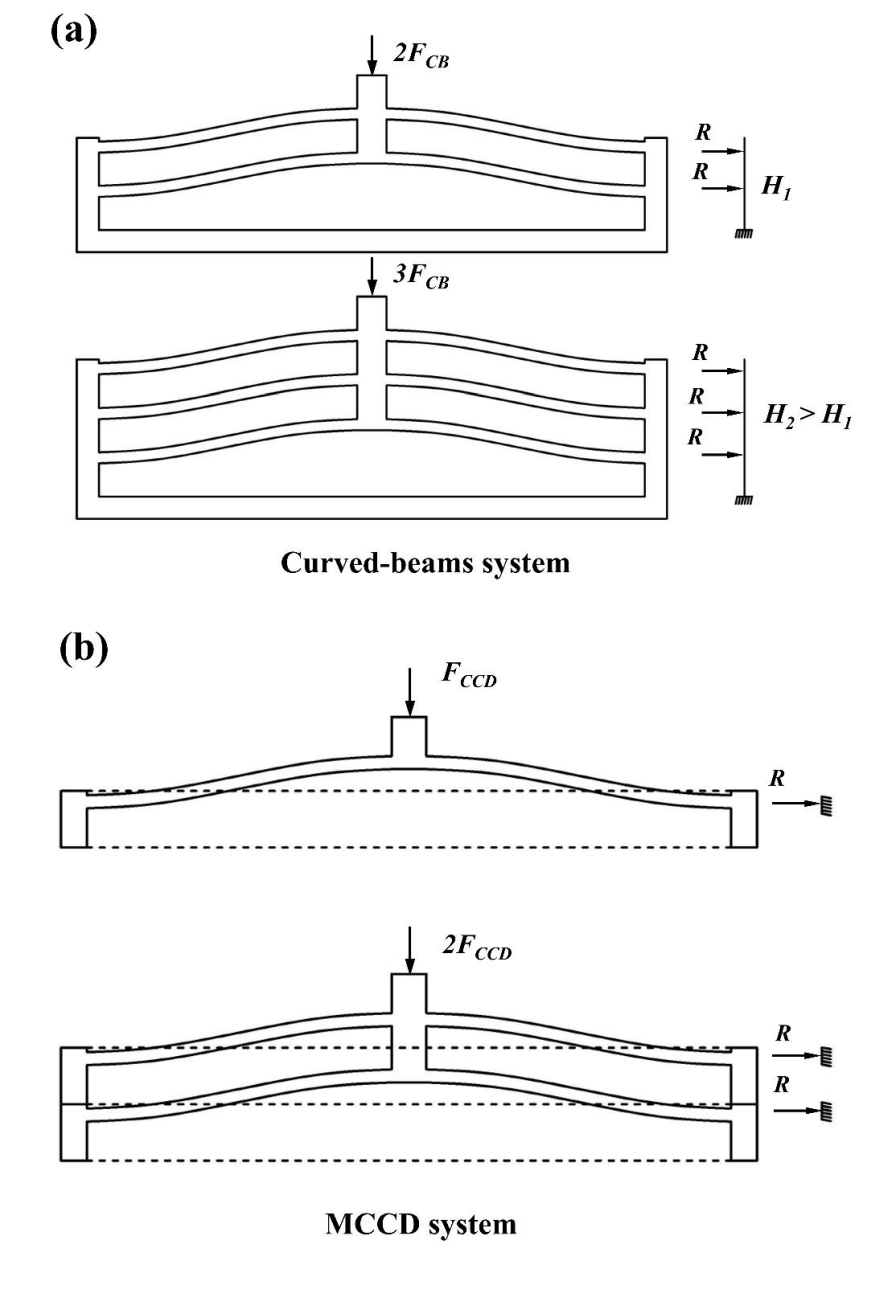


Figure 4.1 Boundary conditions for: (a) curved-beams system, and (b) MCCD system

Even though it may be argued that this issue can be avoided if a system of curved-beams system consisted of many elements in a single layer (horizontal direction), it would still cause a similar effect to that discussed above since the horizontal forces will accumulate causing the system to expand in the horizontal direction in an effect analogous to that of Poisson's ratio on a compressed short strut. Thus, the MCCD system avoids this design limitation by having a self-confining feature that makes it a suitable and practical design for the design of civil structural applications where high forces on such systems are expected.

Numerical studies and experimental tests were conducted on the geometric properties of the individual CCD units and their number in the system to examine the force-displacement and energy dissipation characteristics. Finite element analysis (FEA) was performed to simulate the response of the system to develop multilinear analytical model for the hysteretic response that considers the nonlinear behavior of the system. The model was used to study energy dissipation characteristics of the system. Experimental tests on 3D printed specimens were conducted to analyze the system and validate numerical results.

Multilinear models have been presented in the literature to predict the hysteric forcedisplacement (F- $\Delta$ ) response of systems with multiple multistable elements [33,78]. These models are more suited for systems comprised of units that exhibit a fairly linear force-displacement (F- $\delta$ ) response. This is because such models don't consider the nonlinear effects on the F- $\Delta$  response of the system. For the MCCD system, these nonlinear effects on the F- $\Delta$  response are relatively large and this work takes them into account by introducing an effective stiffness concept.

## 4.3 Multiple Cosine-Curved Dome (MCCD) System

#### 4.3.1 Response of a single CCD unit

The F- $\delta$  response of a single CCD incorporates a negative stiffness part that originates from the dome's geometric shape. The cross-sectional profile of the CCD follows the cosine function given in Equation (4.1) [71].

$$w(x) = h/2[1 - \cos(2\pi x/l)] \tag{4.1}$$

where w(x) is the vertical distance at a distance x from the circumference along a horizontal line at the dome's base passing through the center, as shown in Figure 4.2. The effective geometric parameters on the response of a CCD are the uniform thickness, t, the base diameter or the span length, l, and the apex height, h, as shown in Figure 4.2(a). The parameter d is the diameter of the loading area, which has flat circular shape at the apex region of a CCD. The study in [68] showed that d has a negligible effect on the response of a CCD if  $d/l \le 0.1$ . The circumference edge of a CCD is connected to a rigid ring that constrains edge sliding and rotations under loading, and hence provides fixed boundary conditions for the dome.

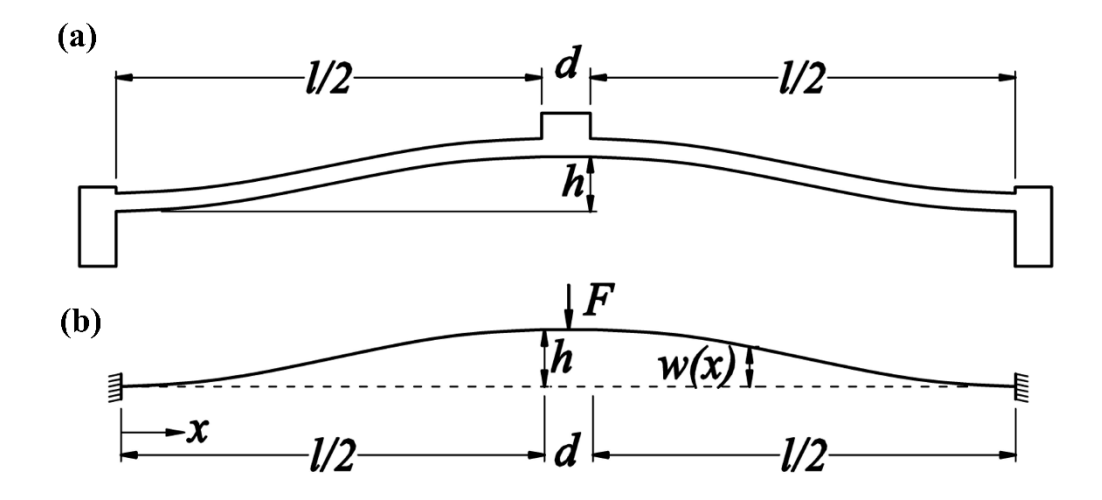


Figure 4.2 Geometric parameters of a typical CCD: (a) cross-section at the apex, and (b) idealized system

The shape of the CCD leads to a highly nonlinear response and a snap-through buckling behavior under a concentrated transverse vertical load at the apex as shown in Figure 4.2(b). Beyond the buckling point, a CCD deforms to a new configuration, yet the exerted deformations on the CCD are recoverable. For a bistable CCD, an external restoring force is required to recover the original shape, while a monostable CCD is self-recoverable. Figure 4.3(a) shows the typical F- $\delta$  responses for monostable and bistable CCDs normalized by their respective buckling load,  $F_b$ , and buckling displacement,  $\delta_b$ . Note that  $\delta$  denotes the local CCD vertical displacement. It can be seen in Figure 4.3(a) that the bistable CCD has a negative minimum force,  $F_n$ , at displacement  $\delta_n$ . In this case, some of the induced energy is trapped in the system and hence the F- $\delta$  curve here has a negative force part [20].

The response of a CCD can be divided into three regions [33]: the initial response region (I) with an effective stiffness,  $k_{II}$ , the snap-through buckling region (II) with the negative effective stiffness,  $k_{II}$ , and the post snap-through buckling region (III) with stiffness,  $k_{III}$ . For given geometric and material properties, the multilinear response of a CCD, as shown in Figure 4.3(b), can be constructed using the expressions provided in Chapter 3 [68] for  $F_b$ ,  $\delta_b$ ,  $F_n$ ,  $\delta_n$ , and  $k_{III}$ . The maximum displacement,  $\delta_m$ , is the displacement at a force level equal to  $F_b$  in region III, see Figure 4.3(b); and it can be calculated as  $\delta_m = \delta_n + (F_b - F_n) / k_{III}$ . Based on these values, the stiffness in each region can be determined. Hence, the linear F- $\delta$  relations in regions I and III are given as follows:

$$F_{l} = k_{l} \, \delta_{l}, \qquad \delta_{l} \le \delta_{b} \tag{4.2}$$

$$F_{III} = F_n + k_{III} \left( \delta_{III} - \delta_n \right) \qquad \delta_{III} \ge \delta_n \tag{4.3}$$

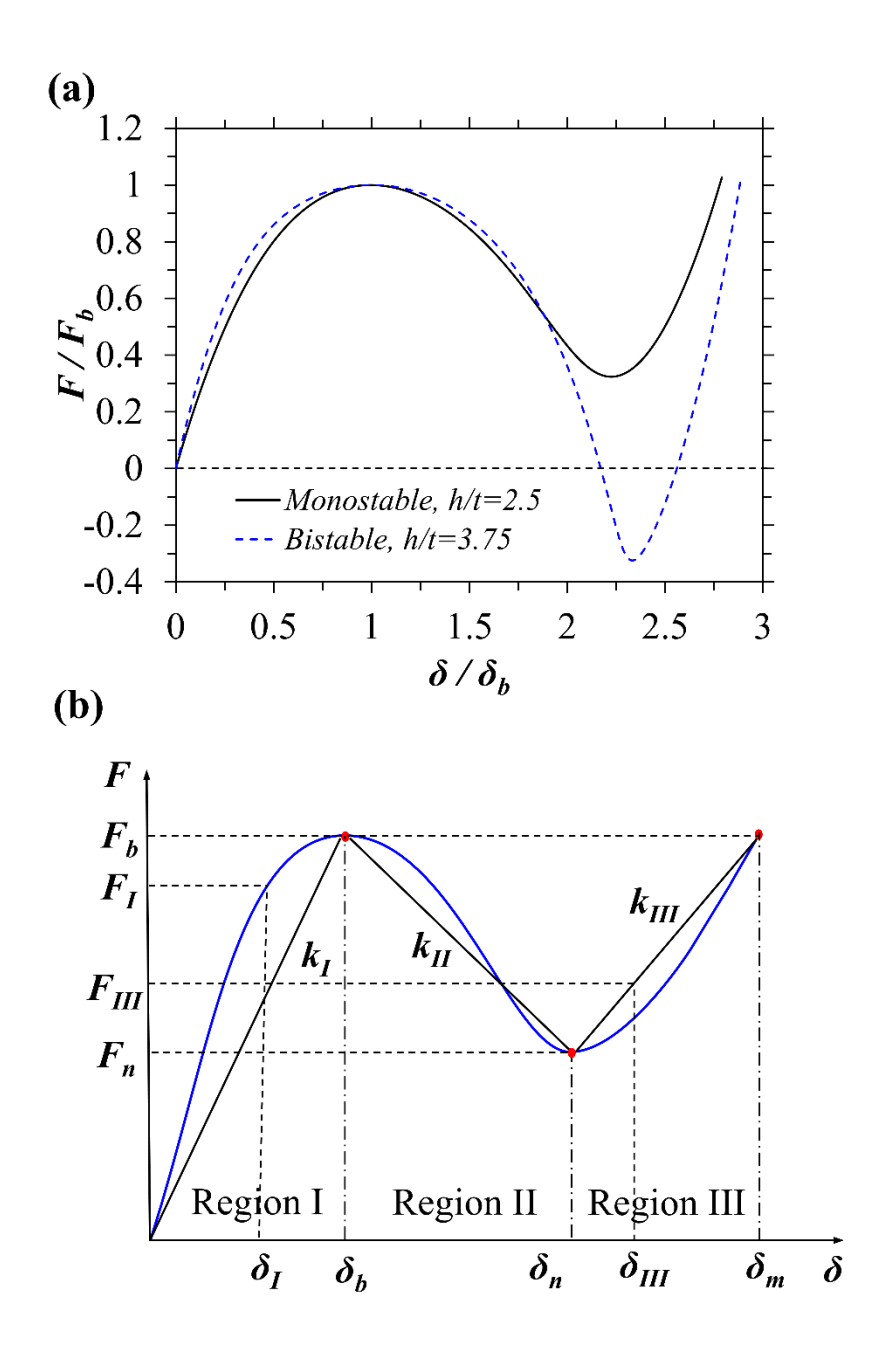


Figure 4.3 (a) Normalized F- $\delta$  response for monostable and bistable CCDs; (b) multilinear approximation of the F- $\delta$  response of a CCD

Due to the high nonlinearity of the F- $\delta$  response of the CCD units, especially in region I, using the above relations (as will be illustrated in Section 4.4) would underestimate and slightly overestimate  $F_I$  and  $F_{III}$ , respectively, as shown in Figure 4.3(b). Therefore, the Michaelis-Menten model [80] was used to develop a nonlinear F- $\delta$  relation for region I. This relation is in terms of

h/t,  $\delta_b$ , and  $F_b$ , and is given in Equation (4.4). This model was selected because of its simplicity to determine  $\delta_I$  for a given force level  $F_I$  and because it closely represents the nonlinear path of the F- $\delta$  response in region I.

$$F_I = \frac{F_b A (\delta_I/\delta_b)}{B + (\delta_I/\delta_b)} \tag{4.4}$$

In Equation (4.4) A and B are constants in terms of h/t and can be determined as follows:

$$A = 0.0368 (h/t)^3 - 0.3488 (h/t)^2 + 0.9559 (h/t) + 0.6574$$

$$B = 0.0368 (h/t)^3 - 0.3488 (h/t)^2 + 0.9559 (h/t) - 0.3426$$

Similarly, an exponential function was used to develop a relation for the F- $\delta$  response in region III. The expression is in terms of h/t,  $\delta_n$ ,  $\delta_m$ ,  $F_n$ , and  $F_b$  as given below [77]:

$$F_{III} = F_n + F_b C \left[ \frac{\delta_{III}}{\delta_m - \delta_n} \right]^D \tag{4.5}$$

where C and D are constants in terms of h/t and can be determined by:

$$C = -0.0648 (h/t)^2 + 0.9261 (h/t) - 1.2407$$

$$D = 0.0993 (h/t)^2 - 0.8157 (h/t) + 3.2967$$

#### 4.3.2 Stacking configuration of CCD systems

To have a better understanding on the effect of stacking multiple CCDs on the behavior of the CCD units, a discussion is presented here to analyze the change in F- $\Delta$  response for different configurations of CCD systems. Note that  $\Delta$  denotes the global vertical displacement of the MCCD system. There are two basic configurations for stacking CCDs in the vertical direction: parallel and series stacking as shown in Figure 4.4, or a combination of the two arrangements. The parallel stacking shown in Figure 4.4(a) is similar to the case of connected springs in parallel, where the applied load is resisted based on the individual stiffness of each spring but with equal displacement on each one. Denoting the number of stacked CCDs in parallel as  $n_p$ , the response of  $n_p$  CCDs

stacked in parallel [see Figure 4.5(a)] consists of one buckling event with buckling force  $n_pF_b$  at displacement  $\Delta_b = \delta_b$ , and minimum force  $n_pF_n$  at displacement  $\Delta_n = \delta_n$ . Here the force is directly scaled by the number of connected CCDs  $(n_p)$ , assuming that they are identical, while the displacements do not change.

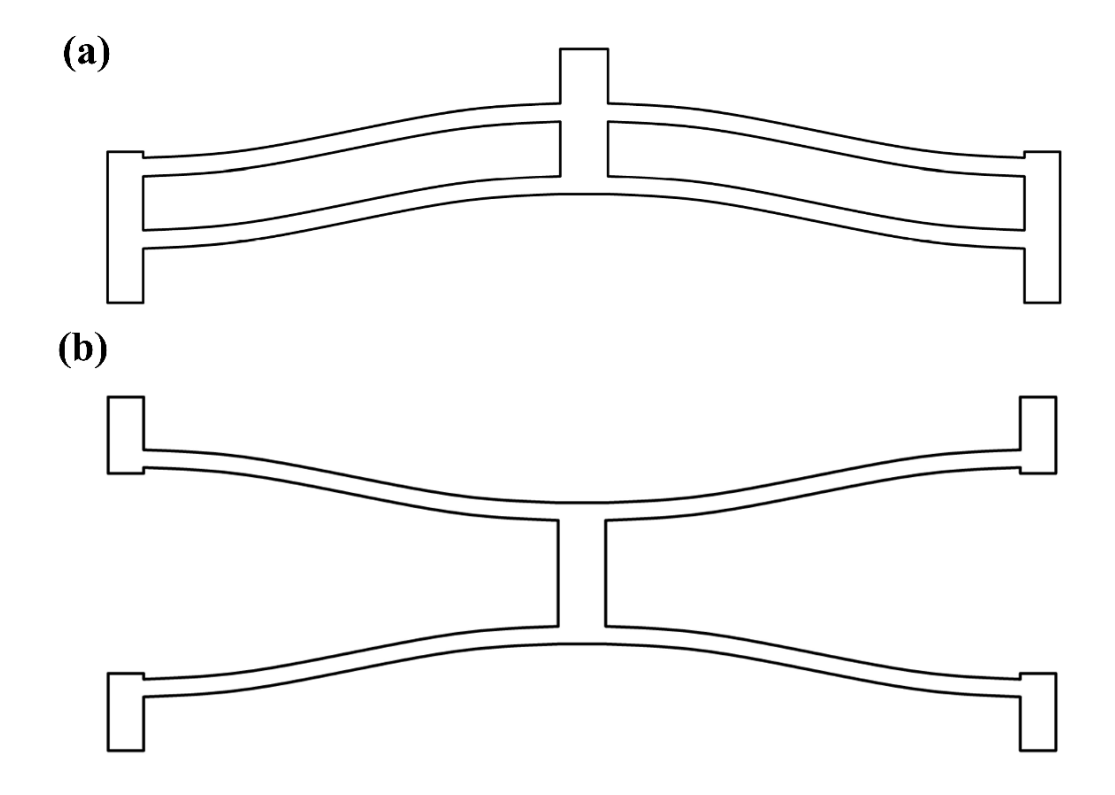


Figure 4.4 Possible configurations of CCD units in the vertical direction: (a) parallel stacking ( $n_p$  = 2), and (b) series stacking ( $n_s$  = 2)

The case of series stacking is similar to the case of connected springs in series, where the load is resisted equally by all springs but with different deformations for each. In this configuration, it is assumed that each CCD is connected to the adjacent CCD by a rigid strut that provides the required height to allow buckling of the unit as shown in Figure 4.4(b). The rigid rings at the base of each CCD also provide the required height to allow unit buckling.

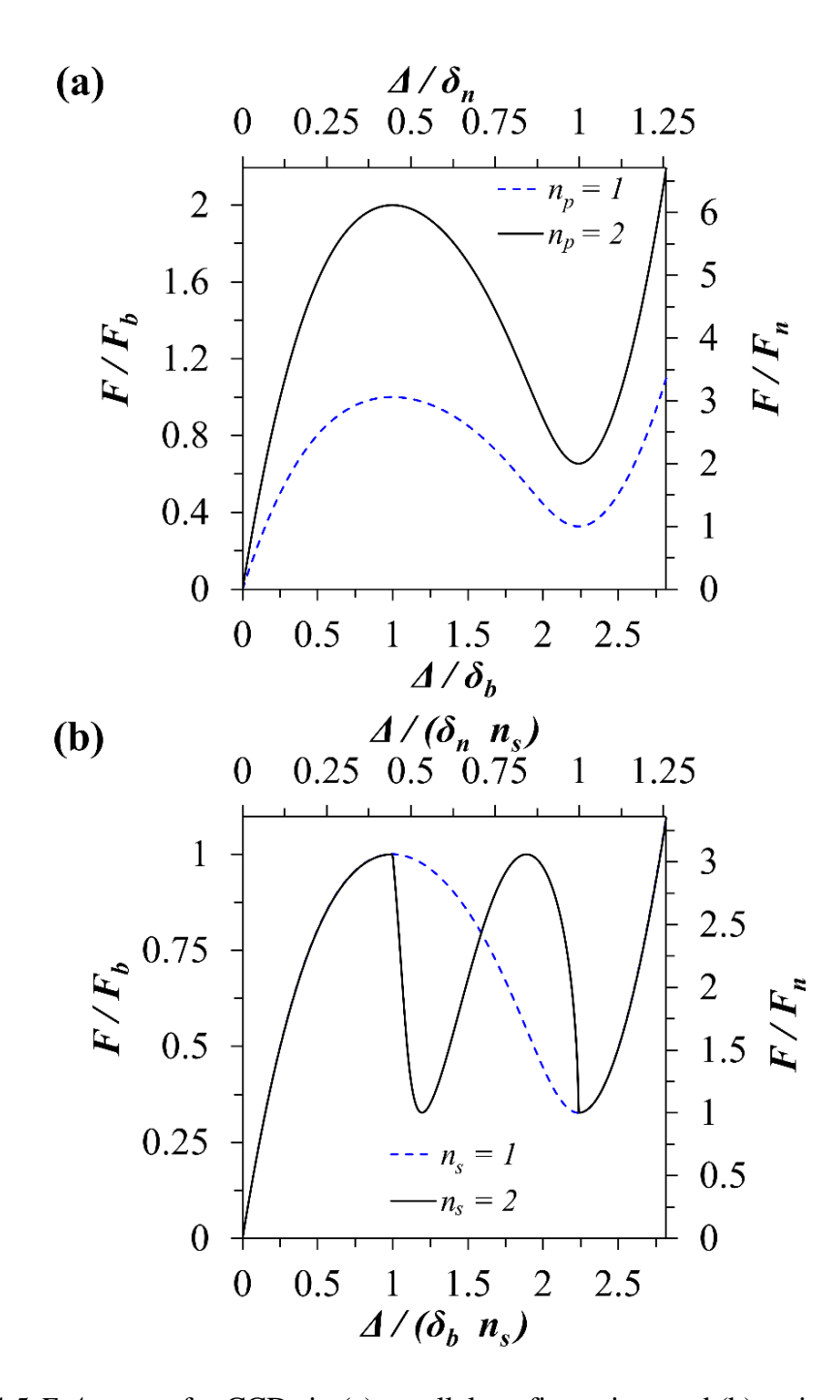


Figure 4.5 *F*-∆ curves for CCDs in (a) parallel configuration, and (b) series configuration

The response of multiple CCDs stacked in series, where  $n_s$  denotes the number of units, is shown in Figure 4.5(b). The response consists of multiple buckling events with buckling forces of  $F_b$  at displacement  $\Delta_b = n_s \delta_b$  for the first buckling event. The subsequent minimum force  $F_n$  (and

its displacement  $\Delta_n$ ), and the next buckling displacement depend on the number of CCDs in the system, which is discussed in Section 4.4.

#### 4.3.3 Finite element modeling

Finite element analysis (FEA) was used to examine the F- $\Delta$  response of the MCCD system. The analyses were performed using the program ABAQUS [73]. The CCD units in the system were modeled as 3D deformable revolved shell objects with four-node shell elements (S4). The material was assumed to have linear elastic isotropic properties. Displacement control was used to apply a dynamic incremental deformation to the system. Large deformations were accounted for by considering the geometric non-linearity in the analysis. The MCCD system was idealized for the analysis as shown in Figure 4.6. The system was analyzed with small variations in the thicknesses of the CCDs to allow a response with consecutive snap-through buckling events.

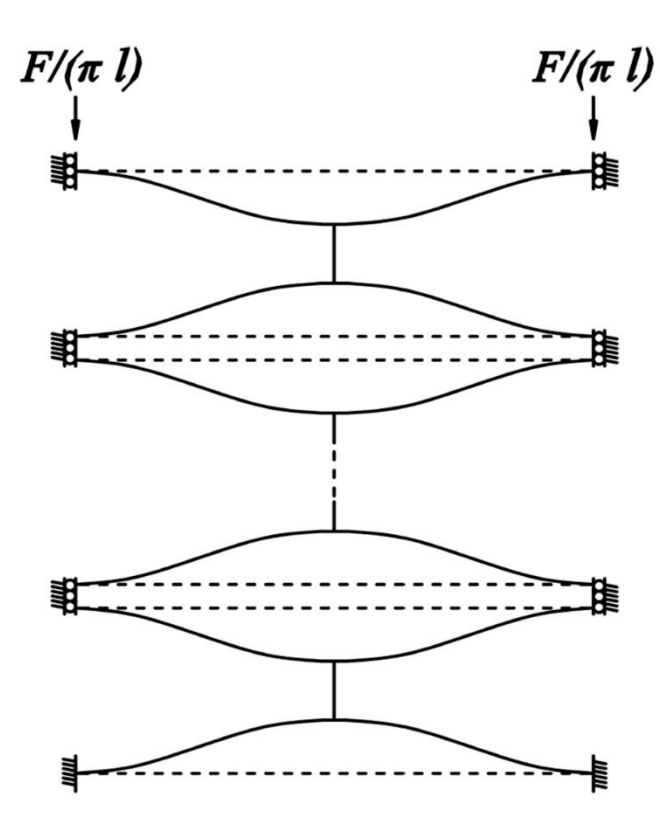


Figure 4.6 The idealized MCCD system

Figure 4.7 shows the F- $\Delta$  response from FEA for two MCCD systems, both with  $n_s = 12$ . A monostable system [Figure 4.7(a)] had CCD units with h = 3 mm, l = 140 mm, and t = 1.2; while a bistable system [Figure 4.7(b)] had t = 0.8 mm. The modulus of elasticity, E, was 1500 MPa, and the Poisson's ratio, v, was 0.33.

The type of response (i.e., monostable or bistable) of a CCD unit can be determined by comparing h/t to the critical height-to-thickness ratio,  $(h/t)_{cr}$ , calculated as proposed in [68]:

$$(h/t)_{cr} = 2.879 \, v^{-0.052} = 3.05 \tag{4.6}$$

Thus, the monostable system has CCD units with h/t = 2.5, which is smaller than  $(h/r)_{cr}$ ; while the bistable system has CCD units with h/t = 3.75, greater than  $(h/r)_{cr}$ .

A few observations can be made from the  $F-\Delta$  curve in Figure 4.7. The force drops after each snap-through and snap-back buckling increase in magnitude with every buckling event in the loading and unloading paths. The smallest force drop occurs after the first buckling events while the largest occurs at the last event. This is also true for the unloading path. The trace of the force-deformation curve between the buckling events have linear and nonlinear segments during the unloading and loading paths, respectively. This is because under loading most of the CCDs in the system are in region I [see Figure 4.3 (b)], which is highly nonlinear, while during unloading most of the CCDs in the system are in region III, which is fairly linear. This also depends on the ratio of  $k_{III}$  to  $k_I$ , where a higher  $k_{IIV}/k_I$  ratio increases the magnitude of the force drops in the last buckling events during loading and unloading, and vice versa.

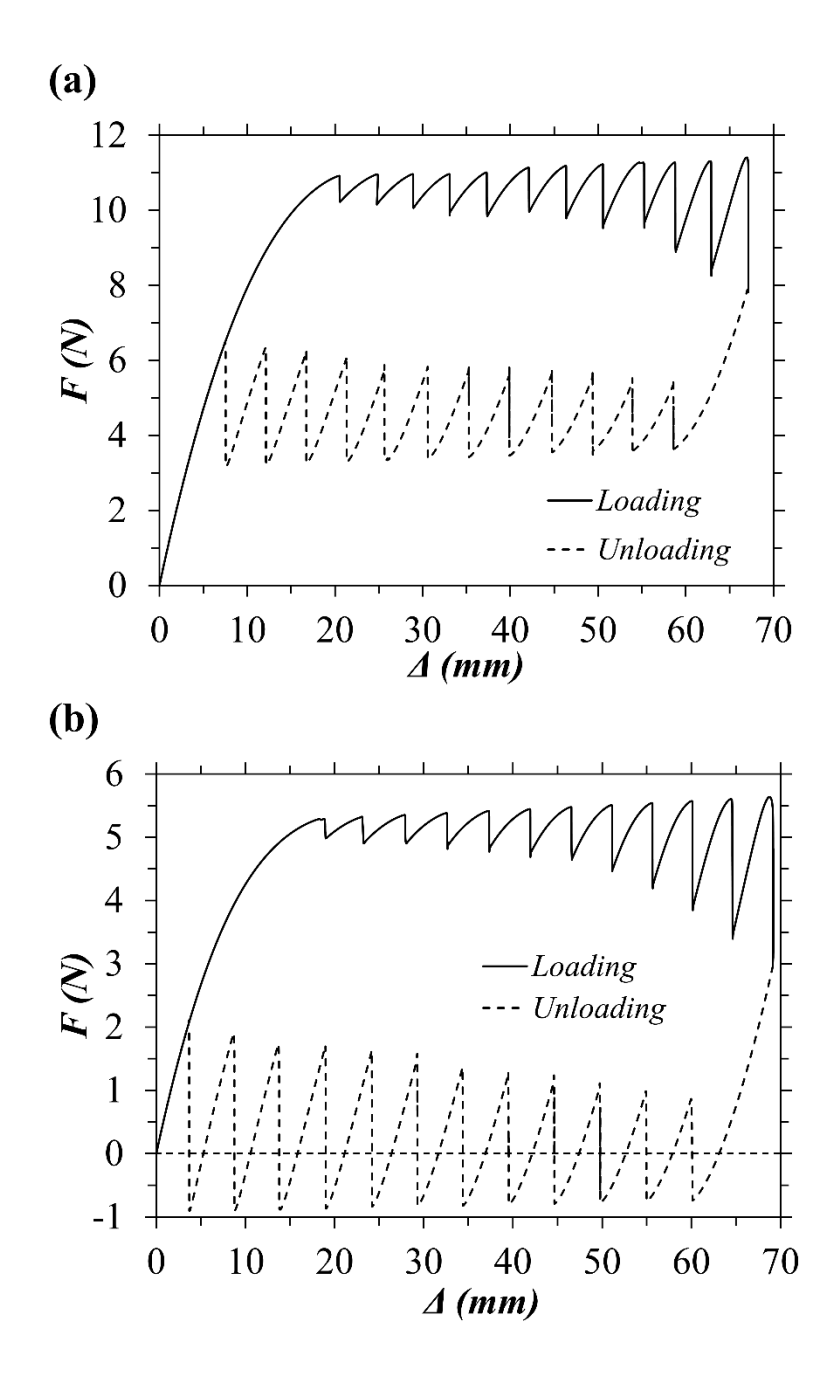


Figure 4.7 Force-deformation curves from FEA for MCCD systems: (a) monostable, and (b) bistable

# 4.4 Analytical Model for MCCD System

This section presents a multilinear model that describes the hysteretic response of the MCCD system. It is assumed that the system consists of similar CCDs stacked in series as shown in Figure 4.6. Due to small manufacturing imperfections, each CCD in a MCCD system has a

slightly different buckling limit ( $F_b$ ). This means that each CCD buckles at a different time, which results in a progressive buckling response of the system under displacement control loading. The CCD with lowest buckling force ( $F_b$ ) buckles first, followed by the one with an immediately higher  $F_b$  limit and so forth until buckling of the CCD with the highest  $F_b$  in the system is reached. A similar process occurs during unloading, where the unit with highest minimum force ( $F_n$ ) snapsback first, followed by the one with a lower  $F_n$  and so forth until snap-back of the CCD with the lowest  $F_n$  in the system.

#### 4.4.1 Loading stages

Consider a MCCD system that consists of  $n_s$  similar CCD units connected in series, each with an F- $\delta$  response as shown in Figure 4.3(b). Since the system buckles progressively, at any given time a unit is in one of the regions I, II, and III. Thus, if  $n_I$ ,  $n_{II}$ , and  $n_{III}$  denotes the number of CCD units in regions I, II, and III [33], respectively, then

$$n_S = n_I + n_{II} + n_{III} \tag{4.7}$$

To explain the behavior of an MCCD, consider a system composed of four CCDs ( $n_s = 4$ ). Upon applying the force F to the system the four CCDs resist the same load and their response is within region I ( $n_I = 4$ ). After the first buckling event, three units are still in region I while one CCD is in region II ( $n_I = 3$  and  $n_{II} = 1$ ). Since the force drops due to the buckling event, the system relaxes and redistributes the local displacements ( $\delta$ ) of each unit when the buckled CCD reaches region III ( $n_I = 3$ ,  $n_{III} = 1$ ). The same process is repeated until all units are in region III ( $n_{III} = 4$ ). Figure 4.8 shows the number of CCDs in each region at each loading stage, n, for a system with  $n_s = 4$ . From Figure 4.8, it can be noted that  $n_{II}$  equals to 0 or 1, which means that only one CCD at a time undergoes buckling.

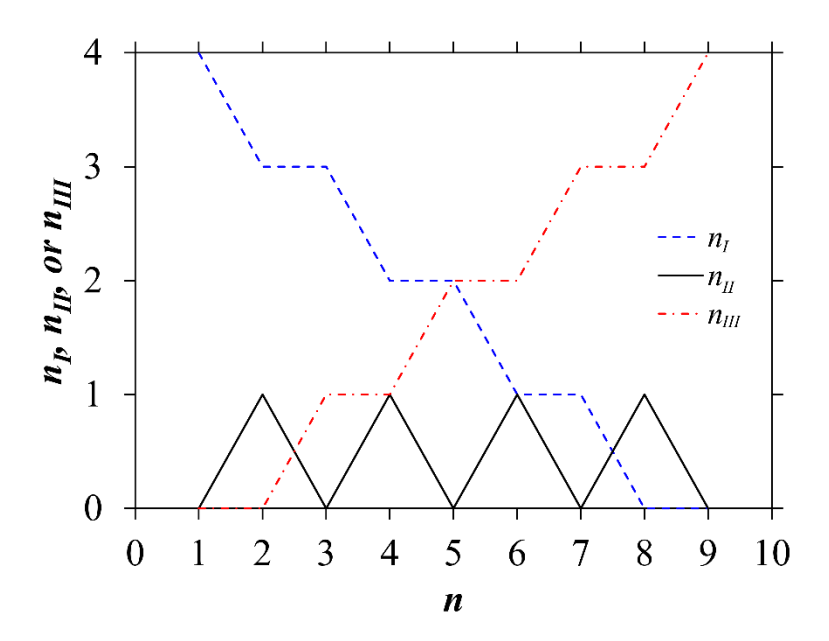


Figure 4.8 Number of CCDs in regions I, II, and III during loading stages for a system of  $n_s = 4$ 

The total number of loading stages,  $n_t$ , is related to the number of CCDs connected in series  $(n_s)$ , as given in Equation (4.8) and shown in Figure 4.8. The relations between  $n_t$ ,  $n_{tt}$ , and  $n_{ttt}$  with n are given in Equations (4.9) to (4.11). Note that a cosine function is used for  $n_{tt}$ , which yields 0 for odd n values and 1 for even values.

$$n_t = 2 n_s + 1$$
 (4.8)

$$n_{II} = \left| \cos(n \, \pi / 2) \right| \tag{4.9}$$

$$n_I = 0.5 [2 ns - n - n_{II} + 1]$$
(4.10)

$$n_{III} = n_S - n_I - n_{II} \tag{4.11}$$

#### 4.4.2 Model development

To develop a multilinear F- $\Delta$  response for the MCCD, the hysteretic response was divided into its loading and unloading paths. Each path consists of two groups of points that lie on the actual system F- $\Delta$  curve connected by line segments, as shown in Figure 4.9(a). The first group of

points in each path (blue circles) includes the points at the force level  $F_b$  with displacement spacing  $s_b$  for the loading path, and the points with a force level of  $F_n$  and displacement spacing  $s_n$  in the unloading path. The second group of points in each path (red squares) includes the buckling drop forces  $F_{bd}$  (from  $F_b$ ) at counterpart displacements for the loading path; and the minimum drop force  $F_{nd}$  (from  $F_n$ ) at counterpart displacements for the unloading path. Figure 4.9(a) shows a schematic  $F_{-\Delta}$  response for the MCCD system with the quantities used to develop the multilinear model. The figure also shows the actual and the multilinear  $F_{-\Delta}$  curves during loading and unloading.

#### 4.4.2.1 <u>Loading path</u>

The unknowns in the first group of points (at  $F_b$  level) are the system displacements at each of the snap-through bucking events,  $\Delta_{bi}$ . The displacement at the first buckling event ( $\Delta_{b0}$ ), for i = 0, is determined based on the well-known equivalent spring concept [81] for  $n_s$  springs connected in series with similar stiffness  $k_I$  and resisting the same force  $F_b$ . The equivalent stiffens of such a system is  $k_I/n_s$ , and hence  $\Delta_{b0} = F_b/(k_I/n_s) = n_s \delta_b$ .

FEA results, as those in Figure 4.7, show that the spacing between the snap-through buckling events is constant. After the system experiences a local CCD snap-through it reloads (when the buckled CCD reaches region III) and it encounters another local snap-through event when the load reaches  $F_b$ . The spacing  $s_b$  is constant and a property of the individual CCD unit F- $\delta$  responses. As shown in Figure 4.9(b), this constant spacing  $(s_b)$  is the distance between  $\delta_b$  and  $\delta_m$  and hence  $s_b = \delta_m - \delta_b$ . Thus,  $s_b$  represents the required displacement for the MCCD system to reload and reach  $F_b$  after snap-through buckling of a CCD unit. Thus, the points defining the local CCD buckling events in the system loading path, i.e., the system displacements  $(\Delta_{bi})$  and the corresponding system buckling forces  $(F_{bi})$ , can be determined as follows:

$$\Delta_{bi} = n_s \, \delta_b + i \, S_b \tag{4.12}$$

$$F_{bi} = F_b \tag{4.13}$$

where *i* is the buckling event [see Figure 4.9(a)] and  $i = 0, 1, 2, ..., (n_s-1)$ .

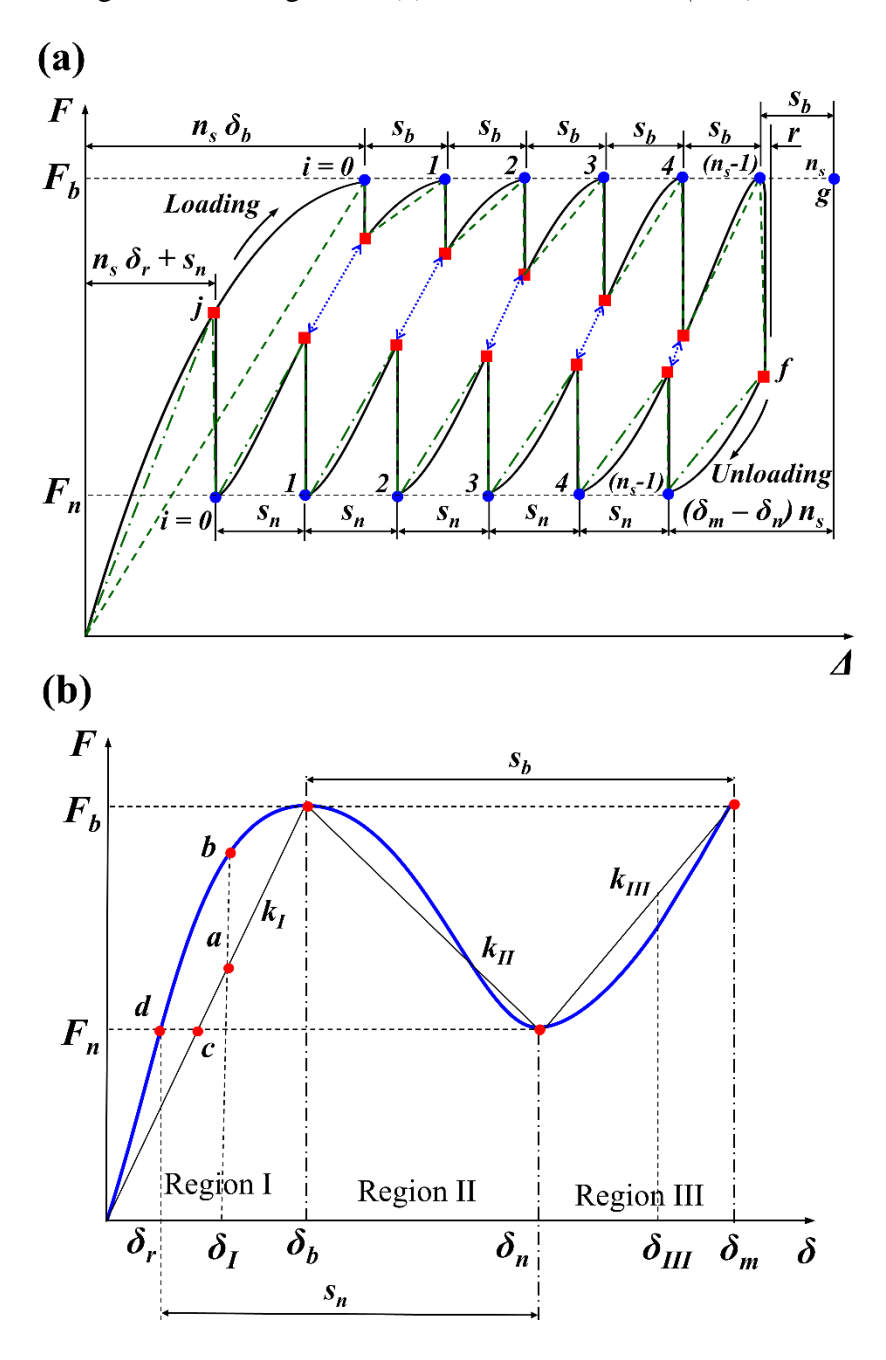


Figure 4.9 (a) Schematic F- $\Delta$  response of the MCCD system with quantities used to develop the multilinear model; (b) Actual and multilinear F- $\delta$  responses of a CCD unit

When the system approaches  $F_b$  during loading, CCDs in regions I and III approach  $\delta_b$  and  $\delta_m$ , respectively. When the system reaches  $F_b$ , a given CCD snaps-through and the force level

drops until the buckled CCD in region II reaches  $\delta_n$ . Deformations for the CCDs are then redistributed at the system displacement  $\Delta_{bi}$ , leading to CCDs in regions I and III to a reduced force level  $F_{bdi}$ . This means that during the load drop the response of one CCD unit transitions from region I to III. Otherwise, if the buckled CCD were to remain at  $\delta_n$  the value of  $F_{bdi}$  would equal  $F_n$ , which is not the case. Consequently, the local displacements  $\delta_I$  and  $\delta_{III}$  shown in Figure 4.9(b) for a CCD in regions I and III decrease below  $\delta_b$  and  $\delta_m$ , respectively. Mathematically this is expressed as:

$$\delta_l < \delta_b$$
 (4.14)

$$\delta_{III} = \delta_n + \delta_{III}' < \delta_m \tag{4.15}$$

where  $\delta_{III}$ ' is the local displacement component in region III.

Since the system is connected in series, all CCDs are experiencing the same force  $F_{bdi}$ . Thus, by determining either  $\delta_I$  or  $\delta_{III}$ ' the force  $F_{bdi}$  can be calculated using Equations (4.2) or (4.3), respectively. Based on the concept of connected springs in series, the contribution of CCDs in regions I and III towards the system response  $\Delta_{bi}$  is given by:

$$(n_s - i - 1) \delta_l + (i + 1) \delta_{lll} = \Delta_{bi}$$

$$(4.16)$$

A linear relation between  $\delta_I$  and  $\delta_{III}$ ' using the stiffnesses  $k_I$  and  $k_{III}$ , respectively, can be established based on the concept of two springs connected in series and resisting an equal load. This relation is given by  $\delta_I k_I = \delta_{III} k_{III}$  and hence:

$$\delta_{III}' = \delta_I k_I / k_{III} \tag{4.17}$$

By substituting Equations (4.15) and (4.17) into (4.16), the local displacement for CCDs in region I during the force drop,  $\delta_{Ibdi}$ , and hence  $F_{bdi}$  can be calculated as follows:

$$\delta_{Ibdi} = \frac{\Delta_{bi} - (i+1) \delta n}{(n_s - i-1) + (i+1) \frac{k_I}{k_{III}}}$$
(4.18)

$$F_{bdi} = \delta_{lbdi} \, k_l \tag{4.19}$$

Due to the nonlinear response of the CCD units during the loading branch, the approach followed to develop Equation (4.17), i.e., assuming that the two springs are linear, underestimates  $F_{bdi}$ . This can be corrected by replacing  $k_I$  in Equation (4.18) by the effective stiffness for the CCD units in region I,  $k_{eI}$ , which mainly depends on  $n_s$ . The value of  $k_{eI}$  can be calculated at the last point in the loading curve, namely point f, as shown in Figure 4.9(a). This point was chosen to determine  $k_{eI}$  because it reduces the unknowns in Equation (4.16) to one. The displacement at this point  $(\Delta_{bf})$  with  $i = n_s - I$  is slightly greater than that determined by Equation (4.12) since it is associated with the last buckling event of the system. The additional distance r [see Figure 4.9(a)] and hence  $\Delta_{bf}$  can be determined with:

$$r = (\delta_n - \delta_b) / n_s \tag{4.20}$$

$$\Delta_{bf} = n_s \, \delta_b + (n_s - 1) \, s_b + r \tag{4.21}$$

Thus, at  $i = n_s - I$ , Equation (4.16) reduces to  $n_s \, \delta_{III} = \Delta_{bf}$  and hence  $\delta_{III}$  can be determined. The local displacement for CCDs in region III at point f (i.e.,  $\delta_{IIIf}$ ) and the drop force ( $F_{bdf}$ ) are determined as:

$$\delta_{IIIf} = \Delta_{bf} / n_s \tag{4.22}$$

$$F_{bdf} = F_n + (\delta_{IIIf} - \delta_n) k_{III} \tag{4.23}$$

Now the equivalent local displacement  $\delta_{If}$  for CCDs in region I for a force equal to  $F_{bdf}$  can be determined by:

$$\delta_{If} = F_{bdf} / k_I \tag{4.24}$$

By using Equation (4.17) for  $i = n_s - 1$  and  $\delta_{Ibdi} = \delta_{If}$ ,  $k_{eI}$  can be calculated as follows:

$$k_{eI} = \frac{(\Delta_{bf} - n_s \,\delta_n) \,k_{III}}{n_s \,\delta_{If}} \tag{4.25}$$

The modified expression for  $\delta_{lbdi}$  with  $k_I$  replaced by  $k_{eI}$  in Equation (4.18) is given in Equation (4.26). The force drop for the loading path can now be determined as given earlier in Equation (4.19)

$$\delta_{Ibdi} = \frac{\Delta_{bi} - (i+1) \, \delta n}{(n_s - i-1) + (i+1) \frac{k_{el}}{k_{III}}} \tag{4.26}$$

Figure 4.10(a) shows the F- $\Delta$  response of a MCCD system with 8 monostable CCDs as obtained from FEA and the analytical model relations just presented above. Visual comparison of the responses shows that the analytical  $F_{bdi}$  values are almost equal to each other and generally smaller (larger force drops) than those from the FEA, which is a consequence of using linear equations to determine  $k_{el}$  and  $F_{bdi}$ .

As can be seen in Figure 4.9(b) for points a and b, Equation (4.19) will underestimate  $F_{bdi}$  because of the nonlinearity of the CCD units' F- $\delta$  response. Therefore, the simulated response can be improved by using the nonlinear expression for  $F_I$  in Equation (4.4) to determine  $k_{eI}$  and  $F_{bdi}$  for the loading path, which is shown in Figure 4.10(b).

#### 4.4.2.2 <u>Unloading path</u>

Similar to the approach followed for the loading path, the unknowns in the first group of points (at  $F_n$  level) are the system displacements at each snap-back event,  $\Delta_{ni}$ . The displacement at the first snap-back event (at  $i = n_s - I$ ) is determined in analogous form to the way in which  $\Delta_{b0}$  was determined for the loading path but with point g as the origin [see Figure 4.9(a)]. The displacement at point g can be determined using Equation (4.12) for  $\Delta_{bi}$  with  $i = n_s$ . Before the first snap-back event all CCDs are in region III with  $k_{III}$ . Consequently, the equivalent system stiffness is  $k_{III}/n_s$  and the displacement from point g is  $n_s$  ( $\delta_m - \delta_n$ ), as shown in Figure 4.9(a).

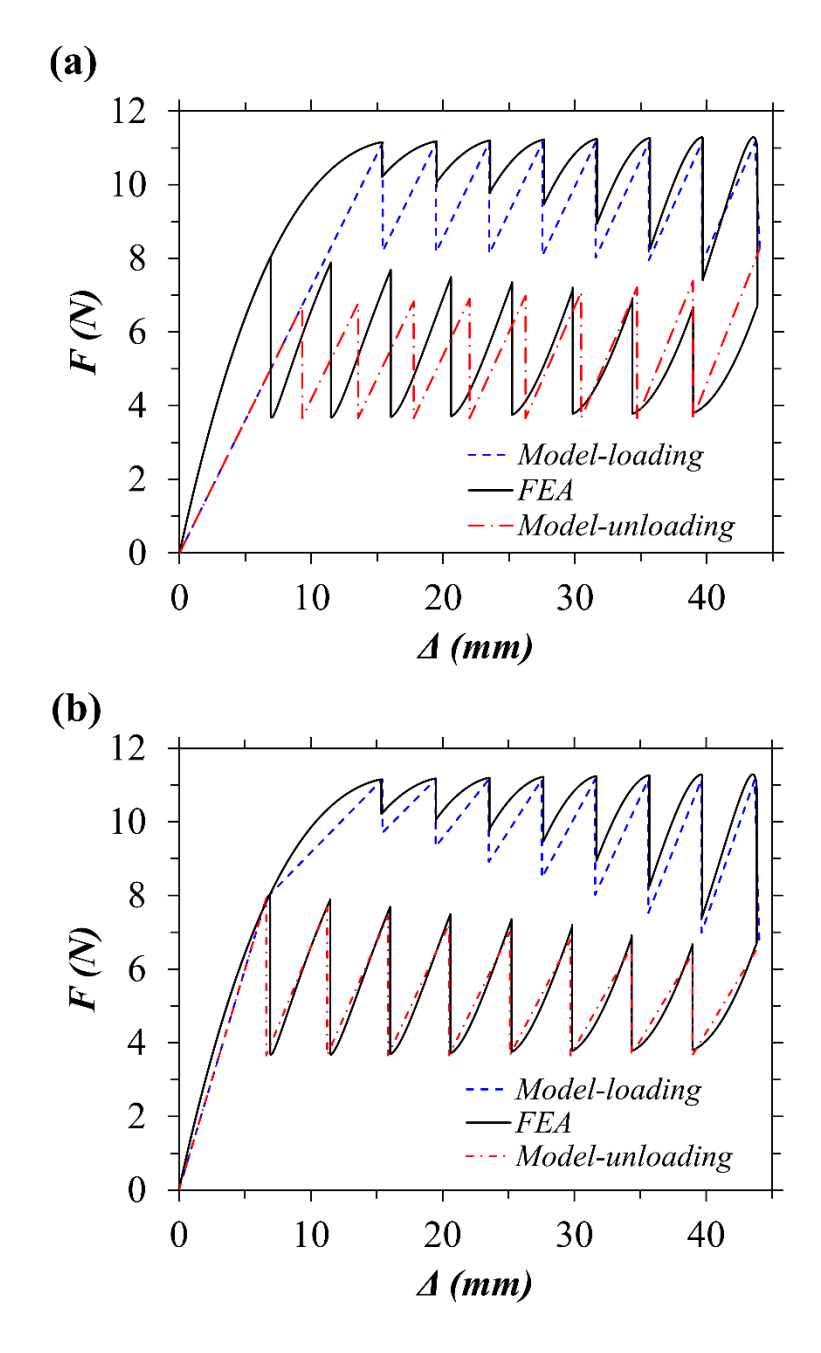


Figure 4.10 F- $\Delta$  curves from FEA and analytical model using (a) linear equations, and (b) nonlinear equations to calculate  $k_{eI}$ ,  $k_{eIII}$ ,  $F_{bdi}$  and  $F_{ndi}$ 

The spacing  $s_n$  in the unloading path was also found to be constant and a property of the F- $\delta$  response of each CCD unit. The spacing  $s_n$  is the distance required to reach the snap-back critical point, which is the distance between  $\delta_n$  and  $\delta_r$ , or  $s_n = \delta_n - \delta_r$  as shown in Figure 4.9(b). It should be noted that determining  $\delta_r$  linearly with stiffness  $k_I$  [i.e., using Equation (4.2)] results in some

error that underestimates  $s_n$ . Thus,  $\delta_r$  can be determined from Equation (4.4) by equating  $F_I$  to  $F_n$  and solving for  $\delta_I$ . Points c and d in Figure 4.9(b) show the effect of using linear and nonlinear relations for region I to determine  $\delta_r$ .

The system displacements during unloading  $(\Delta_{ni})$  and the corresponding snap-back forces,  $F_{ni}$ , can be determined as follows:

$$\Delta_{ni} = n_s \, \delta_r + (i+1) \, s_n \tag{4.27}$$

$$F_{ni} = F_n \tag{4.28}$$

A similar procedure to that followed to determine  $F_{bdi}$  for the loading path is followed to determine the force drops for the unloading path,  $F_{ndi}$ . The contribution of CCDs in regions I and III towards the system response  $\Delta_{ni}$  at each snap-back event is given by:

$$(n_S - i) \delta_I + i \delta_{III} = \Delta_{ni} \tag{4.29}$$

Thus, the local displacement component ( $\delta_{III'ndi}$ ) for CDDs in region III at the force drop can be determined by Equation (4.30), where  $k_{eIII}$  is the effective stiffness for units in region III. Hence, the force  $F_{ndi}$  can be calculated using Equation (4.3) or (4.5).

$$\delta_{III'bdi} = \frac{\Delta_{ni} - i \,\delta_n}{(n_s - i)\frac{k_{eIII}}{k_I} + i} \tag{4.30}$$

The stiffness  $k_{eIII}$  can be calculated at the last point in the unloading curve (j) see Figure 4.9(a). The displacement at point j ( $\Delta_{nj}$ ) is  $n_s$   $\delta_r + s_n$ . At point j, with i = 0, Equation (4.29) reduces to  $n_s$   $\delta_I = \Delta_{nj}$ . Thus, the local displacement at point j ( $\delta_{Ij}$ ) for CCDs in region I is given by:

$$\delta_{lj} = \Delta_{nj} / n_s \tag{4.31}$$

By using  $\delta_{Ij}$  in Equation (4.2), or in Equation (4.4) for more accurate results,  $F_{ndj}$  can be calculated. This is followed by calculating the local displacement component at point j ( $\delta_{III'j}$ ) for CCDs in region III using Equation (4.3) or (4.5) for  $F_{III} = F_{ndj}$ . By using Equation (4.30) with i = 0 and  $\delta_{III'j}$ ,  $k_{eIII}$  can be found as follows:

$$k_{eIII} = \frac{\Delta_{nj} k_I}{n_s \, \delta_{IIIIj}} \tag{4.32}$$

Figure 4.10 shows the simulated unloading path using linear [Figure 4.10(a)] and nonlinear [Figure 4.10(b)] equations to determine  $k_{eIII}$  and  $F_{ndi}$ , plotted along FEA results. It can be seen that using linear relations underestimates  $s_n$  and  $F_{ndi}$  values.

#### 4.4.2.3 <u>Intermediate loading and unloading paths</u>

The intermediate unloading and reloading paths depend on number of the snapped units (i) in the system. When the system is unloaded after snapping event i and before event i+1, the intermediate unloading path follows back the loading path until reaches the drop force at event i and then crosses to the drop force of the unloading path at event i and completes with the unloading path. The reloading paths follow the same analogy but in the opposite direction. The dotted arrows in Figure 4.9(a) represent the intermediate unloading and reloading paths.

# 4.5 Experimental Validation

#### 4.5.1 Test setup

The MCCD specimen shown in Figure 4.11 was fabricated using a 3D polymer-based printer (Stratasys Fortus 250 mc) with acrylonitrile butadiene styrene (ABS) filament. The ABS material had a Poisson's ratio of 0.35; and the compressive modulus of elasticity of the 3D printed CCDs, determined according to ASTM D695, had an average value of 853 MPa.

The printed MCCD system consisted of 10 CCDs with average 'as-printed' dimensions of  $t = 0.75 \pm 0.03$  mm,  $h = 1.76 \pm 0.03$  mm,  $l = 50 \pm 1$  mm, and d = 4.5 mm. The units in the system were designed to ensure that the maximum resisted vertical force ( $F_b$ ) by a CCD unit at the critical section, which is the loading region at the apex, to be much lower than the force that would cause a punching shear failure. This can be typically achieved by increasing t or d (with  $dA \le 0.1$ ). The

specimens were 3D printed monolithically with oversized confining rings. The thickness of the rings was 4.5 mm. Generally, for a CCD specimen, a ring thickness that ranges from 4 to 8 times t was found to be sufficient to eliminate the influence of rotational stiffness and lateral expansion on the behavior of the element. Visual examination of the edges did not show signs of rotation along the edge during load application, or after load removal (damage).

The test was performed using a universal testing machine with a custom fixture (indenter) to apply a vertical load on the rigid ring of the top CCD as shown in Figure 4.11. Testing was conducted under displacement control, applying an incremental displacement at a rate of 0.1 mm/s.

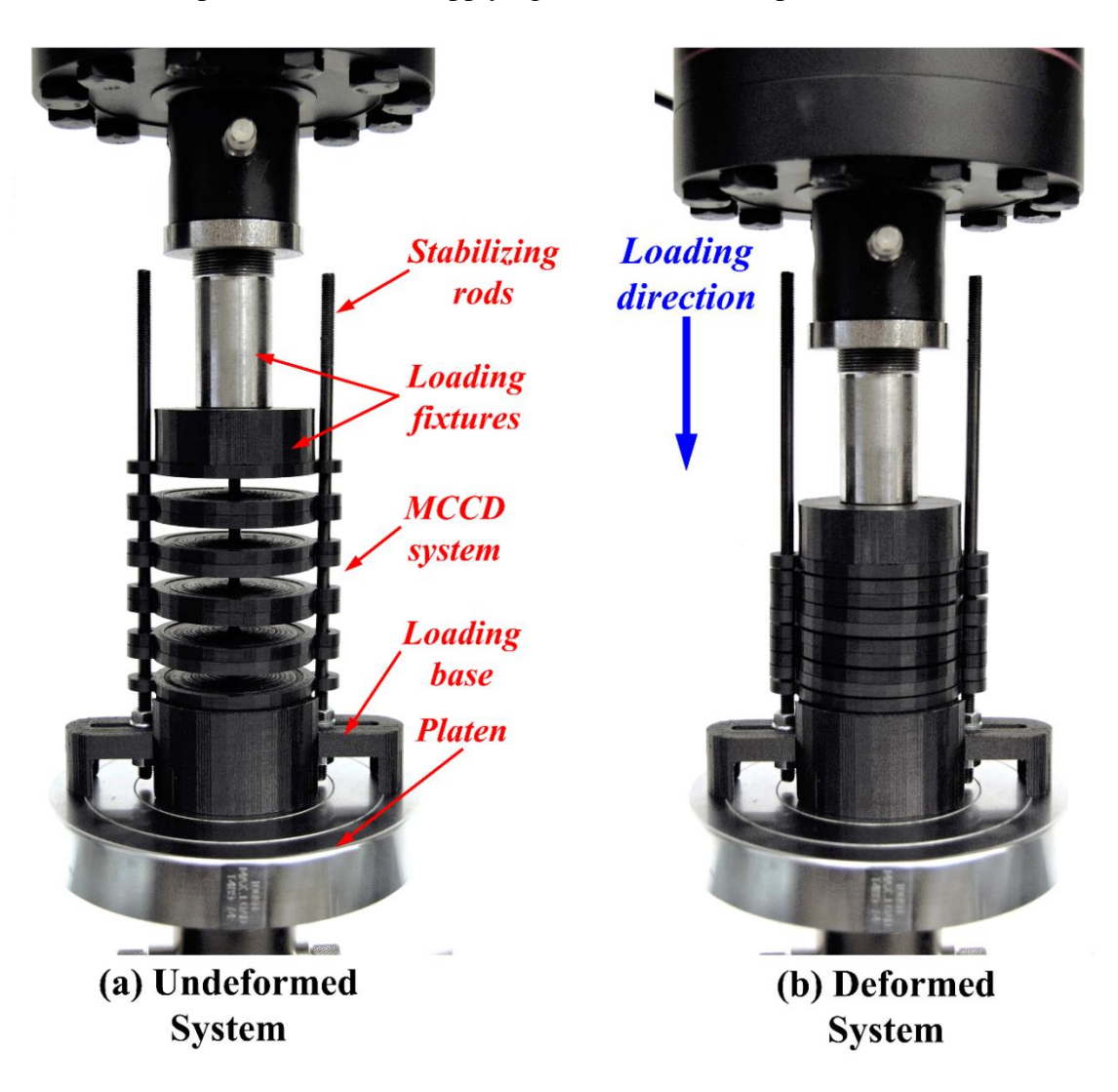


Figure 4.11 Test set up for an MCCD system with ten CCDs ( $n_s = 10$ )

To stabilize the MCCD system against side sway that may occur during testing, the CCD units were designed and 3D printed with two collars on each side as shown in Figure 4.11. This allowed the CCDs to slide in the vertical direction between two rods that were inserted into the collars. The two rods were fixed to a loading base (see Figure 4.11), and the distance between them could be adjusted via slots in the loading base. The rods were fixed to the base using nuts and washers on each side. During testing the guiding rods were coated with a lubricant to minimize friction between them and the collars in the CCD units. This issue can be avoided in MCCD systems that are composed of more than one chain (i.e., one column) of CCD units.

#### 4.5.2 Model validation

Figure 4.12 shows the experimental F- $\Delta$  response of the MCCD specimen compared to the simulated response using the model presented in Section 4.4. The experimental response shows that the buckling force at each buckling event gradually increased. This because the dimensions of the printed CCD units slightly vary and hence F- $\delta$  response of each CCD is different. This does not only vary the buckling force levels but also the corresponding displacements at the buckling events.

Since the F- $\delta$  response for each CCD varies, each unit has a different  $k_I$ . Thus, the initial effective stiffness of the manufactured MCCD system is higher than that of the simulated response based on the average dimensions. This effect triggers the first buckling event on the weakest CCD in the system earlier than the calculated average buckling displacement  $\Delta_{b0} = n_s \, \delta_b$ . This is because the effective stiffness of the MCCD system is greater than the calculated average stiffness based on average dimensions ( $F_b / n_s \, \delta_b$ ). Therefore, during loading, the CCD in the system with lowest  $F_b$  reaches its buckling point ( $\delta_b$ ,  $F_b$ ), while other CCDs in the system are below their buckling limit. Although the buckling limit variation among CCD units complicates calculating an accurate

response for the system, it is an essential feature to obtain a progressive buckling response and hence elastic energy dissipation.

In spite of the complications noted above, it can be noted in Figure 4.12 that the simulated  $F-\Delta$  curve agrees fairly well with the experimental response. This is largely due to the fact that the displacements of the CCD units in the system are minimally affected by dimension variations.

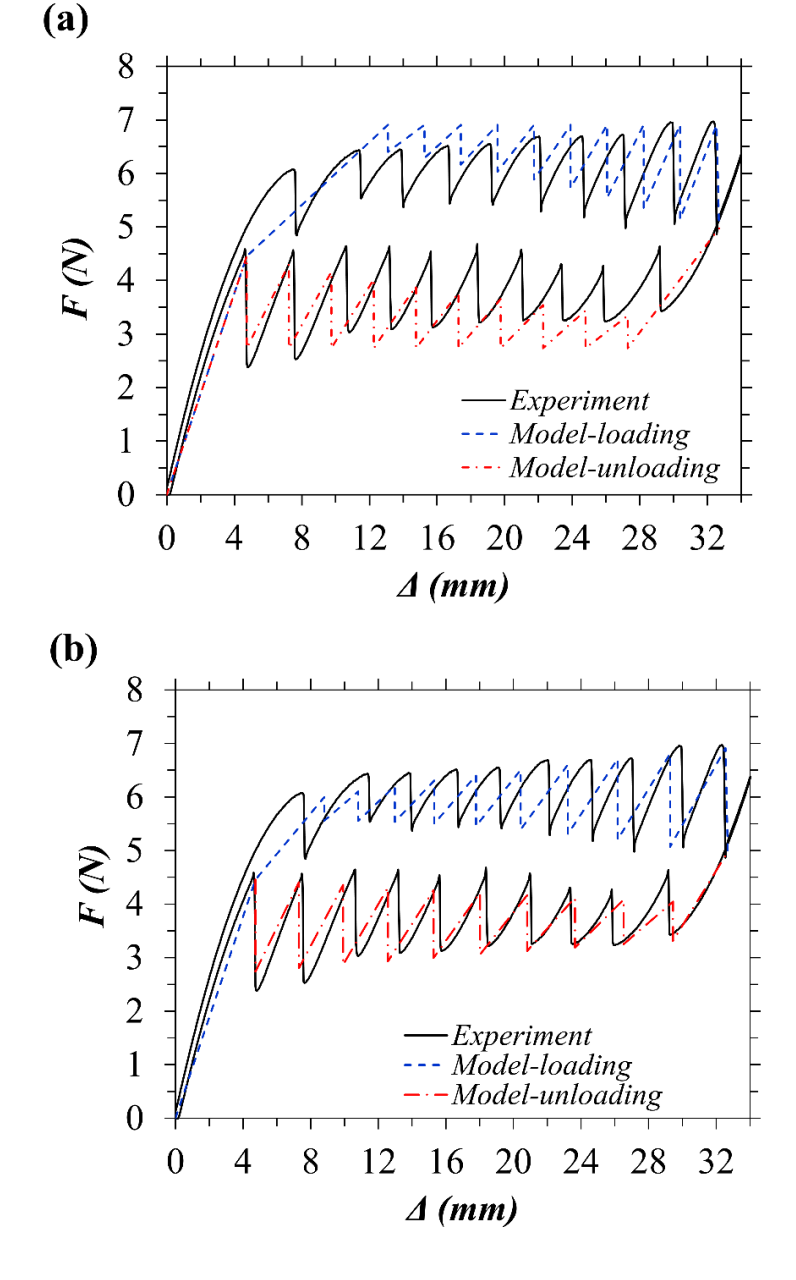


Figure 4.12 *F-*∆ curves for the MCCD system from experimental tests and (a) the analytical model and (b) modified model

#### 4.5.3 Model modification for strength variation

The force and displacement points of the model can be modified to account for the variation in strength among CCD units by knowing the experimental maximum and the minimum values of  $F_b$  and  $F_n$  in the system. These values can be calculated from the dimensions of the CCD with highest h and t and lowest t for maximum values, and the CCD with lowest t and t and highest t for minimum values. The equations below can be used to modify force values at t and t and t and t are expectively, by linearly scaling each value at each buckling event.

$$RF_{bi} = \left(\frac{1 - RF_b}{n_s - 1}\right) (i) + RF_b \tag{4.33}$$

$$RF_b = \frac{F_{b,min}}{F_b} \tag{4.34}$$

$$RF_{ni} = \left(\frac{1 - RF_n}{n_s - 1}\right)(i) + 1\tag{4.35}$$

$$RF_n = \frac{F_n}{F_{n,max}} \tag{4.36}$$

Where  $RF_b$  and  $RF_{bi}$  are the force and the force response modification factors in the loading curve  $(F_b \text{ level})$ ,  $RF_n$  and  $RF_{ni}$  are the force and the force response modification factors in the unloading curve  $(F_n \text{ level})$ ,  $F_{b,min}$  is the minimum  $F_b$  force in the system based on the 'as-printed' dimensions, and  $F_{n,max}$  is the maximum  $F_n$  force in the system based on the 'as-printed' dimensions.

The displacements can also be modified by the equations below at each buckling event along the loading and unloading paths, respectively. These equations linearly shift each drop force line to account for the early buckling of CCD units with lower strengths. Figure 4.12(b) show the modified model compared to experimental results.

$$R\Delta_{bi} = \left(\frac{1 - R\Delta_b}{n_c - 1}\right)(i) + R\Delta_b \tag{4.37}$$

$$R\Delta_b = \frac{F_{b,min} (A-1)}{F_{b,max} A - F_{b,min}}$$
(4.38)

$$R\Delta_{ni} = \left(\frac{1 - R\Delta_n}{n_s - 1}\right)(i) + 1\tag{4.39}$$

$$R\Delta_n = \frac{F_b - F_n}{F_b - F_{n,min}} \tag{4.40}$$

Where  $R\Delta_b$  and  $R\Delta_{bi}$  are the displacement and the displacement response modification factors in the loading curve ( $F_b$  level),  $R\Delta_n$  and  $R\Delta_{ni}$  are the displacement and the displacement response modification factors in the unloading curve ( $F_n$  level),  $F_{b,max}$  is the maximum  $F_b$  force in the system based on the 'as-printed' dimensions, and  $F_{n,min}$  is the minimum  $F_n$  force in the system based on the 'as-printed' dimensions.

#### 4.5.4 Loading rate

To study the effect of loading rate (LR) on the response of the MCCD system, the test was repeated for loading rates of 1, 3, 9, and 15 mm/s. The resulting  $F-\Delta$  curves are shown in Figure 4.13. The figure shows that loading rate had a minimal effect on the response of the system over the examined range of 0.1 to 15 mm/s. However, it can be noted that with increased loading rate, the force drops in the loading and unloading paths decrease slightly. The locations of snap-through and snap-back events also slightly change due to the loading rate. Studies [17,18] on the dynamic behavior of discrete chains with multistable elements indicate that loading rate (in addition to other factors) has dynamic effects on the response of such systems. In fact, even at quasi-static loading conditions, discrete systems exhibit high frequency vibrations upon snap-through events [18]. These damped vibrations are the main contributor to the dissipated energy by discrete systems even at very low loading rates.

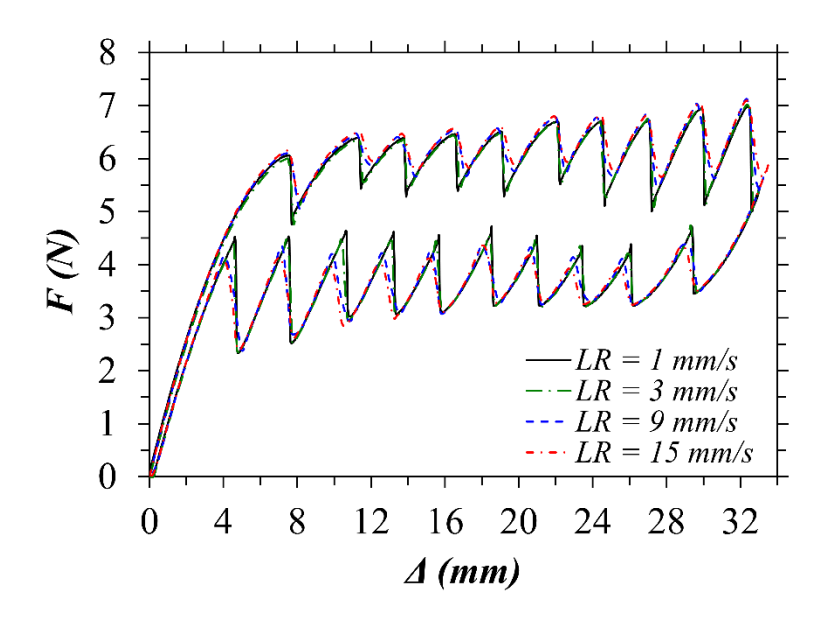


Figure 4.13 Experimental F- $\Delta$  curves for an MCCD system at varying loading rates: 1, 3, 9, and 15 mm/s

### **4.6 Energy Dissipation Characteristics**

The dissipated energy by the MCCD system can be quantified by a general measure of damping called the loss factor,  $\eta$  [64]. This factor is defined as the ratio of the dissipated energy,  $U_d$ , to the total applied work to deform the system,  $W_d$ , in one loading/unloading cycle as given in Equation (4.41).  $W_d$  is the area under the  $F-\Delta$  curve from zero displacement to the maximum displacement at point f in Figure 4.9(a), while  $U_d$  is the enclosed area by the  $F-\Delta$  curve.

$$\eta = U_d / (2\pi W) \tag{4.41}$$

The main parameters of the MCCD system that affect  $\eta$  are h/t and  $n_s$ . The effect of h/t can be studied by knowing the maximum value of  $\eta$ . The theoretical maximum value of  $\eta$  for an MCCD system with  $n_s$  CCDs of a specific h/t occurs when  $n_s \to \infty$ . The F- $\Delta$  response of such as system is similar to the F- $\delta$  response of a single CCD under force control conditions. Figure 4.14(a) shows the F- $\delta$  response of a monostable CCD with h/t = 2.75 under force and displacement control

conditions, where the area enclosed by the force control curve represents the specific maximum dissipated energy. This condition was used to construct a relation between  $\eta$  and h/t, which was found to be linear, as shown in Figure 4.14(b).

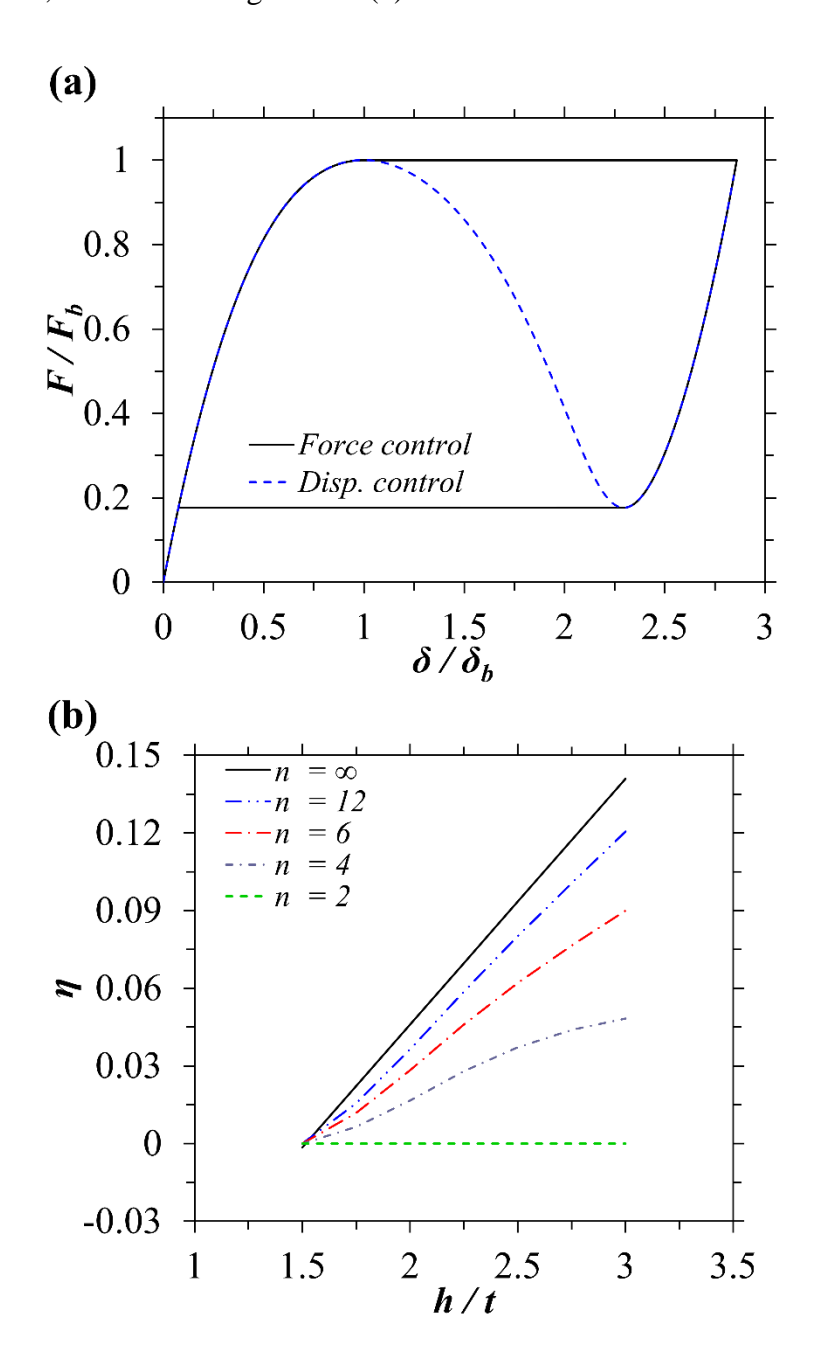


Figure 4.14 (a) Normalized F- $\delta$  curve for a CCD with h/t = 2.75 under force and displacement control conditions, and (b) loss factor with h/t for different  $n_s$  values

The other main parameter of the MCCD system that affects  $\eta$  is  $n_s$ . The analytical multilinear model presented in Section 4.4 was used to calculate  $\eta$  by varying  $n_s$  for a range of h/t values. Figure 4.15(a) shows the F- $\Delta$  response of two MCCD systems with t = 2 mm, h = 5 mm, t = 200 mm, and t = 8 and 14. The curves show that increasing t = 100 mm, and t = 100 mm, with each snap-through and snap-back event, thus increasing the dissipated energy.

To examine the relation between  $\eta$  and  $n_s$  the developed model was used to determine  $\eta$  for  $n_s = 1$  to 1000 and for h/t values ranging from 1.5 to 3 as shown in Figure 4.15(b). The study in [68] showed that a CCD requires h/t of about 1.5 to exhibit a snap-through instability and h/t of about 3 to change the stability state from monostable to bistable, where self-recoverability (preferred) does not occur. From Figure 4.15(b) it can be noted that for  $n_s \le 2$ ,  $\eta = 0$ , which means that the loading and unloading paths coincide. For an MCCD system with  $2 < n_s \le 12$ ,  $\eta$  increases sharply with  $n_s$  over this range, indicating hysteretic responses. For  $n_s > 12$ , a plateau is reached and further increase in  $n_s$  results in very small increases (< 10 %) in  $\eta$ . The same finding can be deduced from the curves in Figure 4.14(b). The  $n_s$ - $\eta$  relation in Figure 4.15(b) shows that 90 % of the maximum value of  $\eta$  is reached with  $n_s = 12$ .

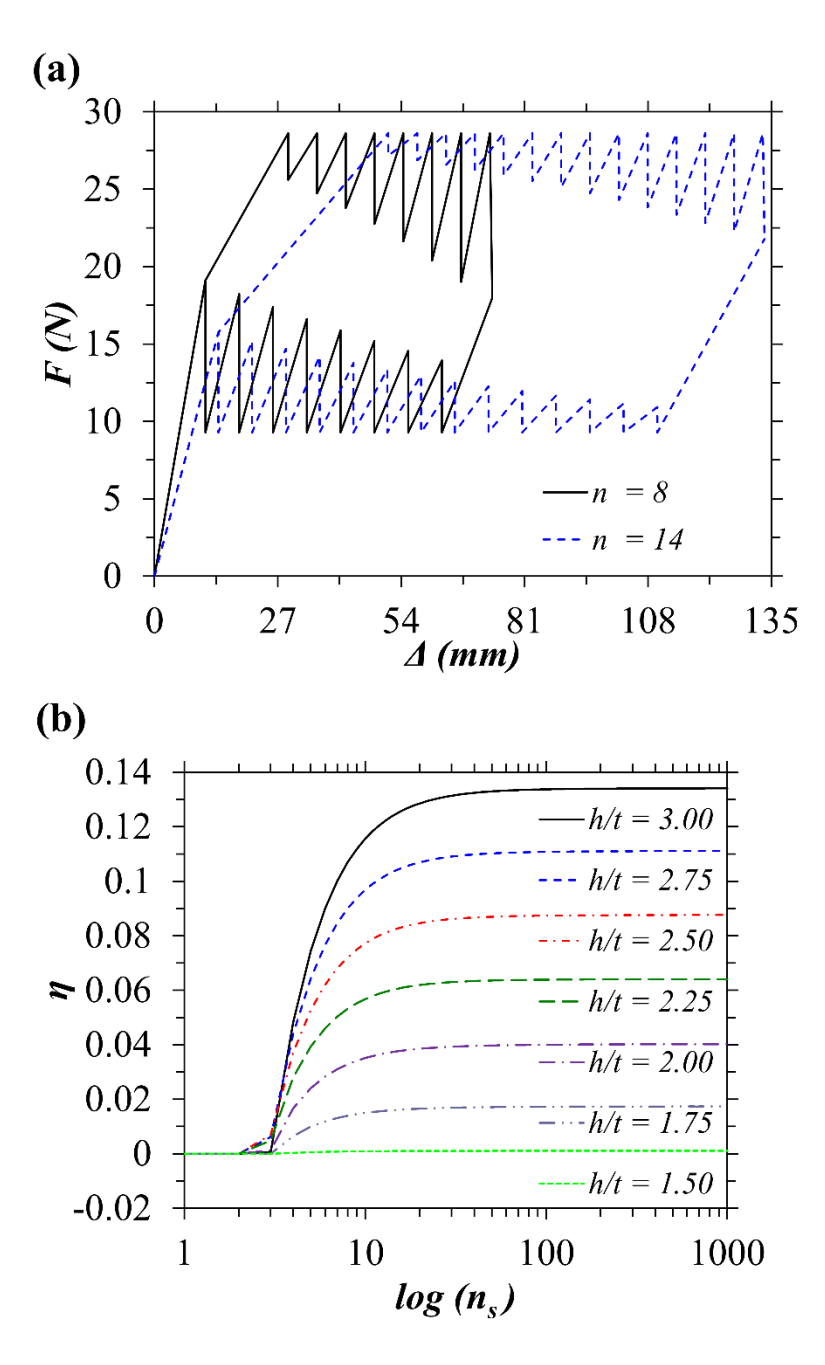


Figure 4.15 (a) F- $\Delta$  curves for MCCDs with h/t = 2.5 and  $n_s = 8$  and 14, and (b) loss factor with  $n_s$  for different h/t ratios

## 4.7 Conclusions

A new system able to dissipate energy through elastic instabilities was presented. The MCCD system proposed in this paper is comprised of multiple cosine-curved domes that exhibit elastic snap-through buckling behavior, which permit the system to display hysteretic force-

deformation response and thus capable of elastically dissipating energy. Numerical studies and experimental tests were conducted to determine the most effective parameters of system response and energy dissipation characteristics. An analytical multilinear model that describes the hysteretic force-displacement response was proposed. The model takes into account the nonlinear effects of the building units of the MCCD system and was shown to yield accurate simulations. The following findings about the MCCD system were drawn:

- The proposed MCCD system can dissipate strain energy by the creation of a hysteretic response through the successive elastic snap-through and snap-back responses of cosinecurved domes connected in series. The hysteretic response is elastic, thus featuring fully recoverable deformations, and has low rate dependence.
- 2. The amount of dissipated energy mainly depends on the number  $(n_s)$  and the height-to-thickness ratio (h/t) of the building units (CCDs). The relation between  $\eta$  and h/t is linear while the relation between  $\eta$  and  $n_s$  is nonlinear. Nonetheless, the higher  $n_s$  and h/t are the higher the amount of the dissipated energy.
- 3. The proposed MCCD system showed a maximum loss factor ( $\eta$ ) value of about 0.14 for a monostable (self-recoverable) system and even higher for a bistable system.
- 4. The loss factor reaches about 90 % of its theoretical maximum value for MCCD systems with about 12 CCDs ( $n_s = 12$ ). Further increase in  $n_s$  yields a very small increase in the value of  $\eta$ .
- 5. Although increasing  $n_s$  increases the amount of dissipated energy, it also decreases the initial stiffness of the MCCD system. This can be compensated by increasing the number of CCDs linked in parallel and/or using more chains of CCDs.

# **CHAPTER FIVE**

# 5 Equivalent Viscous Damping

#### 5.1 Overview

This chapter presents a study to investigate the equivalent viscous damping (EVD) for the hysteretic response of the multiple cosine-curved dome (MCCD) system. The study aims to facilitate the direct displacement-based design of structures incorporating such systems as the main damping mechanism to dissipate seismic energy. Time-history analyses of linear and nonlinear single degree of freedom systems were performed to compare spectral displacements and EVD ratios of the hysteretic response of MCCD systems to their substitute linear systems in terms of maximum displacements. A set of 62 ground motion records were considered for the analysis. A statistical study was conducted on the resulting displacements and the EVD ratios to develop expressions for EVD ratios of the hysteretic response. The study presented in this chapter was submitted to the journal Engineering Structures [82].

### 5.2 Background

The work presented here introduces the use of hysteretic response of the MCCD system [79] to seismic loading and design by investigating the EVD and considering the unique characteristics of the response of the system compared to commonly used inelastic hysteresis models. The uniqueness of multistable element systems originates from the fact that their response cannot be directly described by the displacement ductility or the apparent displacement ductility that is commonly used measure for energy dissipation. Instead, the response is characterized by the number of units in a system and their response, which control the amount of dissipated energy.

Understanding this fundamental difference is the key to properly designing such systems as the main damping mechanism in structures. The work herein is based on this conceptual difference.

Accurate estimation for the EVD ratios is an essential step to the direct displacement-based design, as this quantity relates the hysteretic response of a structure to its corresponding spectral displacement for a given ground motion record. Methods used to investigate the EVD involve conducting dynamic analyses on linear and nonlinear systems. In this study, time-history analyses (THA) were performed on the hysteretic response of MCCD systems and their substitute linear systems in terms of maximum displacements to study the ratio of nonlinear to linear displacements. This was followed by an iterative THA procedure to determine EVD ratios for the equivalent substitute linear systems. A statistical study was then conducted on the results to develop expressions for EVD ratios of the hysteretic response.

#### 5.2.1 Direct displacement-based design

An ideal method to design structures with energy dissipation devices is the direct displacement-based design (DDBD) method [5,83] since it based on the deformation of the structure rather than its strength. Therefore, this method relies on displacement demands and modified linear elastic displacement spectra for the design. To understand the work presented here, it is important to first to recall the main steps of the DDBD method, which is given below with reference to Figure 5.1:

- 1. Determine the design (ultimate) displacement,  $\Delta_u$ . Usually, this displacement is based on maximum allowable drift limits or on sectional/element deformation limits [Figure 5.1(a)].
- 2. Determine the yield (ideal) displacement,  $\Delta_y$ . This displacement is usually based on the target displacement ductility level,  $\mu_{\Delta}$ , serviceability drift limits, or on sectional/element deformation limits [Figure 5.1(a)].

- 3. Based on the displacement ductility, determine the EVD ratio,  $\xi$ , for the proper model of the hysteretic response [Figure 5.1(b)]. Several expressions to estimate  $\xi$  for various hysteresis models are available in the literature [84–88]. These expressions are usually in terms of  $\mu_{\Delta}$ , the structural period, T, and other parameters of the hysteresis model.
- 4. Using  $\xi$  and the design displacement, determine the effective structural period,  $T_{eff}$ , from the modified displacement response spectrum [Figure 5.1(c)].
- 5. Calculate the effective stiffness,  $k_{eff}$ , and hence the design force,  $F_u$ , at the ultimate displacement.

The key step from the DDBD procedure that this study focuses on is the third step, since it links the response of the hysteretic model and the ductility level of the element under consideration to the EVD. The value of  $\xi$  is then used to modify the design linear elastic displacement response spectrum. This eliminates the need to conduct nonlinear THA to obtain nonlinear displacement response spectra for the design process. Therefore, the DDBD method requires an accurate estimation of the  $\xi$  for a substitute linear single degree of freedom (SDF) system that represent, in terms of maximum spectral displacement, the response of the actual nonlinear system for design purpose as shown in Figure 5.1. Consequently, eliminating the need to perform THA for the system.

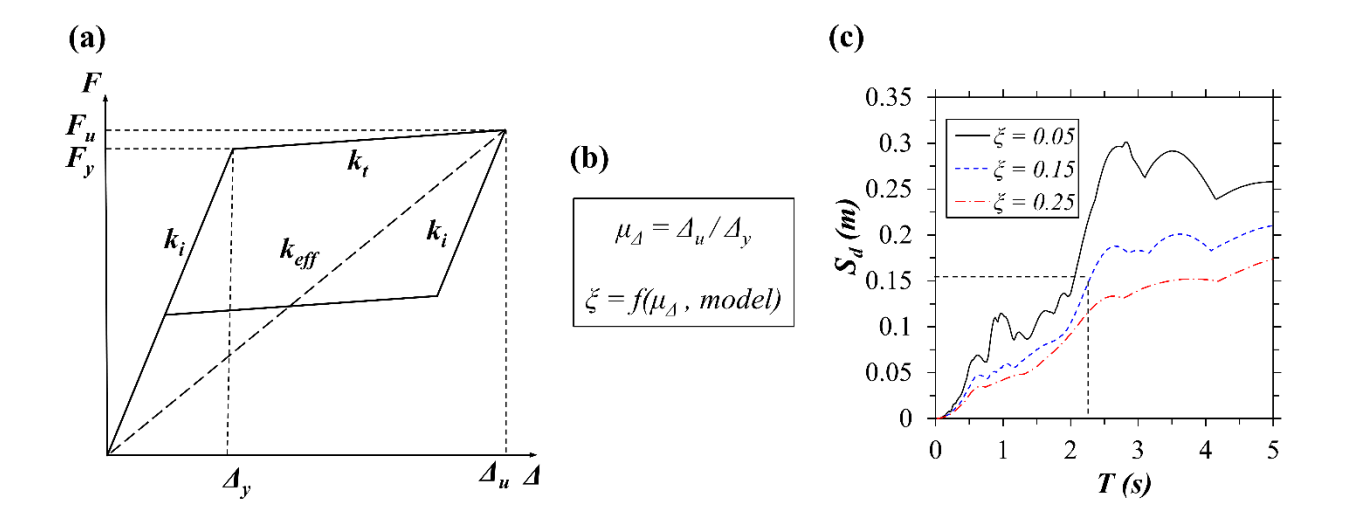


Figure 5.1 Concept of equivalent viscous damping in DDBD method: (a) hysteretic response, (b) relation between  $\xi$  and  $\mu_{\Delta}$ , and (c) displacement response spectra for different values of  $\xi$ 

#### 5.2.2 Approaches to estimate equivalent viscous damping

The equivalent viscous damping ratio ( $\xi$ ) can be divided into two parts: (a) the initial or elastic viscous damping,  $\xi_e$ , and (b) the hysteresis damping,  $\xi_h$ , as given in Equation (5.1). The elastic viscous damping is the damping inherited by the materials of the structure and proportional to the loading rate (velocity). This type of damping usually ranges between 2 to 7 % for common structural materials and elements [89]. The hysteresis damping is the resulting damping due to energy dissipation by the hysteretic response of the system. This damping is significantly higher than the elastic damping.

$$\xi = \xi_e + \xi_h \tag{5.1}$$

Unfortunately, there is no direct procedure to estimate  $\xi$  for a given hysteresis model since the available direct approaches to determine this quantity, such as Jacobsen's approach [90], are affected by many factors such as the forcing function on the SDF system and structural period shift. Thus, such a method can not be directly applied for nonlinear systems excited by ground motion records with nonuniform frequency content. Proper estimations for  $\xi$  are therefore usually achieved by analyzing nonlinear SDFs and their linear equivalents under a wide range of ground motion records. Studies in [84–88] showed that the resulting equivalent damping for SDFs under ground motion records is lower than that determined using on Jacobsen's approach.

There are two main approaches followed to approximately estimate the maximum displacement of a nonlinear hysteretic system from its substitute linear system [91]. In the first approach, the maximum displacement is taken as the product of the displacement of an equivalent linear elastic system with same initial damping ratio ( $\xi_e$ ) and initial lateral stiffness as the nonlinear system multiplied by a displacement modification factor. In the second approach, the maximum displacement is determined from a linear elastic system with a period shift (lower stiffness and higher structural period) and higher damping ratio than that the nonlinear system. In this study, the second approach was followed to determine  $\xi$  to estimate the maximum displacements. Evaluation of different methods and procedure to determine the EVD for various hysteresis models can be found in [91,92].

The concept of EVD for a structure was first presented by Jacobsen [90] to determine approximate solutions for nonlinear SDF systems with a damping force that is proportional to the nth power of the velocity. It is assumed that the two systems are under sinusoidal excitation, having the same stiffness and dissipating the same amount of energy each cycle. Jennings [93,94] modified Jacobsen's concept by changing the initial stiffness of the linear SDF system to a secant stiffness. The modified concept was further investigated and extended by several researchers [92,95].

The modified Jacobsen's equivalent viscous damping ratio,  $\xi_J$ , for a nonlinear system with a hysteresis response compared to a substitute linear system with secant stiffness can be estimated by equating the hysteresis area under a full cycle of loading,  $2A_h$ , to the triangular area under a

straight line from origin to the maximum displacement as shown in Figure 5.2. Thus,  $\xi_J$  is calculated as follows:

$$\xi_I = \frac{A_h}{\pi F_u \Delta_u} \tag{5.2}$$

It should be mentioned that this equation ignores the conditions required for the two systems in the original Jacobsen's approach, which are as follows: (1) they are excited by sinusoidal loading, (2) they are at resonance conditions, and (3) they have the same stiffness.

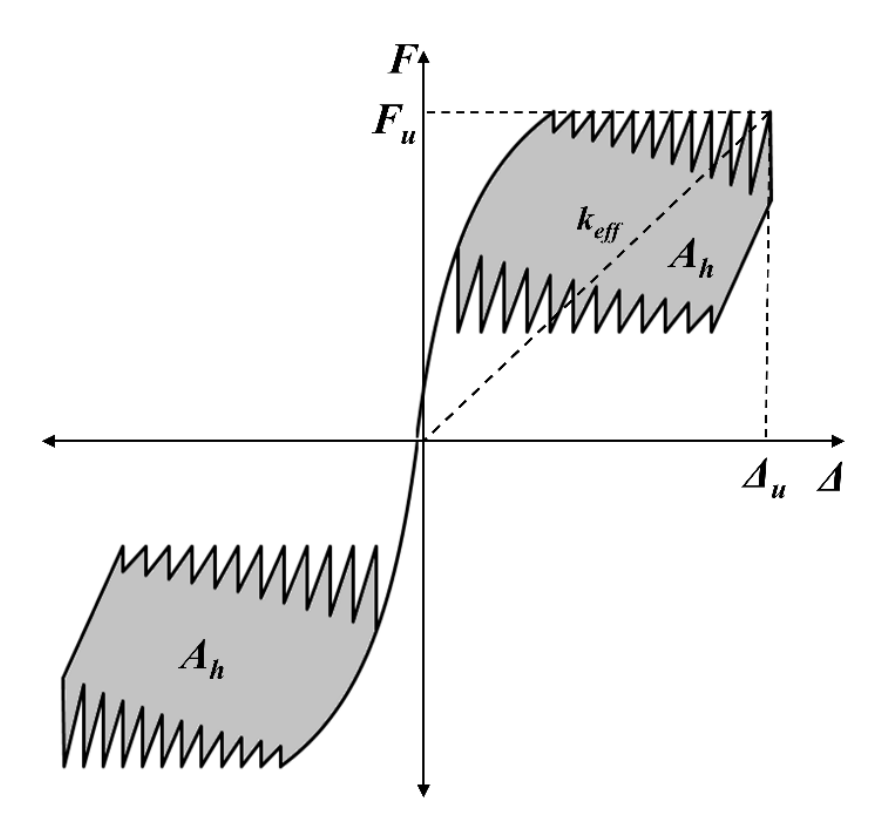


Figure 5.2 Full cycle hysteretic response of the MCCD system with parameters for the modified Jacobsen' approach

## 5.3 Methods

#### 5.3.1 Idealized hysteretic response of the MCCD system

To facilitate the nonlinear time-history analysis of structures incorporating the MCCD system, it is desired to idealize the hysteretic response. The reason is that the sawtooth-shape of

the force-displacement, F- $\Delta$ , curve (Figure 5.2) imposes computational difficulties, and hence commonly used seismic structural analysis programs don't offer modeling tools to represent such a response. Thus, the response of the MCCD system was idealized to a flag-shaped (parallelogram) response by maintaining the energy balance between the actual and the idealized responses. This approach is a similar approach to those widely used approaches in seismic design of structural elements to determine the ideal yield displacement (curvature, or rotation) [4,5].

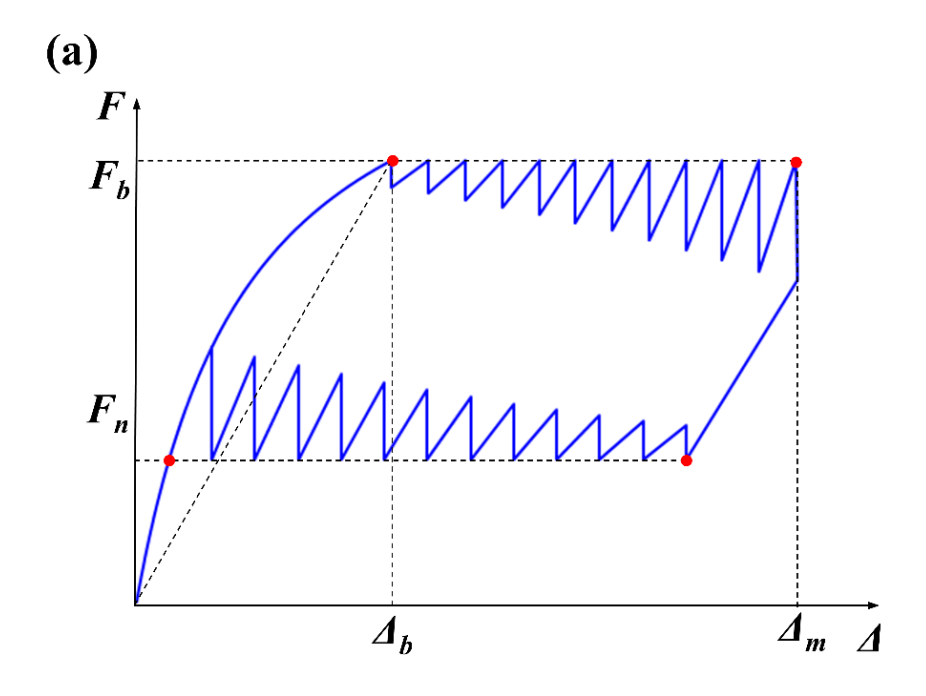
The sawtooth-shape response of the MCCD system shown in Figure 5.3(a) can be calculated using the analytical model presented in [79]. The study in [79] investigated the response characteristics of the MCCD system and its energy dissipation capability. As shown in Figure 5.3(a), the response consists of multiple snap-through (and snap-back) events that equal to the number of units in the system  $(n_s)$ . The snap-through and snap-back events are at the same level as the buckling force,  $F_b$ , and the minimum force,  $F_n$ , respectively. The drop forces from each snap-through,  $F_{bd}$ , and snap-back,  $F_{nd}$ , events vary depending on h/t and  $n_s$ . The effective initial stiffness of the system,  $k_b$ , is taken as the slope of a straight line from the origin to the displacement at the first buckling event,  $\Delta_b$ , of the system as given below:

$$k_b = F_b / \Delta_b \tag{5.3}$$

where  $\Delta_b = n_s \, \delta_b$ , and  $\delta_b$  is the critical (instability) displacement of an individual CCD unit as shown in Figure 5.3(b). The response characteristics of a single CCD unit and its force and displacement values can be calculated using the expressions developed in [68]. The maximum displacement of the system,  $\Delta_m$ , is given as follows:

$$\Delta_m = n_s \, \delta_b + (n_s - 1) \, s_b \tag{5.4}$$

where  $s_b = \delta_b$  -  $\delta_m$ , and  $\delta_m$  is the displacement at a force level equal to  $F_b$  in Region III, see Figure 5.3(b).



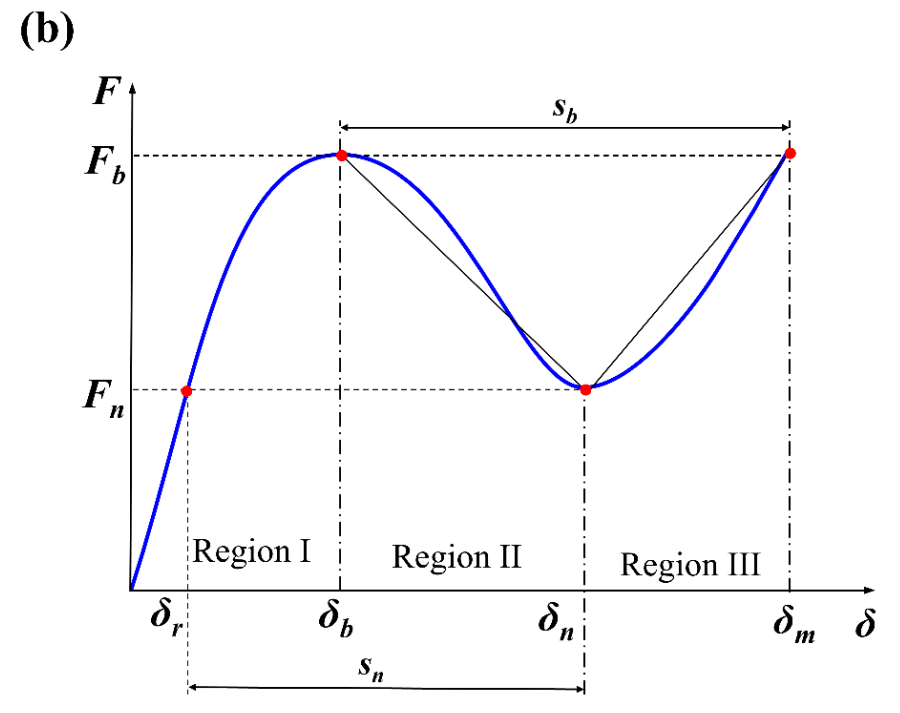


Figure 5.3 (a) F- $\Delta$  response of the MCCD system, and (b) F- $\delta$  responses of a CCD unit with key response quantities

A two-step procedure was developed to idealize the hysteretic response of the MCCD system. In the first step, an ideal initial stiffness was determined in terms of h/t. This stiffness is

needed to correct the initial stiffness ( $k_b$ ) in order to construct a flag-shaped response that maintains the equal energy condition between the actual and idealized responses for a theoretical system with  $n_s = \infty$  (Figure 5.4). In the second step, an ideal buckling force,  $F_b$ ', and a minimum force,  $F_n$ ', were determined based on the characteristics of the hysteretic response of the MCCD system. It should be noted that in practical systems with  $n_s \ll \infty$ ,  $F_b$ ' and  $F_n$ ' are smaller and greater than  $F_b$  and  $F_n$ , respectively. The values of  $F_b$ ' and  $F_n$ ' approach  $F_b$  and  $F_n$ , respectively, when  $n_s$  approaches  $\infty$ .

#### 5.3.1.1 <u>Ideal stiffness</u>

Figure 5.4 shows the F- $\Delta$  response of an MCCD system with  $n_s = \infty$ . The F- $\Delta$  response of such as system is similar to the response of a single CCD under force control conditions. Note that in this case  $F_b$ ' =  $F_b$  and  $F_n = F_n$ '. Figure 5.4 also shows an idealized response based on the initial stiffness of the system  $(k_b)$ . This idealization clearly shows that the energy balance between the enclosed areas of the two curves is not maintained. Therefore, the initial stiffness of an idealized response,  $k_z$ , must be determined in a way that satisfies the energy balance condition. This can be done by solving the following equation for  $k_z$ :

$$A_h = (F_b - F_n) \left( \Delta_m - F_b / k_z \right) \tag{5.5}$$

Equation (5.5) represents the area of the flag-shaped response and the ratio  $F_b / k_z$  represents the ideal displacement at first buckling event,  $\Delta_b$ ', see Figure 5.4.

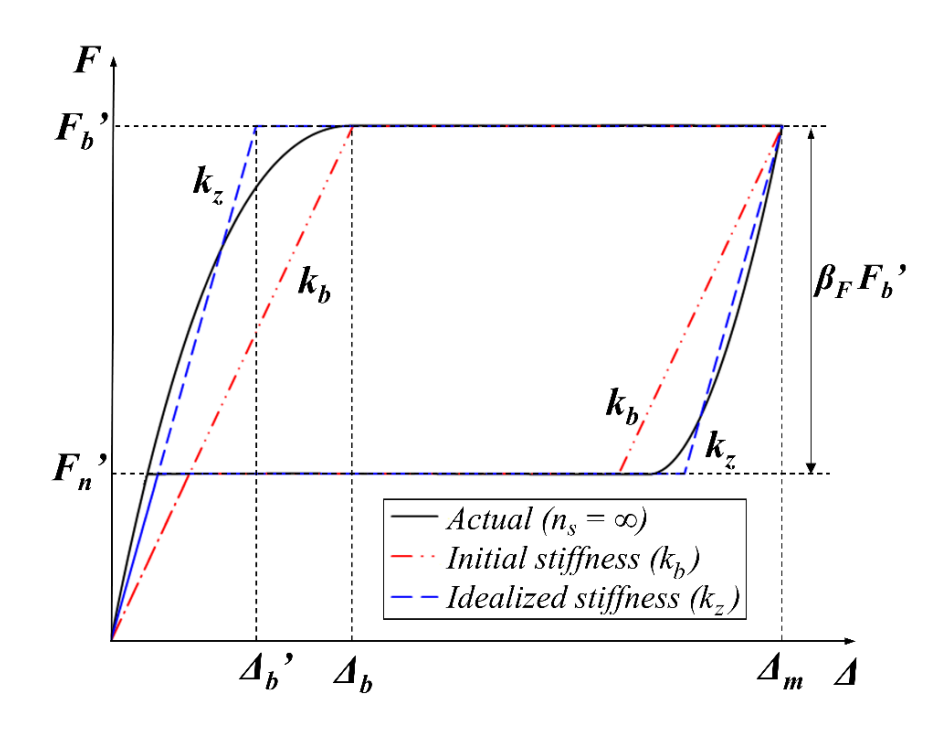


Figure 5.4 The actual and the idealized  $F-\Delta$  curves for an MCCD system with  $n_s = \infty$ 

Figure 5.4 shows the ideal initial stiffness and the resulting hysteretic response of the system. The same process was conducted for h/t ranging from 1.5 to 3 in order to construct a relation between h/t and  $k_z/k_b$ . This relation was found to be linear as shown in Figure 5.5(a). Thus,  $k_z/k_b$  can be calculated using the following expression:

$$k_z/k_b = 0.674 \, h/t$$
 (5.6)

The equivalent viscous damping ratios based on the modified Jacobsen's approach ( $\xi_J$ ) were calculated for h/t ranging from 1.5 to 3 using Equation (5.2). The results show an approximately linear relationship between  $\xi_J$  and h/t. Another important quantity that describes the idealized hysteretic response are the displacement ductility ( $\mu_A$ ) and the force ratio of the difference between  $F_b$ ' and  $F_n$ ',  $\beta_F$  as given in Equations (5.7) and (5.8), respectively. The equations were used to construct a relation for  $\mu_A$  and  $\beta_F$  with respect to h/t as shown in Figure 5.5(b). Both quantities exhibit a generally linear relation with h/t.

$$\mu_{\Delta} = \Delta_m / \Delta_b' \tag{5.7}$$

$$\beta_F = (F_b' - F_n') / F_b' \tag{5.8}$$

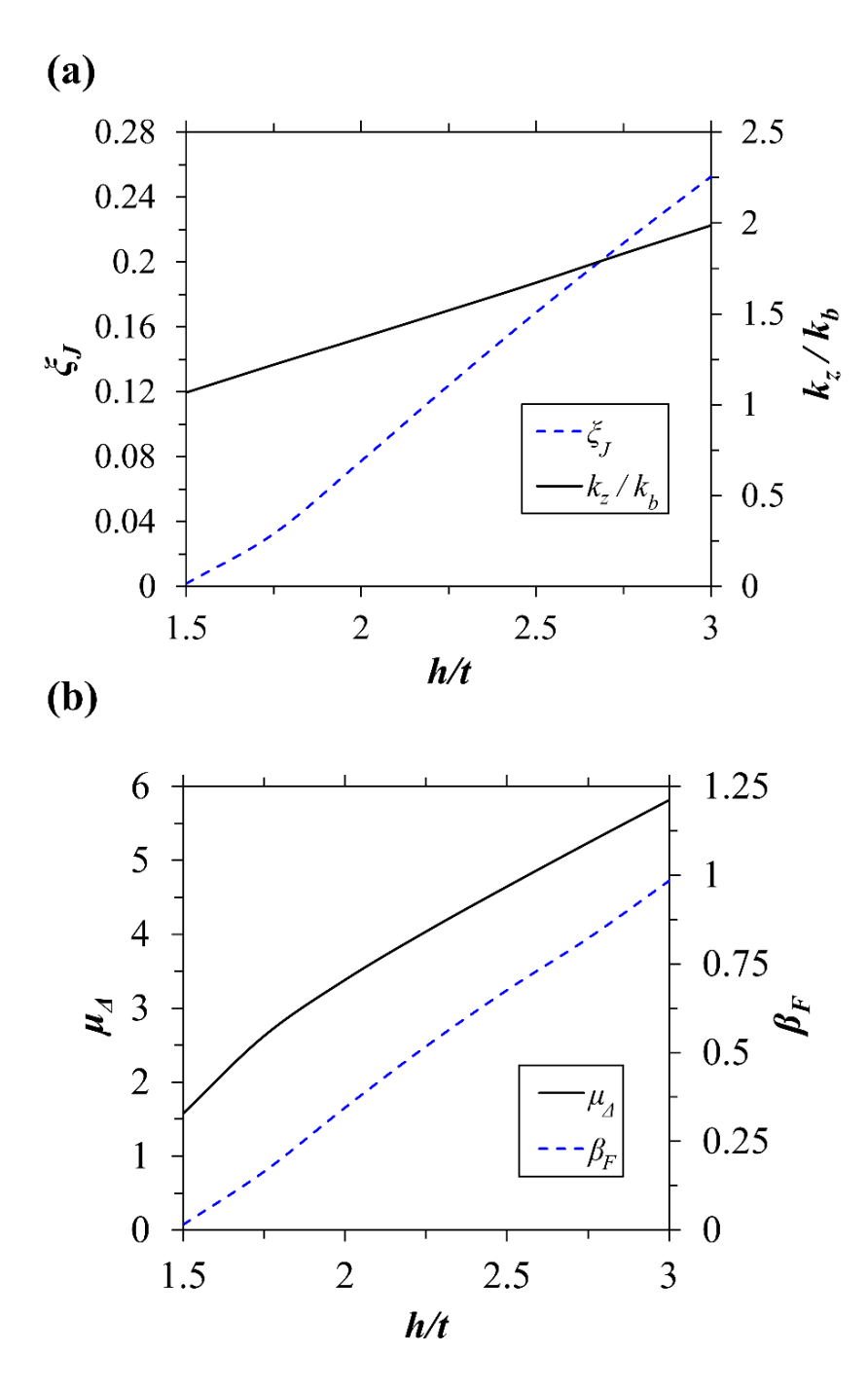


Figure 5.5 (a) EVD ratios based on modified Jacobsen's approach  $(\xi_J)$  and the ideal stiffness ratio  $(k_z/k_b)$  with h/t, and (b) displacement ductility  $(\mu_A)$  and force difference ratio  $(\beta_F)$  with h/t

#### 5.3.1.2 Ideal maximum and minimum forces

For an MCCD system with a finite number of units ( $n_s \ll \infty$ ), the ideal buckling ( $F_b$ ') and minimum ( $F_n$ ') forces are lower and higher than  $F_b$  and  $F_n$ , respectively. Thus, the aim here is to determine the values of  $F_b$ ' and  $F_n$ ' in conjunction with the ideal initial stiffness ( $k_z$ ), determined in the first step, while maintaining the energy balance between the two responses as shown in Figure 5.6. Since the known parameters of the idealized response in Figure 5.6 are only  $k_z$  and  $\Delta_m$ , it is required to establish a relation between  $F_b$ ' and  $F_n$ ' in terms of the average buckling,  $F_{bavg}$ , and minimum,  $F_{navg}$ , forces to solve the enclosed area equation  $A_h = (F_b' - F_n') (\Delta_m - F_b' / k_z)$  for  $F_b$ '. In this relation it was assumed that the difference between  $F_b$ ' and  $F_{bavg}$  equals to the difference between  $F_n$ ' and  $F_{navg}$ , i.e.,  $F_b$ ' –  $F_{bavg}$  =  $F_n$ ' –  $F_{navg}$ . This assumption ensures that idealized forces are relative to the average forces, and the reduction from  $F_b$  and the increase from  $F_n$  are equivalent to each other. The average forces  $F_{bavg}$  and  $F_{navg}$  can be calculated based on the average difference between  $F_b$  and  $F_{bd}$ , and between  $F_n$  and  $F_{ndd}$ , see Figure 5.3(a). The following steps summarize this idealization procedure:

- 1. Calculate the sawtooth-shaped response of the MCCD system and the energy area  $A_h$
- 2. Determine the average forces  $F_{bavg}$  and  $F_{navg}$
- 3. Solve the second-degree Equation (5.9) of the enclosed energy area  $A_h$  and determine  $F_b$ :

$$C_1 F_{b'}{}^2 + C_2 F_{b'} - C_3 = 0 (5.9)$$

where  $C_1$ ,  $C_2$ , and  $C_3$  are as follows:

$$C_1 = -2/k_{z_1}$$

$$C_2 = 2 \Delta_m + (F_{bavg} + F_{navg}) / k_z$$
, and

$$C_3 = \Delta_m (F_{bavg} + F_{navg}) + A_h$$

4. Calculate  $F_n' = F_{navg} - (F_b' - F_{bavg})$ 

5. Calculate  $\Delta_b$ ',  $\Delta_d$ ', and  $\Delta_n$ ' based on the value of  $F_b$ ',  $F_n$ ', and  $k_z$  as shown in Figure 5.6.

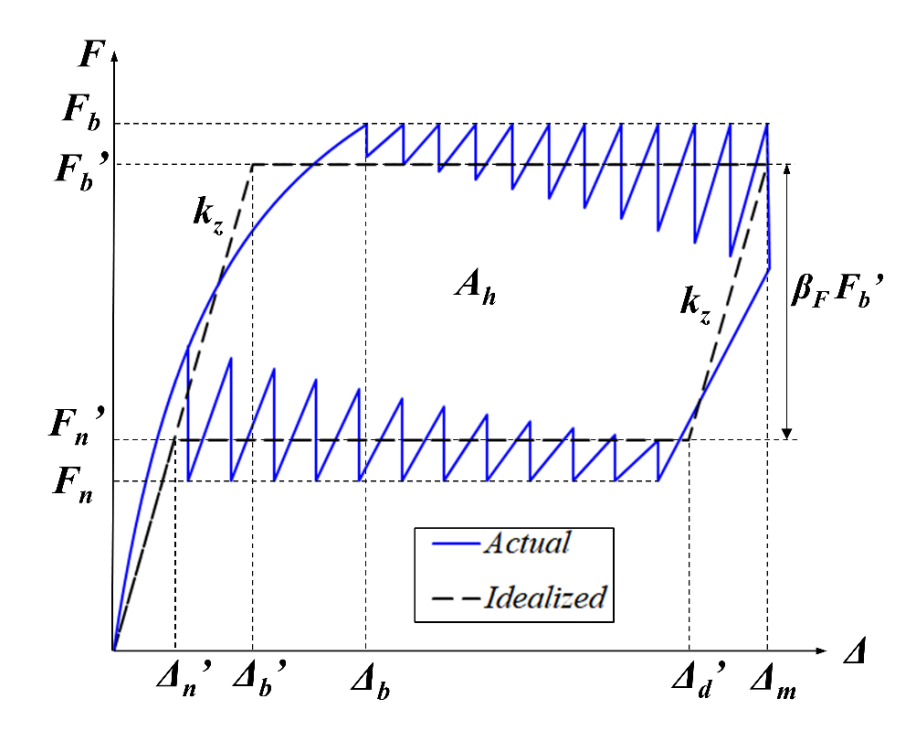


Figure 5.6 The actual and the idealized *F-\Delta* curves for an MCCD system with  $n_s \ll \infty$ 

The procedure above was repeated for h/t ranging from 1.5 to 3 and for  $n_s$  ranging from 1 to 1000 to examine the relation of  $\mu_A$  with  $n_s$  and h/t as shown in Figure 5.7. It can be seen that in general the increase in  $\mu_A$  with  $n_s$  is minimal especially for higher values of  $n_s$ . The reason is that both  $\Delta_m$  and  $\Delta_b$  are in terms of  $n_s$ . Nonetheless,  $\mu_A$  increases at higher rate between  $n_s$  of 3 and 6, and this effect is more pronounced for systems with higher h/t. However, as will be shown latter, the dissipated energy  $(A_h)$  within that range is low.

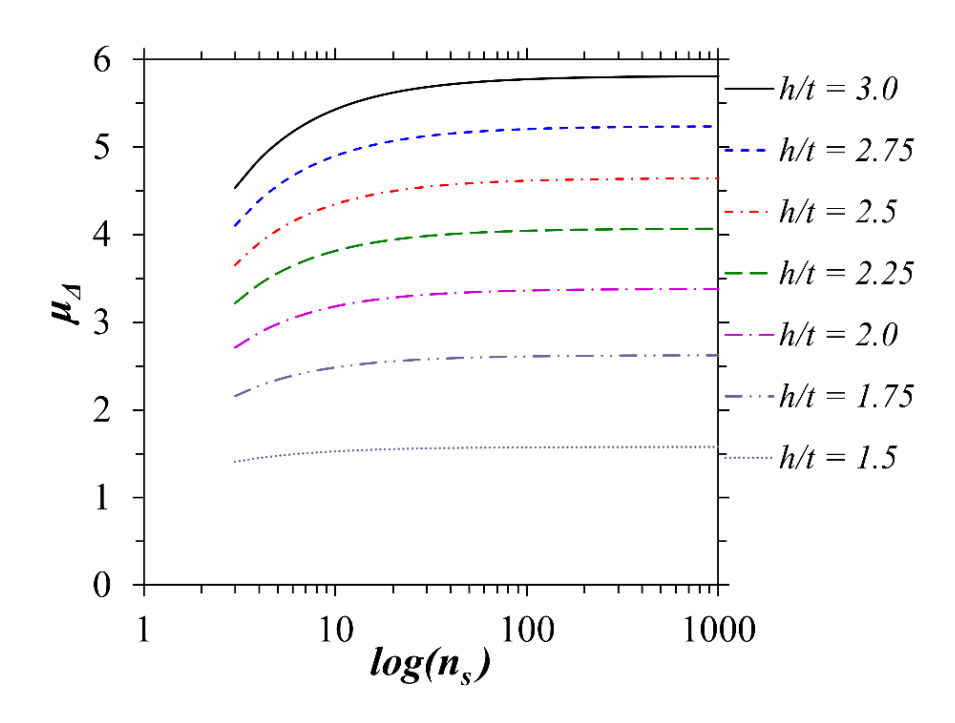


Figure 5.7 The relation between displacement ductility ( $\mu_{\Delta}$ ) with  $n_s$  for a range of h/t values

To study the relation between  $\xi_J$  and  $n_s$  Equation (5.2) was used to determine  $\xi_J$  for  $n_s = 1$  to 1000 and for h/t values ranging from 1.5 to 3. This relation is shown in Figure 5.8(a). It should be noted that an MCCD system requires a h/t of about 1.5 to exhibit a snap-through instability and h/t of about 3 or less to maintain self-recoverability [79]. Figure 5.8(a) shows that for  $n_s \le 2$ ,  $\xi_J = 0$  since the loading and unloading curves coincide, while for  $2 < n_s \le 18$ ,  $\xi_J$  increases sharply. For about  $n_s > 18$ , a further increase in  $n_s$  results in a slight increase (< 10 %) in  $\xi_J$ . In a similar fashion, the force ratio  $\beta_F$  was plotted against h/t and  $n_s$  and it showed comparable trends to  $\xi_J$  as shown in Figure 5.8(b)

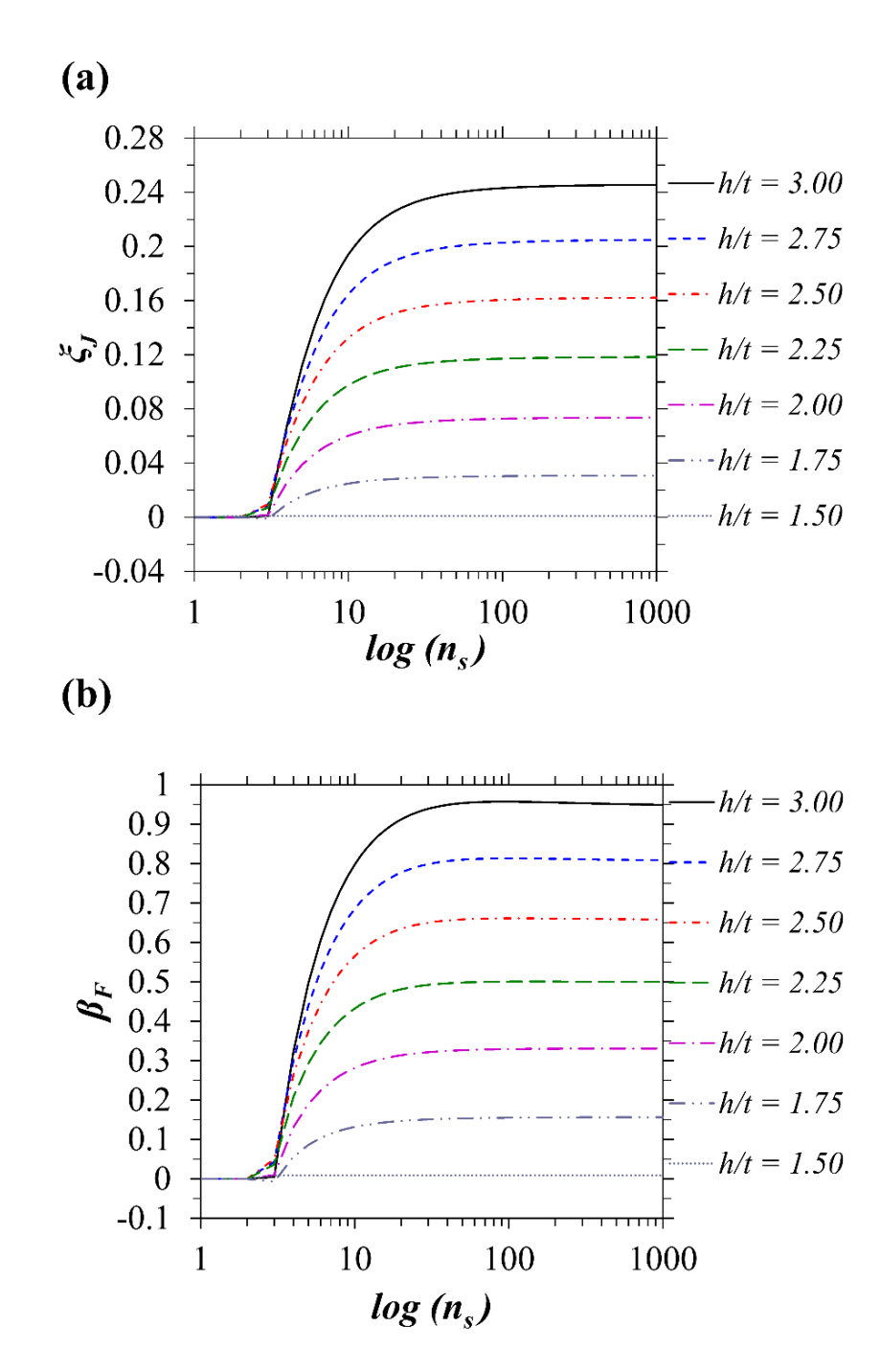


Figure 5.8 (a) The relation between  $\xi_J$  with  $n_s$  for different h/t ratios, and (b)  $\beta_F$  with h/t for different  $n_s$  values

# 5.3.2 Considered cases for the study

Two cases of the hysteresis model were considered for the study: (1) the response of the MCCD system, and (2) the response of the MCCD system coupled with a linear elastic response.

In the first case, it is assumed that the MCCD is the only force resisting system and damping mechanism with a response as shown in Figure 5.9(a). Note that the tangent stiffness,  $k_t$ , is zero in this case. In the second case, the response in the first case (i.e., the response of the MCCD system) was coupled in parallel with a non-yielding linear (NYL) system. The resulting response in the second case is as shown in Figure 5.9(b). The coupled NYL system has a stiffness,  $k_c$ , that is less than or equal to the secant stiffness of the MCCD system,  $k_e$ , as shown Figure 5.9(b). The ultimate force of the NYL system,  $F_c$ , can be linked to  $F_b$  by the force ratio factor,  $\gamma_F$ , as given below.  $\gamma_F$  = 1 and 2 for  $F_c$  = 0 and  $F_c$  =  $F_b$ , respectively. It is should be noted that  $k_{eff}$  in the first case [Figure 5.9(a)] does not equal to  $k_{eff}$  in the second case [Figure 5.9(b)]. The relations governing the parameters of hysteretic responses are as follows:

$$\gamma_F = (F_b' + F_c) / F_b'$$
 (5.10)

$$F_u = k_{eff} \Delta_u \tag{5.11}$$

$$F_{y} = F_{u} \frac{\mu_{\Delta} + \gamma_{F} - 1}{\gamma_{F} \mu_{\Delta}} \tag{5.12}$$

$$k_i = F_y \, \mu_\Delta / \Delta_u \tag{5.13}$$

$$\alpha_F = \frac{\gamma_F - 1}{\mu_\Delta + \gamma_F - 1} \tag{5.14}$$

$$k_t = \alpha_F k_i \tag{5.15}$$

$$\xi_J = \frac{\beta_F (\mu_\Delta - 1)}{\gamma_F \pi \mu_A} \tag{5.16}$$

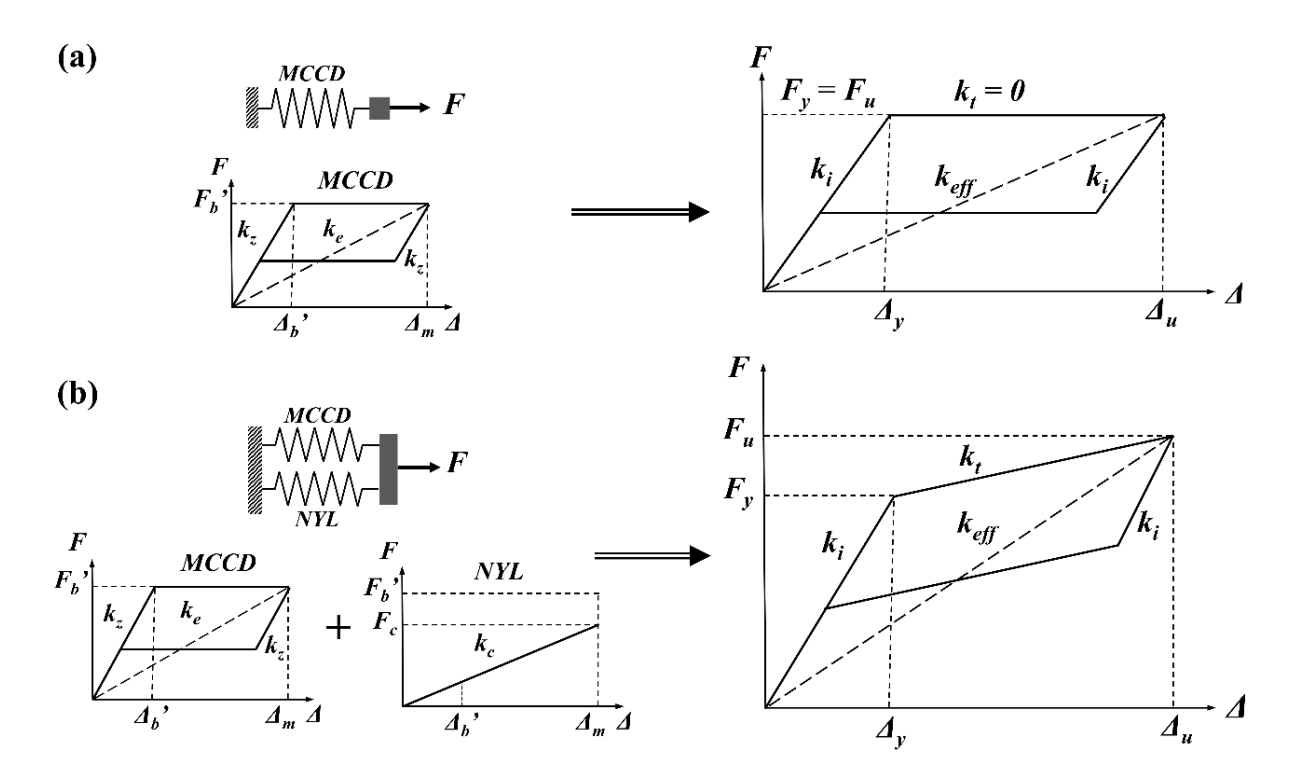


Figure 5.9 Hysteresis models considered: (a) Case 1-response of an MCCD system, and (b) Case 2-response of an MCCD system coupled with a non-yielding linear system

## **5.3.3** Ground motion records

A set of 62 ground motion records was used to conduct the study. The records are from 7 different earthquakes with properties as presented in Table 5.1. The earthquakes had magnitudes (Ms) ranging from 5.8 to 7.1 [96]. The records were recorded on sites corresponding to site class B as per [97]. Figure 5.10 shows the displacement response spectra for the 62 ground motion records with 5 % damping along with the average response spectrum. The curves in Figure 5.10 were normalized based on maximum spectral displacement after the spectral analysis for illustration purposes.

Table 5.1 Recorded earthquake used in this study

Date	Earthquake name	Magnitude (Ms)
02/09/1971	San Fernando	6.5
04/24/1984	Morgan Hill	6.1
07/08/1986	Palm Springs	6.0
10/01/1987	Whittier	6.1
10/17/1989	Loma Prieta	7.1
06/28/1991	Sierra Madre	5.8
01/17/1994	Northridge	6.8

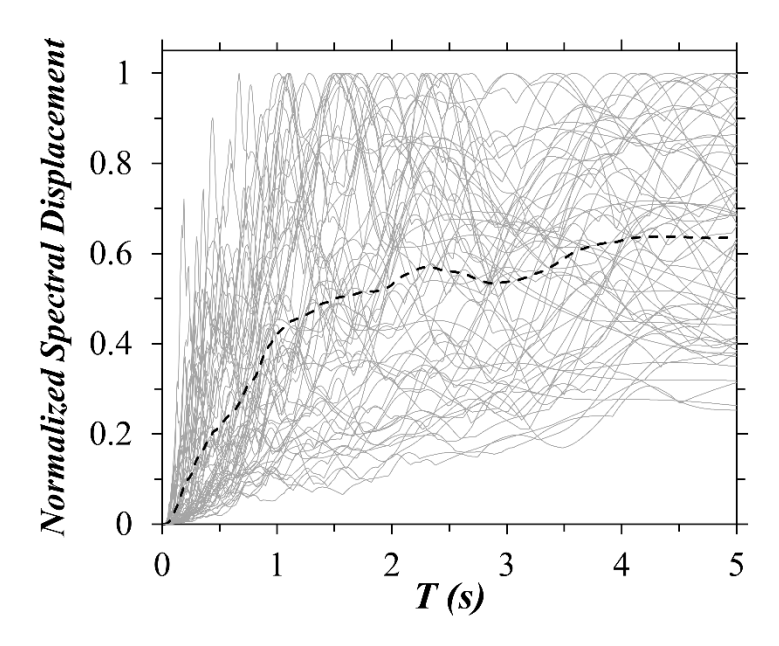


Figure 5.10 Scaled displacement response spectra of the motion records at 5 % damping and their average response

## 5.3.4 Analysis procedure

The procedure followed to determine the  $\xi$  starts with the modified Jacobsen's viscous damping ratio ( $\xi_J$ ) defined by Equation (5.2) in addition to the elastic viscous damping ( $\xi_e$ ) of 2% as an initial estimate for the linear THA of the substitute systems. These ratios are then changed in an iterative process until the resulting  $\xi$  for the equivalent substitute linear SDF systems have the same maximum spectral displacements as the original nonlinear systems. For the nonlinear

THA, a value of 2% Rayleigh damping [98–100] proportional to the current tangent stiffness was considered.

The study was conducted for the two cases noted in Section 5.3.2 with 0.05 s  $\leq T_{eff} \leq 4$  s at 0.05 s increments and h/t ranging from 1.5 to 3 at 0.25 increments. The corresponding values of  $\mu_{\Delta}$  and  $\beta_{F}$  as a function of h/t are shown in Figure 5.5(b) and can be calculated using Equations (5.7) and (5.8), respectively.

The THA of the linear and nonlinear systems were performed using the program OpenSees [101]. The iterative process to determine  $\xi$  for the linear SDF systems were performed using the program Matlab. The process to determine the EVD ratios is as follows:

- 1. Set an h/t and calculate the corresponding values of  $\mu_{\Delta}$  and  $\beta_{F}$ .
- 2. Select a ground motion record.
- 3. Set an effective structural period  $T_{eff}$ .
- 4. Calculate  $\xi_J$  from Equation (5.2) and set the initial EVD ratio,  $\xi_i$ , as  $\xi_i = \xi_e + \xi_J$
- 5. Calculate  $k_{eff} = 4 \pi^2 m / T_{eff}^2$  where m is the mass and it was kept constant at unity.
- 6. Perform linear THA on the SDF system with properties as given above and determine the maximum absolute linear displacement,  $\Delta_L$ .
- 7. Based on the value of  $\Delta_L$  from step 6, and  $\mu_{\Delta}$  and  $\beta_F$  form step 1, calculate the parameters of the hysteretic response of the nonlinear system:  $F_u$ ,  $F_y$ ,  $k_i$ , and  $k_t$  using the relations presented in Section 5.3.2.
- 8. Perform nonlinear THA on the SDF system with properties as given above and determine the maximum absolute nonlinear displacement,  $\Delta_{NL}$ .

- 9. Compare the maximum displacements  $\Delta_L$  and  $\Delta_{NL}$  from steps 6 and 8, respectively, and report the ratio  $\Delta_{NL}/\Delta_L$ . If the error between  $\Delta_L$  and  $\Delta_{NL}$  is less than 1.5%, then the EVD ratio  $\xi$  equals  $\xi_i$  and proceed to step 11, otherwise proceed to step 10.
- 10. For the linear system with properties as given in steps 2 to 5, iteratively change  $\xi$  until the resulting new  $\Delta_L$  equals to  $\Delta_{NL}$  from step 8 within an absolute error of 1.5%, and report the results.
- 11. Repeat the procedure from step 3 to 10 by selecting different values of  $T_{eff}$ . This step will result in linear and nonlinear displacement response spectra.
- 12. Repeat the procedure from step 2 to 11 by selecting another ground motion record.
- 13. Repeat the procedure from step 1 to 12 by selecting a different value of h/t and the corresponding values of  $\mu_{\Delta}$  and  $\beta_{F}$ .

## 5.4 Results and Discussion

#### 5.4.1 Ratio of nonlinear to linear spectral displacements

The linear and nonlinear spectral displacements (analysis results from step 11) for the considered ground motion records were averaged and grouped based on the h/t values and the two considered cases in Section 5.3.2. The calculated ratios of nonlinear to linear spectral displacements ( $\Delta_{NL}/\Delta_L$ ) were averaged for the 62 records over the range of  $T_{eff}$ . A statistical study was conducted on the resulting data to determine the upper and lower bounds using the interquartile range [102] and then eliminating suspected outliers. Figure 5.11(a) and (c) show the averaged ratios of  $\Delta_{NL}/\Delta_L$  for Case 1 and 2, respectively. It can be noted that for approximately  $T_{eff}$  > 0.75 s, the ratio is generally greater than 1. This means that the used  $\xi_i$  based on the modified Jacobsen's approach (step 4) overestimates the  $\xi$ . An opposite conclusion can be made on the

 $\Delta_{NL}/\Delta_L$  values for  $T_{eff}$  < 0.75 s. The coefficient of variation (COV) for  $T_{eff}$  < 0.75 s, shown in Figure 5.11(b) and (d), ranges between 10% and 40% for Case 1, and between 8% and 28% for Case 2.

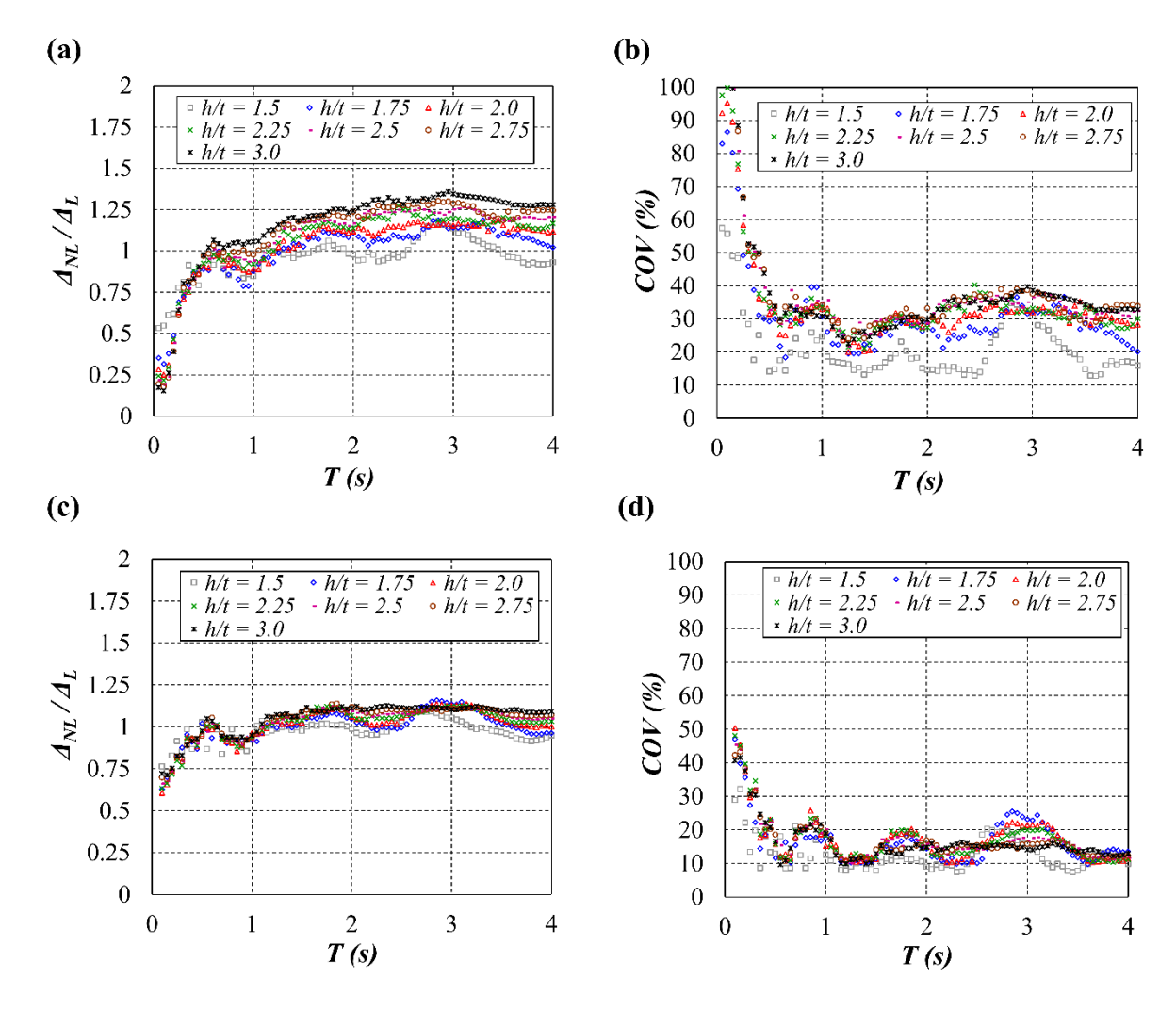


Figure 5.11 Average ratios of linear to nonlinear spectral displacements and coefficient of variation for Case 1 [(a) and (b)], and for Case 2 [(c) and (d)]

## 5.4.2 Equivalent viscous damping ratios

A similar statistical study to that performed for the  $\Delta_{NL}/\Delta_L$  ratios was repeated for the equivalent viscous damping ratio ( $\xi$ ) obtained from the iterative process in step 10. Figure 5.12(a) and (b) show the average  $\xi$  for the 62 records over the range of  $T_{eff}$  and grouped based on the values of h/t and the two considered cases. Figure 5.12(c) and (d) show the relation between h/t and  $\xi$  for selected values of  $T_{eff}$  along with the calculated EVD based on the modified Jacobsen's approach

(MJ). The figures show that the curves are generally lower than the MJ curve except for shorter periods  $T_{eff}$  of 0.5 and 1 s.

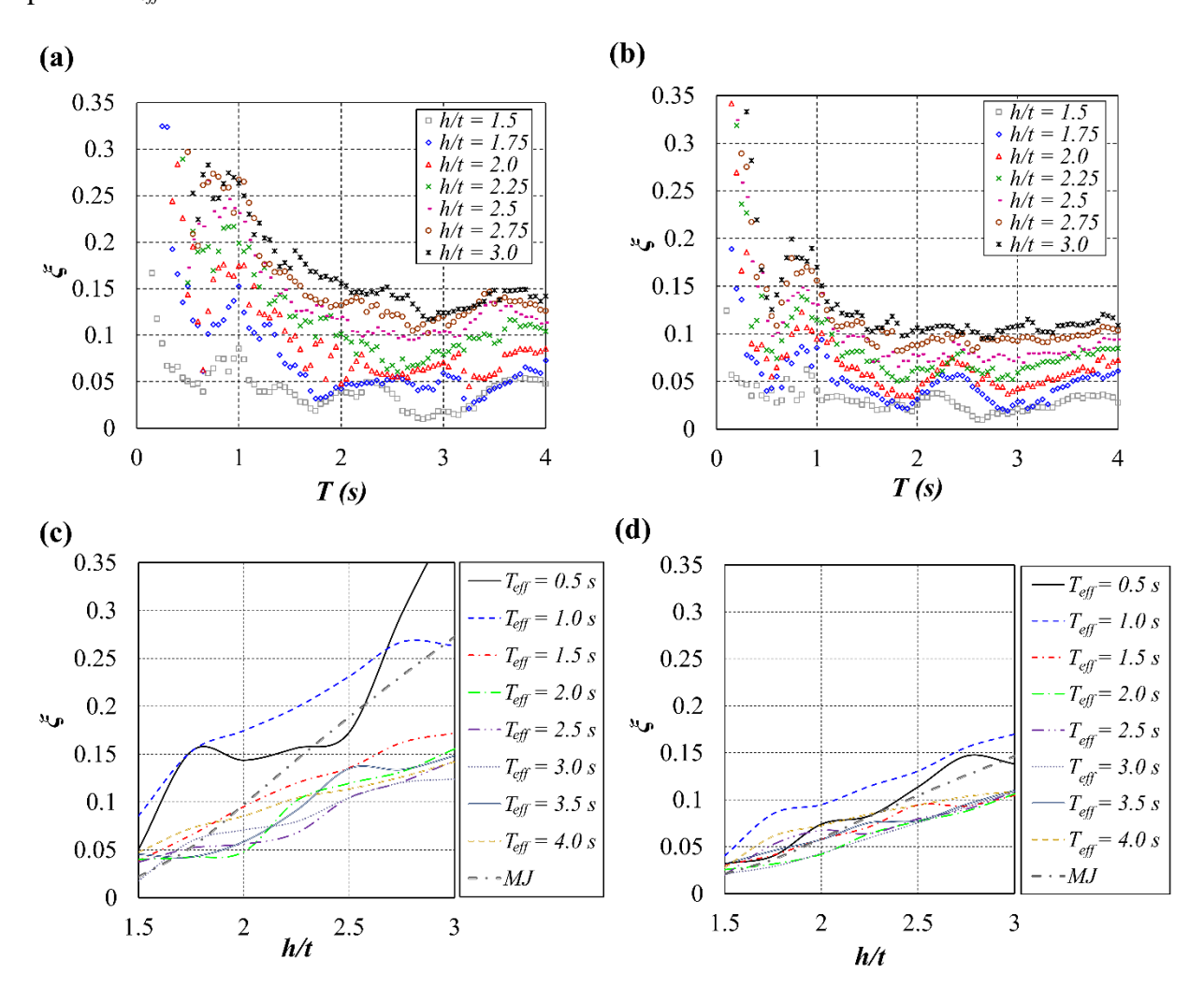


Figure 5.12 Average equivalent viscous damping ratio ( $\xi$ ) with  $T_{eff}$  and h/t for Case 1 [(a) and (c)], and Case 2 [(b) and (d)]

## 5.4.3 Developed expressions for equivalent viscous damping

The resulting equivalent viscous damping ratios from the analysis procedure (Figure 5.12) were used to develop empirical expressions for the EVD ratios ( $\zeta_h$ ) of the idealized hysteretic responses of the MCCD system [see Equation (5.1)]. The data are mainly influenced by height-to-thickness ratio (h/t), the effective structural period ( $T_{eff}$ ), and the force factor of the coupled NYL system ( $\gamma_F$ ). A piecewise linear function was used to develop an expression for  $\zeta_h$  as by Equations

(5.17) to (5.19). The function consists of constant and linear parts that meet at a deviation point,  $T_s$ , along the range of structural period. This point was found to be a function of  $\gamma_F$ . The ideal height-to-thickness ratio,  $(h/t)_n$ , can be calculated using Equation (5.20) based on the values of  $\mu_A$  and  $\beta_F$  of the considered system. For systems with  $n_s = \infty$ ,  $(h/t)_n = h/t$ , while for systems with  $n_s = \infty$ ,  $(h/t)_n < h/t$ .

$$\xi_h = D \left[ 1 + E \left( T_s - T_{eff} \right) \right] \quad \text{for } T_{eff} < T_s \tag{5.17a}$$

$$\xi_h = D \qquad \qquad \text{for } T_{\text{eff}} < T_s \tag{5.17b}$$

$$T_s = -0.5 \, \gamma_F + 2.5 \tag{5.18}$$

$$D = (-0.0188 \gamma_F + 0.0922)(h/t)_n + 0.0215 \gamma - 0.1188$$
(5.19)

$$E = 3.817 (h/t)_n^{-1.422} (5.20)$$

$$(h/t)_n = 0.183 \,\mu_\Delta + 0.768 \,\beta_F + 1.151 \tag{5.21}$$

The developed expression in Equation (5.17) was compared to the expressions proposed in [5,86] for ring-spring response models. Since the ratio h/t does not apply to the expressions in [5,86], the corresponding  $\mu_d$  values to the h/t ratios were set as the basis for the comparison. Figure 5.13 shows the relation between  $\xi_h$  and  $\mu_d$  for  $\gamma$  of 1 and 2. The figure illustrates the conceptual difference in dealing with the MCCD system compared to conventional inelastic systems. It can be seen that at higher values of the  $\mu_d$  the  $\xi_h$  based on the expressions in [5,86] reach a plateau, while the  $\xi_h$  of the MCCD system using the developed expression in Equation (5.17) keeps increasing. This agrees with the trends shown in Figure 5.12(c) and (d). The reason is that increasing  $\mu_d$  results in increasing h/t which in turn increases the force difference factor ( $\beta_F$ ) and hence the area of the dissipated energy. This is shown in Figure 5.5 and Figure 5.8.

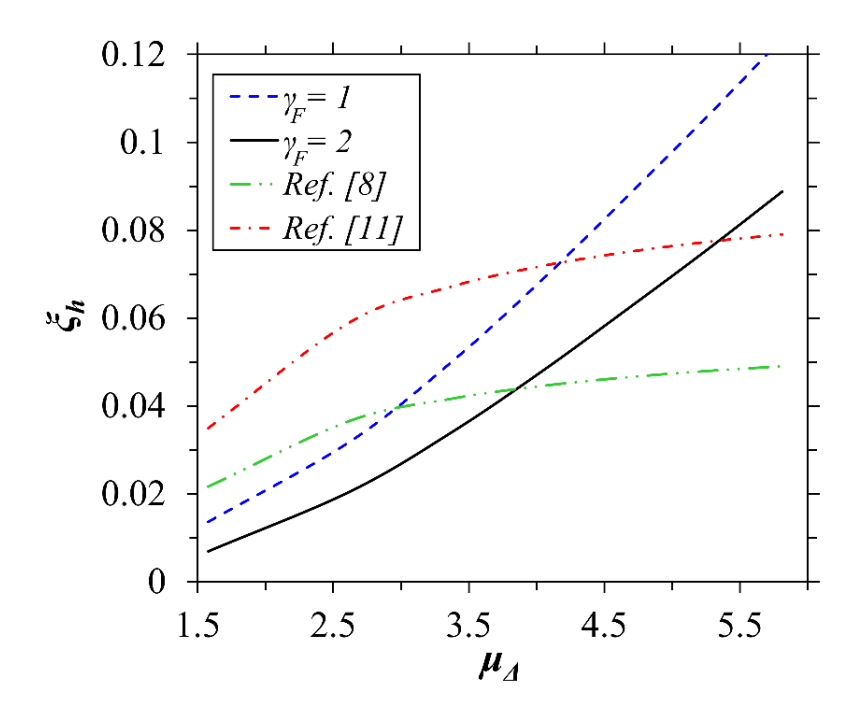


Figure 5.13 Developed expression for EVD compared with other expressions

The linear substitute systems were reanalyzed with damping ratios estimated by the developed expressions. The linear and nonlinear spectral displacements for the considered ground motion records were averaged and grouped based on the values of h/t and the two considered cases. Results are shown in Figure 5.14, from which can be seen that the spectral displacements are in good agreement.

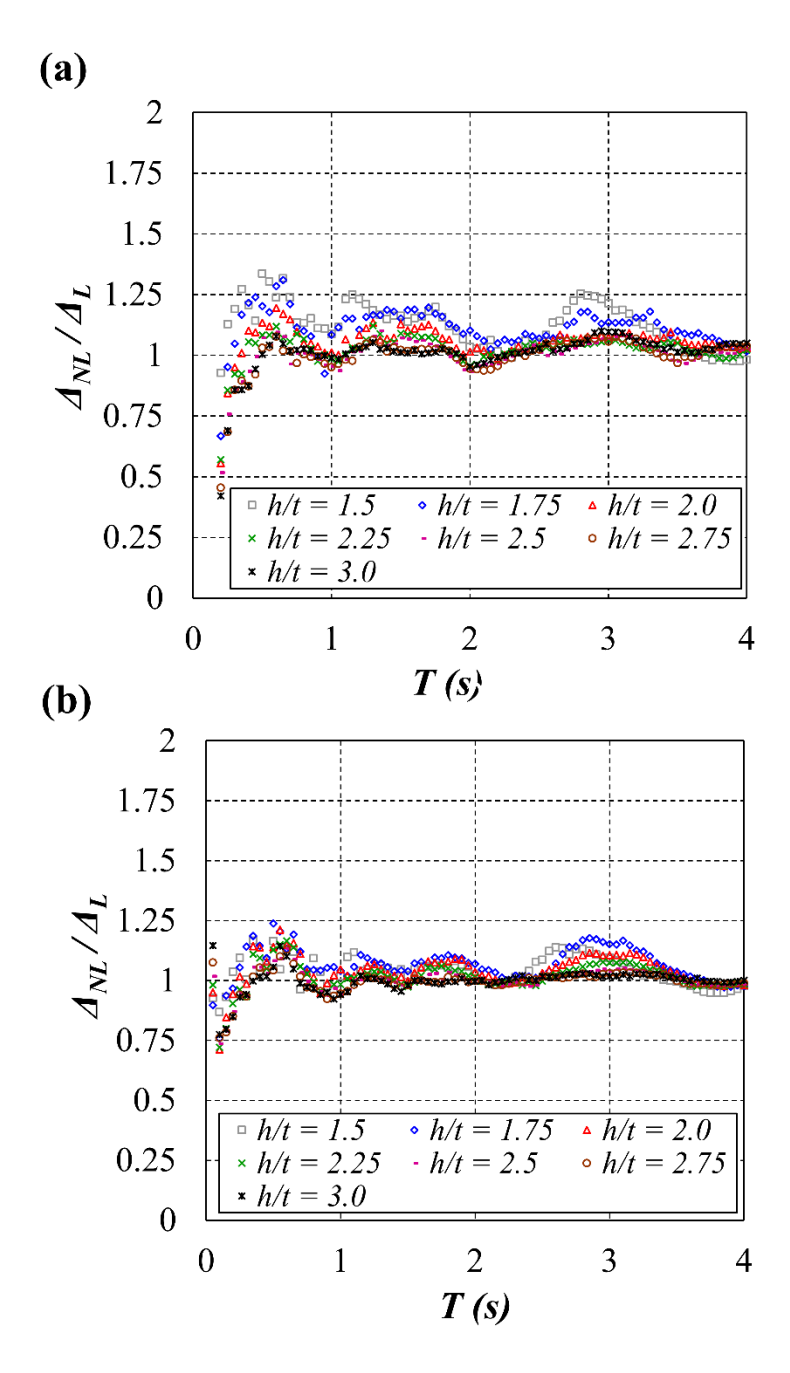


Figure 5.14 Averaged ratio of linear to nonlinear spectral displacements using the developed expression for Case 1 (a) and (b) Case 2,

# 5.5 Conclusions

The hysteretic response of an MCCD system that relies on consecutive snap-through buckling events to dissipate energy was investigated for its equivalent viscous damping. The sawtooth-shape response of the MCCD system was idealized to facilitate dynamic analysis. The

idealization process was based on maintaining energy balance between the original and idealized responses.

The modified Jacobsen's approach was used to initiate the process of determining equivalent viscous damping ratios for the examined hysteretic model. The approach is based on substituting the nonlinear system by a linear system with a secant stiffness at maximum displacement, which agrees with the basic assumptions of the direct displacement-based design method.

Linear and nonlinear time-history analyses were performed on single degree of freedom systems with hysteretic response and linear equivalents, and a systematic analysis procedure was followed to determine corrected equivalent viscous damping ratios for the examined responses. A statistical study was conducted to develop empirical expressions for the idealized hysteretic response of the MCCD system. The following findings of the study were drawn:

- 1. Ratios of nonlinear to linear spectral displacement show that the equivalent viscous damping ratios based on the modified Jacobsen's approach are overestimated. This behavior is more pronounced in intermediate and long period ranges ( $T_{eff} > 0.75$  s). The opposite behavior was observed in the short period range ( $T_{eff} < 0.75$  s).
- 2. The general coefficients of variation of nonlinear to linear spectral displacements were 23% and 11 % for Cases 1 and 2, respectively.
- 3. An expression to estimate the hysteretic equivalent viscous damping ratio was developed. The calculated spectral displacements for the linear substitute systems using the developed expression are in good agreement with the displacements from the analyses of nonlinear systems.

An experimental investigation is being carried out to determine the EVD ratio of the MCCD system for a range of h/t values. Preliminary results show good agreement with the numerical results of this work.

# **CHAPTER SIX**

# **6** Seismic Performance Evaluation

### 6.1 Introduction

This chapter investigates the seismic performance of typical reinforced concrete (RC) structures incorporating the MCCD system in various configurations as the main damping mechanism for seismic protection. Direct displacement-based design and dynamic analysis of three example structures subjected to two historic ground motion records are presented. For each example, nonlinear time-history analyses for the original structure and the modified structure with the MCCD system were performed. The considered systems are (1) a bridge pier-wall, (2) a building frame, and (3) two coupled prestressed rocking walls.

#### **6.2** Seismic Hazards

Two ground motion records were used to evaluate the seismic performance of the example structures. The used records are the El Centro 1940 N00E and the Chile 1985 N10E components, shown in Figure 6.1 with properties as presented in Table 6.1. For each example structure the design was based on the El Centro record. The structure was then subjected to the El Centro and the Chile earthquake records to evaluate its seismic performance. The two records can be roughly considered as a design basis and a maximum considered events [6], respectively.

Table 6.1 Ground motion records used in this study

Date	Record	Magnitude (Ms)	Peak ground acceleration
05/19/1940	El Centro N00E	6.7	0.32 g
03/03/1985	Chile 1985 N10E	7.8	0.71 g

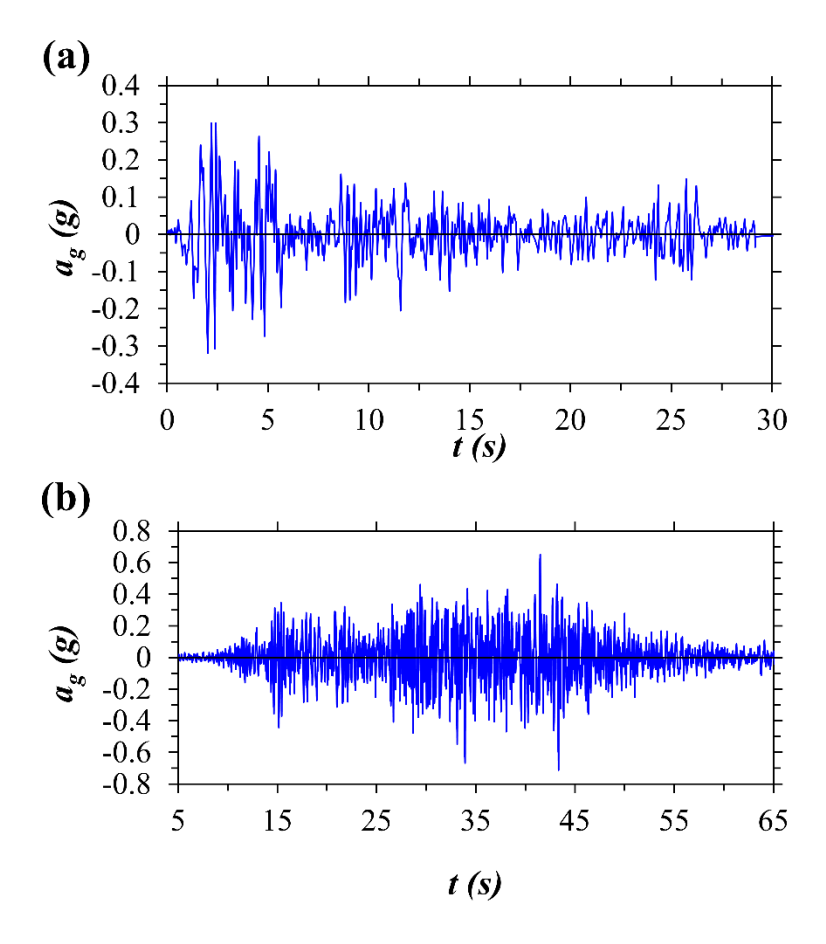


Figure 6.1 Ground acceleration time histories for the earthquake used in the study: (a) 1940 El Centro N00E, and (b) 1985 Chile 1985 N10E

# 6.3 Bridge Pier-Wall

An RC bridge pier-wall with a height,  $h_w$ , of 7000 mm, a length,  $l_w$ , of 3000 mm, and a thickness,  $t_w$ , of 300 mm is considered herein as shown in Figure 6.2(a). The pier-wall is to carry an axial compressive load, P, of 1200 kN, with ratio,  $\gamma_P = 0.056$ , and an effective seismic mass,  $m_e$ , of 214068 kg. The pier-wall was first conventionally designed as a ductile member and then modified with the MCCD [79] and redesigned. Non-linear time-history analyses (NLTHA) were conducted for the two systems to compare the seismic performance under the two ground motion records. Since the nonstructural components are not of concern in this case, the lateral drift,  $\theta_{AV}$ , of the of bridge pier-wall can be as high as 0.04 [5]. Therefore, comparison between the original

and the modified systems is in terms of limiting structural damage. In other words, the aim here is to modify the pier-wall with the MCCD system to avoid permanent inelastic deformations. Nonetheless, the maximum drift should not exceed the code limit ratio of 0.03 [5]. It should be noted that the design and analysis were only carried out about the strong axis of the wall (the transverse direction of the bridge).

The capacity design and detailing requirements of the systems are as per AASHTO LRFD Bridge Design Specifications [103] and AASHTO Guide Specifications for LRFD Seismic Bridge Design [104].

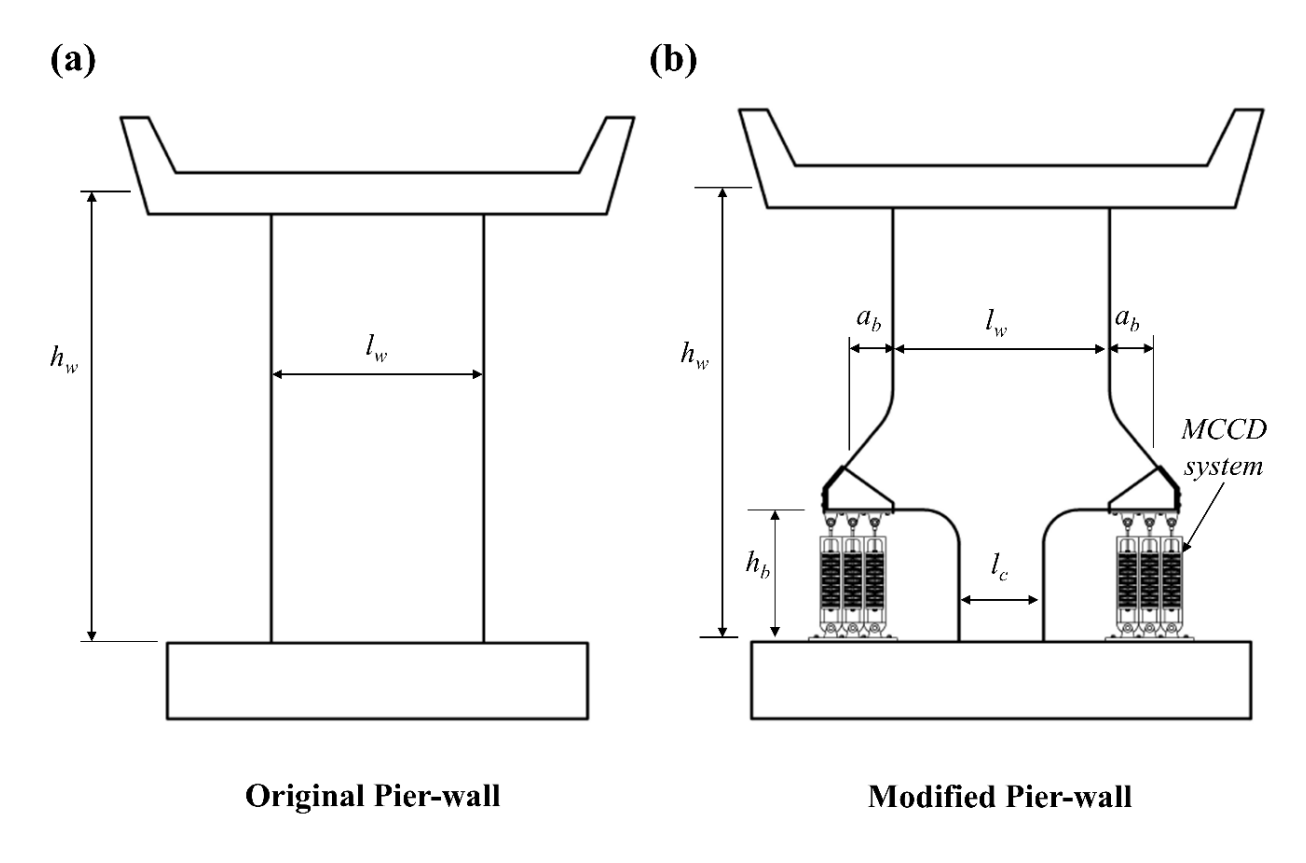


Figure 6.2 Example structure 1: (a) original pier-wall, and (b) modified pier-wall

## **6.3.1** Modified system

The pier-wall is modified by removing the two edge parts at the bottom of the pier-wall and replacing them with the MCCD system as shown in Figure 6.2(b). The remaining middle part

at the bottom the wall, called inner column, is capable of carrying gravity loads, base shear, and uplifting forces (tension). Depending on sectional detailing, the column could have very low lateral stiffness providing the necessary flexibility under seismic demands to deform without yielding. The column could also be detailed as a hinge support.

When the system is loaded laterally, it will rotate in roughly as a rigid body (further discussed below). This rotation causes the MCCD system to be compressed at one side and tensioned at the other side. Thus, the column and the MCCD systems contribute to the lateral stiffness of the modified pier-wall. Upon load removal, the MCCD system will restore its original unreformed shape helping the wall to self-center.

The design objective of the modified system is to prevent permanent deformations and to restore the original configuration upon lateral load removal. To meet this design objective, the system is designed to a maximum displacement that is governed by yield displacement of the column or the maximum allowable drift, whichever is smaller.

### **6.3.2** Material properties

Table 6.2 presents the material properties of the concrete and the reinforcing steel used for the pier-wall and the modified system.

Table 6.2 Properties of concrete and reinforcing steel used for the pier-wall

Property	Value
Specified compressive strength of the concrete	$f_c$ ' = 35 MPa
Specified yield strength of the reinforcing steel bars	$f_{sy} = 420 MPa$
Elastic modulus of the reinforcing steel bars	$E_s = 200 \text{ GPa}$
Yield strain of the reinforcing steel bars	$\varepsilon_{\rm y} = 0.0021$
Diameter of longitudinal reinforcing steel bars	$d_{sl}=15.9~mm$
Diameter of transverse reinforcing steel bars	$d_{st}=12.7~mm$
Concrete cover to the center of first layer of reinforcements	$d_c = 50 mm$

#### 6.3.3 Conventional design of the pier-wall

#### 6.3.3.1 Idealized system

The pier-wall was idealized as a cantilever member with the effective seismic mass lumped at its height  $h_w$  as shown in Figure 6.3(a). The plastic deformation,  $\Delta_{vp}$ , is considered to be concentrated in the plastic hinge region at bottom end of the pier-wall. Additional details about the bridge configuration, pier-wall connection to superstructure, and the idealized system can be found in [105].

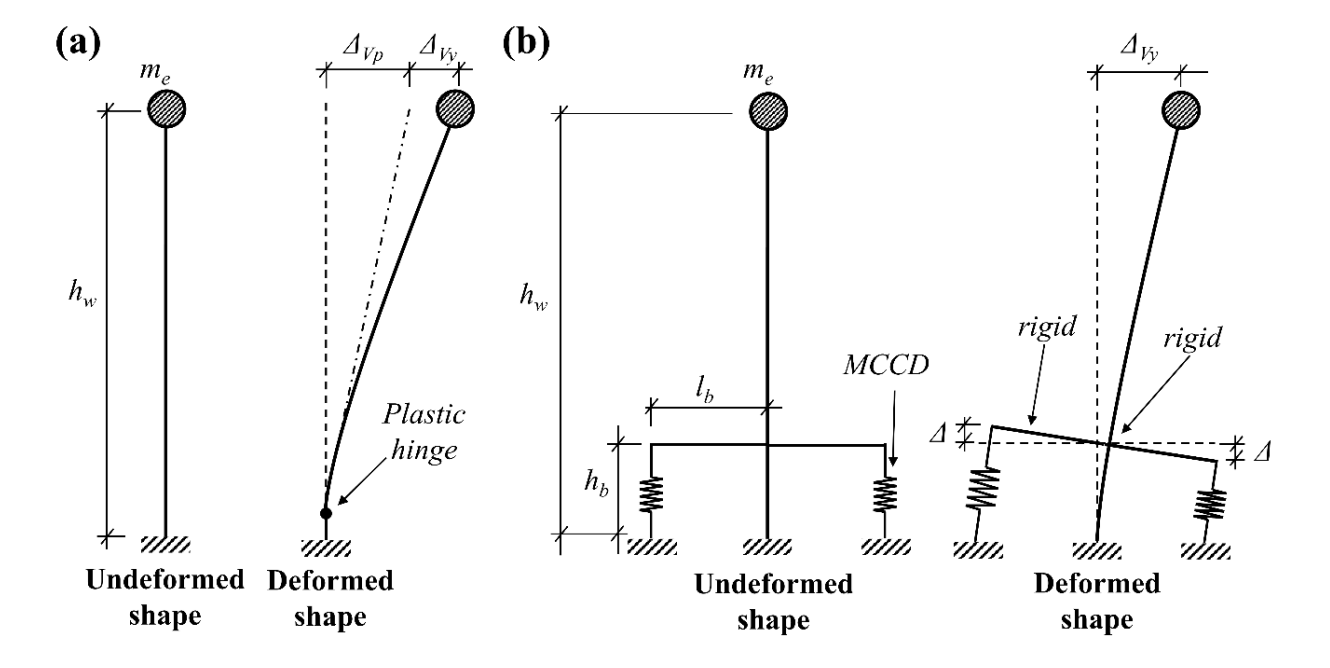


Figure 6.3 System idealization for analysis: (a) original pier-wall, and (b) modified pier-wall 6.3.3.2 <u>Design</u>

The direct displacement-based design (DDBD) method was used estimate seismic demands. First the ideal yield curvature,  $\varphi_y$ , and displacement,  $\Delta_y$ , were estimated as follow [5]:

$$\varphi_y = 2 \varepsilon_y / l_w = 1.4 1/km$$

$$\Delta_y = \varphi_y h_w^2 / 3 = 22.87 mm$$

A demand displacement ductility,  $\mu_D$ , value of 3.5 was determined based on the proposed prespecified displacement values in [105] for a wall with aspect ratio,  $AR = l_w / t_w$ , of 10 and slenderness ratio,  $SR = h_w / l_w$ , of 2.34. The design displacement,  $\Delta_D$ , was thus calculated as:

$$\Delta_D = \mu_D \Delta_y = 80.1 \text{ mm}$$

The equivalent viscus damping ratio,  $\xi$ , which consists of the elastic,  $\xi_e$ , and the hysteresis,  $\xi_h$ , parts, was estimated as follows [5]:

$$\xi = \xi_e + \xi_h = 0.05 + 0.444 \left(\frac{\mu_D - 1}{\mu_D \pi}\right) = 0.05 + 0.101 = 0.151$$

The effective structural period,  $T_e$ , was determined by performing linear displacement spectral analysis with damping ratio as estimated above. The displacement response spectrum is shown in Figure 6.4.  $T_e$  was found to be 1.617 s. The base shear,  $V_e$ , and bending moment,  $M_e$ , were calculated as follows:

$$V_e = 4 \Delta_D \pi^2 m_e / T_e = 258.7 \text{ kN}$$

$$M_e = V_e h_w = 1810.8 \text{ kN.m}$$

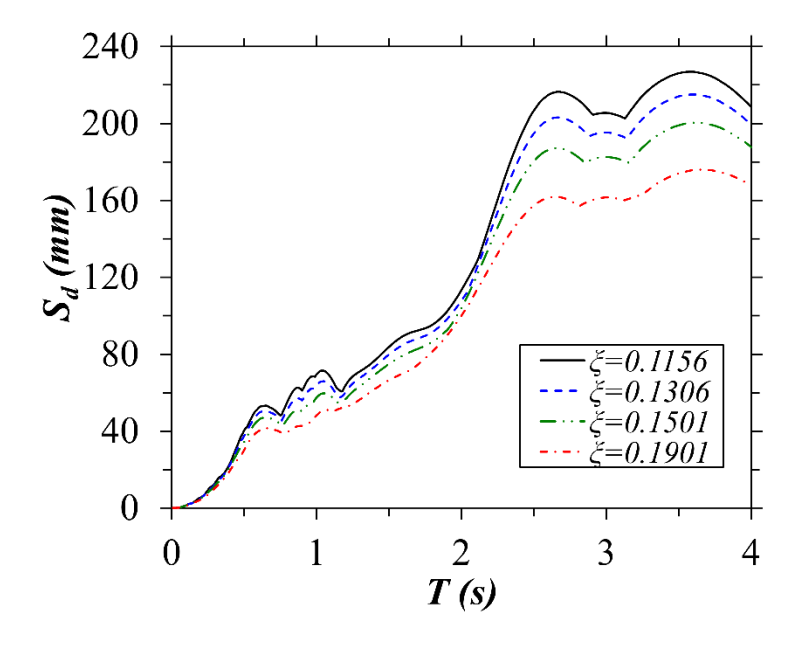


Figure 6.4 Displacement response spectrum of the 1940 El Centro ground motion record used for the design

Based on the moment  $M_e$  and the capacity design requirements as per the AASHTO LRFD specifications [103,104] the pier-wall was designed for flexure and shear with sectional properties as shown in Figure 6.5(a). Figure 6.6(a) shows the force-displacement curves for the designed pier-wall with the specified material properties calculated following plastic hinge analysis procedure detailed in the Appendix [105]. The figure also shows shear strength capacity curves based on the model proposed by Priestley and Paulay [4] for web crushing.

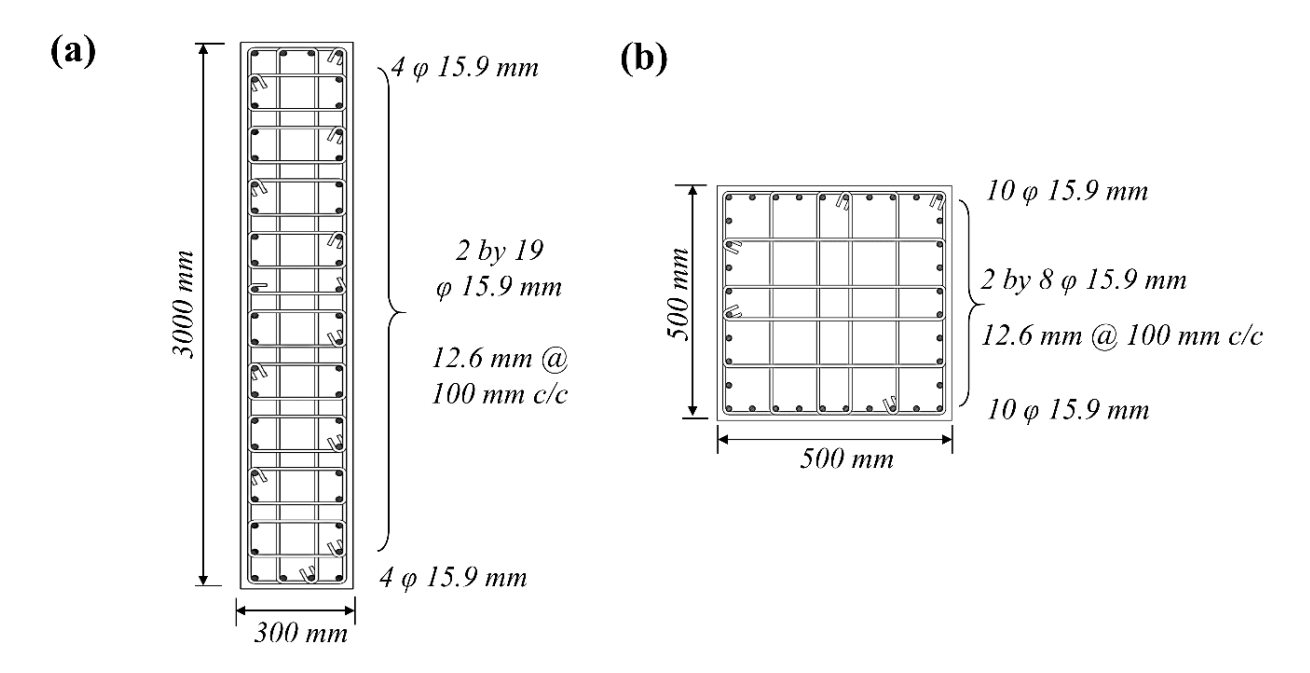


Figure 6.5 Cross-sectional details: (a) original pier-wall, and (b) modified pier-wall

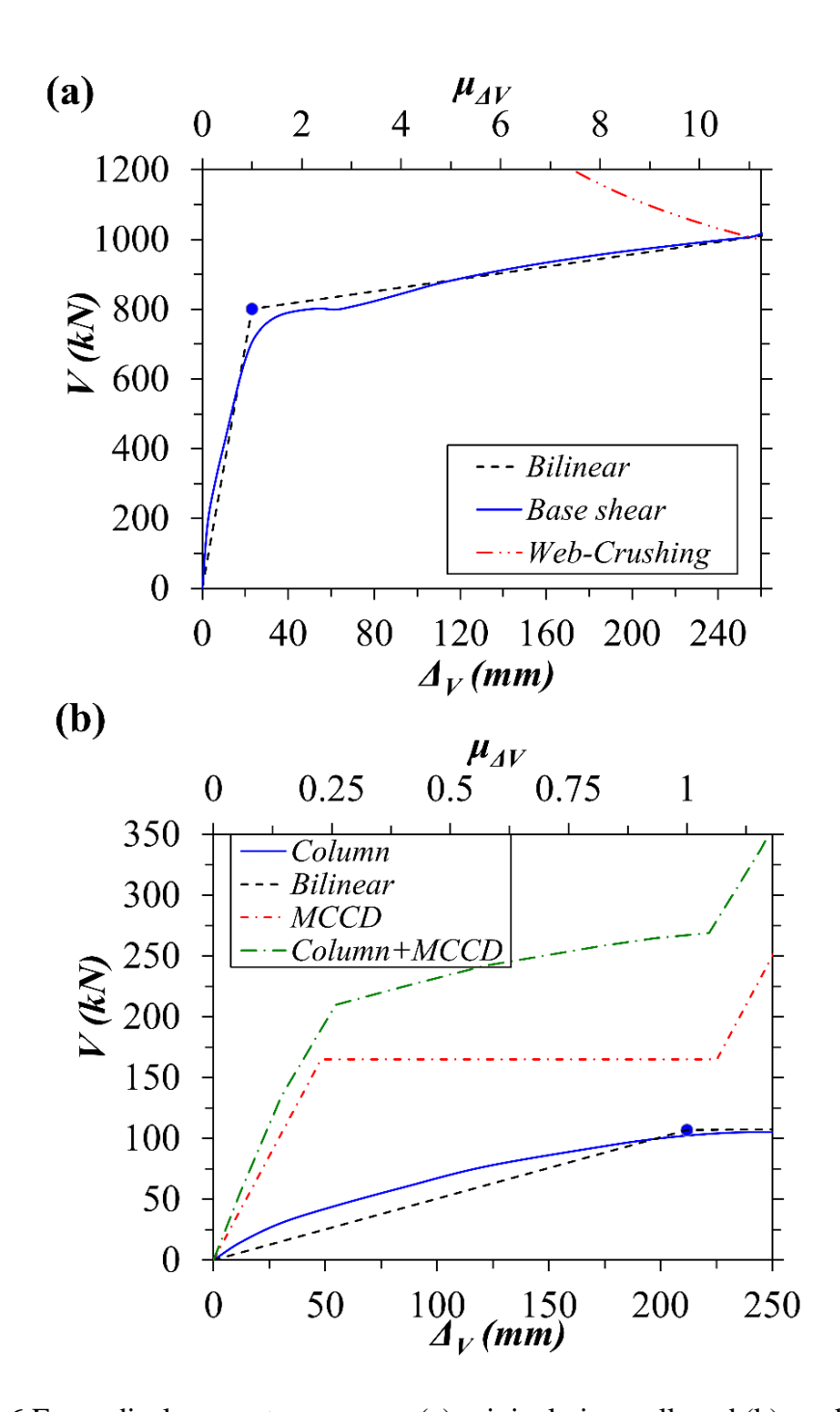


Figure 6.6 Force-displacement responses: (a) original pier-wall, and (b) modified pier-wall

# 6.3.4 Design of the modified pier-wall

#### 6.3.4.1 <u>Idealized system</u>

Figure 6.3(b) shows the idealized system for the modified pier-wall with the MCCD system. In this idealization, the MCCD system at each side of the pier-wall are represented by

axial spring elements with flag-shaped response that are located at a horizontal lever arm distance,  $l_b$ , from the mid-length of the pier-wall as given in Equation (6.1). The location of the MCCD system are moved further from the edges of the pier-wall by a distance,  $a_b$ , of 700 mm (see Figure 6.2). This increases  $l_b$ , which in turn increases axial displacement demands on the MCCD system and results in a higher lateral shear force,  $V_b$ , carried by the MCCD system for a given axial force,  $F_b$ , as given in the equilibrium Equation (6.2) below. This leads to a reduction in the demand forces on the MCCD system ( $F_b$ ).

$$l_b = l_w / 2 + a_b \tag{6.1}$$

$$V_b = F_b \, I_b \, / \, h_w \tag{6.2}$$

Equation (6.2) is, however, not accurate since the modified system does not deform in a rigid body rotation and hence the actual relation between  $V_b$  and  $F_b$  is based on the deformations of the inner column. With reference to Figure 6.3(b) the relation between the top lateral displacement,  $\Delta_V$ , and the axial vertical displacement,  $\Delta$ , on the MCCD systems due to a lateral shear force, V, can be established based on the expression for transverse flexure deformations in a cantilever member as given in Equation (6.3) [106]:

$$\Delta_V(x) = V(3h_W x^2 - x^3) / (6EI) \tag{6.3}$$

where x is a distance along the height of pier-wall from the bottom. The term  $V/(E\ I)$  can be determined from the sectional curvature,  $\varphi$ , and top displacement,  $\Delta v$ , of the inner column as follows:

$$\Delta_V = V h_{w^3} / (3 E I) = \varphi h_{w^2} / 3 \tag{6.4}$$

$$Vh_{\scriptscriptstyle W}/(EI) = \varphi/h_{\scriptscriptstyle W} \tag{6.5}$$

Thus, Equation (6.3) can be rewritten as follows:

$$\Delta_V(x) = \varphi (3x^2 - x^3 / h_w) / 6 \tag{6.6}$$

By taking the first derivative of  $\Delta_V(x)$  with respect to x, the slope of the tangent line,  $m_t$ , at  $x = h_b$ , where  $h_b$  is height of the MCCD system [see Figure 6.3(b)], is determined as follows:

$$m_t = \Delta_V'(x) = \varphi (6x - 3x^2/h_w)/6$$
 (6.7)

The slope of the perpendicular line,  $m_p$ , is determined as  $-1/m_t$ . Thus, this slope is used to calculate the displacement on the MCCD system ( $\Delta$ ) at a distance  $l_b$  from mid-length of the pier-wall ( $l_w/2$ ) at a lateral displacement ( $\Delta_V$ ) for values of curvature  $\varphi$  from 0 to the ideal yield curvature of the column,  $\varphi_y$ . The relation between the ratio  $\theta_F = \Delta / \Delta_V$  and  $\varphi$  was found to be constant for a given  $l_b$  and  $l_b$  lengths with value of 0.3018 for  $l_b = 2200$  mm, and  $l_b = 2800$  mm, as shown in Figure 6.7. The figure shows  $\theta_F$  for a range of  $l_b$  and  $l_b$  values. The ratio of  $l_b$  can thus be used to calculate the force demands of the MCCD system as follows:

$$V_b = \theta_F F_b \tag{6.8}$$

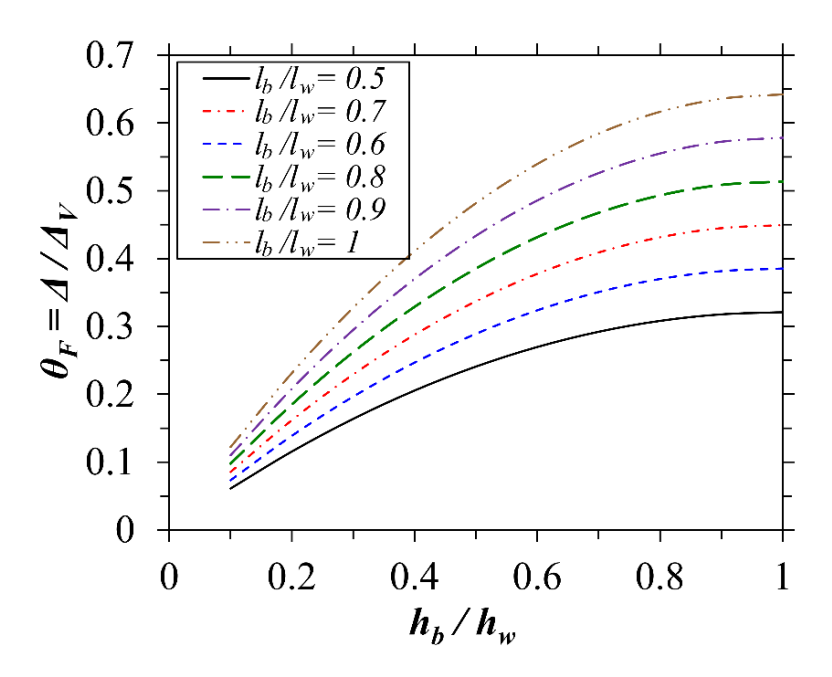


Figure 6.7 Relation between the lateral ( $\Delta v$ ) and axial ( $\Delta$ ) displacements with lengths  $h_b$  and  $l_b$ 

#### 6.3.4.2 Design of the inner column

The first step in the design of the modified system is to design the inner column to have adequate elastic displacement under maximum lateral loading. Therefore, it must have high flexibility and thus lower lateral capacity compared to the conventional pier-wall. The design of this element is similar to the design of any reinforced concrete column to seismic loading in addition to satisfying elastic displacement demands. To facilitate the design, a few assumptions were followed for the sizing and the reinforcing of the column as follows:

1. The cross-section dimensions of the inner column are determined based on that the axial load ratio ( $\gamma_P$ ), expressed in Equation (6.9), is not greater than the code specified vale of 0.2 [104].

$$\gamma = P / (f_c t_c l_c) \le 0.2 \tag{6.9}$$

2. The ability to carry gravity loads, base shear, and uplifting forces (tension).

A square section with side length,  $t_c$ , of 500 mm and reinforcement ratio,  $\rho$ , of 2.85% were used for the column section as shown in Figure 6.5(b). The column was designed for shear as per capacity design requirements in [103]. The force-displacement response of the column was calculated following plastic hinge analysis procedure presented in [105] is shown in Figure 6.6(b). It should be mentioned that shear design of the inner column was based on the shear force determined based on capacity design principles plus the additional shear forces developed due to the MCCD system [Column + MCCD in Figure 6.6(b)]. The ideal yield curvature and displacement, nominal bending moment, and the capacity shear force were calculated from the section properties of the column as follows, respectively:

$$\varphi_{\rm V} = 12.5 \; 1/{\rm km}$$

$$\Delta_v = 211 \text{ mm}$$

$$M_n = 747.7 \, kN.m$$

$$V_n = 1017 \, kN$$

### 6.3.4.3 Design of the MCCD system

The yield displacement of the column ( $\Delta_y$ ) represents the ultimate design displacement ( $\Delta_D$ ) for the modified system. Assuming an MCCD system with properties determined according to the study in Chapter 5 [82] and Table 6.3, the equivalent viscus damping ( $\xi$ ) can be determined by the proposed expression in Equation (5.17) [82] assuming  $T_{eff} > T_s$  as follows:

$$\xi = \xi_e + \xi_h = (-0.0188\gamma + 0.0922)(h/t)_n + 0.0215\gamma - 0.1188 = 0.05 + 0.0557 = 0.1057$$

Table 6.3 Properties of the MCCD system for the modified pier-wall

Property	Value
Height-to-thickness ratio of the CCD in the system	h/t = 2.5
Number of connected CCDs in series	$n_s = 12$
Force ratio of the difference	$\beta_F = 0.5586$
Displacement ductility of the MCCD system	$\mu_{\Delta} = 4.6676$
Force ratio factor	$\gamma_F = 1.649$
Ideal height-to-thickness ratio of the CCD in the system	$(h/t)_n = 2.4341$

The effective structural period for the system ( $T_{eff}$ ) was determined from the displacement spectrum shown in Figure 6.4.  $T_e$  was found to be 2.57 s resulting in a base shear  $V_e = 271$  kN. The shear force carried by the MCCD systems ( $V_b$ ) was calculated as follows:

$$V_b = V_e - M_n / h_w = 164 \text{ kN}$$

The axial force acting on one of the MCCD systems due to  $V_b$  can be determined using the ratio  $\theta_F$ . With reference to the idealized system shown in Figure 6.3(b), the axial force demand  $F_b$  on one MCCD system was determined as follows:

$$F_b = V_b / (2 \theta_F) = 272 \, kN$$

To carry this load ( $F_b$ ), an MCCD system with units made of carbon fiber composites with an elastic modulus of 300 GPa was used. The CCD units have thickness, t, of 1.2 mm, height, h,

of 3 mm, and length, l, of 100 mm with ideal buckling force,  $F_b$ ' of 3.8 kN. The MCCD system consists of 3 by 6 vertical chains of CCDs with total number of chains,  $n_c$ , of 18 in each side of the wall. Each chain has 12 serially connected units ( $n_s = 12$ ) of 4 parallel units ( $n_p = 4$ ), as shown in Figure 6.8(a). The system results in an axial force capacity of 273.6 kN as determined below. The actual and idealized force-displacement response of the MCCD system as per Chapter 4 [79] and Chapter 5 [82] is shown in Figure 6.8(b). Note that the system in Figure 6.8(a) is capable of carrying global compressive and tensile forces that cause the CCD units in the system to compress in the both cases. The response of the modified pier-wall system is shown in Figure 6.6(b). Although the  $F_b$ ' value of 3.8 kN may seem large, it has a moderate value when compared with other structural units. To put this in perspective, the value of 3.8 kN is smaller than that developed by a steel rod with 3.4 mm diameter.

$$F_b = F_b' n_p n_c = 273.6 \text{ kN}$$

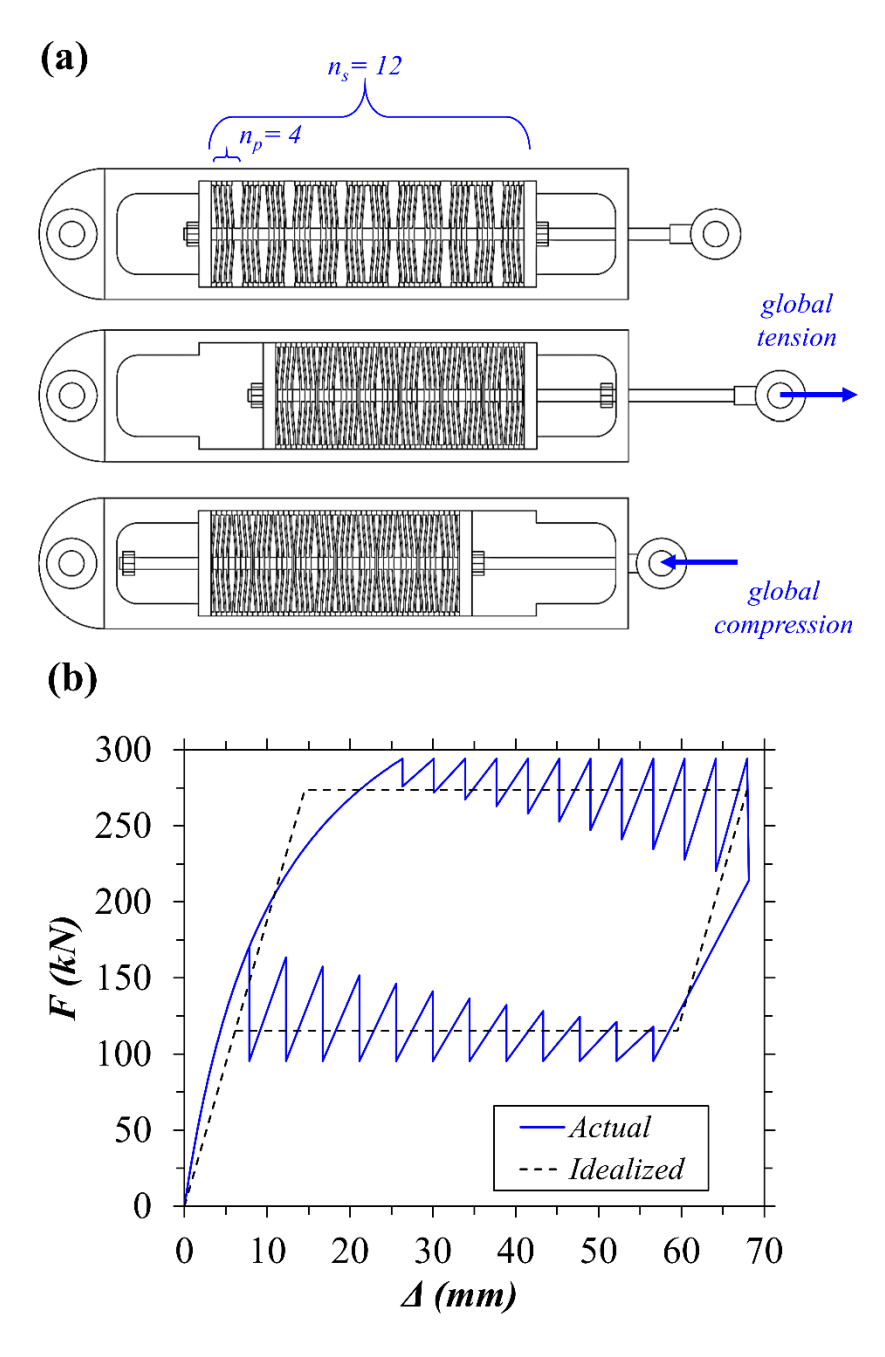


Figure 6.8 (a) Loading mechanism for one chain of the CCD units, and (b) force-displacement response of the MCCD system

## **6.3.5** Time-history analysis

Non-linear time-history analyses (NLTHA) were performed for the two designed systems using OpenSees [107] under two ground motion records of El Centro 1940 and Chile 1985 earthquakes. The MCCD system was modeled using the self-centering flag-shaped material object.

Figure 6.9 shows the lateral displacement time-history response for the original and modified pierwall systems. Although, the modified system showed higher maximum displacement in both cases with 113 mm and 156 mm than the original pier-wall with 91 mm and 105 mm, respectively, it is still less than the design displacement ( $\Delta_y$ ) of 211 mm. It should be mentioned that the reference wall was designed for a much lower design displacement of 81 mm. Therefore, the modified pierwall with the MCCD system satisfied the design demands and did not exceed the yield point of the inner column (156 < 211 mm), which means that no damage occurred. Figure 6.10 shows the resulting hysteretic shear force-lateral displacement responses of both systems for the two ground motion records. It can be seen that the dissipated energy by the inelastic action from the response of the pier wall in Figure 6.10(a) and (c) is larger than that by the modified system in Figure 6.10(b) and (d). However, in the latter case no permanent damage is observed; while for the conventional pier-wall permanent displacements of 10 mm and 24 mm were predicted for the El Centro and Chile records, respectively.

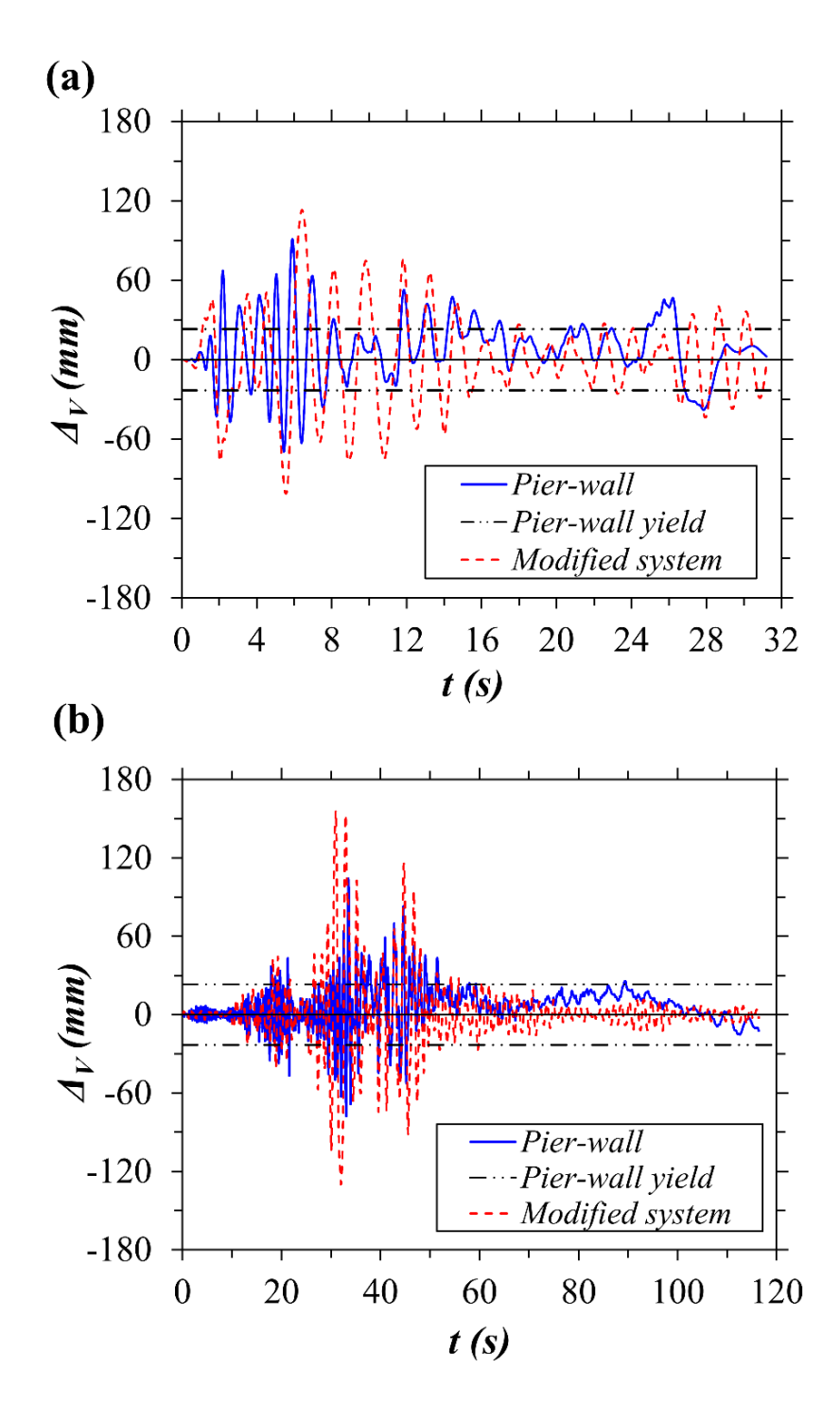


Figure 6.9 Lateral displacement time-history of the bridge pier-walls: (a) 1940 El Centro, and (b) 1985 Chile earthquakes

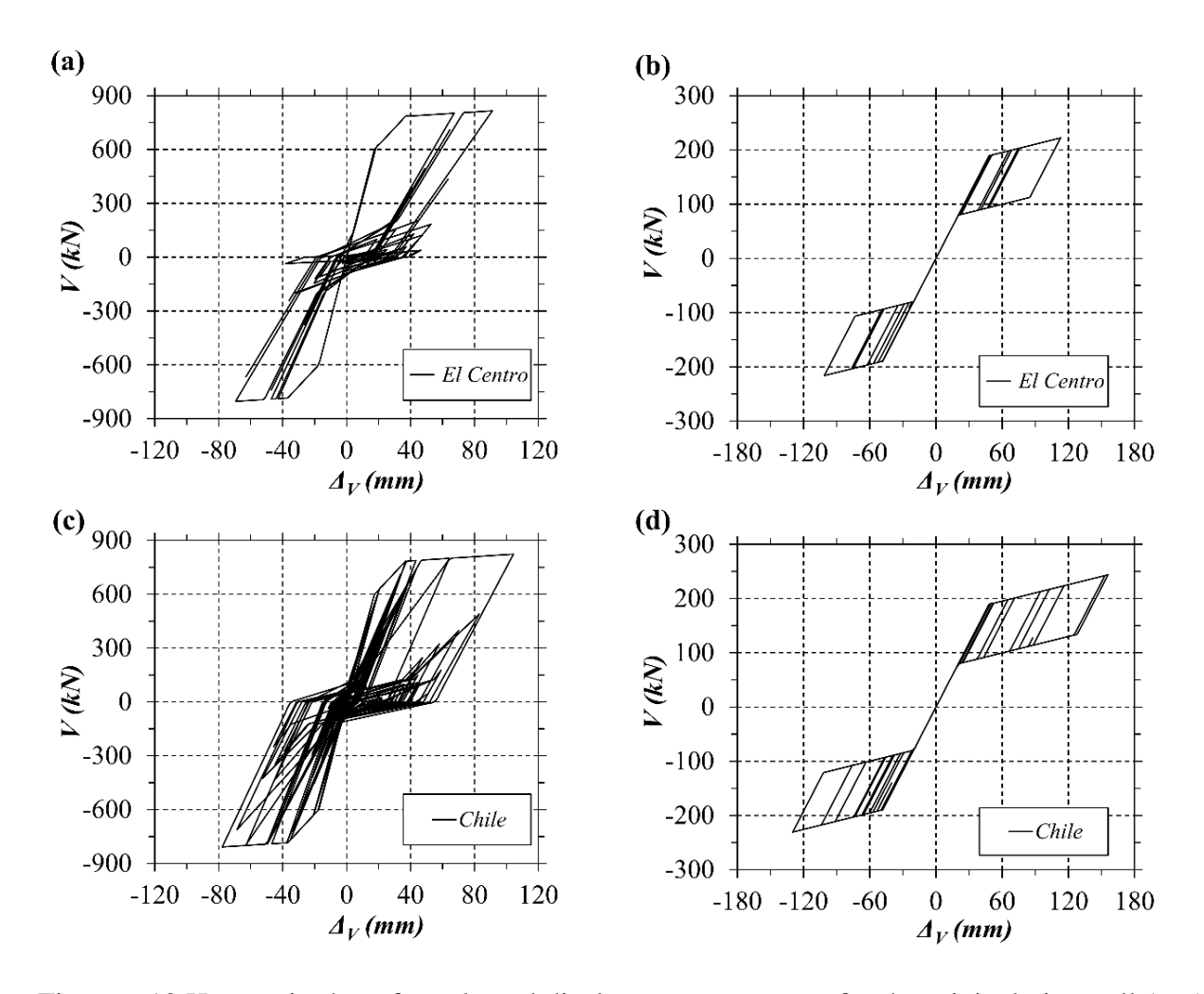


Figure 6.10 Hysteretic shear force-lateral displacement responses for the original pier-wall (a, c), and the modified pier-wall (b, d)

# **6.4** Building Frame

The second example structure is a one-story one-bay RC frame shown in Figure 6.11(a). The frame has two rectangular columns with height,  $h_c$ , of 4000 mm and cross-sectional length,  $l_c$ , and thickness,  $t_c$ , of 400 mm and 250 mm, respectively. The two columns are connected by a beam with length,  $l_g$ , of 6400 mm, cross-sectional height,  $h_g$ , 400 mm, and thickness,  $t_g$ , of 250 mm. The frame was designed for an effective mass  $m_e = 18838 \, kg$  determined from a tributary area of 5000 mm width. The axial force and ratio on the columns are  $P = 93 \, kN$  and  $\gamma_P = 0.264$ . The frame was first conventionally designed as a ductile member and then modified with the MCCD system and

redesigned. Similar to the pier-wall, the aim was to limit the columns' deformation to the elastic range of response. The design and analysis were only carried out in the in-plane direction of the frame.

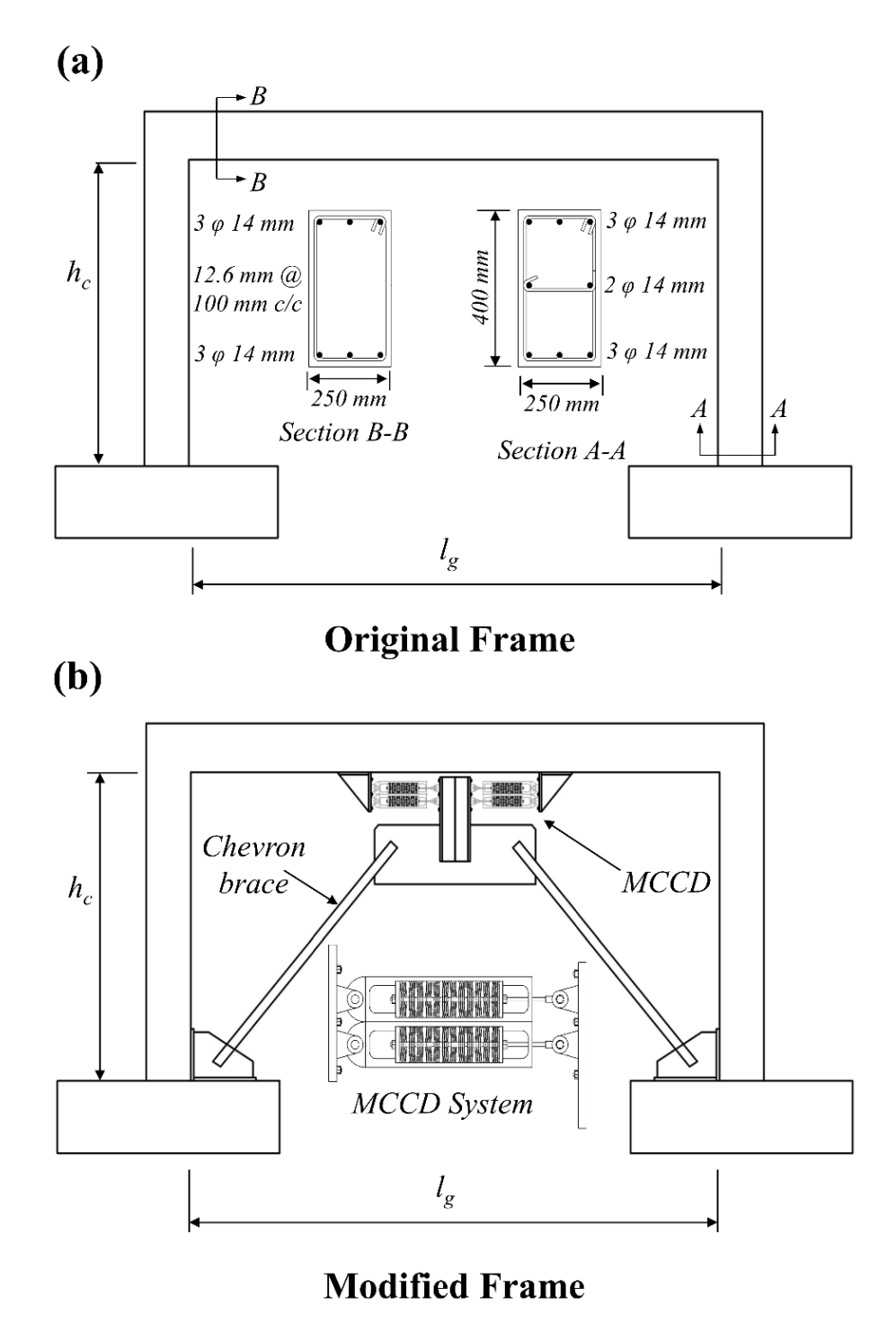


Figure 6.11 Example structure 2: (a) original frame, and (b) modified frame with chevron brace

### 6.4.1 Modified system

The frame was modified by adding a rigid chevron brace that is connected to the beam by an MCCD system as shown in Figure 6.11(b). Since the frame is supporting the floor at the frame height level, it is assumed that the beam is axially rigid. When the system is loaded laterally the beam will displace and activate the MCCD system. The design objective is to prevent permanent deformations and restore the original configuration upon lateral load removal. Therefore, the system design displacement is governed by yield displacement of the columns or the maximum allowable drift, whichever is smaller. The material properties of concrete and reinforcing steel are the same to those presented in Table 6.2 for the pier-wall.

### **6.4.2** Conventional design of the frame

### 6.4.2.1 <u>Idealized system</u>

The columns were assumed to be fixed at the bottom and rigidly connected to the beam at the top. The effective seismic mass was assumed to lumped at beam level. It was also assumed that the plastic deformations are concentrated in plastic hinges at the ends of the columns the beam as shown in Figure 6.12(a). To determine the lateral stiffness of the system,  $k_A$ , the stiffness method was used to construct the stiffness matrix of the system as discussed in the Appendix. An equation to determine  $k_A$  in terms of the beam-to-column stiffness ratio,  $\rho_F$  is given below [89].

$$k_{\Delta} = 12 E_c I_c (6 \rho_F + 1) / (3 \rho_F + 2)$$
 (6.10)

$$\rho_F = (E_g I_g / I_g) / (E_c I_c / h_c) \tag{6.11}$$

where  $E_g$  and  $E_c$  are the elastic moduli of the beam and the column, respectively,  $I_g$  and  $I_c$  are the second moments of area of the beam and the columns, respectively. The values of  $E_gI_g$  and  $E_cI_c$  can be determined based on the ideal yield curvatures and moments of the beam,  $M_g/\varphi_{gy}$  and the column,  $M_c/\varphi_{cy}$ , respectively.

The frame can also be idealized as single degree of freedom (SDF) system, as shown in Figure 6.12(a), by modifying the height of the cantilever using  $k_{\perp}$  as given in Equation (6.12). This idealization can only be used to design the frame using the DDBD method and to calculate the lateral response of the frame.

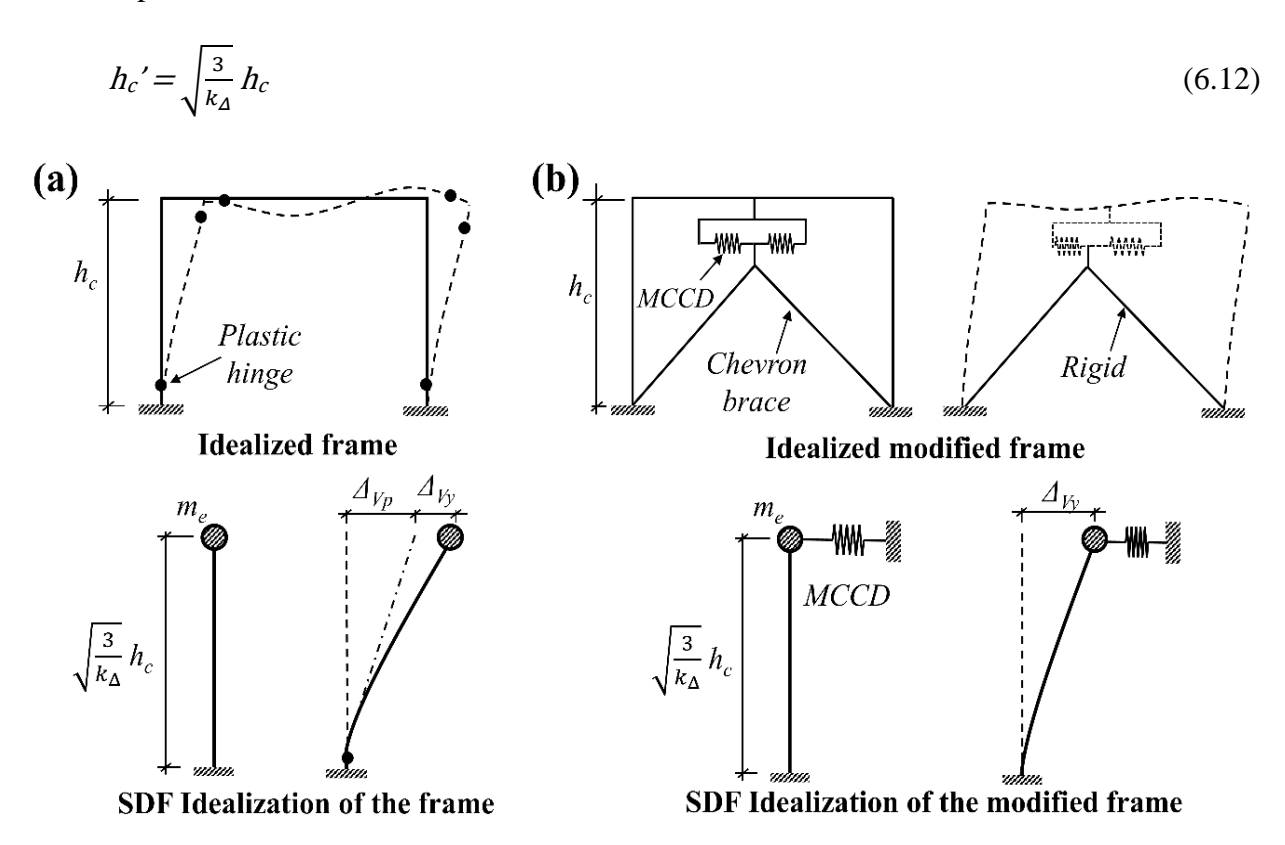


Figure 6.12 System idealization for analysis: (a) original frame, and (b) modified frame

### 6.4.2.2 Design

The DDBD method was used estimate seismic demands. First the ideal yield curvature,  $\varphi_y$ , and displacement,  $\Delta_y$ , were estimated as follow [5]:

$$\varphi_y = 2.3 \, \varepsilon_y / l_w = 1.15 \, 1/km$$

$$\Delta_y = \varphi_y h_w 2 / k_\Delta = 27.8 \, mm$$

A demand displacement ductility ( $\mu_D$ ) value of 5 was determined based on the proposed prespecified displacement values in [105] for a column with AR = 1.6 and SR = 10.5. The design displacement ( $\Delta_D$ ), is thus determined as follows:

$$\Delta_D = \mu_D \Delta_V = 139 \text{ mm}$$

Since this displacement results in a lateral drift ( $\theta_{\Delta V}$ ) that is greater than 3%, the  $\Delta_D$  was determined based on  $\theta_{\Delta V} = 3\%$ :

$$\Delta_D = \theta_{\Delta V} h_c = 126 \text{ mm}$$

The demand  $\mu_D$  was recalculated based on the used  $\Delta_D$  as follows:

$$\mu_D = \Delta_D / \Delta_V = 4.532$$

The equivalent viscus damping ( $\xi$ ) using the proposed expression for RC frames in [5] leads to:

$$\xi = \xi_e + \xi_h = 0.05 + 0.565 \left(\frac{\mu_D - 1}{\mu_D \pi}\right) = 0.05 + 0.1401 = 0.1901$$

The effective structural period  $(T_e)$  was determined from the linear displacement response spectrum for the damping ratio as estimated above. The displacement spectrum is shown in Figure 6.4.  $T_e$  was found to be 2.19 s. The base shear  $(V_e)$  was calculated as follows:

$$V_e = 4 \Delta_D \pi 2 m_e / T_e = 19.6 \text{ kN}$$

The bending moment demands at the column bases and at the beam ends were determined using the constructed stiffness matrix and the fixed-end moments (see the Appendix). The resulting moment due to the effective design force in the columns and the beam were 24.8 kN.m and 10 kN.m, respectively. Based on these moments and the capacity design requirements as per ACI 318-11 [108] the columns and the beam were designed with sectional properties as shown in Figure 6.11(a). Figure 6.13(a) shows the frame's force-displacement response curve for the specified material properties calculated following the plastic hinge analysis procedure presented in [105].

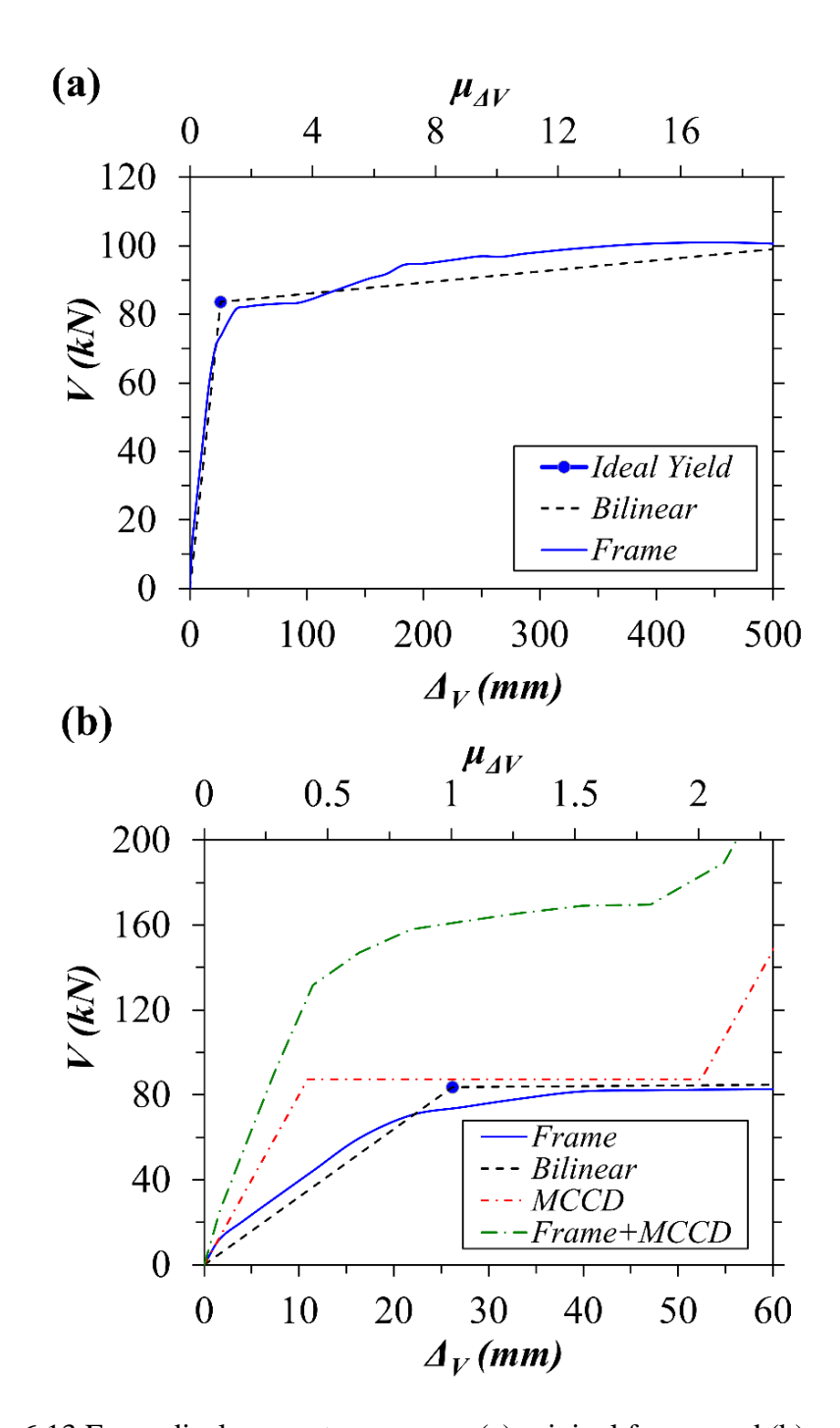


Figure 6.13 Force-displacement responses: (a) original frame, and (b) modified frame

# 6.4.3 Design of the modified frame

### 6.4.3.1 <u>Idealized system</u>

Figure 6.12(b) shows the idealized system for the modified frame with the chevron brace. In this idealization, the MCCD system is represented by two axial spring elements with flag-shaped

response that are parallelly connected to the beam. The location of the MCCD system in this case is the most efficient since the MCCD system is directly resisting induced lateral loads transmitted through the beam. This eliminates the reduction in the lateral forces produced by the MCCD system due to the lever arm effect. It also eliminates the reduction in the imposed demand displacements to efficiently activate the MCCD system

### 6.4.3.2 Design of the MCCD system

The yield displacement  $\Delta_y = 26.2 \ mm$  of the frame determined from the plastic hinge analysis as shown in Figure 6.13(a) was considered as the ultimate design displacement ( $\Delta_D$ ) for the modified system. Assuming an MCCD system with properties determined as presented in Chapter 5 [82] and Table 6.4, the equivalent viscus damping ( $\zeta$ ) was determined in an iterative process using the proposed expression in Equation (5.17) [82] assuming  $T_{eff} < T_s$  as given below.

$$D = (-0.0188\gamma + 0.0922)(h/t)_n + 0.0215\gamma - 0.1188 = 0.06054$$

$$E = 3.817 (h/t)_n - 1.422 = 1.0507$$

$$\xi_h = D [1 + E (T_s - T_{eff})] = 0.1306$$

$$T_s = -0.5 \gamma_F + 2.5 = 1.521$$

$$\xi = \xi_e + \xi_h = 0.05 + 0.1306 = 0.1806$$

Table 6.4 Properties of the MCCD system for the modified frame

Property	Value
Height-to-thickness ratio of the CCD in the system	h/t = 2.545
Number of connected CCDs in series	$n_{s} = 10$
Force ratio of the difference	$\beta_F = 0.5814$
Displacement ductility of the MCCD system	$\mu_{\Delta} = 4.807$
Force ratio factor	$\gamma_F = 1.956$
Ideal height-to-thickness ratio of the CCD in the system	$(h/t)_n = 2.477$

The effective structural period for the system ( $T_{eff}$ ) was determined from the displacement spectrum shown in Figure 6.4.  $T_e$  was found to be 0.42 s resulting in a base shear  $V_e = 111 \text{ kN}$ . The

shear force carried by the MCCD systems was calculated by subtracting the force carried by the frame at yield  $V_n = 84 \text{ kN}$  as follows:

$$V_b = V_e - V_n = 27 \, kN$$

Since  $V_b$  is much lower than  $V_n$ , the MCCD system was designed for a higher force to ensure effective energy dissipation. This is because if a smaller value was used the energy dissipation capacity of the combined system will not be significant. Therefore, the MCCD system was designed for  $V_b = V_n$ .

In the case of chevron brace,  $V_b = F_b$  because the lateral force is directly transmitted to the MCCD system. To carry this load  $(F_b)$ , an MCCD system with units made of carbon fiber composites with elastic modulus of 300 GPa was used. The CCD units have  $t = 1.1 \, mm$ ,  $h = 2.8 \, mm$ , and  $l = 100 \, mm$  with ideal buckling force,  $F_b$ ' of 2.732 kN. The MCCD system consists of 2 by 4 horizontal chains of CCDs with  $n_c = 8$  chains. Each chain has 10 serially connected units  $(n_s = 10)$  of 4 parallel units  $(n_p = 4)$ , as shown in Figure 6.11(b). The system results in an axial force capacity of 87.4 kN as determined below. The actual and idealized force-displacement response of the MCCD system as per [82] is shown in Figure 6.14. The response of the modified frame system is shown in Figure 6.13(b).

$$F_b = F_b' n_p n_c = 87.4 \text{ kN}$$

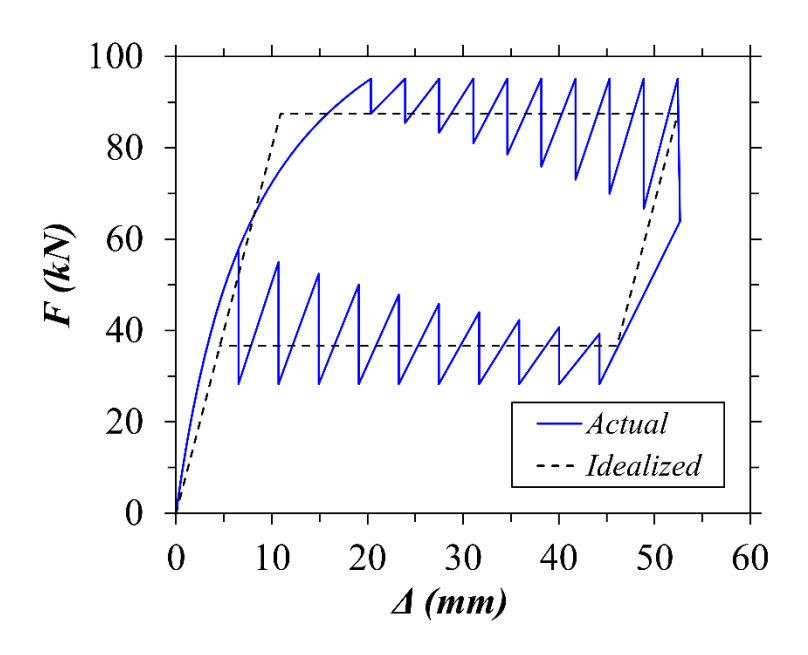


Figure 6.14 Force-displacement response of the MCCD system

## **6.4.4** Time-history analysis

NLTHA were performed for the two designed systems under the 1940 El Centro and 1985 Chile ground motion records. Figure 6.15 shows the lateral displacement time-history responses for the original and the modified frame systems. The maximum displacement of the modified system for the El Centro record is 15 mm, which is smaller than the one for the original frame of 40 mm and the yield displacement of 26.2 mm. For the Chile record, the modified system has a maximum displacement of 35 mm that exceeds the yield displacement of the frame as shown in Figure 6.15(b) and resulted in a residual displacement of 8.8 mm, as shown in Figure 6.16(d). It should be noted that the Chile record was considered as a maximum considered event. The original frame had a maximum displacement of 62 mm and a permanent displacement of 36 mm. This displacement is about 4 times larger than that predicted for the modified system. Figure 6.16 shows the resulted hysteretic shear force-lateral displacement responses of both systems for the two ground motion records.

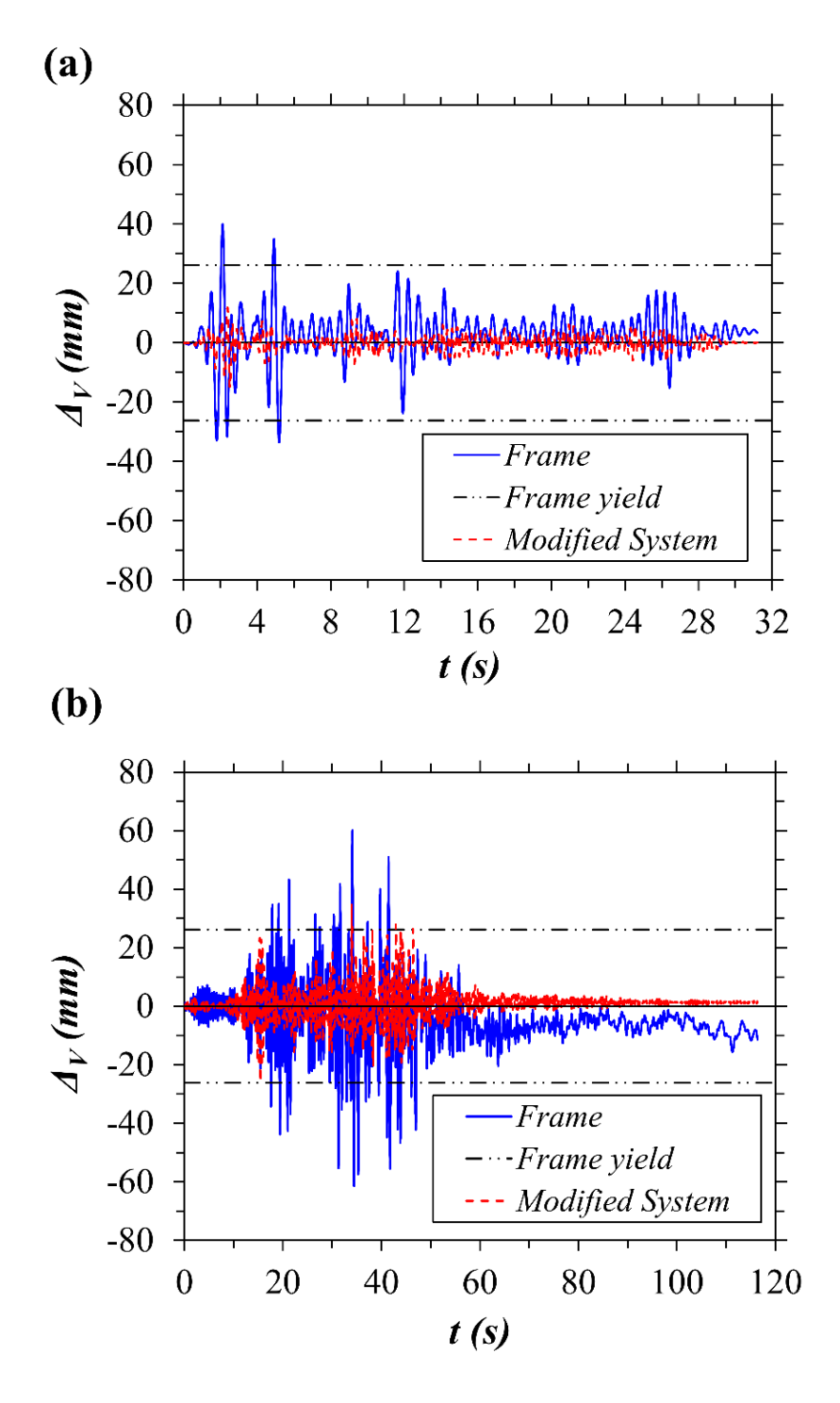


Figure 6.15 Lateral displacement time-history of the RC frame: (a) 1940 El Centro, and (b) 1985 Chile earthquakes

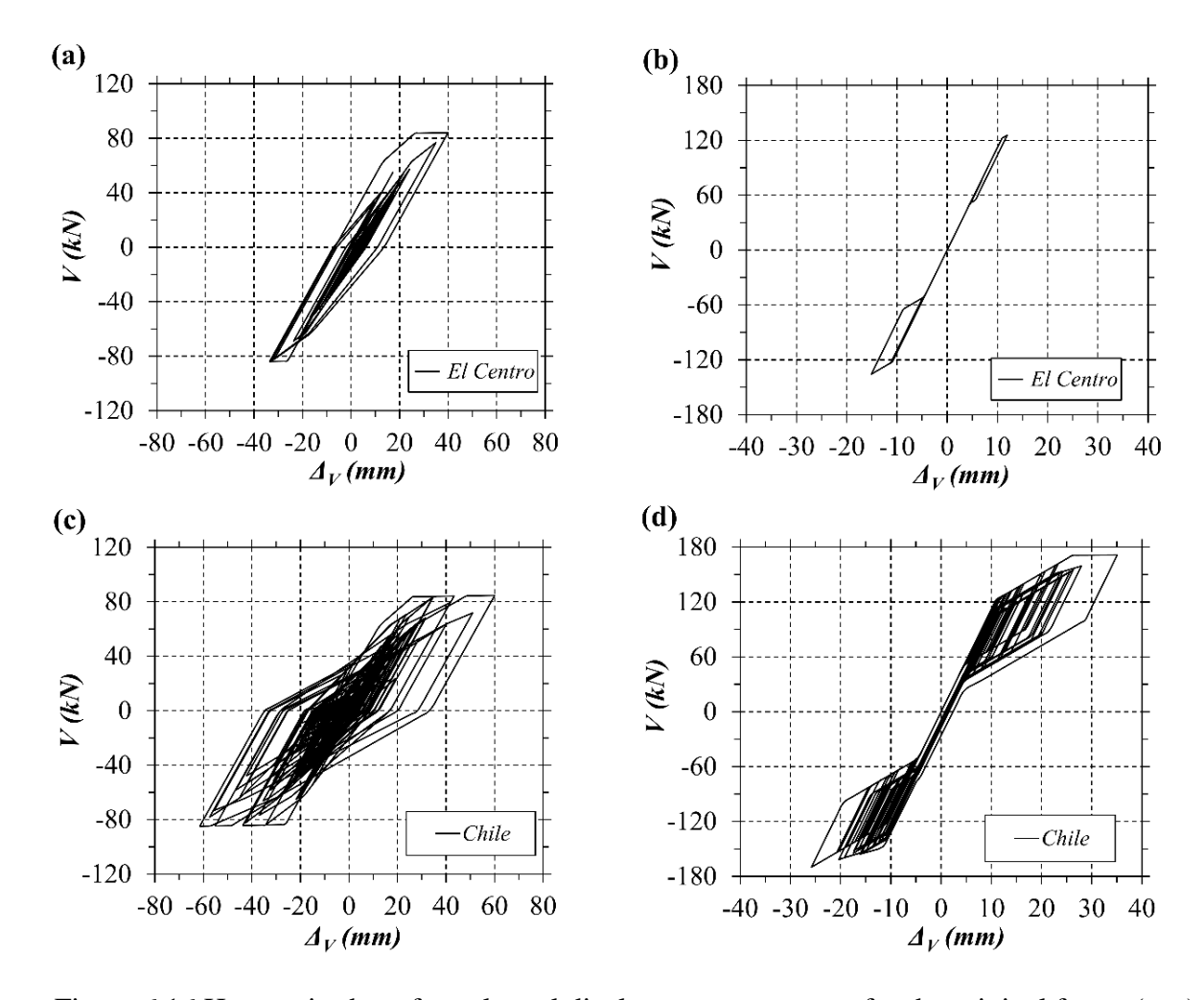


Figure 6.16 Hysteretic shear force-lateral displacement responses for the original frame (a, c), and the modified frame (b, d)

# 6.5 Coupled Rocking Walls

Two precast post-tensioned coupled rocking walls with unbonded tendons are considered in this example. The two walls are similar, with  $h_w = 3300$  mm,  $l_w = 1200$  mm,  $t_w = 120$  mm, and one 3600 mm long post-tensioning tendon at its mid-length as shown in Figure 6.17(a). The two walls are connected by hinged links that transfer shear between them, see Figure 6.17(a). The coupled walls are to be designed for an effective seismic mass  $m_e = 18000$  kg. The axial force on each wall is P = 83 kN. The walls were first designed as rocking member and then modified with the MCCD system and redesigned. The aim here is to limit the lateral drift of the walls and

maintain the response within the elastic range of the prestressing tendons. The design and analysis are only carried out in the in-plane direction of the coupled walls.

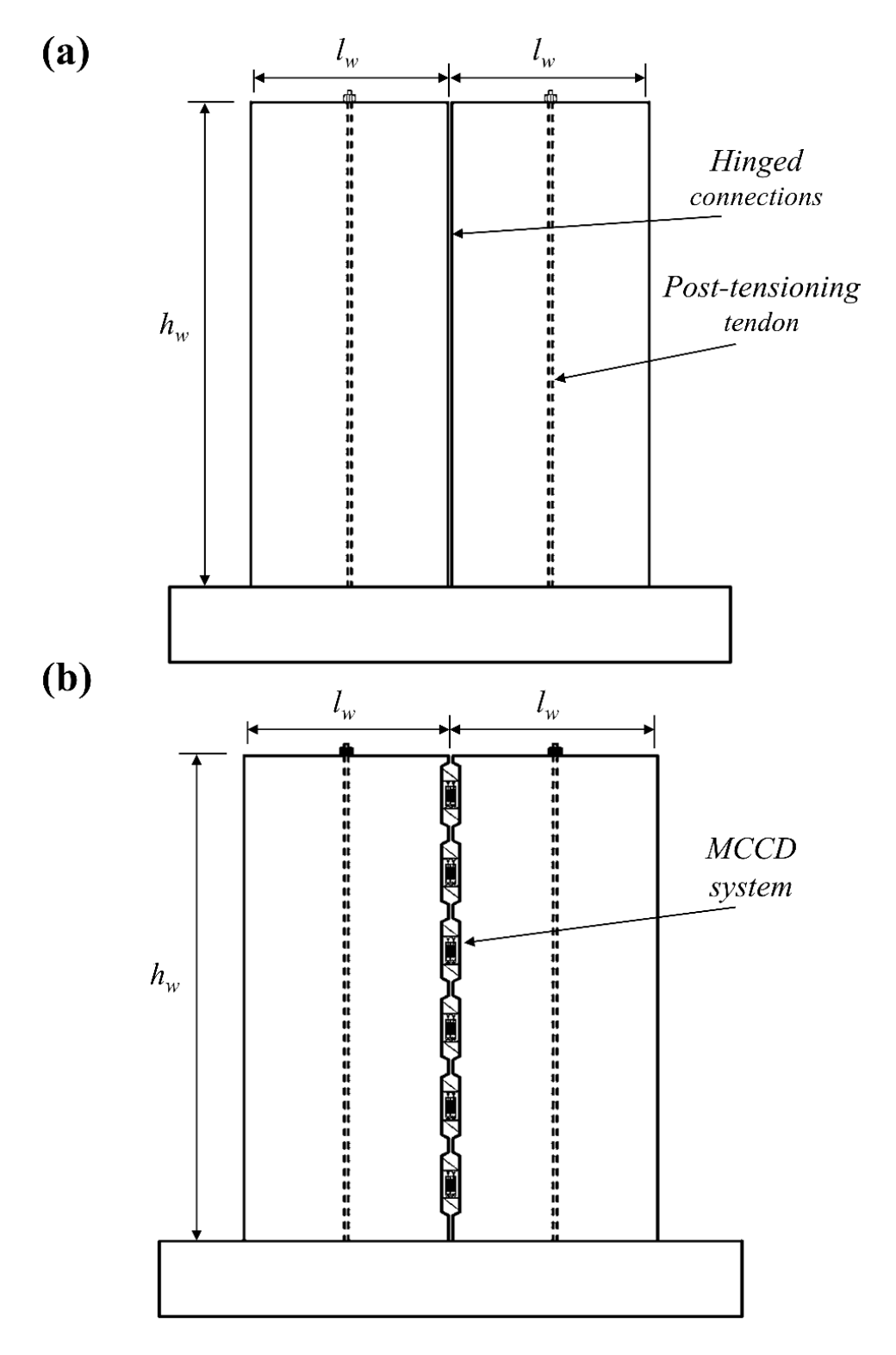


Figure 6.17 Example 3: (a) original coupled walls, and (b) modified coupled walls

### 6.5.1 Modified system

Rocking wall systems have gained increased attention in the past two decades due to their performance in resisting lateral loads compared to conventional structural walls. The main advantage of rocking wall systems over conventional ones is damage avoidance and self-centering capability. The response of such system is nonlinear elastic with large drift capacity; nonetheless, they are prone to lose of stability due to lack of significant energy dissipation. Therefore, it is common to couple such systems with supplementary energy dissipation devices to control their drift [109,110].

The coupled walls in this example are modified by replacing the hinged connections between the walls with the MCCD system as shown in Figure 6.17(b). Under lateral loading, the two inner edges of the walls displace relative to each other. This relative displacement is used to activate the MCCD system in tension or in compression as will be shown later. The design objective is to limit the lateral drift of the walls and maintain their response within the elastic range of the prestressing tendons. Therefore, the system design displacement is governed by the displacement corresponding to yielding of the prestressing tendons or the maximum allowable drift, whichever is smaller. The concrete material properties were taken as those presented in Table 6.2 for the pier-wall.

### 6.5.2 Conventional design of the coupled walls

### 6.5.2.1 <u>Idealized system</u>

The walls were assumed to be rigid elements supported by a hinge support and connected to a rotational spring. The two rigid elements are linked via hinged connections throughout their height as shown Figure 6.18(a). The effective seismic mass was assumed to lumped at the top level of the walls. The system was designed and analyzed using the proposed analysis method in [111]

and discussed in the Appendix. The walls were idealized as a single-degree-of-freedom (SDOF) system, as shown in Figure 6.18(a), by linking their responses in parallel.

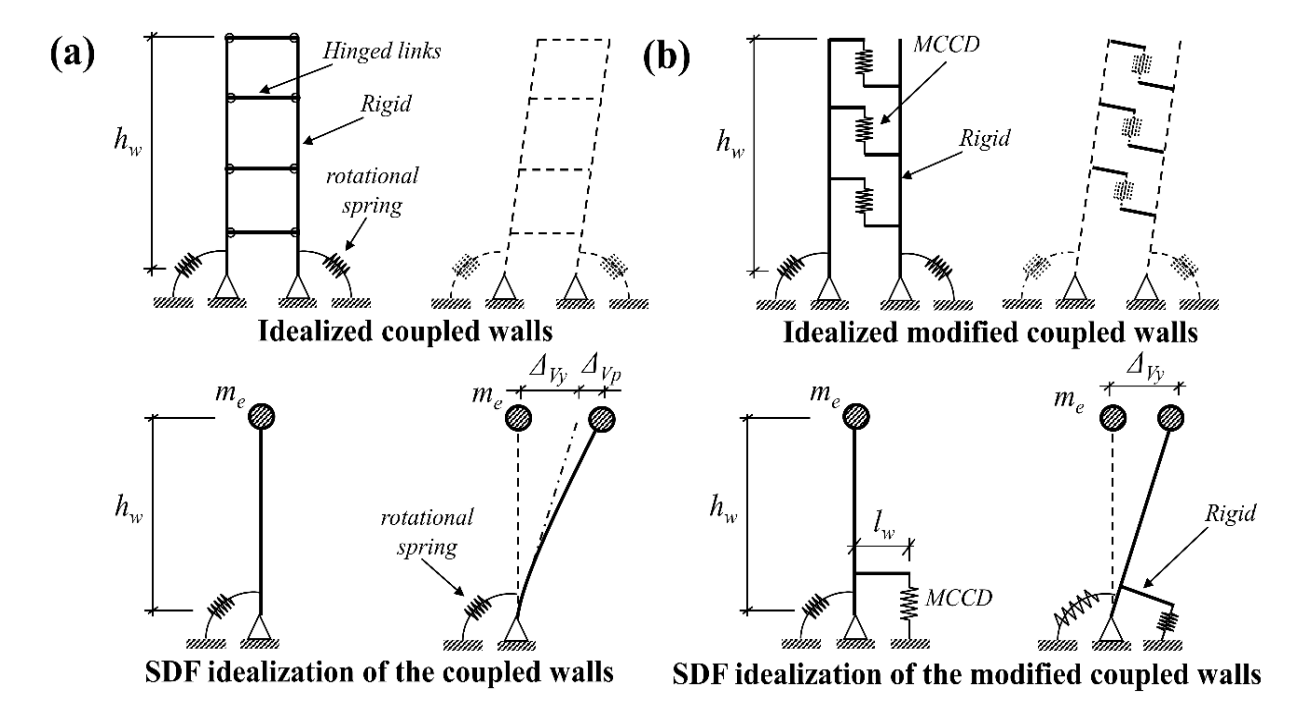


Figure 6.18 System idealization for analysis: (a) original coupled walls, and (b) modified coupled walls

### 6.5.2.2 Design

The DDBD method was used estimate seismic demands. The criteria to design rocking walls is to limit their response to the yield onset of the tendons or by a lateral drift limit. A yield displacement  $\Delta_y = 86 \, mm$  was estimated in an iterative process using the proposed analysis method in [111]. This value is less than a 3% drift-based value of 99 mm. Since the total response of the walls is within the elastic range and through rocking of a rigid body motion, researchers [109,112] suggest a low equivalent viscus damping ( $\zeta$ ) ratio ranging from 1% to 3%. An equivalent viscous damping  $\xi = 3$ % was used here for the design. An effective structural period  $T_e = 0.8 \, s$  was determined from the linear displacement response spectrum in Figure 6.4 for the damping ratio as discussed above. The base shear ( $V_e$ ) was thus calculated as follows:

$$V_e = 4 \Delta_D \pi^2 m_e / T_e = 95.6 \, kN$$

The walls were designed in an iterative process to develop the required lateral capacity  $V_n$  to the estimated base shear force  $V_e$ . Table 6.5 presents the design properties of the unbonded post-tensioning tendon. A nominal lateral capacity  $V_n = 97.9 \text{ kN}$  was calculated for the system. Figure 6.19(a) shows the force-displacement curves for coupled walls calculated following the analysis procedure presented in [111] and discussed in the Appendix with the specified material properties.

Table 6.5 Properties of the unboned post-tensioning tendon used for the coupled walls

Property	Value
Specified yield strength of the strands	$f_{py} = 1500  MPa$
Specified ultimate strength strands	$f_{pu} = 1700  MPa$
Elastic modulus of the strands	$E_s = 200 \text{ GPa}$
Yield strain of the strands	$\varepsilon_{\rm y} = 0.0075$
Total length of the tendon	$h_p = 3900 \ mm$
Diameter of the tendon	$d_{sl}=15.2~mm$
Initial prestressing	$f_{po} = 850 MPa$

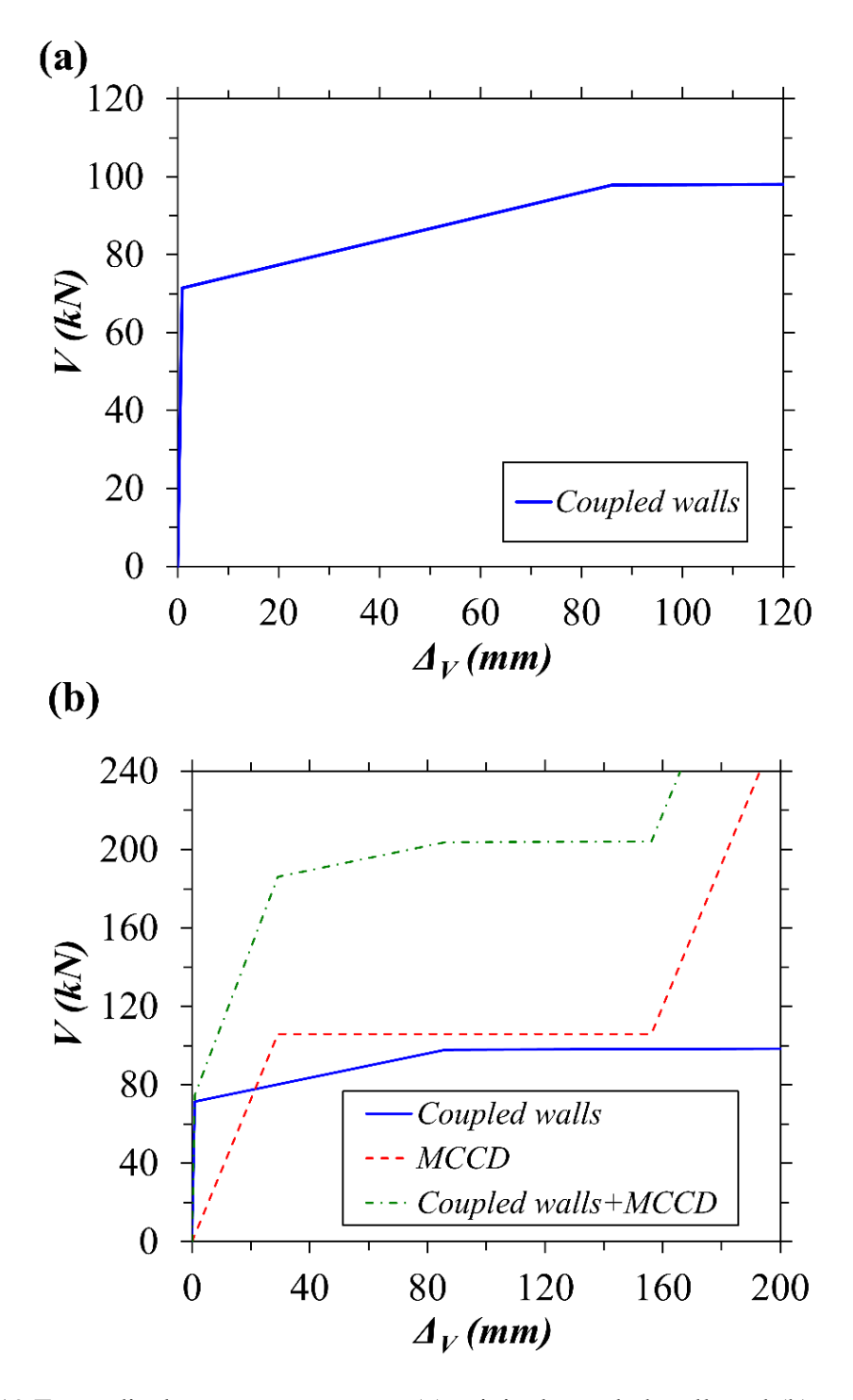


Figure 6.19 Force-displacement responses: (a) original coupled wall, and (b) modified coupled walls

### 6.5.3 Design of the modified coupled walls

### 6.5.3.1 <u>Idealized system</u>

Figure 6.18(b) shows the idealized system for the modified coupled walls. In this idealization, the MCCD system is represented by axial spring elements with flag-shaped response that replace the hinged connections. Each element is vertically oriented and connected to one wall at one end and to the other wall at the other end, see Figure 6.20(a).

## 6.5.3.2 Design of the MCCD system

The yield displacement of the tendons,  $\Delta_y = 86 \, mm$  as shown in Figure 6.19, was considered as the ultimate design displacement ( $\Delta_D$ ) for the modified system. Assuming an MCCD system with properties determined as presented in [82] and Table 6.6, the equivalent viscus damping ( $\xi$ ) was determined in an iterative process using the proposed expression in Equation (5.17) [82] assuming  $T_{eff} < T_s$  as given below.

$$D = (-0.0188\gamma + 0.0922)(h/t)_n + 0.0215\gamma - 0.1188 = 0.0685$$

$$E = 3.817 (h/t)_n - 1.422 = 0.9575$$

$$T_s = -0.5 \gamma_F + 2.5 = 1.5377$$

$$\xi_h = D [1 + E (T_s - T_{eff})] = 0.0664$$

$$\xi = \xi_e + \xi_h = 0.02 + 0.0664 = 0.0864$$

Table 6.6 Properties of the MCCD system for the modified coupled walls

Property	Value
Height-to-thickness ratio of the CCD in the system	h/t = 2.7273
Number of connected CCD in series	$n_{s} = 10$
Force ratio of the difference	$\beta_F = 0.6685$
Displacement ductility of the MCCD system	$\mu_{\Delta} = 5.3549$
Force ratio factor	$\gamma_F = 1.92448$
Ideal height-to-thickness ratio of the CCD in the system	$(h/t)_n = 2.6443$

The effective structural period for the system ( $T_{eff}$ ) was determined from the displacement spectrum shown in Figure 6.4.  $T_e$  was found to be 1.53 s resulting in a base shear  $V_e = 26 \, kN$ . The estimated shear demands are lower than that for original coupled walls since the shear force is estimated for the same displacement ( $\Delta_y = 86 \, mm$ ) and a higher damping ratio. Therefore, this force can be carried by the coupled walls without the added MCCD system provided that 3% or more damping ratio is available. However, in the case when the seismic excitation exceeds the design level, as will be shown later, the MCCD system is essential to control the response of the system. Thus, the MCCD system was designed for  $V_b = V_n$ , which results in  $\gamma_F = 2$ .

Similar to the case of the pier-wall, the MCCD system is not directly resisting the lateral force and thus it depends on its location and the relative displacement between the inner edges of the walls. Since the walls displace in a rigid body rotation the relation between the shear force demand carried by the MCCD system:

$$V_b = 2 F_b (I_w/2) / h_w = F_b I_w / h_w$$
(6.13)

The developed force by the MCCD system is as follows:

$$F_b = V_b h_w / I_w = 269.2 \text{ kN}$$

The factor of two (2) in Equation (6.13) is due to using two walls where the reaction of the MCCD system from one wall is carried by the other wall. To carry this load ( $F_b$ ), six MCCD systems of four chains each with a total number of  $n_c = 24$  chains were used as shown in Figure 6.17(b). The units were assumed to be made of carbon fiber composites with an elastic modulus of 300 GPa. The CCD units have t = 1.1 mm, h = 3 mm, and l = 100 mm with an ideal buckling force,  $F_b$  of 3.033 kN. Each chain has ten serially connected units ( $n_s = 10$ ) of four parallel units ( $n_p = 4$ ), as shown in Figure 6.20(a). The system results in an axial force capacity of 291.2 kN as determined

below. The actual and idealized force-displacement response of the MCCD system as per [82] is shown in Figure 6.20(b). The response of the modified frame system is shown in Figure 6.19(b).

$$F_b = F_b' n_p n_c = 291.2 \text{ kN}$$

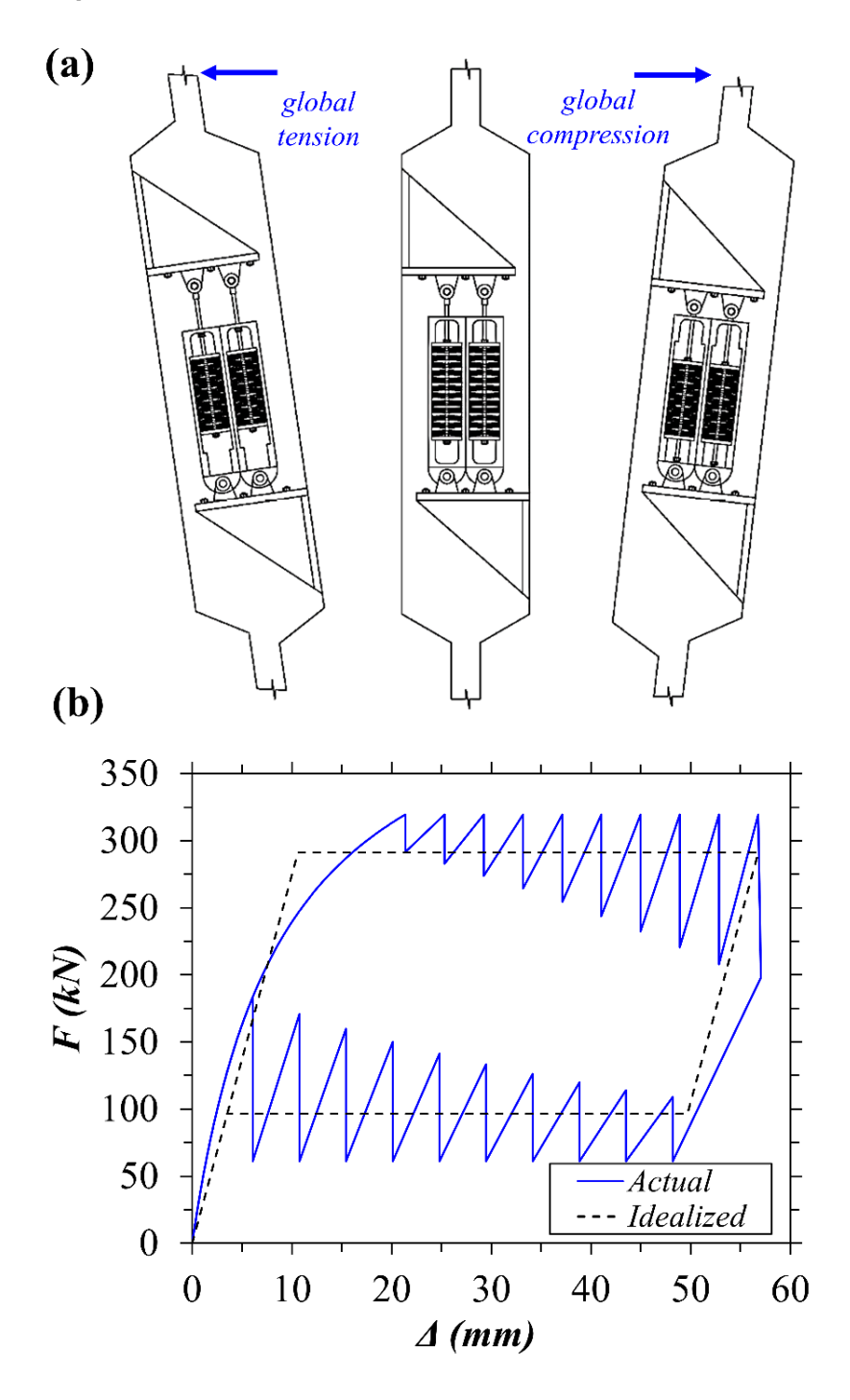


Figure 6.20 (a) Loading mechanism of the MCCD system, and (b) force-displacement response of the MCCD system

### 6.5.4 Time-history analysis

NLTHA were performed for the two designed systems under scaled records of the 1940 El Centro and 1985 Chile ground motion records as presented in Table 6.7. Figure 6.21 shows the lateral displacement time-history responses for the original and modified frame systems. The maximum displacement of the modified system for the El Centro record with scale factors of 1 and 1.25 were 1.9 mm and 12 mm, which are lower than displacement corresponding to yielding of the tendon ( $\Delta_y$ ). However, for all other scale factors presented in Table 6.7, the maximum displacements were larger than 390 mm, which indicates that the system is unstable. On the other hand, the modified system had lower maximum displacements than  $\Delta_y$ , except for the case of 1.5 scaled Chile record, for which the maximum displacement was higher than  $\Delta_y$  resulting in a permanent displacement of 52 mm. This case, however, is very extreme. Figure 6.22 shows the resulted hysteretic shear force-lateral displacement responses of both systems for selected cases from Table 6.7.

Table 6.7 Scale factors used for the NLTHA for the coupled walls example

Ground motion record	Scale factor	Peak ground acceleration	Maximum displacement (mm)	Permanent displacement (mm)
1940 El Centro	1	0.32 g	1.7	0
	1.25	0.4 g	18	0
	1.5	0.48 g	19	0
	2	0.64	43	0
1985 Chile	1	0.71	76	0
	1.5	1.065	138	52

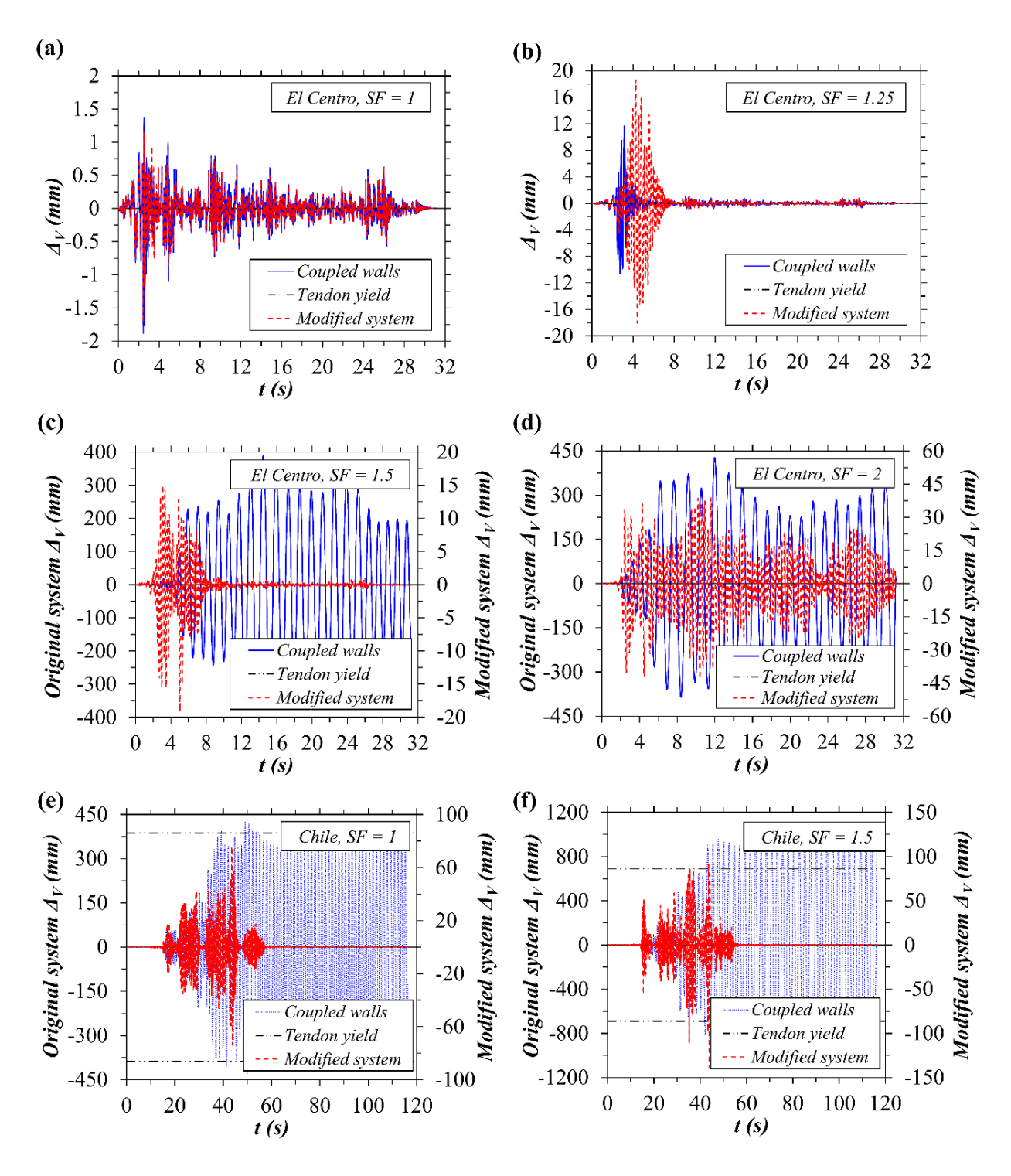


Figure 6.21 Lateral displacement response time-histories: (a-d) 1940 El Centro, and (e-f) 1985 Chile earthquakes

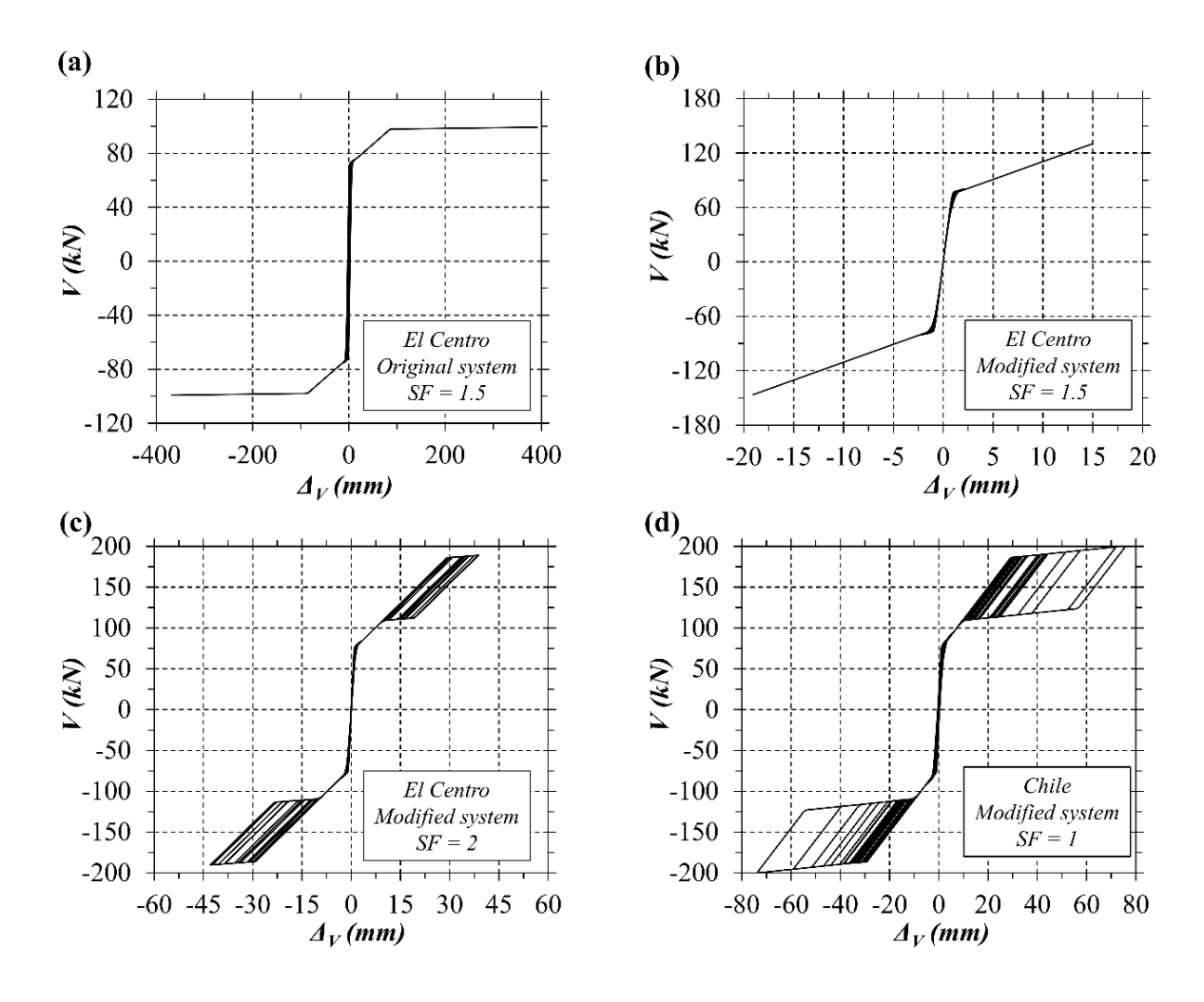


Figure 6.22 Hysteretic shear force-lateral displacement responses for the original coupled walls (a), and the modified coupled walls (b-d)

# **6.6 Design Recommendations**

The positioning considerations of the MCCD system within a structure is generally similar to those for typical hysteretic energy dissipation devices used for seismic protection. However, it should be noted that the MCCD system requires relatively higher displacement demands to be activated (apparent yield displacement  $\Delta_b$ ). Thus, it is more efficient in terms of demand displacement and capacity force to position the MCCD system to directly resist the induced seismic load. For example, in the pier-wall example, the demand displacement on the system is lower than the lateral displacement by  $1/\theta_F$  (or  $\Delta = \theta_F \Delta_V$ ), and the shear force capacity provided

by the system is also lower by  $1/\theta_F$  (or  $V_b = \theta_F F_b$ ). In contrast, in building frame example, the MCCD system is directly the induced seismic load and hence no reduction in displacement demand or shear force capacity.

The design of the MCCD system for given displacement and force demands is affected by many factors as follows:

- 1. The force ratio factor  $\gamma_F$ : The higher the factor  $\gamma_F$ , the lower the contribution of the MCCD system in resisting the induced seismic load ( $\gamma_F = 1$  means that the MCCD system is totally carrying the load). Thus, it is recommended to use  $\gamma_F \leq 2$  even if the force demand on the MCCD system is low (high  $\gamma_F$ ). This will ensure effective damping and avoids inelastic deformation in case the seismic demands exceed the design level.
- 2. Thickness of CCDs: The thickness, t, is an important parameter that may govern the design of the MCCD system. It is the most effective parameter when high capacity force is required since as can be seen in Equation (3.2) it has the highest power of 2.412. However, increasing t, while keeping t constant, increases t0 (and hence t0) and decreases t1 (and hence t2). It should be noted that increasing t2 also increases t3. Thus, a balance between the values of t3 and t4 should be reached to keep t3 (low and satisfy force demands.
- 3. Number of the CCDs  $n_s$ : As discussed in Chapter 4 and Chapter 5, higher  $n_s$  results in higher  $\xi$ ; however, this also leads to higher  $\Delta_b$ . Therefore,  $n_s$  should be high enough to result in sufficient damping and low enough to keep  $\Delta_b$  low. The study presented in Chapter 4 shows that  $n_s = 12$  results in about 90% of the theoretical maximum of the amount of energy dissipation. Thus, the value of  $n_s$  shall range from 8 to 12 depending on the displacement requirements.

### **6.7** Conclusions

The seismic performance of typical reinforced concrete structures incorporating the MCCD system in different configurations was evaluated. The structures were designed using the direct displacement-based design with and without the MCCD system. Nonlinear time-history analyses were conducted for the original and modified structural systems under the 1940 El Centro and 1985 Chile ground motion records to compare their seismic performance. The following findings were drawn from the study:

- Displacement-based design methods are the most suitable for structures modified with the MCCD system, or supplementary energy dissipation devices. The reason is that for such system the main aim is to prevent damage which can only be quantified using deformationbased methods.
- 2. Positioning of the MCCD system highly affects the force and the displacement demands on the system. Positioning the system to directly resist the induced seismic loads, such as the case of the chevron braced frame, is the most efficient.
- 3. The design of the MCCD system to a given force and displacement demands is highly dependent on the thickness (t) of the CCDs in the system. Thus, a balance between the values of t, h, and other parameters (l, d, and E) of the CCD response should be reached to satisfy force and displacement demands.
- 4. The structural systems modified with the MCCD system showed enhanced seismic performance compared to the original structures. In all cases, no inelastic deformations were observed in the main structural elements under the design basis loads.

# **CHAPTER SEVEN**

# 7 Conclusions

### 7.1 Research Contributions

This research developed a new research avenue on the use of elastic energy dissipation from multistable element systems for seismic protection in building and bridge structures. Preliminary results show that using such systems improves the seismic performance of RC structures by reducing lateral drifts and avoiding damage.

This research develops and proposes a displacement-based design procedure that considers the unique characteristics of the hysteretic response of multistable element systems compared to hysteresis energy dissipation devices. The uniqueness of multistable element systems originates from the fact that their response cannot be described by the commonly used measure of energy dissipation, which is the displacement ductility or apparent displacement ductility. Instead, the response is characterized by their geometry (i.e., height-to-thickness ratio), which controls the amount of dissipated energy. Understanding this issue is the key to properly designing these systems as a main damping mechanism in structures, and this research provides an explanation of this conceptual issue.

A review of the published literature further shows that systems comprised of surface revolution elements don't exist since a multistable element with such shape and a reliable response is not available. This research addresses this knowledge gap by proposing and characterizing a dome-shaped shaped element with controllable snap-through behavior used in constructing a system capable of exhibiting a desirable hysteretic response.

### 7.2 Conclusions

The following provides a summary of the contributions and the conclusions from the presented research:

- 1. A new shallow dome-shaped structural element with cosine-curved profile (CCD) that exhibits a tunable multistable elastic behavior was developed. The element offers reliable and reversible large elastic deformation that can be used as a building unit for devices subjected to relatively high forces for energy dissipation and repeated use. The main factor affecting their response is their height-to-thickness ratio (*h/t*). Increase of *h/t* changes their response from monostable to bistable. It was found that CCDs have a critical height-to-thickness ratio (*h/t*)<sub>cr</sub> at which the response is pseudo-bistable allowing designing CCDs with a targeted snap-through instability type. Expressions to estimate key parameters in the force-deformation response were developed to construct a multilinear force-deformation response, and shown to facilitate the response analysis for a system of multiple CCDs.
- 2. A new self-centering energy dissipation system comprised of multiple cosine-curved domes (MCCD) connected in series was developed and characterized. The building units of the MCCD system are dome-shaped shell elements with cosine-curved profile. The MCCD system shows a consecutive snap-through and snap-back response resulting in a hysteresis. The proposed MCCD system avoids some design disadvantages of other multistable elastic systems that limit the practicality of using such systems when multiple units in a system are stacked in parallel. A new analytical multilinear model that describes the hysteretic force-displacement response and takes into account the nonlinear effects of the CCD units was proposed. The model was shown to yield accurate simulations. The amount of dissipated energy mainly depends on the number  $(n_s)$  and the height-to-thickness

ratio (h/t) of the CCD units. The higher  $n_s$  and h/t are the higher the amount of the dissipated energy. The system showed a maximum loss factor ( $\eta$ ) value of about 0.14 for a monostable (self-recoverable) response. The loss factor reaches about 90 % of its theoretical maximum value for systems with about 12 CCDs. Increasing  $n_s$  increases the amount of dissipated energy, but it also decreases the initial stiffness of the MCCD system.

- 3. The hysteretic response of the MCCD system was investigated for its equivalent viscous damping. The sawtooth-shape response of the MCCD system was idealized, based on maintaining energy balance between the original and idealized responses, to facilitate dynamic analysis. Linear and nonlinear time-history analyses were performed on single degree of freedom systems with hysteretic response and linear equivalents. A statistical study was conducted to develop empirical expressions for the idealized hysteretic response of the MCCD system. An expression to estimate the hysteretic equivalent viscous damping ratio was developed. The calculated spectral displacements for the linear substitute using the developed expression are in good agreement with the displacements from the analyses of nonlinear systems.
- 4. The seismic performance of typical reinforced concrete (RC) structures incorporating the MCCD system is in various configurations in as a damping mechanism was evaluated. Nonlinear time-history analyses for the original structure and the modified structure with the MCCD system were performed. The structural systems modified with the MCCD system showed an enhanced seismic performance compared to the original structures. In all cases, no inelastic deformations were observed in the main structures under the design basis loads.

### 7.3 Future Research

The work presented in this dissertation introduces the use of elastic instabilities for seismic protection of structures. The capabilities of and the expected demands on the proposed MCCD system were explored. It was shown that the MCCD system in particular and systems with elastic instabilities in general have great potential for applications in energy dissipation and shock absorption. Nonetheless, there are still areas and issues that require investigation and development to produce a reliable and practical product that meets the ultimate objective of this research. These aspects are as follows:

- 1. Experimental and numerical investigations should be conducted to develop an optimal design for the CCD for use in seismic protection. The design shall be capable of withstanding large forces with lower snapping displacements, as discussed in Chapter 6, while ensuring that the CCD can be tailored in practical manner. Consideration shall be given to the way the load is transferred from one serially connected CCD to another. In addition, the effect of a hole at the apex for the loading shaft shall also be comprehensively investigated, since this could alter the response of the CCD by shifting the response curve and reducing the displacements.
- 2. The material selection of the CCD units must also be investigated. In general, materials with high stiffness and high elastic strength are the best suited for such a design. Possible example materials are carbon and glass fiber reinforced composites and spring steel. In addition, the complex geometric shape and the fabrication process of the CCD units are important factors to be considered in the material selection.
- 3. Investigation of the dynamic behavior of the MCCD system should be performed.

  Although seismic loads on structures are applied at low loading rates, the response of a

- structure incorporating the MCCD system is elastic and hence dynamic effects may be more pronounced in comparison to yielding devices.
- 4. Shaking table tests are the most representative of actual ground motions on a structure. Therefore, tests should be conducted on structures provided with the MCCD system as a supplementary energy dissipation device, such as those presented in Chapter 6, to evaluate their seismic performance.

**APPENDIX** 

# **Appendix: Analysis and Design Calculations**

This appendix presents sample calculations for the design and analysis results presented for the example structures in Chapter 6.

# A.1 Bridge Pier-Wall

The design procedure of the pier-wall for flexural is based on the method proposed by Alturki and Burgueño [105]. The shear design and detailing of the pier-wall are based on the AASHTO Guide Specifications for LRFD Seismic Bridge Design [104]. In addition, some information and design details were obtained from the AASHTO LRFD Bridge Design Specifications [103].

# A.1.1 Flexure design

### A.1.1.1 Estimation of seismic demands

Displacement ductility demand:

$$\mu_D = 3.5$$

Displacement demand:

$$\Delta_D = 80 \text{ mm}$$

Ideal yield displacement:

$$\Delta_V = \Delta_D / \mu_D = 23 \text{ mm}$$

Ideal yield curvature:

$$\varphi_V = 3 \Delta_V / h_W^2 = 1.4 1/km$$

### A.1.1.2 Determination of sectional properties

Influence factor of the longitudinal reinforcement yield strength:

$$k_s = 1.15 - 0.00036 f_v = 1.000$$

Influence factor of the concrete compressive strength:

$$k_c = 1.14 (f_c)^{-0.1} = 0.98$$

Influence factor of the longitudinal reinforcement:

$$k_{\rho} = \varphi_{y} l_{w} / (k_{s} k_{c} \varepsilon_{y}) = 2$$

Required longitudinal reinforcement and axial load ratios:

For 
$$\rho_l \le 0.0125$$

$$k_{\rho} = (30 + 385 \gamma - 1615 \gamma^{2}) \rho_{l} + (26.8 \gamma - 5.75) \gamma + 1.85$$

OK

$$\rho_l = 0.0083 < 0.0125$$

use 
$$\rho_l = 0.01$$

Provided longitudinal reinforcement:

$$46 φ 15.9 bars: A_{sp} = 9131 mm^2$$

Bar diameter of the longitudinal reinforcement:

$$d_b = 15.9 \text{ mm}$$

Nominal moment capacity:

$$M_n = 6335 \text{ kN.m}$$

Overstrength factor:

$$\lambda_0 = 1.4$$

Overstrength moment:

$$M_{no} = \lambda_o M_n = 8869 \text{ kN.m}$$

### A.1.2 Shear design

Overstrength shear force:

$$V_o = M_o / h_w = 1267 \, kN$$

Effective shear area:

$$A_e = 0.8A_g = 720000 \text{ mm}^2$$

Shear reinforcement ratio (found by iteration):

$$\rho_W = 0.0169 > 0.004$$

Shear reinforcement strength factor:

$$f_{w} = 2.41 \, MPa$$

Concrete shear stress adjustment factor:

$$\alpha' = f_w / 0.15 + 3.67 - \mu_D = 17.2$$

Shear stress carried by concrete:

$$v_c = 0.032 \, \alpha' [1 + P/(2 \, A_g)] \sqrt{f_c'} = 6.8 > 1.82 > 1.71 \, MPa$$

$$v_c = 1.71 \, MPa$$

Shear force carried by concrete:

$$V_c = v_c A_e = 1230 \text{ kN}$$

Spacing of transverse reinforcement:

$$s = 100 \text{ mm} < minimum$$
 
$$\begin{cases} t_w/2 = 150 \text{ mm} \\ 6 d_b = 100 \text{ mm} \\ 150 \text{ mm} \end{cases}$$

Provided shear reinforcement:

$$A_v = t_w \, s \, \rho_w = 506 \, \text{mm}^2$$
: 4 legs  $\varphi$  12.7 mm bars @ 100 mm c/c

Bar diameter of the transverse reinforcement:

$$d_t = 12.7 \, mm$$

Effective shear depth:

$$d_v = 0.72 l_w = 2160 mm$$

Shear force carried by shear reinforcement:

$$V_s = A_v f_{yt} d_v / s = 4596 > 3496 \text{ kN (controls)}$$

Nominal shear capacity:

$$V_n = V_c + V_s = 4727 \, kN$$

Shear resistance factor:

$$\varphi_s = 0.9$$

Factored nominal shear capacity:

$$\varphi_{s} V_{n} = 4254 \text{ kN} > V_{o}$$

The designed section with reinforcement details is shown in Figure A.1.

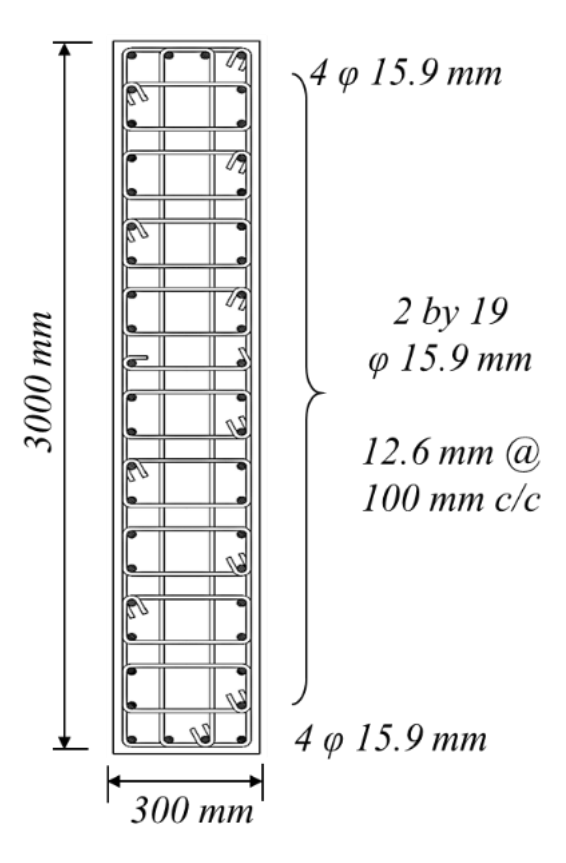


Figure A.1 Pier-wall cross-section and reinforcements details

## A.1.3 Plastic analysis

A moment-curvature analysis and plastic hinge analysis were performed for the designed pier-wall. The result of these analyses is the shear force-lateral displacement curve. Shear capacity curve for web-crushing strength was also constructed.

#### A.1.3.1 Moment-curvature analysis:

The moment-curvature analysis for the pier-wall section was performed using the Section Designer tool of the program SAP2000 [113]. The concrete stress-strain model used for the moment-curvature analyses was that proposed by Mander *et al.* [114] for confined and unconfined concrete. A simple stress-strain model was used for the reinforcing steel, featuring a plastic plateau, and parabolic strain-hardening response. The limiting tensile strains and strengths defined in the AASHTO Guide Specifications [104] for ASTM A615 were used to define each of the model regions. The key moments and curvature values are:

First yield moment:

$$M_{\rm V} = 4123 \, \rm kN.m$$

First yield curvature:

$$\varphi'_{V} = 1.042 \, 1/km$$

Nominal moment:

$$M_n = 5603 \text{ kN.m}$$

Ideal yield curvature:

$$\varphi_y = \varphi' y Mn / My = 1.42 1/km$$

Ultimate curvature based on flexural response (not necessarily achieved by the pier-wall before shear failure occurs):

$$\varphi_u = 35.4 \ 1/km$$

## A.1.3.2 Plastic hinge analysis:

In plastic hinge analysis, a region within the pier-wall's height undergoes inelastic deformations whereas other locations remain elastic. The approach allows determining the element's lateral response, in terms of shear forces and displacements, based on the section's

moment-curvature behavior. The curvatures along the region where inelastic deformations concentrate are assumed to be constant. The inelastic rotation,  $\theta_p$ , is determined by multiplying the inelastic sectional curvature,  $\varphi_p$ , by the plastic hinge length,  $L_p$ . The plastic hinge length model adopted is that proposed by Priestley *et al.* [5] for RC walls.

Strain penetration length:

$$L_{sp} = 0.022 \, f_y \, d_b = 147 \, mm$$

Plastic hinge length:

$$L_D = 0.08 h_W + L_{SD} + 0.1 l_W = 1007 mm$$

First yield shear force:

$$V_V = 589 \text{ kN}$$

First yield displacement:

$$\Delta'_{v} = \varphi'_{v} h_{w^{2}} / 3 = 17 \, \text{mm}$$

Nominal shear force:

$$V_n = 800 \, kN$$

Ideal yield displacement:

$$\Delta_V = \Delta'_V V_n / V_V = 23 mm$$

Ultimate displacement based on flexural response (not necessarily achieved by the pierwall before shear failure occurs):

$$\Delta_u = \Delta_y + (\varphi_u - \varphi_y) L_p h_w = 267 mm$$

The shear force-lateral displacement curve can be obtained from the sectional analysis results by dividing the moment-curvature response into two parts: (1) before first yield with moments, M, and curvatures,  $\varphi$ , and (2) after first yield with moments, M, and curvatures,  $\varphi$ . The

shear force-lateral displacement curve is shown in Figure A.2. The figure also shows the overstrength and shear strength curves.

Shear force:

$$V = M/h_W$$

Overstrength shear force:

$$V_o = \lambda M / h_w$$

Displacements up to first yield:

$$\Delta = \varphi' h_{w^2} / 3$$

Displacements after first yield:

$$\Delta = \Delta'_{V} M / M_{V} + (\varphi - \varphi'_{V} M / M_{V}) L_{p} h_{w}$$

#### A.1.3.3 Web-crushing capacity

Web-crushing capacity can be considered as upper limit at which increasing shear reinforcement would not increase the shear strength of the RC member [4].

Web-crushing stress:

$$v_{WC} = [0.22 \lambda_o / (\Delta / \Delta_y) + 0.03] f_c < 0.16 f_c \le 6 MPa$$

Shear force based on web-crushing:

$$V_{WC} = V_{WC}A_e$$

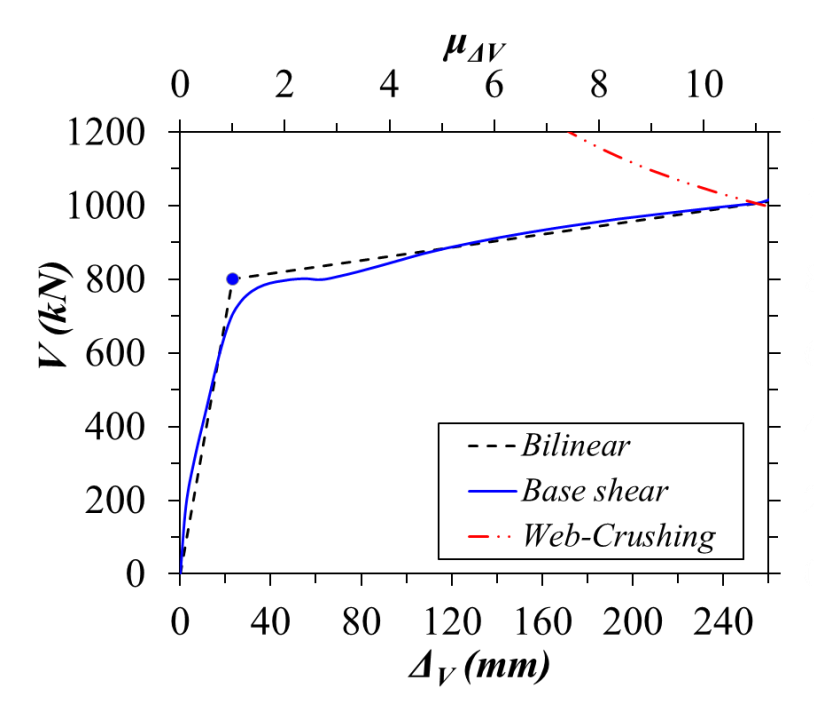


Figure A.2 Shear force-lateral displacement response of the designed pier-wall based on plastic analysis

# A.2 Building Frame

Three degrees of freedom were considered in the formulation of the stiffness matrix as shown in Figure A.3. The stiffness matrix is given as follows:

$$\begin{bmatrix} \frac{4E_c I_c}{h_c} + \frac{4E_g I_g}{l_g} & \frac{6E_c I_c}{h_c^2} & \frac{2E_g I_g}{l_g} \\ \frac{6E_c I_c}{h_c^2} & \frac{24E_c I_c}{h_c^3} & \frac{6E_c I_c}{h_c^2} \\ \frac{2E_g I_g}{l_g} & \frac{6E_c I_c}{h_c^2} & \frac{4E_c I_c}{h_c} + \frac{4E_g I_g}{l_g} \\ \end{bmatrix} \begin{bmatrix} v_1 \\ v_2 \\ v_3 \end{bmatrix} = \begin{bmatrix} 0 \\ -V \\ 0 \end{bmatrix}$$

$$\begin{bmatrix} \frac{4E_c I_c}{h_c} & (1 + \rho_F) & \frac{6E_c I_c}{h_c^2} & \frac{2E_g I_g}{l_g} \\ \frac{6E_c I_c}{h_c} & \frac{24E_c I_c}{h_c^3} & \frac{6E_c I_c}{h_c^2} \\ \frac{2E_g I_g}{l_g} & \frac{6E_c I_c}{h_c^2} & \frac{4E_c I_c}{h_c} & (1 + \rho_F) \end{bmatrix} \begin{bmatrix} v_1 \\ v_2 \\ v_3 \end{bmatrix} = \begin{bmatrix} 0 \\ -V \\ 0 \end{bmatrix}$$

$$v_1 = v_3 = \frac{V h_c^2}{4 E_c I_c (6\rho_F + 1)}$$

$$v_2 = \frac{-V h_c^3 (3\rho_F + 2)}{12 E_c I_c (6\rho_F + 1)}$$

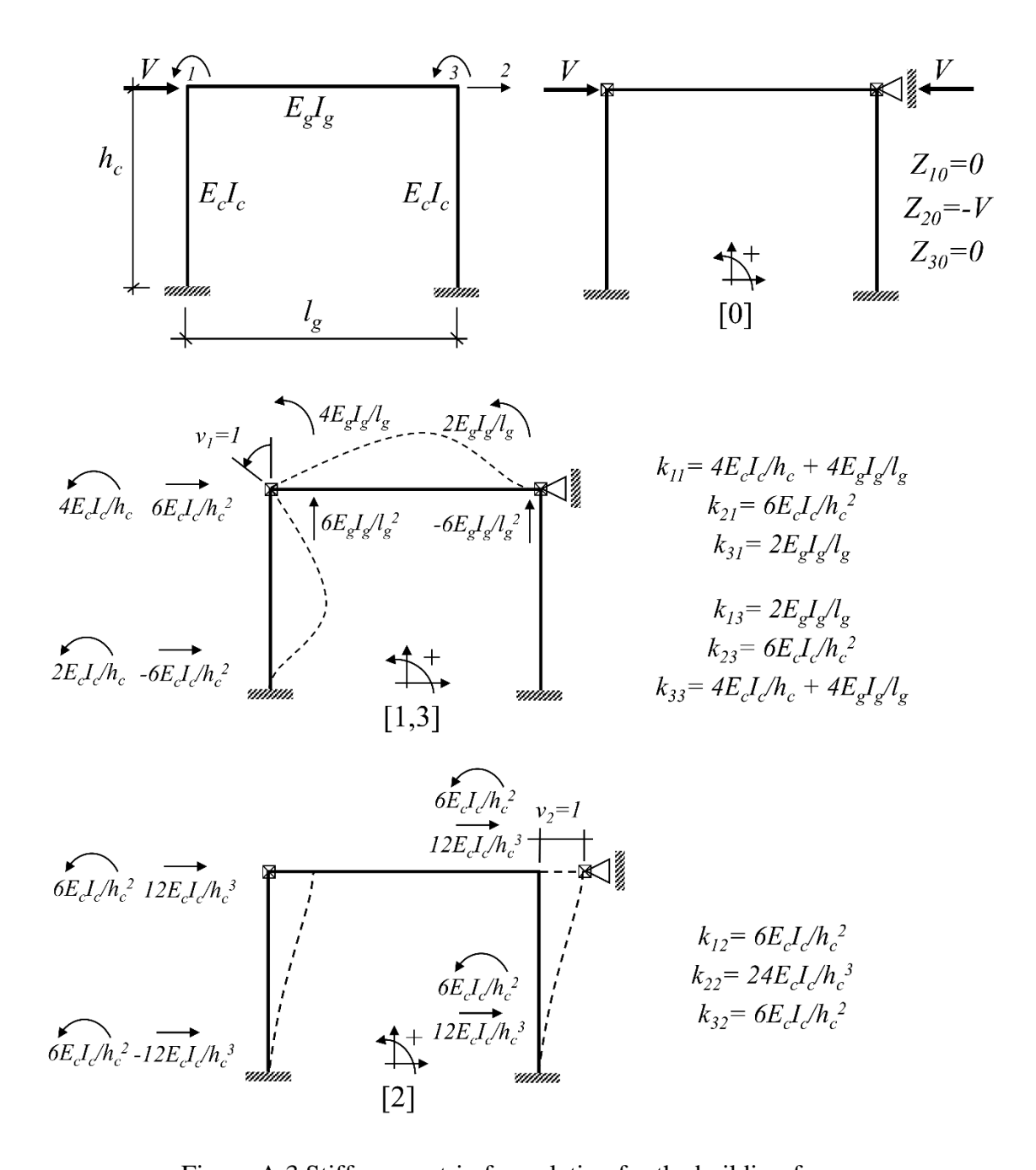


Figure A.3 Stiffness matrix formulation for the building frame

The resulted bending moment and shear force diagrams are shown in Figure A.4. The moments  $M_A$  and  $M_B$  are as follows:

$$\begin{split} M_A &= \frac{V \, h_c \, [1 - (3\rho_F + 2)]}{2 \, (6\rho_F + 1)} \\ \\ M_B &= \frac{V \, h_c \, [1 - 2 \, (3\rho_F + 2)]}{2 \, (6\rho_F + 1)} - \frac{V \, h_c}{(\rho_F + 1)} \end{split}$$

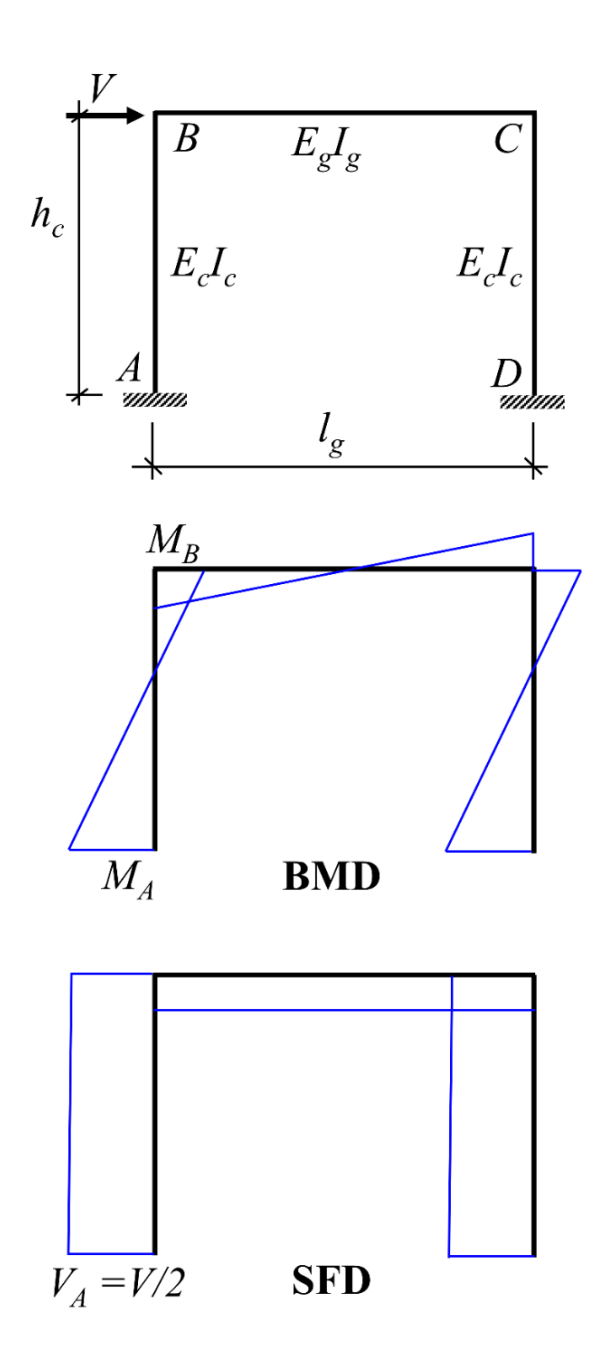


Figure A.4 Bending moment diagram (BMD) and shear force diagram (SFD) for the building frame

# **A.3 Coupled Rocking Walls**

There are key limit states in the response of an unbounded post-tensioned precast concrete wall as follows (see Figure A.5) [111]: (1) decompression of the wall base (DC), (2) softening the concrete in compression (SO), (3) yielding of the prestressing tendons (TY), and

(4) crushing of the concrete (CC). Figure A.5(b) shows the limit states in the shear force-displacement  $(V-\Delta)$  response of the precast wall.

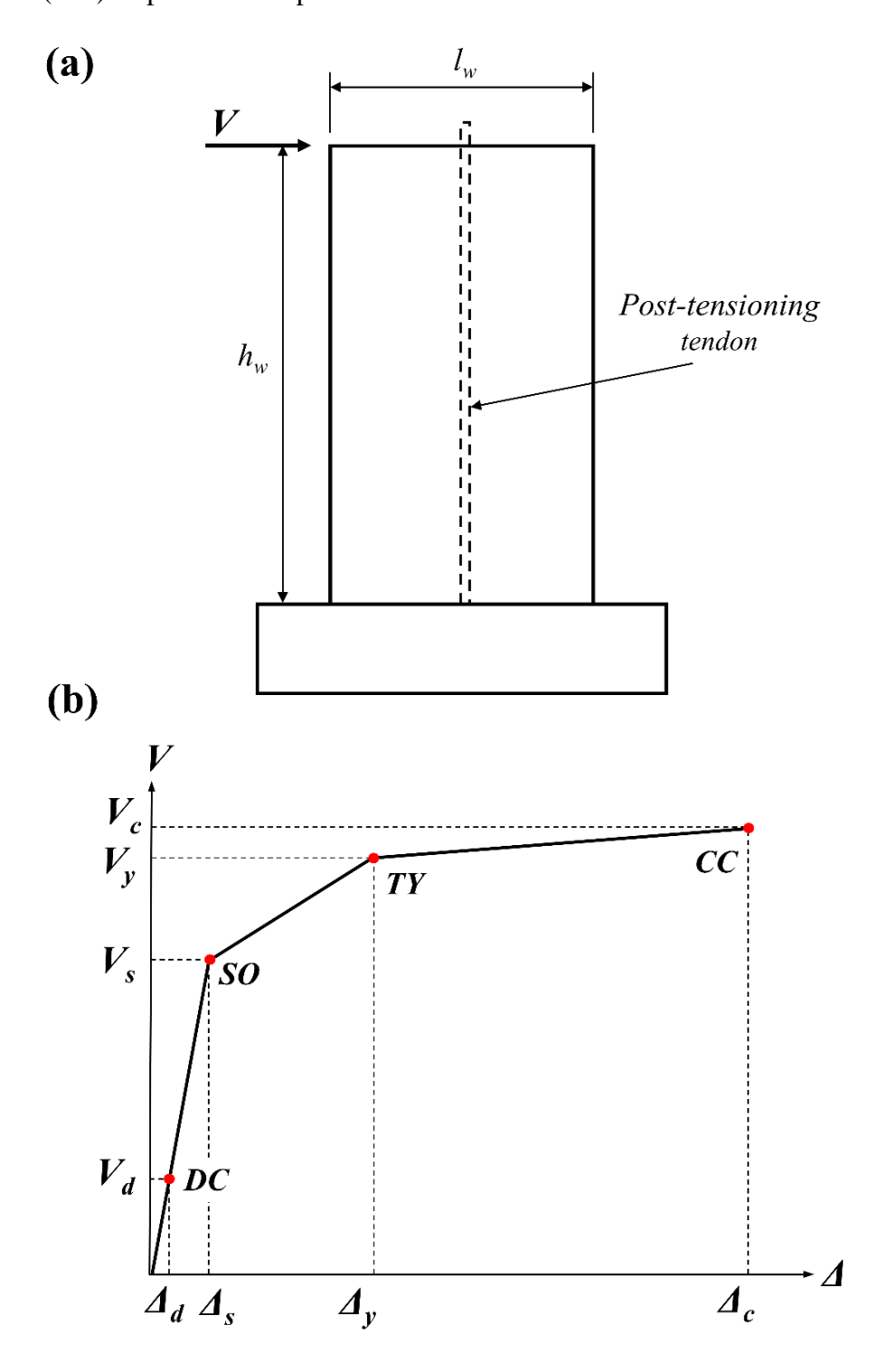


Figure A.5 (a) An unbounded post-tensioned precast concrete wall, and (b) shear force-displacement curve with response limit states

Figure A.6 shows the free body diagram at the base of the precast wall for the four limit states. The resistance moments, base shear forces, and top displacements are calculated for each limit state with reference to Figure A.6 in the following sections.

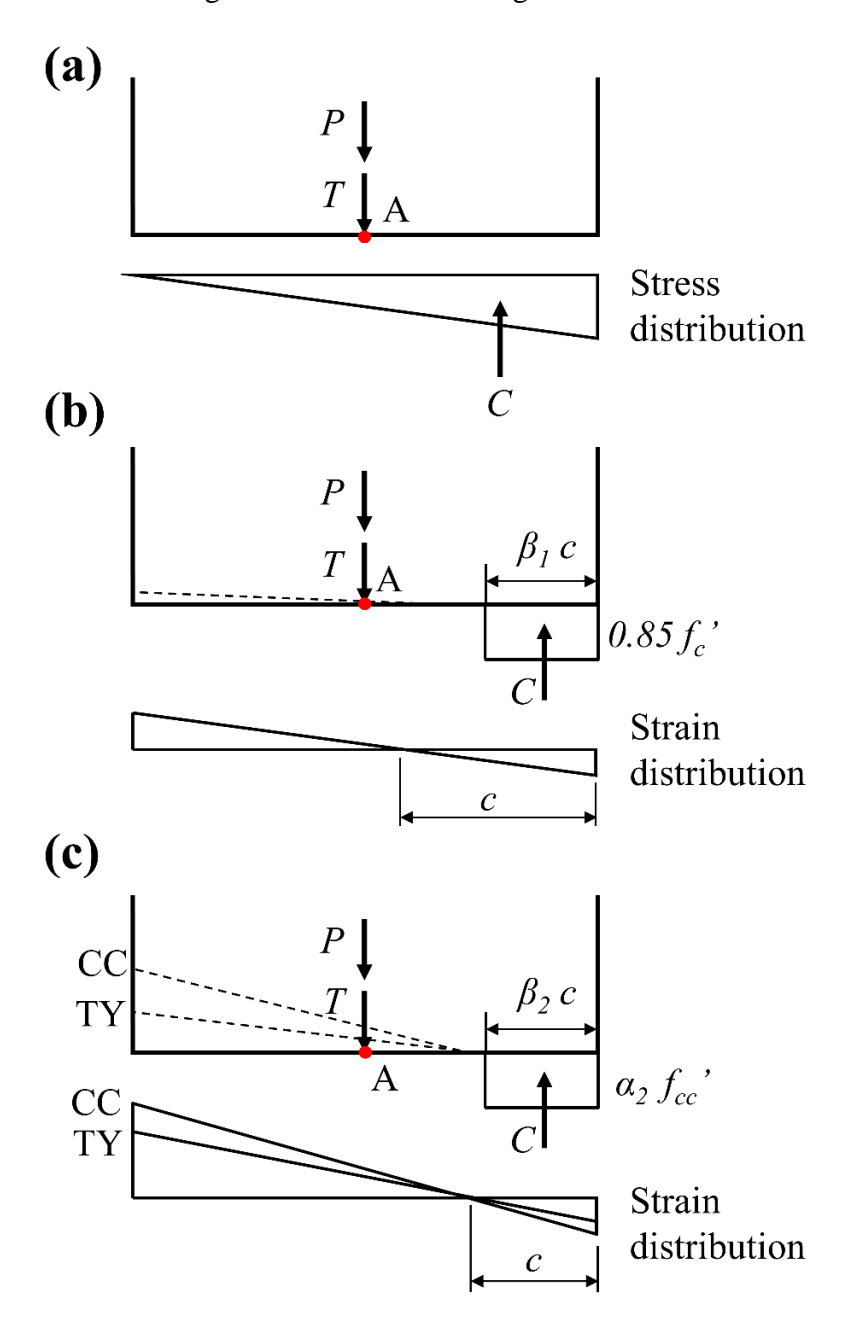


Figure A.6 Free body diagram for each limit state of the precast wall: (a) decompression, (b) softening, and (c) tendons yielding (TY) and concrete crushing (CC)

#### A.3.1 Decompression (DC)

Moment about point A in Figure A.6(a):

$$M_d = C I_w / 6 = 41.2 \text{ kN.m}$$

$$C = P + T = 206 \text{ kN}$$

$$T = A_p f_{po} = 118 \text{ kN}$$

Shear force:

$$V_d = M_d / h_w = 12.5 \text{ kN}$$

Displacement:

$$\Delta_d = V_d h_w^3 / (3 E_c I_c) = 0.32 \, mm$$

$$E_c = 4700 \sqrt{f_c'} = 27800 \text{ MPa}$$

$$I_c = t_W I_W^3 / 12 = 0.01728 \, \text{m}^4$$

### A.3.2 Softening (SO)

Moment about point A in Figure A.6(b):

$$M_S = C (I_w/2 - c \beta_1/2) = 118 \text{ kN.m}$$

$$C = P + T = c \beta_1 0.85 f_c' t_w = 206 kN$$

$$T = A_p f_{po} = 118 \text{ kN}$$

The value of  $\beta_I$  can be determined according to Whitney rectangular stress distribution adopted in the ACI 318 code [108].

Shear force:

$$V_s = M_s / h_w = 35.7 \, kN$$

Displacement:

$$\Delta_s = V_s h_w^3 / (3 E_c I_c) = 0.93 \, \text{mm}$$

#### A.3.3 Tendons yielding (TY)

Moment about point A in Figure A.6(c):

$$M_y = C (l_w/2 - c \beta_2/2) = 161 \text{ kN.m}$$
  
 $C = P + T = c \beta_2 \alpha_2 f_{cc}' t_w = 296 \text{ kN}$   
 $T = A_p f_{py} = 208 \text{ kN}$ 

The values of  $\beta_2$  and  $\alpha_2$  can be determined according to the procedure presented [111].

Shear force:

$$V_V = M_V / h_W = 48.9 \text{ kN}$$

Displacement:

$$\theta_y = (\varepsilon_{py} - \varepsilon_{po}) h_p / (l_w/2 - c) = 0.026$$

$$\Delta_v = \theta_v h_w = 86.2 \text{ mm}$$

## A.3.4 Concrete crushing (CC)

Moment about point A in Figure A.6(c):

$$M_c = C (l_w/2 - c \beta_2/2) = 163 \text{ kN.m}$$
 $C = P + T = c \beta_2 \alpha_2 f_{cc}' t_w = 299 \text{ kN}$ 
 $T = A_p f_p = 211 \text{ kN}$ 
 $f_p = f_{py} + (\varepsilon_p - \varepsilon_{py}) E_{pt} = 1506 \text{ MPa}$ 
 $\varepsilon_p = \varepsilon_{po} + \theta_c (l_w/2 - c) / h_p = 0.0093$ 

The ultimate response of the wall was limited by the maximum drift ratio before the crushing of the concrete:

$$\theta_{\rm c} = 0.004$$

Shear force:

$$V_c = M_c / h_w = 49.3 \text{ kN}$$

Displacement:

$$\Delta_c = \theta_c h_w = 132.4 \text{ mm}$$

**REFERENCES** 

#### REFERENCES

- [1] A. Goretti, C. Molina Hutt, L. Hedelund, Post-earthquake safety evaluation of buildings in Portoviejo, Manabí province, following the Mw7.8 Ecuador earthquake of April 16, 2016, Int. J. Disaster Risk Reduct. 24 (2017) 271–283. doi:10.1016/j.ijdrr.2017.06.011.
- [2] J. Takagi, A. Wada, Recent earthquakes and the need for a new philosophy for earthquake-resistant design, Soil Dyn. Earthq. Eng. 119 (2018) 499–507. doi:10.1016/j.soildyn.2017.11.024.
- [3] X. Li, Strong motions and engineering structure performances in recent major earthquakes, Earthq. Sci. 23 (2010) 1–3. doi:10.1007/s11589-010-0004-7.
- [4] T. Paulay, M.J.N. Priestley, Seismic Design of Reinforced Concrete and Masonry Buildings, Wiley & Sons, New York, NY, 1992.
- [5] M.J.N. Priestley, G.M. Calvi, M.J. Kowalsky, Displacement-Based Seismic Design of Structures, IUSS Press, Pavia, Italy, 2007.
- [6] ASCE/SEI 7-10, Minimum Design Loads for Buildings and Other Structures, American Society of Civil Engineers, Reston, VA, 2010.
- [7] M.C. Constantinou, T.T. Soong, G.F. Dargush, Passive Energy Dissipation Systems for Structural Design and Retrofit, Multidisciplinary Center for Earthquake Engineering Research, Buffalo, NY, 1998.
- [8] J.B. Mander, C.T. Cheng, Seismic resistance of bridge piers based on damage avoidance design, National Center for Earthquake Engineering Research, Buffalo, NY, 1997.
- [9] M.D. Symans, F.A. Charney, A.S. Whittaker, M.C. Constantinou, C.A. Kircher, M.W. Johnson, R.J. McNamara, Energy dissipation systems for seismic applications: current practice and recent developments, J. Struct. Eng. 134 (2008) 3–21.
- [10] G. Puglisi, L. Truskinovsky, Rate independent hysteresis in a bi-stable chain, J. Mech. Phys. Solids. 50 (2002) 165–187. doi:10.1016/S0022-5096(01)00055-2.
- [11] N. Hu, R. Burgueño, Buckling-induced smart applications: recent advances and trends, Smart Mater. Struct. 24 (2015) 063001. doi:10.1088/0964-1726/24/6/063001.
- [12] S. Liu, Harnessing elastic instabilities for energy transduction, Doctoral dissertation, Michigan State University, 2019.
- [13] Z.P. Bažant, L. Cedolin, Stability of Structures: Elastic, Inelastic, Fracture and Damage Theories, World Scientific, Hackensack, NJ, 2010.
- [14] N.A. Alfutov, E. Evseev, Y.B. Balmont, Stability of Elastic Structures, 1st ed., Springer-

- Verlag Berlin Heidelberg, Berlin, Germany, 2000.
- [15] A. Madhukar, D. Perlitz, M. Grigola, D. Gai, K. Jimmy Hsia, Bistable characteristics of thick-walled axisymmetric domes, Int. J. Solids Struct. 51 (2014) 2590–2597. doi:10.1016/j.ijsolstr.2014.03.022.
- [16] A. Brinkmeyer, M. Santer, A. Pirrera, P.M. Weaver, Pseudo-bistable self-actuated domes for morphing applications, Int. J. Solids Struct. 49 (2012) 1077–1087. doi:10.1016/j.ijsolstr.2012.01.007.
- [17] J. Liu, H. Qin, Y. Liu, Dynamic behaviors of phase transforming cellular structures, Compos. Struct. 184 (2018) 536–544. doi:10.1016/j.compstruct.2017.10.002.
- [18] B.F. Feeny, A.R. Diaz, Twinkling phenomena in snap-through oscillators, J. Vib. Acoust. 132 (2010) 061013. doi:10.1115/1.4000764.
- [19] T. Frenzel, C. Findeisen, M. Kadic, P. Gumbsch, M. Wegener, Tailored buckling mcrolattices as reusable light-weight shock absorbers, Adv. Mater. 28 (2016) 5865–5870. doi:10.1002/adma.201600610.
- [20] S. Shan, S.H. Kang, J.R. Raney, P. Wang, L. Fang, F. Candido, J.A. Lewis, K. Bertoldi, Multistable architected materials for trapping elastic strain energy, Adv. Mater. 27 (2015) 4296–4301. doi:10.1002/adma.201501708.
- [21] B. Haghpanah, L. Salari-Sharif, P. Pourrajab, J. Hopkins, L. Valdevit, Multistable shape-reconfigurable architected materials, Adv. Mater. 28 (2016) 7915–7920. doi:10.1002/adma.201601650.
- [22] B. Haghpanah, A. Shirazi, L. Salari-Sharif, A. Guell Izard, L. Valdevit, Elastic architected materials with extreme damping capacity, Extrem. Mech. Lett. 17 (2017) 56–61. doi:10.1016/j.eml.2017.09.014.
- [23] C.S. Ha, R.S. Lakes, M.E. Plesha, Design, fabrication, and analysis of lattice exhibiting energy absorption via snap-through behavior, Mater. Des. 141 (2018) 426–437. doi:10.1016/j.matdes.2017.12.050.
- [24] T. Chen, J. Mueller, K. Shea, Design and fabrication of a bistable unit actuator with multimaterial additive manufacturing, in: 27th Annu. Int. Solid Free. Fabr. Symp., University of Texas at Austin, Austin, TX, 2016: pp. 2060–2076.
- [25] Y. Guan, L.N. Virgin, D. Helm, Structural behavior of shallow geodesic lattice domes, Int. J. Solids Struct. 155 (2018) 225–239.
- [26] D. Orlando, C.H.L. de Castro, P.B. Gonçalves, Nonlinear vibrations and instability of a bistable shallow reticulated truss, Nonlinear Dyn. 94 (2018) 1479–1499. doi:10.1007/s11071-018-4437-1.
- [27] S. Liu, A.I. Azad, R. Burgueño, Architected materials for tailorable shear behavior with

- energy dissipation, Extrem. Mech. Lett. 28 (2019) 1–7. doi:https://doi.org/10.1016/j.eml.2019.01.010.
- [28] A.G. Izard, R.F. Alfonso, G. McKnight, L. Valdevit, Optimal design of a cellular material encompassing negative stiffness elements for unique combinations of stiffness and elastic hysteresis, Mater. Des. 135 (2017) 37–50. doi:10.1016/j.matdes.2017.09.001.
- [29] D.M. Correa, T. Klatt, S. Cortes, M. Haberman, D. Kovar, C. Seepersad, Negative stiffness honeycombs for recoverable shock isolation, Rapid Prototyp. J. 21 (2015) 193–200. doi:10.1108/RPJ-12-2014-0182.
- [30] C. Ren, D. Yang, H. Qin, Mechanical performance of multidirectional Buckling-based Negative Stiffness metamaterials: An analytical and numerical study, Materials (Basel). 11 (2018). doi:10.3390/ma11071078.
- [31] Y. Gerson, S. Krylov, B. Ilic, D. Schreiber, Design considerations of a large-displacement multistable micro actuator with serially connected bistable elements, Finite Elem. Anal. Des. 49 (2012) 58–69. doi:10.1016/j.finel.2011.08.021.
- [32] H.T. Pham, D.A. Wang, A quadristable compliant mechanism with a bistable structure embedded in a surrounding beam structure, Sensors Actuators A Phys. 167 (2011) 438–448. doi:10.1016/j.sna.2011.02.044.
- [33] D. Restrepo, N.D. Mankame, P.D. Zavattieri, Phase transforming cellular materials, Extrem. Mech. Lett. 4 (2015) 52–60. doi:10.1016/j.eml.2015.08.001.
- [34] C. Findeisen, J. Hohe, M. Kadic, P. Gumbsch, Characteristics of mechanical metamaterials based on buckling elements, J. Mech. Phys. Solids. 102 (2017) 151–164. doi:10.1016/j.jmps.2017.02.011.
- [35] Q. Chen, X. Zhang, B. Zhu, Design of buckling-induced mechanical metamaterials for energy absorption using topology optimization, Struct. Multidiscip. Optim. 58 (2018) 1395–1410. doi:10.1007/s00158-018-1970-y.
- [36] A. Rafsanjani, A. Akbarzadeh, D. Pasini, Snapping mechanical metamaterials under tension, Adv. Mater. 27 (2015) 5931–5935. doi:10.1002/adma.201502809.
- [37] N. Kidambi, R.L. Harne, K.W. Wang, Energy capture and storage in asymmetrically multistable modular structures inspired by skeletal muscle, Smart Mater. Struct. 26 (2017) 1–15. doi:10.1088/1361-665X/aa721a.
- [38] P. Cazottes, A. Fernandes, J. Pouget, M. Hafez, Bistable buckled beam: Modeling of actuating force and experimental validations, J. Mech. Des. 131 (2009) 101001–101010. doi:http://dx.doi.org/10.1115/1.3179003.
- [39] S. Palathingal, G.K. Ananthasuresh, Design of bistable arches by determining critical points in the force-displacement characteristic, Mech. Mach. Theory. 117 (2017) 175–188. doi:10.1016/j.mechmachtheory.2017.07.009.

- [40] L.N. Virgin, Y. Guan, R.H. Plaut, On the geometric conditions for multiple stable equilibria in clamped arches, Int. J. Non. Linear. Mech. 92 (2017) 8–14. doi:10.1016/j.ijnonlinmec.2017.03.009.
- [41] J.F. Mescall, Large Deflections of Spherical Shells Under Concentrated Loads, J. Appl. Mech. 32 (1965) 936. doi:10.1115/1.3627340.
- [42] F.A. Penning, Experimental Buckling Modes of Clamped Shallow Shells Under Concentrated Load, J. Appl. Mech. (1966) 297–304. doi:10.1115/1.3625041.
- [43] J.R. Fitch, The buckling and post-buckling behavior of spherical caps under concentrated load, Int. J. Solids Struct. 4 (1968) 421–446. doi:10.1016/0020-7683(68)90048-6.
- [44] G.W. Brodland, H. Cohen, Deflection and snapping of spherical caps, Int. J. Solids Struct. 23 (1987) 1341–1356. doi:10.1016/0020-7683(87)90001-1.
- [45] N. Lajnef, R. Burgueño, W. Borchani, Y. Sun, A concept for energy harvesting from quasistatic structural deformations through axially loaded bilaterally constrained columns with multiple bifurcation points, Smart Mater. Struct. 23 (2014) 055005. doi:10.1088/0964-1726/23/5/055005.
- [46] S. Liu, R. Burgueño, Controlled elastic postbuckling of bilaterally constrained non-prismatic columns, Smart Mater. Struct. 25 (2016) 125010. doi:10.1088/0964-1726/25/12/125010.
- [47] R. Burgueño, N. Hu, A. Heeringa, N. Lajnef, Tailoring the elastic postbuckling response of thin-walled cylindrical composite shells under axial compression, Thin-Walled Struct. 84 (2014) 14–25. doi:10.1016/j.tws.2014.05.009.
- [48] N. Hu, R. Burgueño, Elastic postbuckling response of axially-loaded cylindrical shells with seeded geometric imperfection design, Thin-Walled Struct. 96 (2015) 256–268. doi:10.1016/j.tws.2015.08.014.
- [49] J.M. Kelly, R.I. Skinner, A.J. Heine, Mechanisms of energy absorption in special devices for use in earthquake resistant structures, Bull. New Zeal. Soc. Earthq. Eng. 5 (1972) 63–88.
- [50] A. Whittaker, V. Bertero, J. Alonso, C. Thompson, Earthquake simulator testing of steel plate added damping and stiffness elements, Earthquake Engineering Research Center, University of California at Berkeley, Berkeley, CA, 1989. doi:10.13140/RG.2.1.1455.3207.
- [51] M. Fujimoto, A. Wada, E. Saeki, T. Takeuchi, A. Watanabe, Development of unbonded brace, Q. Column. 115 (1990) 91–96.
- [52] R. Aghlara, M.M. Tahir, A passive metallic damper with replaceable steel bar components for earthquake protection of structures, Eng. Struct. 159 (2018) 185–197. doi:10.1016/j.engstruct.2017.12.049.

- [53] H. Tagawa, T. Yamanishi, A. Takaki, R.W.K. Chan, Cyclic behavior of seesaw energy dissipation system with steel slit dampers, J. Constr. Steel Res. 117 (2016) 24–34. doi:10.1016/j.jcsr.2015.09.014.
- [54] D.R. Sahoo, T. Singhal, S.S. Taraithia, A. Saini, Cyclic behavior of shear-and-flexural yielding metallic dampers, J. Constr. Steel Res. 114 (2015) 247–257. doi:10.1016/j.jcsr.2015.08.006.
- [55] M. Jarrah, H. Khezrzadeh, M. Mofid, K. Jafari, Experimental and numerical evaluation of piston metallic damper (PMD), J. Constr. Steel Res. 154 (2019) 99–109. doi:10.1016/j.jcsr.2018.11.024.
- [56] M.D. Titirla, P.K. Papadopoulos, I.N. Doudoumis, Finite element modelling of an innovative passive energy dissipation device for seismic hazard mitigation, Eng. Struct. 168 (2018) 218–228. doi:10.1016/j.engstruct.2018.04.081.
- [57] M. Raquibul Hossain, M. Ashraf, F. Albermani, Numerical modelling of yielding shear panel device for passive energy dissipation, Thin-Walled Struct. 49 (2011) 1032–1044. doi:10.1016/j.tws.2011.03.003.
- [58] S. Demir, M. Husem, Saw type seismic energy dissipaters: development and cyclic loading test, J. Constr. Steel Res. 150 (2018) 264–276. doi:10.1016/j.jcsr.2018.08.015.
- [59] M. Motamedi, F. Nateghi-A, Study on mechanical characteristics of accordion metallic damper, 142 (2018) 68–77.
- [60] A.S. Pall, C. Marsh, P. Fazio, Friction Joints for Seismic Control of Large Panel Structures, J. Prestress. Concr. Inst. 25 (1980) 38–61. doi:10.15554/pcij.11011980.38.61.
- [61] B.G. Morgen, Y.C. Kurama, Characterization of two friction interfaces for use in seismic damper applications, Mater. Struct. 42 (2009) 35–49. doi:10.1617/s11527-008-9365-y.
- [62] J. Erochko, C. Christopoulos, R. Tremblay, Design, testing, and detailed component modeling of a high-capacity self-centering energy-dissipative brace, J. Struct. Eng. 141 (2014) 04014193. doi:10.1061/(asce)st.1943-541x.0001166.
- [63] A. Issa, Innovative spring & piston based self-centering bracing systems for enhanced seismic performance of buildings, University of British Columbia, 2018.
- [64] M. Carfagni, E. Lenzi, M. Pierini, The loss factor as a measure of mechanical damping, in: 16th Int. Modal Anal. Conf., Society for Experimental Mechanics, Bethel, CT, 1998: pp. 580–584.
- [65] W. Wang, C. Fang, A. Zhang, X. Liu, Manufacturing and performance of a novel self-centring damper with shape memory alloy ring springs for seismic resilience, Struct. Control Heal. Monit. 26 (2019) 1–17. doi:10.1002/stc.2337.
- [66] J.W. Hu, M.-H. Noh, Seismic response and evaluation of SDOF self-centering friction

- damping braces subjected to several earthquake ground motions, Adv. Mater. Sci. Eng. 2015 (2015) 1–17. doi:10.1155/2015/397273.
- [67] C. Christopoulos, R. Tremblay, H.-J. Kim, M. Lacerte, Self-centering energy dissipative bracing system for the seismic resistance of structures: Development and validation, J. Struct. Eng. 134 (2008) 96–107. doi:10.1061/(asce)0733-9445(2008)134:1(96).
- [68] M. Alturki, R. Burgueño, Response characterization of multistable shallow domes with cosine-curved profile, Thin-Walled Struct. 140 (2019) 74–84. doi:10.1016/j.tws.2019.03.035.
- [69] M. Radwanska, A. Stankiewicz, A. Wosatko, J. Pamin, Plate and Shell Structures, Wiley & Sons, Kraków, Poland, 2017.
- [70] B. Fedelich, G. Zanzotto, Hysteresis in discrete systems of possibly interacting elements with a double-well energy, J. Nonlinear Sci. 2 (1992) 319–342. doi:10.1007/BF01208928.
- [71] M. Vangbo, An analytical analysis of a compressed bistable buckled beam, Sensors Actuators A Phys. 69 (1998) 212–216. doi:https://doi.org/10.1016/S0924-4247(98)00097-1.
- [72] J. Qiu, J.H. Lang, A.H. Slocum, A curved-beam bistable mechanism, J. Microelectromechanical Syst. 13 (2004) 137–146. doi:10.1109/JMEMS.2004.825308.
- [73] Dassault Systèmes, Abaqus user manual, Dassault Systemes, Providence, RI, 2012.
- [74] C.S. Lee, S.G. Kim, H.J. Kim, S.H. Ahn, Measurement of anisotropic compressive strength of rapid prototyping parts, J. Mater. Process. Technol. 187–188 (2007) 627–630. doi:10.1016/j.jmatprotec.2006.11.095.
- [75] C. Casavola, A. Cazzato, V. Moramarco, C. Pappalettere, Orthotropic mechanical properties of fused deposition modelling parts described by classical laminate theory, Mater. Des. 90 (2016) 453–458. doi:10.1016/j.matdes.2015.11.009.
- [76] C. Perkowski, Tensile-compressive asymmetry and anisotropy of fused deposition modeling PLA under monotonic conditions, Master's theses, University of Central Florida, 2017.
- [77] Scott A. Pardo, Empirical Modeling and Data Analysis for Engineers and Applied Scientists, Springe, Parsippany, NJ, 2016. doi:10.1007/978-3-319-32768-6.
- [78] I. Benichou, S. Givli, Structures undergoing discrete phase transformation, J. Mech. Phys. Solids. 61 (2013) 94–113. doi:https://doi.org/10.1016/j.jmps.2012.08.009.
- [79] M. Alturki, R. Burgueño, Multistable cosine-curved dome system for elastic energy dissipation, J. Appl. Mech. 86 (2019) 091002. doi:10.1115/1.4043792.
- [80] Jeroen G. W. Raaijmakers, Statistical analysis of the Michaelis-Menten equation,

- Biometrics. 43 (1987) 793–803.
- [81] D. Radomirovic, I. Kovacic, An equivalent spring for nonlinear springs in series, Eur. J. Phys. 36 (2015) 055004. doi:10.1088/0143-0807/36/5/055004.
- [82] M. Alturki, R. Burgueño, Equivalent viscous damping for system with energy dissipation via elastic instabilities, Eng. Struct. In review (n.d.).
- [83] M.J.N. Priestley, Performance based seismic design, in: 12th World Conf. Earthq. Eng., New Zealand Society for Earthquake Engineering, Upper Hutt, New Zeland, 2000: p. 2831.
- [84] M.J.N. Priestley, D.N. Grant, Viscous damping in seismic design and analysis, J. Earthq. Eng. 9 (2005) 229–255. doi:10.1142/S1363246905002365.
- [85] C.A. Blandon, M.J.N. Priestley, Equivalent viscous damping equations for direct displacement based design, J. Earthq. Eng. 9 (2005) 257–278. doi:10.1142/S1363246905002390.
- [86] H.M. Dwairi, M.J. Kowalsky, J.M. Nau, Equivalent damping in support of direct displacement-based design, J. Earthq. Eng. 11 (2007) 512–530. doi:10.1080/13632460601033884.
- [87] D. Pennucci, T.J. Sullivan, G.M. Calvi, Displacement reduction factors for the design of medium and long period structures, J. Earthq. Eng. 15 (2011) 1–29. doi:10.1080/13632469.2011.562073.
- [88] E. Khan, M.J. Kowalsky, J.M. Nau, Equivalent viscous damping model for short period reinforced concrete bridges, J. Bridg. Eng. 21 (2016) 04015047. doi:10.1061/(ASCE)BE.1943-5592.0000803.
- [89] A.K. Chopra, Dynamics of Structures: Theory and Applications to Earthquake Engineering, 4th ed., Prentice Hall, Upper Saddle River, NJ, 2012.
- [90] L.S. Jacobsen, Steady forced vibration as influenced by damping, Trans. Am. Soc. Mech. Eng. 52 (1930) 169–181.
- [91] E. Miranda, J. Ruiz-Garca, Evaluation of approximate methods to estimate maximum inelastic displacement demands, Earthq. Eng. Struct. Dyn. 31 (2002) 539–560. doi:10.1002/eqe.143.
- [92] A.H. Hadjian, A re-evaluation of equivalent linear models for simple yielding systems, Earthq. Eng. Struct. Dyn. 10 (1982) 759–767. doi:10.1002/eqe.4290100602.
- [93] P.C. Jennings, Periodic response of a general yielding structure, J. Eng. Mech. Div. 90 (1964) 131–166.
- [94] P.C. Jennings, Equivalent viscous vamping for yielding structures, J. Eng. Mech. Div. 94 (1968) 103–116.

- [95] W.D. Iwan, N.C. Gates, The effective period and damping of a class of hysteretic structures, Earthq. Eng. Struct. Dyn. 7 (1979) 199–211. doi:10.1002/eqe.4290070302.
- [96] E. Miranda, Inelastic displacement ratios for structures on firm sites, J. Struct. Eng. 126 (2000) 1150–1159.
- [97] Federal Emergency Management Agency, Improvement of nonlinear static seismic analysis procedures, Washington, D.C., 2005.
- [98] J.F. Hall, Problems encountered from the use (or misuse) of Rayleigh damping, Earthq. Eng. Struct. Dyn. 35 (2006) 525–545. doi:10.1002/eqe.541.
- [99] F.A. Charney, Unintended consequences of modeling damping in structures, J. Struct. Eng. 134 (2008) 581–592. doi:10.1061/(ASCE)0733-9445(2008)134:4(581).
- [100] L. Petrini, C. Maggi, M.J.N. Priestley, G.M. Calvi, Experimental verification of viscous damping modeling for inelastic time history analyzes, J. Earthq. Eng. 12 (2008) 125–145. doi:10.1080/13632460801925822.
- [101] G.L. Mazzoni, S., McKenna, F., Scott, M. H., & Fenves, OpenSees command language manual, 2006.
- [102] D.S. Moore, G.P. McCable, B.A. Craig, Introduction to the practice of statistics, 6th ed., W.H. Freeman, New York, NY, 2009.
- [103] AASHTO, LRFD Bridge Design Specifications, 6th Editio, American Association of State Highway and Transportation Officials, Washington, D.C., 2012.
- [104] AASHTO, Guide Specification for LRFD Seismic Bridge Design, 2nd Editio, American Association of State Highway and Transportation Officials, Washington, DC, 2011.
- [105] M. Alturki, R. Burgueño, Displacement-based design procedure for ductile reinforced concrete bridge pier walls, ACI Struct. J. 114 (2017) 1407–1416. doi:10.14359/51689497.
- [106] R.C. Hibbeler, Structural Analysis, 6th ed., Pearson Prentice Hall, Upper Saddle River, NJ, 2006.
- [107] F. McKenna, G.L. Fenves, M.H. Scott, Open System for Earthquake Engineering Simulation, (2004).
- [108] ACI Committee 318, Building Code Requirements for Structural Concrete (ACI 318-14) and Commentary, American Concrete Institute, Farmington Hills, MI., 2014.
- [109] H.A.D.S. Buddika, A.C. Wijeyewickrema, Seismic shear forces in post-tensioned hybrid precast concrete walls, J. Struct. Eng. 144 (2018) 04018086. doi:10.1061/(ASCE)ST.1943-541X.0002079.
- [110] T. Holden, J. Restrepo, J.B. Mander, Seismic performance of precast reinforced and

- prestressed concrete walls, J. Struct. Eng. 129 (2003) 286–296. doi:10.1061/(ASCE)0733-9445(2003)129:3(286).
- [111] S. Aaleti, S. Sritharan, A simplified analysis method for characterizing unbonded posttensioned precast wall systems, Eng. Struct. 31 (2009) 2966–2975. doi:10.1016/j.engstruct.2009.07.024.
- [112] D. Marriott, S. Pampanin, D. Bull, A. Palermo, Dynamic testing of precast, post-tensioned rocking wall systems with alternative dissipating solutions, Bull. New Zeal. Soc. Earthq. Eng. 41 (2008) 90–103.
- [113] SAP2000, Integrated Software for Structural Analysis and Design, Computers and Structures, Inc, Berkeley, CA, 2019.
- [114] J.B. Mander, M.J. Priestley, R. Park, Theoretical stress-strain model for confined concrete, J. Struct. Eng. 114 (1988) 1804–1826. doi:10.1061/(ASCE)0733-9445(1988)114:8(1804).